

White matter hyperintensities in sporadic and familial Alzheimer's disease: investigations into their pathological basis and biomarker potential

Ella Phoebe Walsh

A dissertation submitted in partial fulfillment
of the requirements for the degree of
Doctor of Philosophy
of
University College London.

Dementia Research Centre
Queen Square Brain Bank of Neurological Disorders
University College London

June 24, 2021

I, Ella Phoebe Walsh, confirm that the work presented in this thesis is my own. Where information has been derived from other sources, I confirm that this has been indicated in the work.

Abstract

This thesis is a detailed investigation into white matter hyperintensities (WMHs) in Alzheimer's disease (AD). WMHs, of presumed vascular origin, are increasingly recognised in the aetiology of AD. However their underlying pathology may be variable and their relationship to the hallmark pathological features of AD is not yet fully understood.

Associations of WMHs with CSF amyloid beta ($A\beta$) and tau at baseline were explored in a cohort from the Alzheimer's Disease Neuroimaging Initiative (ADNI). A further study in ADNI was carried out exploring associations between plasma neurofilament light (NFL) and WMHs. WMH accrual across the disease course was modelled using longitudinal data from the Dominantly Inherited Alzheimer Network (DIAN) cohort. Finally, to enable exploration of the pathological basis of WMHs, an *ex vivo* MRI pipeline with subsequent pathological investigations was developed and carried out.

Firstly, a higher WMH burden was found to associate with lower CSF $A\beta$ across diagnostic groups, but no significant associations were found with CSF tau biomarkers. Plasma NFL was found to associate with WMHs, in an age dependent, but vascular-risk independent manner. Secondly, WMH accrual was found to increase throughout the disease course as demonstrated by associations with estimated years to onset (EYO) in the DIAN cohort. The highest rate of accrual was seen in the *APP* mutation group. Additionally, WMHs and brain atrophy changes were shown to track together across the disease course. Lastly, the *ex vivo*-histology pipeline was shown to be effective, enabling the registration of multiple modalities and revealing varying degrees of myelin loss.

In summary, this work extends existing knowledge about how WMHs associate with classical AD markers such as $A\beta$, tau and brain atrophy. Furthermore this work suggests that, instead of just reflecting vascular comorbidity, WMHs are a core feature of AD.

Impact Statement

Alzheimer's disease (AD) is a neurodegenerative disease with no effective treatment or cure. Not only does AD have debilitating consequences for patients and carers, it places a huge socio-economic burden on society as a whole. Evidence suggests that AD is a multifactorial disease for which early intervention is necessary for effective treatment. It is therefore imperative that biomarkers identifying early-stage disease, as well as capturing the full spectrum of pathological changes, are identified and characterised. This thesis investigates white matter hyperintensities (WMHs) as a potential biomarker of AD.

A key finding in this PhD is that WMHs associate with amyloid beta ($A\beta$) across the full disease course. This result aids understanding of how WMHs interact with other AD biomarkers and creates opportunities for further research into the mechanism underlying this finding. The fact that my paper on this work has been cited five times since its publication last year in 2020, shows that there is active demand for this research.

In Chapter 5 I provided evidence that WMHs are an important marker of disease progression in a cohort of autosomal dominant inherited AD (ADAD) patients and their relatives. As well as being an important finding in terms of the use of WMHs as a biomarker, very little research into WMHs in ADAD has been carried out previously, meaning that this work will be important to the AD field. I also found differences in WMH accrual between mutation groups, which has important implications for future treatments in ADAD as it highlights the heterogeneous nature of the disease.

In Chapter 6 I developed a novel MRI-histology pipeline in order to answer key

and under-researched questions about the underlying pathology of an MRI signal. The impact of the development of this methodology could be substantial, providing the starting point for a tool that could predict the underlying pathology of WMHs based on appearance and location, for eventual use in a clinical setting.

WMHs have long been considered a marker of SVD, however I have shown how WMH are increased in AD and associated with key AD biomarkers, both in a cohort of low vascular risk (ADNI) and in a young ADAD cohort (DIAN). This thesis provides important evidence that WMH on their own should not automatically be taken as evidence of a vascular contribution.

Acknowledgements

Much of the work in this thesis has used MRI scans from individuals who have participated in the ADNI and DIAN studies, and individuals who have donated brain tissue. I would like to thank these people for their generous contributions to research, as without them this work would not have been possible.

I would like to thank my supervisors, Dr Jo Barnes, Professor Tammarnyn Lashley and Dr Natalie Ryan for all their help and support throughout my PhD. They have truly been the best supervisors I could have asked for, and have consistently gone out of their way to make it an enjoyable experience for me. Thank you Jo for our weekly catch-up meetings, where your enthusiasm and warmth made first thing on a Monday morning something to look forward to. Thank you to Tammarnyn for all your support over the years, you are truly an inspirational supervisor and scientist who finds time for everyone. Thank you to Natalie for all your enthusiasm and wisdom, and for your ability to provide extremely helpful guidance across all of my projects, even when you were on maternity leave.

I am also extremely grateful to my funders, the Leonard Wolfson Foundation, and to Professor Nick Wood for leading the Wolfson Neurodegeneration PhD program. Thanks also to Desmond Bates who has provided much needed assistance throughout the COVID-19 pandemic. I also owe a great deal of thanks to Elizabeth Halton, who has provided support in all aspects of my PhD.

Thank you to all my collaborators Dr Carole Sudre, Professor Chris Frost, Dr Jennifer Nicholas, Dr David Thomas, Tom Veale, Dr David Cash, Dr Emily Manning, Dr Eugenio Iglesias, Shauna Crampsie, Dr Zane Zaubmukatane and Professor Nick Fox. I am especially grateful to Professor Chris Frost for all his outstanding

statistical support.

Thank you to all my friends at the Queen Square Brain Bank for making my time there so enjoyable - Dr Christina Toomey, Dr Sandrine Foti, Dr Lauren Gittings, Dr Melissa Wren, Alex Bampton, Dr Yasmine Asi, Dr Ariana Gatt, Dr Barbara Frias Garrido, Dr Zeinab Abdi, Dr Conceicao Bettencourt, Neve Costello Heaven, Kate Strand and Rob Courtney.

Thank you to all my friends at the Dementia Research Centre - Tom Veale, Dr Emily Manning, Dr Cassy Fiford, Dr Martina Bochetta, Dilek Ocal, Maggie Fraser, Lloyd Prosser and Dr Ian Malone.

Finally thank you to Will, Mum, Dad and Ron for always being there with whatever I need, especially during this last year of COVID-19. Writing my PhD locked down with you all made it all the more bearable.

Contents

1	Introduction	25
1.1	Background	25
1.2	Alzheimer's disease	27
1.2.1	The Amyloid cascade hypothesis	27
1.2.2	Preclinical AD: a window of opportunity?	30
1.2.3	Beyond amyloid and tau: a multifactorial disease	31
1.2.4	Autosomal dominant inherited Alzheimer's disease	32
1.3	Cerebrovascular disease and Alzheimer's disease	35
1.3.1	Overview	35
1.3.2	Shared risk factors	36
1.3.3	Vascular pathology in AD	37
1.3.4	Interactions between AD pathology and CVD	39
1.4	Biomarkers in Alzheimer's disease	40
1.4.1	Overview	40
1.4.2	Fluid biomarkers	42
1.4.3	Imaging biomarkers	43
1.4.4	Modelling of biomarkers	47
1.5	White matter hyperintensities	49
1.5.1	Overview	49
1.5.2	Relevance of WMHs to AD	50
1.5.3	Underlying Pathology of WMHs	51
1.5.4	Pathogenic mechanisms of WMH formation	51
1.5.5	Quantification	53

1.6	Thesis rationale	54
2	Methods	57
2.1	Cohorts	57
2.1.1	ADNI	57
2.1.2	DIAN	58
2.2	In vivo MRI acquisition	59
2.2.1	ADNI	59
2.2.2	DIAN	59
2.3	MRI analysis	59
2.3.1	WMH segmentation	59
2.3.2	Boundary shift integral	63
2.3.3	Total intracranial volume (TIV)	63
2.4	Pathology	63
2.4.1	Cases	63
2.4.2	Histological staining	64
2.4.3	Immunohistochemistry	64
2.5	Software	65
2.5.1	NiftyMIDAS	65
2.5.2	Stata	66
2.5.3	Olympus VS-desktop	66
2.5.4	ImageJ	66
3	Associations of WMHs and CSF biomarkers in sporadic AD	67
3.1	Introduction	67
3.2	Methods	68
3.2.1	Cohort	68
3.2.2	WMH segmentation	68
3.2.3	CSF measurements	69
3.2.4	Statistical analyses	70
3.3	Results	73

3.3.1	WMH segmentation training	73
3.3.2	Group demographics	73
3.3.3	WMHs and age	74
3.3.4	CSF biomarkers and age	75
3.3.5	CSF biomarkers and WMHs in each group	79
3.3.6	CSF biomarkers and WMHs in the full cohort	83
3.3.7	Vascular risk analysis	87
3.3.8	Parietal lobe vs whole brain analysis	87
3.4	Discussion	90
4	Associations of WMHs and plasma NFL in sporadic AD	96
4.1	Introduction	96
4.2	Methods	97
4.2.1	Cohort	97
4.2.2	Plasma NFL measurements	97
4.2.3	WMH segmentation	97
4.2.4	Statistical analyses	98
4.3	Results	100
4.3.1	Group demographics and biomarker summary	100
4.3.2	Plasma NFL and WMHs	101
4.3.3	NFL and age	102
4.3.4	NFL and $A\beta$	104
4.3.5	Plasma NFL and WMHs: sensitivity analyses	105
4.3.6	Exploring the WMHs and NFL relationship: the potential role for vascular risk	106
4.4	Discussion	106
5	Associations of WMHs and brain atrophy in ADAD	112
5.1	Introduction	112
5.1.1	Cohort	113
5.1.2	Quality control	113

5.1.3	WMH segmentation	114
5.1.4	Brain volume	118
5.1.5	Statistical analysis	118
5.2	Results	121
5.2.1	Demographic and imaging summary statistics	121
5.2.2	WMH change over time by mutation group	123
5.2.3	WMH change over time by symptom group	125
5.2.4	WMH change and associations with estimated years to onset	126
5.2.5	Jointly modelling brain volume and WMH changes	128
5.3	Discussion	129
6	Pathological investigations of WMHs using <i>ex vivo</i> MRI with histological correlations	134
6.1	Introduction	134
6.1.1	Literature review: <i>ex vivo</i> MRI-histology correlations in the study of WMHs	135
6.1.2	Gaps in the literature	149
6.1.3	Aims	149
6.2	Methods	150
6.2.1	<i>In vivo</i> MRI imaging	152
6.2.2	Brain donation	152
6.2.3	<i>Ex vivo</i> MRI imaging	152
6.2.4	Brain sampling	153
6.2.5	Brain sectioning and histology	154
6.2.6	Staining analysis	155
6.2.7	MRI image registration	157
6.2.8	Registration of <i>ex vivo</i> MRI and histological sections	160
6.2.9	WMH segmentation and assessment of WMH change	160
6.3	Results	163
6.3.1	Demographics	163
6.3.2	White matter hyperintensities	163

6.3.3	Question 1: Can high quality <i>ex vivo</i> MRI images be obtained?	169
6.3.4	Question 2: Is registration of <i>in vivo</i> and <i>ex vivo</i> MRI scans possible?	172
6.3.5	Question 3: Is registration of histological sections to <i>ex vivo</i> MRI images possible?	178
6.3.6	Question 4: Can similarities or differences in WMHs between the last <i>in vivo</i> MRI and the <i>ex vivo</i> scan be observed?	180
6.3.7	Question 5: Can any pathological changes be observed in regions of WMHs?	184
6.4	Discussion	196
6.4.1	Question 1: Can high quality <i>ex vivo</i> MRI images be obtained?	198
6.4.2	Question 2: Is registration of <i>in vivo</i> and <i>ex vivo</i> MRI scans possible?	199
6.4.3	Question 3: Is registration of histological sections to <i>ex vivo</i> MRI images possible?	200
6.4.4	Question 4: Can similarities or differences in WMHs between the last <i>in vivo</i> MRI and the <i>ex vivo</i> scan be observed?	202
6.4.5	Question 5: Can any pathological changes be observed in regions of WMHs?	205
6.5	Limitations	209
6.6	Future directions of study	213
6.7	Conclusions	216
7	General Discussion	217
7.1	Summary of main findings	218
7.1.1	Chapter 3	218
7.1.2	Chapter 4	219
7.1.3	Chapter 5	219
7.1.4	Chapter 6	220
7.2	Importance of this work	221

Contents

14

8 Contributions

223

9 Publications

225

Bibliography

226

List of Tables

1.1	NIA-AA Biomarker profiles and categories.	41
3.1	Demographic, imaging and CSF summary statistics	74
3.2	Regression model results for the relationship between WMHs and age, by group	74
3.3	Regression model results for the relationship between CSF biomarkers and age, by group	78
3.4	Regression model results for the relationship between WMHs and CSF A β 1-42, by group	79
3.5	Regression model results for the relationship between WMH and CSF t-tau, by group	80
3.6	Regression model results for the relationship between WMHs and CSF p-tau, by group	81
3.7	Elecsys CSF summary statistics, by group.	82
3.8	Regression model results for the relationship between WMHs and CSF A β 1-42 (Elecsys assay), by group	82
3.9	Regression model results for the relationship between WMHs and CSF t-tau (Elecsys assay), by group	83
3.10	Regression model results for the relationship between WMHs and CSF p-tau (Elecsys assay), by group	83
3.11	Regression model results examining the association between CSF A β 1-42 and WMHs with various covariates	84
3.12	Regression model results examining the association between CSF t-tau and WMHs with various covariates	85

3.13	Regression model results examining the association between CSF p-tau and WMHs with various covariates	86
3.14	Regression model results for the relationship between WMHs and age by group, adjusting for vascular risk	88
3.15	Regression models results for the relationship between WMHs and CSF $A\beta$ 1-42 with adjustment for smoking status, history of hypertension, history of diabetes and BMI by group	89
3.16	Regression models of the associations between CSF biomarkers and either the parietal lobe WMHs or the rest of the brain WMHs.	89
4.1	Demographic and imaging data summary statistics	101
4.2	Regression model results for the relationship between WMHs and plasma NFL, by group	102
4.3	Regression model results for the relationship between plasma NFL and age, by diagnostic group	104
4.4	Regression model results for the relationship between plasma NFL and WMH, divided into those who are $A\beta$ positive and $A\beta$ negative.	104
4.5	Regression model results for the relationship between WMHs and plasma NFL by diagnostic group, after the inclusion of two outliers	105
4.6	Regression models results for the relationship between WMHs and plasma NFL with adjustment for smoking status, history of hypertension, history of diabetes and BMI by group	106
5.1	DIAN subset selection	115
5.2	Differences in segmentation methods in assessing WMH change over time from mixed effect modelling	118
5.3	Demographic and imaging data in each mutation group	122
5.4	Frequency of participants with each maximum visit number, in each mutation group	122
5.5	Regression model results for the mean change in WMHs over time, in each mutation group	123

5.6	Regression model results for the mean change in WMHs over time, in each symptom group	125
5.7	Regression model results for the relationship between WMHs and estimated years to onset, in each mutation group	126
6.1	Studies using <i>ex vivo</i> MRI-histology correlation to characterise WMHs	136
6.2	Clinical, imaging and pathological information	162
6.3	Grade of lesion change.	180
6.4	Regression results for difference in percentage area of MBP staining in NAWM vs WMHs	184
6.5	Regression results for the percentage area of SMI31 staining in WMHs vs NAWM	184
6.6	Increased panel of staining	214

List of Figures

1.1	The order of major pathogenic events leading to AD, as set out in the amyloid cascade hypothesis.	28
1.2	The order of major pathogenic events leading to AD, as set out in the amyloid cascade hypothesis.	31
1.3	Schematic overview of genes linked to Alzheimer’s disease.	33
1.4	The relationship between VCI and vascular dementia.	36
1.5	T1-weighted image and T2 FLAIR weighted images demonstrating white matter hyperintensities (WMHs).	49
1.6	Common hyperintense artefact.	54
3.1	Scatter plots showing a) the comparison of the raw WMH volumes segmented using BaMoS and the semi-automated protocol and b) Dice score coefficients demonstrating the degree of overlap.	73
3.2	Box plot showing WMH volume per group	75
3.3	Scatter plots showing the relationship between WMHs and age in controls, SMC, EMCI, LMCI and AD groups.	76
3.4	Scatter plots showing the relationship between CSF A β 1-42 and age in controls, SMC, EMCI, LMCI and AD groups.	76
3.5	Scatter plots showing the relationship between CSF t-tau and age in controls, SMC, EMCI, LMCI and AD groups.	77
3.6	Scatter plots showing the relationship between CSF p-tau and age in controls, SMC, EMCI, LMCI and AD groups.	77
3.7	Scatter plots showing the relationship between WMHs and CSF A β 1-42 in controls, SMC, EMCI, LMCI and AD groups.	79

3.8	Scatter plots showing the relationship between WMHs and CSF τ in controls, SMC, EMCI, LMCI and AD groups.	80
3.9	Scatter plots showing the relationship between WMHs and CSF $p\tau$ in controls, SMC, EMCI, LMCI and AD groups.	81
4.1	Scatter plots showing the relationship between WMHs and plasma NFL in controls, SMC, EMCI, LMCI and AD groups.	103
4.2	Scatter plots showing the relationship between plasma NFL and age in controls, SMC, EMCI, LMCI and AD groups.	103
5.1	A scatter plot demonstrating similarities in the BaMoS generated baseline WMH segmentation volumes from FLAIR and T1 space . .	116
5.2	Bland-Altman plot of BaMoS generated baseline WMH volumes compared to semi-automated baseline WMH volumes.	117
5.3	A scatter plot showing the Dice score coefficient as a measure of segmentation overlap between the BaMoS and semi-automated volumes, against the mean WMH volume	118
5.4	Plots showing WMH change over time for each participant in a) non-carriers, b) <i>PSEN1</i> , c) <i>PSEN2</i> and d) <i>APP</i> mutation groups. . .	124
5.5	Plots showing WMH change over time for each participant in a) non-carriers, b) P-Sym, c) Q-Sym and d) Sym mutation groups. . . .	125
5.6	Plots of WMH accrual with estimated years to onset in each mutation group.	127
5.7	Scatter plots showing the crude relationship between atrophy rate and WMH accrual rate for a) <i>PSEN1</i> , b) <i>PSEN2</i> and c) <i>APP</i>	128
6.1	The full pipeline for the correlation of <i>ex vivo</i> imaging and histology	151
6.2	Grading of the ventricular ependymal lining.	155
6.3	The pipeline for the registration of the <i>ex vivo</i> T2-weighted and <i>in vivo</i> T1-weighted and FLAIR images	158
6.4	A demonstration of the imperfect alignment achieved when the <i>in vivo</i> WMH segmentation is transformed to the <i>ex vivo</i> space.	161

6.5	Lesion guide for Cases 1-5.	168
6.6	Plots showing the coefficient of variation for the whole brain region with the addition of each subsequent acquisition for all Cases 1-5 . . .	170
6.7	Plots showing the coefficient of variation for the 10 grey matter regions with the addition of each subsequent acquisition for all Cases 1-5.	170
6.8	Plots showing the coefficient of variation for the 10 white matter regions with the addition of each subsequent acquisition for all Cases 1-5.	171
6.9	Images demonstrating the hippocampus on the <i>ex vivo</i> T2-weighted images for Case 5, with the addition of each acquisition.	171
6.10	Example coronal, sagittal and axial slices of the <i>ex vivo</i> MRI T2-weighted scan (an average of all five acquisitions) for Case 5.	172
6.11	T1-weighted images for Case 5, in which the f3d non-linear registration was carried out with the default linear elasticity of 0.01 and then with a linear elasticity of 0.	173
6.12	T1-weighted images for Case 5, in which the spline options were varied to give control points at 3, 5, 10 and 15mm spacings.	174
6.13	T1-weighted images for Case 5, in which the bending energy was varied between 0.00001 and 0.1.	174
6.14	Unsuccessfully registered T1-weighted images for Case 5, where landmarks were used to try and improve the registration.	175
6.15	Non-linearly registered <i>ex vivo</i> T2, <i>in vivo</i> T1-weighted and <i>in vivo</i> FLAIR images in a) <i>ex vivo</i> T2-weighted image space and b) <i>in vivo</i> FLAIR space, for Case 1.	176
6.16	Non-linearly registered <i>ex vivo</i> T2, <i>in vivo</i> T1-weighted and <i>in vivo</i> FLAIR images in a) <i>ex vivo</i> T2-weighted image space and b) <i>in vivo</i> FLAIR space, for Case 2.	176

6.17	Non-linearly registered <i>ex vivo</i> T2, <i>in vivo</i> T1-weighted and <i>in vivo</i> FLAIR images in a) <i>ex vivo</i> T2-weighted image space and b) <i>in vivo</i> FLAIR space, for Case 3.	177
6.18	Non-linearly registered <i>ex vivo</i> T2, <i>in vivo</i> T1-weighted and <i>in vivo</i> FLAIR images in a) <i>ex vivo</i> T2-weighted image space and b) <i>in vivo</i> FLAIR space, for Case 4.	177
6.19	Non-linearly registered <i>ex vivo</i> T2, <i>in vivo</i> T1-weighted and <i>in vivo</i> FLAIR images in a) <i>ex vivo</i> T2-weighted image space and b) <i>in vivo</i> FLAIR space, for Case 5.	178
6.20	<i>Ex vivo</i> T2-weighted scans for Case 5 registered into the space of the histological section, shown with the corresponding H&E, LFB, MBP and SMI31 stained sections.	179
6.21	<i>Ex vivo</i> T2-weighted scans for Case 3 registered into the space of the histological section, shown with the corresponding stained sections.	180
6.22	Example lesions from Case 1	181
6.23	Example lesions from Case 2	182
6.24	Example lesions from Case 3	182
6.25	Example lesions from Case 4	183
6.26	Example lesions from Case 5	183
6.27	Graphs to show differences in % area of a) MBP and b) SMI31 staining between NAWM and WMHs in each lesion.	185
6.28	Immunohistochemical staining example for the a) MBP and b) SMI31 antibodies.	186
6.29	A tortuous ependymal layer.	186
6.30	Segmental intramyelin oedemas	187
6.31	<i>In vivo</i> MRI, <i>ex vivo</i> MRI and histological staining for example lesions.	195
6.32	Figure from Cognat et al. (2014) showing segmental intramyelin oedema using electron microscopy.	207

Acronyms

ADAD Autosomal dominant inherited Alzheimer's disease.

ADNI Alzheimer's Disease Neuroimaging Initiative.

APOE Apolipoprotein E.

APP Amyloid precursor protein.

AxD Axial diffusivity.

BaMoS Bayesian Model Selection.

BMI Body mass index.

BSI Boundary shift integral.

CAA Cerebral amyloid angiopathy.

CADASIL Cerebral Autosomal Dominant Arteriopathy with Subcortical Infarcts and Leukoencephalopathy.

CSF Cerebrospinal fluid.

CVD Cerebrovascular disease.

DAB Diaminobenzidine.

DIAN Dominantly Inherited Alzheimer's Disease Network.

DIAN-TU Dominantly inherited Alzheimer's Network trials unit.

EMCI Early mild cognitive impairment.

EYO Estimated years to onset.

FA Fractional anisotropy.

FDG Fluoro-deoxy-D-glucose.

GIF Geodesic Information Flows.

H&E Hematoxylin and oesin.

LFB Luxol fast blue.

LMCI Late mild cognitive impairment.

MAO Monoamine oxidase.

MBP Myelin basic protein.

MCI Mild cognitive impairment.

MD Mean diffusivity.

MMSE Mini-Mental State Exam.

MS Multiple sclerosis.

NAWM Normal appearing white matter.

NFL Neurofilament light chain protein.

NFT Neurofibrillary tangle.

NIA-AA National Institute on Ageing-Alzheimer's Association.

P-Sym Presymptomatic.

PCA Posterior cortical atrophy.

PET Positron emission tomography.

PiB Pittsburgh compound B.

PSEN1 Presenilin 1.

PSEN2 Presenilin 2.

Q-Sym Questionably Symptomatic.

QSBB Queen Square Brain Bank.

RD Radial diffusivity.

SMC Significant memory concern.

SVD Small vessel disease.

SWI Susceptibility weighted imaging.

Sym Symptomatic.

TIV Total intracranial volume.

VaD Vascular dementia.

VCI Vascular Cognitive Impairment.

WMH White matter hyperintensities.

Chapter 1

Introduction

1.1 Background

Dementia is one of the most important socio-economic problems of our time. Current estimates suggest that there are over 46 million people worldwide living with dementia (Prince et al., 2015). The prevalence is only predicted to rise as the global population ages, reaching 131.5 million people by 2050 (Prince et al., 2015). In England and Wales, dementia is the leading cause of death, accounting for 12.8% of all deaths registered (Office for National Statistics, 2020). Dementia is an overall term for a syndrome characterised by progressive cognitive impairment interfering with daily life activities. Alzheimer's disease (AD) is the leading cause of dementia, accounting for 50-75% of cases followed by vascular dementia, frontotemporal dementia and Lewy body dementia (Prince et al., 2014a).

AD is a progressive neurodegenerative disease, with the large majority of cases over the age of 65 years. Approximately 5% of AD patients develop symptoms earlier than the age of 65, known as young onset AD (Prince et al., 2014b). A small proportion of those with young onset AD have a genetic form of AD, known as autosomal dominant inherited AD (ADAD). The disease duration of AD is typically around 10 years for all forms of AD (Godbolt et al., 2004, Pavisic et al., 2020, Ryman et al., 2014), although there are reports of shorter disease duration for some more aggressive ADAD mutations (Holmes, 2002).

Clinically, typical AD patients initially present with amnesia and correspond-

ing hippocampal atrophy, before progressing to a loss of function in multiple cognitive domains and more widespread atrophy. There are also subtypes of atypical AD where cortical, rather than hippocampal regions are the most vulnerable. The most common form of atypical AD is posterior cortical atrophy (PCA), where atrophy is initially observed in posterior brain regions, and accompanied by visuospatial and visuo-perceptual deficiencies and a relative sparing of episodic memory (Crutch et al., 2012).

AD is the only leading cause of death for which no disease-modifying therapy is currently available. The failure of several AD drugs in clinical trials is often attributed to the treatment being initiated too late in the disease course (Salloway et al., 2014, Sperling et al., 2011). AD has a long prodromal stage that is thought to begin decades prior to the onset of clinical symptoms, during which time pathological changes are occurring in the brain undetected. This long preclinical stage means that the development of biomarkers that can identify early pathological stages of disease is a highly important first step on the path to an effective treatment.

The field of AD research has largely focused on the hallmark senile plaques and neurofibrillary tangles (NFTs) initially described over 100 years ago by Alois Alzheimer, and now known to be formed of amyloid beta ($A\beta$) and hyperphosphorylated tau, respectively. More recently the field is beginning to look beyond $A\beta$ and tau, with increased recognition of a broader spectrum of pathology that includes vascular dysfunction, neuroinflammation, neuronal loss and white matter changes. The characterisation of new biomarkers to encompass all aspects of disease is therefore highly pertinent, and is the overarching rationale for this thesis. The main biomarker of interest to this thesis is white matter hyperintensities (WMHs); widely thought to be a marker of cerebrovascular disease (CVD) (Wardlaw et al., 2013), but with a heterogeneous pathological basis that is suggestive of multiple origins (Gouw et al., 2008a).

Unravelling the complex interactions between genetic, environmental and lifestyle factors that all influence the onset and trajectory of AD requires large datasets that track individuals across multiple stages of disease. Pioneered in the

early 20th century, cohort studies are an invaluable resource in the study of diseases such as Alzheimer's, with over 50 different cohorts existing in the UK alone (Medical Research Council, 2014). The global cohort studies of the Alzheimer's Disease Neuroimaging Initiative (ADNI) and the Dominantly Inherited Alzheimer Network (DIAN) are longitudinal studies of sporadic and familial Alzheimer's disease respectively, collecting imaging, biological, genetic, demographic and clinical data from multiple countries, and are therefore ideally placed to answer some of the key questions in this thesis.

In this introduction, I first provide an overview of the genetics and biology of AD, including ADAD. The link between AD and CVD is then discussed. I then move onto an exploration of biomarker research in AD, before focusing in on an overview of WMHs and their relevance to AD.

1.2 Alzheimer's disease

1.2.1 The Amyloid cascade hypothesis

The cardinal features of Alzheimer's disease pathology are $A\beta$ plaques and NFTs of tau, which have been the focus of much of the research into the aetiology of AD since the identification of their constituent proteins in the 1980s (Glennner and Wong, 1984, Grundke-Iqbal et al., 1986). The amyloid cascade hypothesis (Figure 1.1), the prevalent theory of AD pathogenesis, suggests a causal role for $A\beta$ accumulation in a series of downstream processes, such as the aggregation of tau into NFTs, neuroinflammation and neuron and synapse loss (Hardy and Higgins, 1992). This idea has been the driving factor for the development of the majority of therapies in recent years that aim to modify disease, either through reduction in the production of $A\beta$ or through an increase in its clearance.

Compelling evidence of a central role for $A\beta$ in AD comes from genetic studies of the disease, whereby causal mutations in the *amyloid precursor protein* (APP) gene (Goate et al., 1991) and two genes related to APP's cleavage, *Presenilin 1* (PSEN1) (Sherrington et al., 1995) and *Presenilin 2* (PSEN2) (Levy-Lahad et al., 1995) were found to cause ADAD. Much of our understanding about $A\beta$ pathology

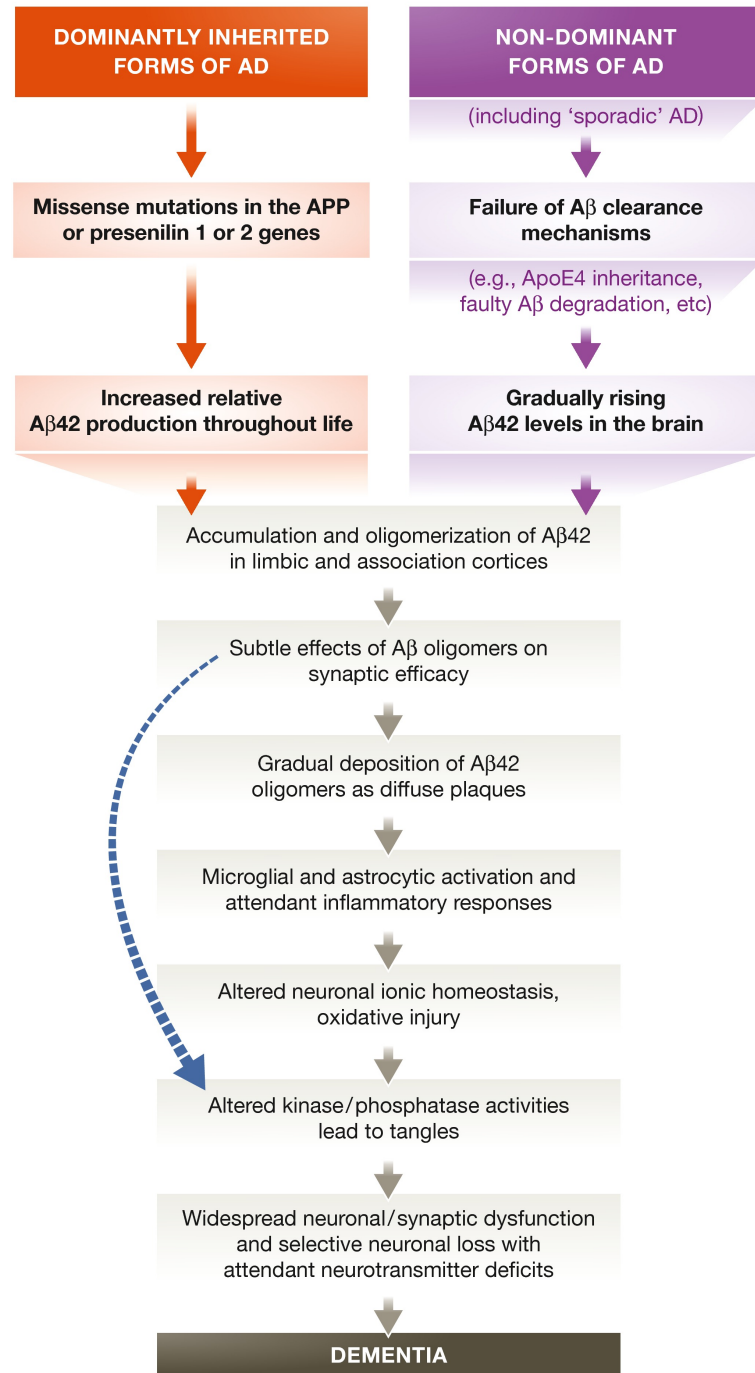


Figure 1.1: The order of major pathogenic events leading to AD, as set out in the amyloid cascade hypothesis. The curved blue arrow indicates that A β oligomers may directly damage synapses and neurites and induce tau hyperphosphorylation, in addition to activating damaging cascades. Figure taken from Selkoe and Hardy (2016).

in AD has come from this rarer familial form of the disease. The *APP*, *PSEN1* and *PSEN2* genes encode proteins involved in the $A\beta$ generation pathway. Amyloid precursor protein is sequentially cleaved by β and γ secretases to give rise to $A\beta$. *PSEN1* and *PSEN2* proteins make up the catalytic subunit of γ secretase, which is able to cleave *APP* at various different sites, yielding an $A\beta$ peptide between 39 and 43 amino acids in length. The most prevalent $A\beta$ peptide produced under normal conditions is $A\beta$ 1-40, whereas the longer and more amyloidogenic $A\beta$ 1-42 isoform is more abundant within plaques (Jarrett et al., 1993). The exact physiological function of *APP* is unknown. Overexpression studies in mice have shown a positive effect on cell growth and health, but knockout studies appear to produce very little alteration to phenotype (O'Brien and Wong, 2011).

There are different subtypes of $A\beta$ plaques; mature neuritic plaques feature dense amyloid cores and are associated with a microglial response, compared to diffuse plaques which have no associations with neuroinflammation or neuronal cell death (D'Andrea and Nagele, 2010). Although the fibrillar $A\beta$ 1-42 present in the dense core of mature plaques has long been thought of as integral to AD pathogenesis, more recent research suggests that it is actually the soluble $A\beta$ oligomers that are the most toxic (Olsson et al., 2018, Shankar et al., 2008).

The amyloid cascade hypothesis proposes that an accumulation of $A\beta$ is brought about by an imbalance between $A\beta$ production and clearance. While mutations in the *APP*, *PSEN1* and *PSEN2* genes have all been shown to increase production or deposition of $A\beta$ (Selkoe, 1997), the initial cause of pathology in sporadic AD remains unclear. There are several hypotheses about the mechanism of amyloid clearance in the brain and include the enzymatic degradation by proteases, the direct absorption into the blood through the blood brain barrier via transporter proteins, and the perivascular drainage pathway (Tarasoff-Conway et al., 2015).

A key downstream process of $A\beta$ aggregation is the formation of NFTs from paired helical filaments of hyperphosphorylated tau. Under physiological conditions, natively unfolded tau is involved in the assembly and stability of microtubules; polymers that are important for neuronal integrity and function, providing

structure to axonal processes and transportation to and from synapses (Spillantini and Goedert, 2013). Under pathological conditions, the binding of tau to microtubules is disrupted, leading to an increase in the unbound tau fraction. This increase of tau in the cytosol increases the chances of misfolding that can result in aggregation and fibrillation of tau. It has also been demonstrated that pathological tau can propagate further conformational changes in normal forms of the protein (Wolfe, 2012).

Research suggests that the formation of NFTs is more highly correlated to AD clinical features and disease severity than $A\beta$ (Nelson et al., 2012). Tau pathology typically begins in the locus coeruleus and entorhinal cortex, before spreading to the hippocampus and then to the neocortex (Braak and Braak, 1991). This spread of tau pathology closely maps to AD patterns of atrophy and occurs in brain regions linked to specific clinical symptoms (Ossenkoppele et al., 2016, Xia et al., 2017).

1.2.2 Preclinical AD: a window of opportunity?

The development of biomarkers (variables measured *in vivo* that reflect specific disease-related processes, discussed in detail in section 1.4), has enabled a greater understanding of the long asymptomatic phase of AD. Biomarkers of $A\beta$ and tau pathology measured using cerebrospinal fluid (CSF) and positron-emission tomography (PET), and structural imaging biomarkers of neurodegeneration have enabled the tracking of changes that occur years prior to the onset of symptoms. Evidence from these studies suggests that $A\beta$ pathology develops years before tau pathology, which in turn predates clinical symptoms (Bateman et al., 2012, Jack et al., 2010a) (Figure 1.2).

Given this evidence that the AD pathophysiological process begins years prior to symptom onset, there is a general consensus that the best opportunity for intervention is early on in the disease process (Sperling et al., 2011). This is supported by the failure of several secondary prevention trials of anti-amyloid antibodies in individuals with overt clinical symptoms of AD, even at the early stages (Honig et al., 2018, Ostrowitzki et al., 2017, Vandenberghe et al., 2016). Very recent evidence from the Dominantly inherited Alzheimer's Network trials unit (DIAN-TU)

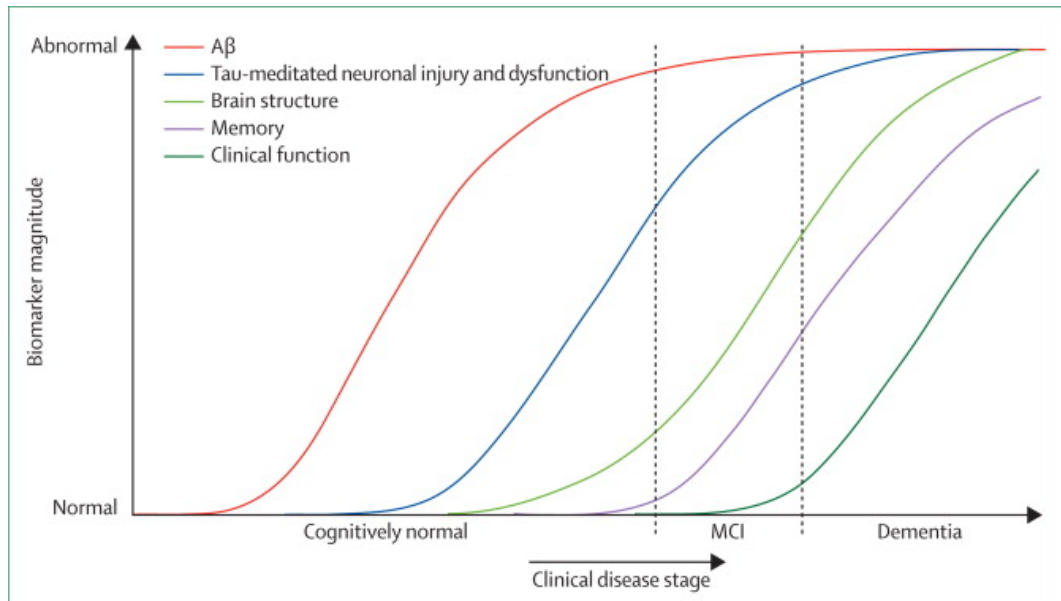


Figure 1.2: Dynamic biomarkers of the Alzheimer's pathological cascade. In this hypothetical model $A\beta$ is identified by CSF $A\beta_{42}$ or PET imaging, tau-mediated neuronal injury and dysfunction is identified by CSF tau or fluorodeoxyglucose-PET and structural changes are measured using MRI. MCI = mild cognitive impairment. Figure taken from Jack et al. (2010a)

clinical trial in asymptomatic and symptomatic carriers of autosomal dominant AD showed a lack of any clinical effect in the symptomatic group, despite movement towards normal levels of CSF $A\beta$ and tau. The asymptomatic carriers were some years away from expected onset and so whether targeting the disease earlier will halt or delay the onset of clinical symptoms remains unclear (<https://dian.wustl.edu/our-research/clinical-trial/research-updates/>).

1.2.3 Beyond amyloid and tau: a multifactorial disease

$A\beta$ and tau pathologies are clearly highly important in AD and the advancement in disease biomarkers has enabled greater insight into their respective and additive roles in disease pathogenesis. There are however contradictions to an integral role for $A\beta$ and tau in AD disease pathogenesis; healthy individuals without AD symptoms have been found to have $A\beta$ and tau pathology at post-mortem examination, as well as individuals diagnosed clinically as having AD, but with no $A\beta$ and tau pathology at post-mortem examination (Nelson et al., 2012). Additionally,

the consistent failure of clinical trials of $A\beta$ modifying therapies that rely on the amyloid hypothesis continue to cast significant doubt on its validity (Honig et al., 2018, Ostrowitzki et al., 2017, Vandenberghe et al., 2016). Moreover, the recent news from the DIAN-TU trial that Gantenerumab reduces amyloid PET deposition and causes a shift towards normal CSF tau and $A\beta$ levels despite no effect on cognition, does challenge theories of $A\beta$ and tau as important drivers to clinical AD (<https://dian.wustl.edu/our-research/clinical-trial/research-updates/>).

AD is a hugely complex, multifactorial disease. Large genome wide association studies have contributed to the idea of AD as a multisystem disorder, with the identification of genetic risk factors for AD associated with the immune system, inflammation, cholesterol and lipid metabolism and endosomal and vesicle recycling (Cuyvers and Sleegers, 2016). In recent years, more emphasis is being placed on understanding other aspects of AD pathology or contributors to disease, including cerebrovascular disease, neuroinflammation, synaptic dysfunction, oxidative stress and mitochondrial dysfunction (Hase et al., 2018, Schneider et al., 2007, Swerdlow, 2018, Tonnie and Trushina, 2017, Wyss-Coray and Rogers, 2012). As our understanding of AD pathology and genetics increases, the complex nature of the disease is becoming clearer. Research is subsequently moving away from the simplistic ideas of the linear causality featured in the amyloid cascade hypothesis and towards consideration of the full spectrum of AD pathology (DeStrooper and Karran, 2016, Jack et al., 2018).

1.2.4 Autosomal dominant inherited Alzheimer's disease

Mutations in either *APP*, *PSEN1* and *PSEN2* are rare and virtually fully penetrant. This is in contrast to the genetics of the sporadic form of the disease where polymorphisms in risk genes for sporadic AD are frequent in the general population, but only have a small contribution to overall disease risk (Figure 1.3). The most important genetic risk factor identified for AD is the *Apolipoprotein E* (*APOE*) $\epsilon 4$ allele, increasing the risk of AD by ~ 10 -fold for homozygotes and ~ 3 -fold for *APOE* $\epsilon 3$ and *APOE* $\epsilon 4$ heterozygotes (Frikke-Schmidt et al., 2001, Slooter et al., 1998).

Since the discovery of the autosomal dominantly inherited mutations in the

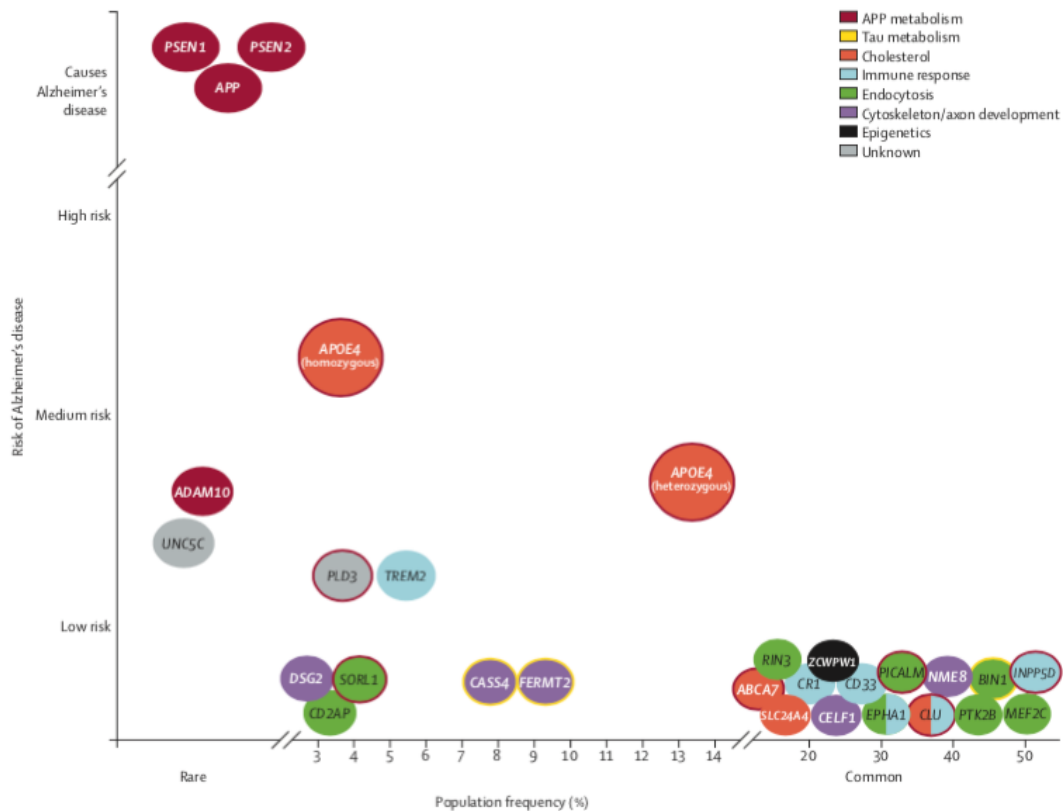


Figure 1.3: Schematic overview of genes linked to Alzheimer's disease. Genes affecting APP metabolism are circled in red, and those affecting the tau pathway are circled in yellow. The circle colours give functional information about the genes. Figure taken from Scheltens et al. (2016).

1990s, many hundreds of variants that cause ADAD have been identified. Mutations in *PSEN1* are the most common, with 322 recorded to date, followed by 68 *APP* and 64 *PSEN2* (<https://www.alzforum.org/mutations>). Mutations in ADAD may increase production of $A\beta_{1-42}$ or $A\beta_{1-40}$, alter the ratio between them, or increase the likelihood of protofibril formation which accelerates $A\beta$ deposition (Nilsberth et al., 2001, Ryan and Rossor, 2010). Whilst different ADAD-causing mutations affect $A\beta$ generation through a variety of mechanisms, they all lead to qualitative shifts in the $A\beta$ profiles produced, towards the generation of longer peptides which are more prone to aggregation (Chávez-Gutiérrez et al., 2012, Szaruga et al., 2015). There is considerable heterogeneity within ADAD, with differences in clinical phenotypes and pathological presentations both within and between mutation types. The young age at onset typically seen in ADAD compared to sporadic

AD shows variability between the mutation groups with *PSEN1* carriers falling between 35-55 years, the *APP* carriers between 40-65 years and the *PSEN2* carriers between 40-70 years (Holmes, 2002, Shea et al., 2016). Atypical phenotypes of ADAD also exist, with certain mutations presenting with language impairment, behavioural symptoms, pyramidal signs including spastic paraparesis and extrapyramidal signs (Ryan and Rossor, 2010, Ryan et al., 2016, Shea et al., 2016, Tang et al., 2016).

Pathological findings have also demonstrated variability in neuronal loss, tau tangle load and the type, distribution and size of $A\beta$ plaques (Maarouf et al., 2008, Shepherd et al., 2009). It appears that the mutation location can play an important role in determining pathological features in ADAD. Certain *APP* mutations located in the $A\beta$ coding region are typically associated with severe cerebral amyloid angiopathy (CAA) and can present with haemorrhage as well as dementia. These mutations include the Arctic (p.Glu693Gly), Dutch (p.Glu693Gln), Flemish (p.Ala692Gly), and Iowa (p.Asp694Asn) mutations (Revesz et al., 2009, Shepherd et al., 2009). Two distinct histopathological groups can be identified within *PSEN1* mutation carriers, appearing to be linked to the mutation position. Mutations occurring before codon 200 are typically associated with diffuse and cored $A\beta$ plaques and few white matter plaques, compared to mutations after codon 200 with larger plaques concentrated around blood vessels, and more severe CAA and WMHs (Mann et al., 2001, Ryan et al., 2015).

Although the genetic form of AD probably accounts for less than 1% of all AD cases, it has contributed much to our understanding of the pathological basis of the more common sporadic form. As well as elucidating the potential pathogenic mechanisms of AD as a whole, ADAD is an invaluable model to study the presymptomatic phases of disease. As intervention strategies are being trialed on individuals at an early stage in the disease process, research has shifted to identifying those patients who are in the long presymptomatic period before the onset of symptoms. Initiatives like DIAN (Bateman et al., 2011) enable research to be carried out on patients who with near certainty, due to almost 100% penetrance of ADAD genes,

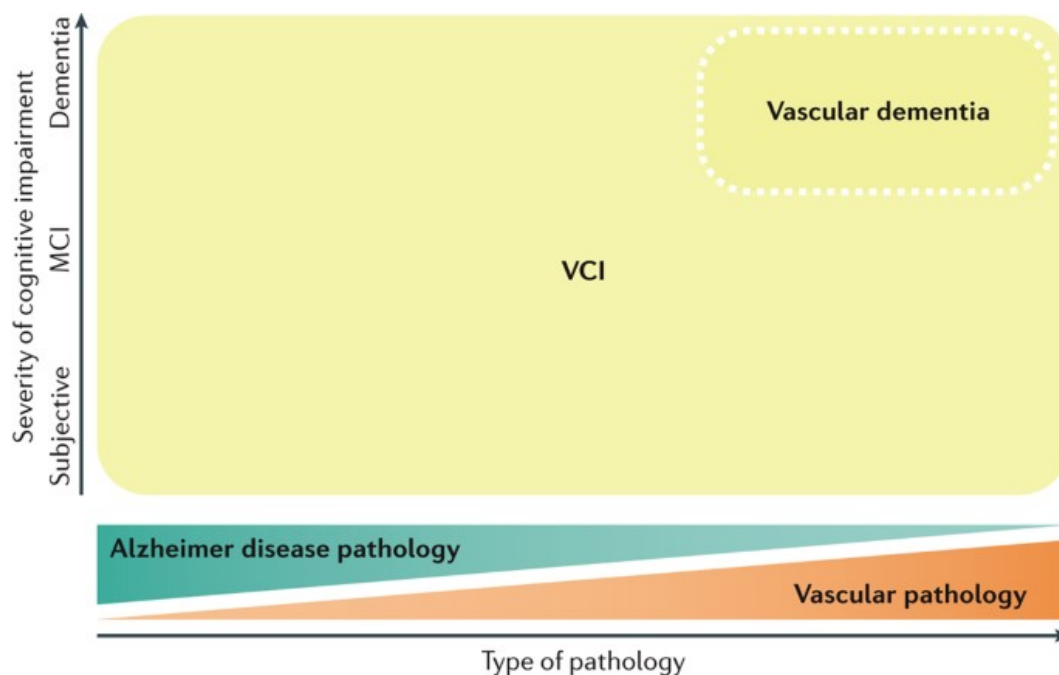
will go on to develop the disease. The young age of ADAD individuals enables the study of AD features that are unrelated to the age-related comorbidities often present in older sporadic AD patients. This is particularly important to enhance our understanding of the AD-vascular disease relationship (discussed in detail in the following section 1.3), helping to tease apart contributions from AD pathology and those from vascular pathology.

1.3 Cerebrovascular disease and Alzheimer's disease

1.3.1 Overview

The close linkage between AD and CVD is becoming increasingly well recognised, with multiple shared risk factors and overlapping pathological presentations (Attems and Jellinger, 2014, Santos et al., 2017). CVD is a generic term for a heterogeneous set of insults to the cerebral vasculature, often leading to cognitive impairment. There are three main diseases of cerebral blood vessels that are referred to as CVD: large vessel atherosclerosis; small vessel disease (SVD); and cerebral amyloid angiopathy (CAA) (McAleese et al., 2016). Atherosclerosis results in the formation of atherosclerotic plaques in large cerebral arteries, leading to narrowing and possible plaque rupture. Small vessel disease refers to degenerative alterations to the vessel walls of smaller cerebral arteries, including small vessel atherosclerosis and arteriosclerosis. CAA is characterised by the deposition of $A\beta$ in the walls of arteries and capillaries.

Vascular dementia (VaD) is the second most common cause of dementia after AD, and occurs as a result of CVD or stroke (Kalaria, 2018). Recently, the broader term of vascular cognitive impairment (VCI) is preferred and refers to the whole spectrum of cognitive impairment caused, to some extent, by vascular pathologies, ranging from a subjective memory impairment through to dementia (van der Flier et al., 2018). The cognitive manifestations of VCI include a decline in processing speed and problems with executive function. Memory problems and behavioural or psychological symptoms are also common, along with other neurological symptoms such as walking difficulties, dysarthria and autonomic features (van der Flier



Nature Reviews | Disease Primers

Figure 1.4: The relationship between VCI and vascular dementia. VCI is any level of impairment that can be attributed, at least in part, to cerebrovascular pathology. Vascular dementia represents a severe form of VCI attributable to a large burden of cerebrovascular pathology. Figure taken from van der Flier et al. (2018).

et al., 2018). Whilst pure VaD refers to a form of VCI whose sole cause is vascular pathology, the broader term VCI can also be given to those who also have AD pathology. Indeed, VCI in combination with AD is very common demonstrated by the large amount of AD cases demonstrating vascular pathology *post mortem* (Boyle et al., 2018, Brayne et al., 2009) (Figure 1.4).

1.3.2 Shared risk factors

AD and CVD both develop over many years and so understanding the effects of long-term exposure to risk requires large, longitudinal studies. Many population-based epidemiological studies have provided robust evidence for a link between AD and vascular health. AD and CVD share important cardiometabolic and lifestyle risk factors such as diabetes, obesity, hypertension, high cholesterol, major depression, smoking and low physical fitness (Santos et al., 2017). Hypertension in middle aged adults has shown to be associated with cognitive decline and dementia (Launer

et al., 2000, Skoog et al., 1996), as has midlife obesity (Qizilbash et al., 2015). Recent research using the 1946 birth cohort demonstrated that midlife hypertension was associated with WMH and atrophy (Lane et al., 2019b). The Framingham Heart study found that a lower cardiac index (a measure of cardiac performance) was associated with an increased risk of AD (Jefferson et al., 2015). As well as increasing risk, vascular risk factors such as atrial fibrillation, systolic hypertension and angina have been shown to associate with a more rapid cognitive decline in AD (Mielke et al., 2007).

It is estimated that over 35% of AD risk is comprised of these modifiable risk factors (Livingston et al., 2017, 2020, Mukadam et al., 2019). This percentage is calculated from population attributable fractions, estimates of the proportion of disease cases that would not occur in a population if an individual risk factor were to be eliminated. This high proportion of potentially modifiable risk offers the potential for wide-reaching primary prevention strategies. It is important to note though that these estimates are dependent on accurate prevalence data, which in turn are dependent on accurate measurement of a risk factor in the population. There are other risk factors for both CVD and AD that are non-modifiable, including the largest of them all: increasing age. The largest genetic risk factor for sporadic AD, the *APOE* $\epsilon 4$ allele, is also associated with incidence of cerebrovascular disease (Schilling et al., 2013) and has functions in cholesterol metabolism and $A\beta$ clearance through the blood brain barrier (Masters et al., 2015).

1.3.3 Vascular pathology in AD

It is estimated that only 24% of patients with dementia have pure AD pathology, compared to over 50% with some form of vascular co-pathology (Iadecola and Gottesman, 2018). There is a large body of research demonstrating the co-occurrence AD and CVD pathology (Brayne et al., 2009, Esiri et al., 2014, Jellinger and Attems, 2006, Kapasi et al., 2017, Schneider et al., 2007, 2009). In a study comparing autopsy cases of AD and age-matched controls, CVD pathology was significantly more frequent in AD compared with controls (Jellinger and Attems, 2006). Several UK based longitudinal population studies have demonstrated the

high incidence of overlapping pathology; the MRC Cognitive Function and Ageing Study demonstrated that more than half of AD subjects had a significant vascular burden (Fernando and Ince, 2004) and the Cambridge City over-75s Cohort study showed that 22% of those presenting with dementia had mixed pathology, with AD and CVD frequently coexisting (Brayne et al., 2009). The most frequent vascular pathologies observed in AD are CAA and SVD (Attems and Jellinger, 2014).

1.3.3.1 CAA

CAA is highly prevalent amongst AD patients, occurring in 82% to 98% of cases, compared to only about 30% of elderly controls (Biffi and Greenberg, 2011, Love et al., 2003, 2014, Vinters, 1987). CAA has been shown to contribute to AD dementia, over and above AD pathology (Boyle et al., 2015). CAA is characterised by the deposition of $A\beta$ in the vessel walls of cortical and leptomeningeal arteries, arterioles and capillaries (Vinters, 1987), most commonly in the occipital lobe (Thal et al., 2002a). The more soluble $A\beta$ 1-40 is the prominent form in CAA, compared to $A\beta$ 1-42 which is more commonly found in plaques. CAA has been divided into two pathological subtypes: CAA type 1, characterised by amyloid deposits in cortical capillaries (as well as other vessels), and CAA type 2, where amyloid deposition is restricted to cortical arteries or arterioles (Thal et al., 2002a).

It has been suggested that $A\beta$ is drained along the perivascular interstitial fluid pathways of the brain parenchyma and leptomeninges. A failure of this mechanism to effectively drain $A\beta$ leads to deposition along the basement membranes of vessels (Weller et al., 2008). This build-up of $A\beta$ in vessel walls causes loss of smooth muscle cells and can lead to severe disruption of the vascular architecture (Revesz et al., 2002). Intracerebral haemorrhage is a well-established consequence of CAA due to the weakening of vessel walls. Additionally, $A\beta$ deposits that decrease the vessel lumen lead to ischaemia-related problems (Biffi and Greenberg, 2011). Recently, more diverse clinical manifestations have been linked to CAA, including cognitive decline with associated brain atrophy (Smith, 2018).

1.3.3.2 SVD

SVD affects small cerebral arteries and arterioles and refers to degenerative alterations in small vessel walls consisting of atherosclerotic plaques, deposition of a hyaline substance (lipohyalinosis), fibrotic changes causing stiffening and microvascular distortion (arteriolosclerosis) and total loss of vascular wall integrity (Thal et al., 2012). The affected vessels are commonly located in the white matter and in the basal ganglia. The multiple causes of SVD, can all lead to various vascular lesions, including infarcts, enlarged perivascular spaces, haemorrhages and white matter lesions. Small blood vessels are not directly visible on conventional MRI and so the downstream consequences of damage are visualised instead, such as WMHs, small subcortical infarcts, lacunes, prominent perivascular spaces and cerebral microbleeds (Wardlaw et al., 2013). The most well characterised imaging markers of SVD are WMHs, which are discussed in detail in section 1.5, and are the main topic for this thesis.

1.3.4 Interactions between AD pathology and CVD

The frequent coexistence of AD and CVD pathology means that disentangling their contributions to cognitive decline presents a huge challenge and one that has led to several theories. An additive theory describes two independent pathologies that can contribute to a greater cumulative risk of cognitive decline when they appear together. On the other hand, a synergistic theory suggests that one pathology influences another pathology, resulting in a cognitive decline greater than the sum of their parts.

In the literature, an additive relationship has been demonstrated, with AD and vascular pathologies shown to act independently of each other to predict brain atrophy (Barnes et al., 2013, Gordon et al., 2015, Haight et al., 2013, Provenzano et al., 2013), neurodegeneration (Bos et al., 2017) and/or cognitive decline (Lopez et al., 2014, Vemuri and Knopman, 2016, Vemuri et al., 2015). There is also evidence supporting a synergistic relationship with a potential interaction between the two pathologies. One study demonstrated that WMHs interact with $A\beta$ to increase hippocampal atrophy (Freeze et al., 2016). Two recent studies from the same group

demonstrated that $A\beta$ and vascular risks act synergistically on cognitive decline (Rabin et al., 2018) and cortical tau burden (Rabin et al., 2019).

Evidence from autopsy studies have suggested that vascular disease lowers the threshold for AD expression. Snowdon et al. (1997) demonstrated that in a study of autopsies nuns fitting the neuropathological criteria for AD, a higher prevalence of clinical dementia was observed when infarcts were present. Other studies have suggested that the presence of concomitant vascular pathology at earlier disease stages is important; lower cognitive scores were observed in those patients with early stage AD and vascular lesions (Esiri et al., 1999).

Many mechanistic theories of how one pathology might exacerbate the effects of the other have centered around the idea that vascular risk factors potentiate $A\beta$ deposition or visa versa. Studies have demonstrated that vascular damage could reduce the ability to clear $A\beta$ from the brain, enhancing it's deposition in blood vessel walls as CAA (Weller et al., 2008). Conversely, $A\beta$ deposition can cause a reduction in cerebral perfusion, increasing the susceptibility of the brain to ischaemia (Iadecola and Gottesman, 2018).

1.4 Biomarkers in Alzheimer's disease

1.4.1 Overview

Biomarkers, or biological markers, are quantifiable characteristics of *in vivo* pathology allowing analysis of normal biological processes, pathogenic processes or pharmacologic responses to a therapeutic intervention (Biomarkers Definitions Working Group, 2001). Biomarkers are hugely important tools in diseases such as AD, where clinical symptoms are not evident until the advanced pathological disease stages, when any intervention strategy may be too late (Salloway et al., 2014, Sperling et al., 2011).

Biomarkers are now commonplace in AD research, of which the most widely used are cerebrospinal fluid (CSF) measures and neuroimaging. In 2018, a major shift in the characterisation of AD was proposed by the National Institute on Ageing-Alzheimer's Association in a research framework (NIA-AA) (Jack et al.,

AT(N) profiles	Biomarker category	
A-T-(N)-	Normal AD biomarkers	
A+T-(N)-	Alzheimer's pathologic change	Alzheimer's continuum
A+T+(N)-	Alzheimer's disease	
A+T+(N)+	Alzheimer's disease	
A+T-(N)+	Alzheimer's and concomitant suspected non-Alzheimer's pathologic change	
A-T+(N)-	Non-AD pathologic change	
A-T-(N)+	Non-AD pathologic change	
A-T+(N)+	Non-AD pathologic change	

Table 1.1: NIA-AA Biomarker profiles and categories. Three biomarkers types Amyloid (A), tau (T) and neurodegeneration (N) categorise individuals into eight biomarker profiles (Jack et al., 2018).

2018), in which disease diagnosis is defined by *in vivo* biomarkers as opposed to clinical phenotypes. The AT(N) classification system places different biomarkers (from both imaging and CSF modalities) into the pathological process they measure. Individuals are defined as being positive or negative for $A\beta$, T (tau) and N (neurodegeneration) (Table 1.1). Whilst $A\beta$ and tau define the presence or absence of AD, neurodegeneration biomarkers combined with cognitive symptoms are used for staging the severity of disease. The authors also stress that the framework can be adapted to reflect the multifactorial nature of AD and new biomarkers can be added, such as those relating to CVD or inflammation, once they become available.

As our understanding of AD shifts to one of a more multifactorial disease, there is a need to explore new biomarkers to complement those of $A\beta$ and tau in order to aid in an early and accurate diagnosis of AD and to monitor the effect of a therapeutic intervention. The failure of multiple AD clinical trials highlights more than ever the need for a larger panel of biomarkers in order to understand any effect on a broader range of pathogenic pathways.

1.4.2 Fluid biomarkers

1.4.2.1 CSF

The classical method of a biomarker-led approach to AD diagnosis has been to quantify $A\beta$ and tau levels in the CSF. Although lumbar puncture procedures are invasive, the CSF is potentially the most informative fluid biomarker about biochemical changes in the brain due to the direct contact between them. Decreased CSF $A\beta$ and increased total-tau (t-tau) and phosphorylated tau (p-tau) show a high specificity and sensitivity to AD diagnosis. While CSF $A\beta$ has demonstrated a robust correlation with pathology in the brain (Strozyk et al., 2003), the findings from the CSF tau markers are less clear. Studies have demonstrated correlations of CSF tau with AD neurodegeneration and tangle pathology at *post mortem* (Buerger et al., 2006, Tapiola et al., 1997), but to a lesser extent than CSF $A\beta$ -pathology correlations, and a relationship is not demonstrated in all studies (Engelborghs et al., 2007). Increases in CSF t-tau are not specific to AD, and are also seen in diseases with severe neurodegeneration, such as Creutzfeldt-Jakob disease, which has led some to consider t-tau as a marker of general neurodegeneration. However other studies have demonstrated an AD-specific increase in CSF t-tau and p-tau that is not reflected in other tauopathies (Itoh et al., 2001, Skillback et al., 2015). There is evidence to suggest that levels of CSF t-tau are related to the severity of disease, with high t-tau values predicting rapid cognitive decline (Buchhave et al., 2012, Wallin et al., 2010).

As discussed in section 1.2.2, findings suggests that $A\beta$ and tau pathology in the brain predates symptom onset quite considerably. Although there is some evidence that the AD CSF profile shows changes 10-15 years before symptom onset (Bateman et al., 2012), some studies have demonstrated a lack of association with cognitive decline (Toledo et al., 2013). Other reports hypothesise that these core CSF biomarkers are not good markers of progression over the complete disease time course as they are relatively stable in clinical AD (Jack et al., 2010b, Zhou et al., 2009). The multifaceted nature of AD means that a larger panel of biomarkers needs to be developed in order to improve early diagnosis and prognosis. There are many

new potential CSF biomarkers that are in the process of being characterised. These are involved in a range of pathogenic pathways and include inflammatory markers such as YKL-40, markers of synaptic dysfunction such as neurogranin and markers of microglial disruption such as TREM2 (Dhiman et al., 2019). A particularly promising CSF biomarker is neurofilament light chain protein (NFL), a marker of axonal degeneration. NFL, although not an AD-specific disease marker, is a highly sensitive marker of neurodegeneration that has been shown to differentiate between AD and control patients and to be associated with cognitive decline, white matter change and brain atrophy (Mattsson et al., 2016, Zetterberg et al., 2016).

1.4.2.2 Blood

Brain derived biomarkers are detectable in the blood, opening the possibility of an inexpensive and less invasive way of diagnosing and monitoring AD progression. Although a newer field than CSF biomarkers, recent research has shown promising results. The plasma $A\beta$ 42/40 ratio has been shown to decrease in a similar way to CSF $A\beta$ and has around a 90% diagnostic accuracy (Nakamura et al., 2018). Plasma t-tau has consistently been shown to be elevated in AD compared with controls, although not to such a high level as in the CSF (Olsson et al., 2016) and with less clear results in those with mild cognitive impairment (MCI) (Mattsson et al., 2016). Plasma p-tau has shown perhaps more promising results (Mielke et al., 2018), with a recent study by O'Connor et al. (2020) demonstrating increased levels in symptomatic and presymptomatic ADAD. Plasma NFL has also been shown to be highly correlated with CSF NFL, and is increased in the early stages of familial and sporadic AD (Preische et al., 2019, Weston et al., 2019, Zetterberg and Blennow, 2018).

1.4.3 Imaging biomarkers

1.4.3.1 T1 and T2-weighted imaging

The role of imaging in AD has historically been to exclude any alternative pathologies that could be causing the observed cognitive impairment such as space-occupying lesions. However recent diagnostic criteria have recommended that the presence of medial temporal lobe atrophy on magnetic resonance imaging (MRI)

be included in AD diagnosis (Dubois et al., 2015, Jack et al., 2018, McKhann et al., 2011).

Single timepoint T1-weighted imaging has great diagnostic potential by enabling patterns of brain atrophy to be uncovered. Volumetric T1-weighted scans are high resolution images that are typically obtained with good contrast between grey and white matter. In research, this enables measurement of volumes in specific structures and analysis of detailed atrophy patterns at the level of the voxel or using surface-based techniques. Serial T1-weighted imaging can detect change in volume or thickness of the cortex or specific structures and have been used as outcome measures in clinical trials (Dubois et al., 2015, Fox et al., 2005, Salloway et al., 2009).

The pattern of brain atrophy seen in AD on MRI, initiating in medial temporal lobe structures and the limbic system before spreading out to cortical areas (Scahill et al., 2002), closely fits the pattern outlined in histopathological studies of the spread of neurofibrillary tau tangles (Braak and Braak, 1991). It is becoming clear that by the time that a clinical diagnosis of AD is given (according to the McKhann criteria, 1984), the atrophy in the brain is already widespread. Evidence from longitudinal imaging studies suggests that hippocampal volumes are already reduced by 10% 3 years prior to diagnosis, with a whole brain loss of 6% by the time a diagnosis is made (Johnson et al., 2012, Ridha et al., 2006). It is therefore important to be able to predict those who are on the AD pathway. Medial temporal lobe atrophy has been shown to be an effective predictor of future AD, with several studies demonstrating high sensitivity and specificity values (DeCarli et al., 2007, Korf et al., 2004).

T2-weighted FLAIR imaging is particularly useful for visualising changes in tissue characteristics caused by cerebrovascular pathological processes. FLAIR imaging has been used in the identification of WMHs. As WMHs are commonly found around the lateral ventricles, the suppression of the CSF signal by the FLAIR sequence enables better delineation of these lesions compared with standard T2-weighted imaging. Current research surrounding the use of FLAIR imaging in

WMH quantification is discussed in detail in section 1.5. Unlike volumetric T1-weighted imaging, volumetric FLAIR imaging is still in its relative infancy, which means the potential of precise and accurate changes has not yet been fully realised.

1.4.3.2 Positron emission tomography imaging

Positron emission tomography (PET) imaging has enabled the visualisation of AD pathology *in vivo* using radioactive ligands. Fluoro-deoxy-D-glucose (FDG)-PET, a glucose analogue, is a widely accepted biomarker of overall brain metabolism and has a high sensitivity and specificity in the diagnosis of AD and MCI (Bloudek et al., 2011, Mosconi et al., 2008). Hypometabolism has been shown to precede cognitive decline and to be predictive of AD progression (de Leon et al., 2001).

PET imaging has also been utilised to visualise $A\beta$ pathology. Pittsburgh compound B (PiB) binds to $A\beta$ with a high affinity many years prior to symptom onset, and replicates the sequence of $A\beta$ deposition confirmed at *post mortem* (Ikonomic et al., 2008). More recently fluorine-based PET tracers have been developed, with a high correlation to PiB tracer binding, but with a longer half-life (Villemagne et al., 2012).

$A\beta$ PET imaging has been shown to have a high sensitivity in diagnosing AD (Klunk, 2011). There is evidence that a positive $A\beta$ PET scan in MCI patients is predictive of AD conversion, especially those with a typical amnesic presentation (Jack et al., 2008b). An increase in $A\beta$ PET uptake has been demonstrated very early on in the disease process in an ADAD cohort (McDade et al., 2018). $A\beta$ PET is stable in clinical AD, as is the case for CSF $A\beta$ and therefore there is little evidence for correlation between $A\beta$ PET and cognitive impairment (Klunk, 2011). $A\beta$ PET has also shown utility in the imaging of CAA, with several studies demonstrating detection of cerebrovascular amyloid (Farid et al., 2017, Johnson et al., 2007).

Compared to $A\beta$ PET imaging, tau PET imaging is still in its infancy. Several tau PET ligands, known as the first generation of tau tracers, including [^{18}F]THK5317, [^{18}F]THK5351, [^{18}F]AV1451 and [^{11}C]PBB3) have been tested extensively in several studies. Patients with AD have higher levels of tau tracer

binding compared to controls (Johnson et al., 2016, Ossenkoppele et al., 2016), with some studies also showing differences between MCI and controls (Cho et al., 2016). The few longitudinal tau PET tracer studies have suggested that tau PET accumulation appears to be more uniform than the well characterised spread of pathology (Jack et al., 2018). A recent study in ADAD has shown that tau PET uptake is tied to the onset of cognitive decline (Gordon et al., 2019). The first generation tau tracers have demonstrated considerable off-target binding to non-tau protein, such as monoamine oxidase (MAO)-B, leading to the need for development of second generation tau tracers. These tracers, including [^{18}F]MK-6240, [^{18}F]RO-948 [^{18}F]PI-2620, [^{18}F]GTP1, [^{18}F]PM-PBB3, although much less extensively characterised, have showed less off-target binding (Leuzy et al., 2019).

1.4.3.3 Diffusion weighted imaging

Diffusion weighted imaging can provide information about changes to the integrity of grey and white matter in the brain. By examining the diffusion of water molecules, diffusion weighted imaging can give information about the orientation, location and anisotropy of the brain's white matter tracts. The three-dimensional nature of diffusion weighted imaging is characterised by a diffusion tensor, from which metrics can be derived. Fractional anisotropy (FA) provides information about the directional preference of diffusion, with axial (AxD) and radial diffusivity (RD) representing the diffusion in the main direction of the tract and the transverse direction to this. Mean diffusivity (MD) on the other hand reflects the overall movement of water in each voxel. Diffusion weighted imaging has been used to show differences between AD patients and controls in multiple white matter regions (Acosta-Cabronero et al., 2012). Additionally, diffusion weighted imaging can be effective in imaging changes that occur early in the disease process, with alterations in diffusion weighted imaging metrics shown in presymptomatic ADAD patients (Ringman et al., 2007, Ryan et al., 2013).

1.4.3.4 Susceptibility weighted imaging

Susceptibility weighted imaging (SWI) utilises the magnetic susceptibility differences of compounds, such as deoxygenated blood, blood products, iron and cal-

cium to generate new contrasts. SWI is useful in detecting micro and macro haemorrhages and revealing abnormalities to the cerebral vasculature. SWI has been shown to have useful clinical applications, such as in the detection of microbleeds caused by CAA and haemorrhages as a result of stroke (Halefoglul and Yousem, 2018). Additionally the ability of SWI to detect alterations in iron deposition is of importance in numerous neurodegenerative diseases including AD, where increases in iron has been linked to disease pathogenesis (Gao et al., 2017, Halefoglul and Yousem, 2018) .

1.4.4 Modelling of biomarkers

The use of biomarkers in AD is helping to elucidate changes occurring at early disease stages that would otherwise be undetectable. Understanding the temporal ordering of these biomarkers across the disease course is hugely important and is an area of research which is growing rapidly. In the traditional hypothetical model of Alzheimer's disease proposed by Jack et al. (2010a), changes occur first in CSF $A\beta$ and amyloid PET, followed by CSF tau and FDG PET, then structural MRI, then clinical symptoms.

There have been several models derived from the analysis of data from dominantly-inherited AD, where those in the presymptomatic period can be identified and their estimated years to onset (EYO) predicted from the age of onset of their parent or family. Bateman et al. (2012) demonstrated a similar ordering of biomarkers to those proposed by Jack et al. (2010a) in cross-sectional data from the DIAN cohort, with declining CSF $A\beta$ levels estimated to occur 25 years before symptom onset, and with amyloid PET change, increasing CSF tau levels and brain atrophy observed at 15 years prior to onset. Other multimodal biomarker studies in ADAD are in general agreement over this sequence (Benzinger et al., 2013, Fleisher et al., 2015). Models derived from longitudinal data, although largely agreeing with the hypothesised temporal ordering of biomarkers, have demonstrated some interesting differences from cross-sectional studies. McDade et al. (2018) showed that, although predictions of changes in amyloid, cortical metabolism, atrophy and cognition appeared at similar times to cross-sectional estimates, longitudinal estimates

of CSF tau and p-tau elevation occurred 10 years later. A marked decrease in p-tau was also observed close to symptom onset, as opposed to the consistent increase in cross-sectional studies.

Although longitudinal data is more informative about an individual's disease trajectory, reconstruction of complete biomarker trajectories requires extensive longitudinal data collection from across the entire disease course. Due to the great difficulty of collecting such data, the vast majority of longitudinal studies collect short-interval data. Moreover, the majority of previous modelling studies rely on crude pre-defined disease stages (Yang et al., 2011) or use EYO as a proxy of disease progression; EYO being only available in familial AD and can be imprecise (Ryman et al., 2014). To overcome these issues, more complex data-driven approaches to modelling disease are being developed that can provide a greater precision in disease staging (Oxtoby and Alexander, 2017). Approaches such as event-based modelling, where disease progression is considered as a series of events of single biomarker changes, enable sequences of biomarker abnormalities to be determined and can be used to understand different trajectories within AD (Fonteiijn et al., 2012, Oxtoby et al., 2018, Venkatraghavan et al., 2019).

1.5 White matter hyperintensities

1.5.1 Overview

There is currently no cerebrovascular biomarker included in the research framework proposed by Jack et al. (2018). WMHs, largely thought to be vascular in origin, have emerged as a good candidate marker to enhance our understanding of the associations between AD and vascular pathology. WMHs appear hyperintense on T2-weighted or FLAIR imaging and hypointense on T1-weighted imaging and are commonly found in the periventricular region or in the deep white matter (Figure 1.5).

Although WMHs are widely considered to be a surrogate marker of SVD, WMHs also appear in other diseases such as inflammatory conditions like multiple sclerosis (MS), and in inherited leukodystrophies (Sarbu et al., 2016). Even within AD, recent evidence suggests that not all WMHs may have the same origin; some may be degenerative rather than vascular, as a result of AD pathology (McAleese et al., 2017). Research suggests that the pathological basis of WMHs is heterogeneous and that location is important in terms of their underlying cause

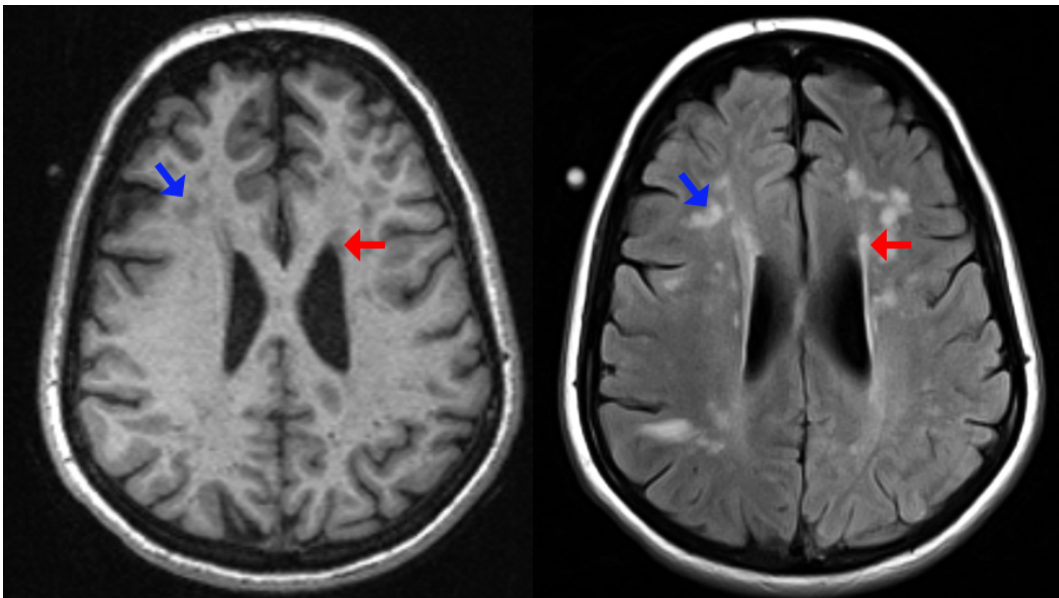


Figure 1.5: T1-weighted image and T2 FLAIR weighted images demonstrating white matter hyperintensities (WMHs). The red arrows indicate periventricular WMHs and the blue arrows demonstrate deep WMHs.

(Gouw et al., 2011, McAleese et al., 2017, Murray et al., 2012). It is clear that more extensive characterisation of WMHs is essential in order to fully understand their potential as a biomarker in AD.

1.5.2 Relevance of WMHs to AD

WMHs are highly associated with age (de Leeuw et al., 2001a, Ylikoski et al., 1995), but they are not always a benign consequence of ageing. WMHs are associated with a greater decline in cognition, in particular in executive function and processing speed (De Groot et al., 2002, Garde et al., 2005, Prins et al., 2005). Individuals with WMHs are also at greater risk of stroke, dementia and death (DeBette and Markus, 2010).

WMHs have been shown to be an important consideration in AD; WMH burden is increased in AD and in patients with MCI compared to controls (Scheltens et al., 1992, Yoshita et al., 2006), predicting controls or MCI patients who convert to clinical AD or dementia (Lopez et al., 2014). There is evidence to suggest that WMHs have direct associations with hallmark AD features; WMHs have been shown to associate with longitudinal brain volume changes (Barnes et al., 2013, Enzinger et al., 2005, Schmidt et al., 2005) and hippocampal volume changes (Fiford et al., 2017). WMHs have also been shown to associate with both CSF A β 1-42 and amyloid PET in both control and disease groups (Marnane et al., 2016, Pietroboni et al., 2018, Zhou et al., 2015). More mixed results have been demonstrated with CSF tau, but some studies have demonstrated a positive association (Tosto et al., 2015, Vemuri et al., 2017).

WMHs have been shown to be an early change in AD. Evidence from ADAD suggests that changes in WMHs could occur in the presymptomatic stage of disease, with total WMH volume deviating from normal controls around 6 years before symptom onset, with increases up to 22 years prior to onset observed in the parietal and occipital lobes (Lee et al., 2016). A second study from the same group demonstrated increases in WMHs up to 20 years prior to estimated onset in a subset of the same cohort (Lee et al., 2018). Another long-term study of healthy elderly controls suggested that an increase in WMH volume was observed around 10 years

before conversion to MCI (Silbert et al., 2012).

1.5.3 Underlying Pathology of WMHs

Compared to the numerous imaging studies on WMHs, research into their pathological basis remains relatively scarce. Pathological studies face the considerable challenge of matching up a relatively small or focal lesion observed on a historical MRI scan, to the corresponding area in the *post mortem* brain, that may have faced distortion after death and fixation methods (Fazekas et al., 1993, Gouw et al., 2008a). The pathological studies that have been carried out have suggested a heterogeneous aetiology, with numerous potential histopathological correlates including demyelination, axonal loss and gliosis (Fazekas et al., 1993, Gouw et al., 2008a, 2011, Murray et al., 2012).

Some evidence suggests that the location and appearance of WMHs could be associated with differences in underlying pathology. It is suggested that WMHs in the periventricular region have myelin and oligodendrocyte loss and astrogliosis, whereas deep WMHs demonstrate a loss of myelin that is not accompanied by oligodendrocyte loss (Fazekas et al., 1993, Gouw et al., 2008a, 2011, Murray et al., 2012). Some studies have suggested that deep WMHs are more related to ischaemic changes as a result of SVD, whereas periventricular WMHs are particularly related to age and due to alterations in fluid dynamics at the ventricular lining (Smith et al., 2016). Other research has differentiated WMHs even further, suggesting that both mild, well-defined periventricular WMHs and deep punctate WMHs may not be clinically relevant, whereas diffuse periventricular WMHs and confluent deep WMHs correspond to more severe tissue changes of ischaemic origin (Gouw et al., 2011). Other theories however are that periventricular and deep WMHs are more likely part of a continuous pathology, and differences are more related to disease stage than anything else (Fazekas, 2014, Wardlaw et al., 2015).

1.5.4 Pathogenic mechanisms of WMH formation

The prevailing theory is that WMHs are a result of some form of vascular dysfunction, most commonly ischaemia. WMHs tend to be located in areas that receive

their blood supply from long perforating arteries with a long and tortuous course, resulting in an increased susceptibility to ischaemic changes (Black et al., 2009, Fazekas, 2014). Arteriolosclerosis and hyaline wall thickening of these long arteries, along with impaired autoregulation could result in the ischaemia of the white matter in these areas, leading to WMHs (Prins and Scheltens, 2015).

There is also evidence to suggest that CAA could be a factor in WMHs. One proposed mechanism for this is that the vascular deposition of $A\beta$ in the walls of cerebral blood vessels can lead to a reduction in blood supply to the white matter and subsequent ischaemia (Reijmer et al., 2016). The failure of interstitial fluid drainage through perivascular pathways has been proposed to underlie the amyloid deposition seen in CAA (Weller et al., 2015). Associations between CAA and posterior locations of WMHs have been demonstrated in both sporadic and familial Alzheimer's disease (Ryan et al., 2015, Thanprasertsuk et al., 2014, Weaver et al., 2019).

Another theory of WMH formation, is that they are related to cerebrovascular endothelial failure, causing increased permeability of the blood-brain barrier. This could lead to leakage of material into the vessel wall and surrounding brain tissue causing downstream consequences such as thickening of the vessel wall, inflammation and impaired autoregulation, leading to ischaemia (Wardlaw et al., 2013, 2017). It has also been hypothesised that periventricular hyperintensities could be due to changes in CSF dynamics at the ependymal lining of ventricles (Fernando et al., 2006, Simpson et al., 2007a).

As well as AD, WMHs are also a feature of inflammatory conditions such as MS. Unlike MS, it is improbable that inflammation is the major cause of WMHs seen in AD, however some large studies have demonstrated a potential involvement for inflammatory pathways (Lin et al., 2017, Swardfager et al., 2017). Elevations of peripheral inflammatory markers have been found in people with clinical AD and extensive WMHs (Swardfager et al., 2017).

Recently, it has been proposed that WMHs may, at least in part, be a result of Wallerian degeneration in the context of cortical AD pathology. McAleese et al.

(2017) found that parietal WMHs were not related to SVD, instead associating with Wallerian degeneration as a result of phosphorylated tau pathology, in AD, but not controls (McAleese et al., 2017).

It is looking increasingly likely that WMHs are not the product of one unifying mechanism. Much more work is necessary to identify if there are any characteristics, such as location, size or disease type or presence, that can point to a particular pathogenesis before any widespread use as an AD biomarker.

1.5.5 Quantification

In order to undertake any analysis of WMHs, a suitable method of identification must be used. This needs to be effective in detecting such heterogeneous lesions as WMHs, where there are large variances in size, confluence and location. MRI scans commonly have regions of artefact that resemble WMHs (Figure 1.6), such as those attributable to vascular or CSF flow (Bakshi et al., 2000, Gawne-Cain et al., 1997), corticospinal tracts, motion (Gawne-Cain et al., 1997) and magnetic susceptibility due to bone, air and teeth fillings at the base of the frontal lobe (Lavdas et al., 2014). Additionally, FLAIR images, although the easiest modality on which to visualise WMHs, are susceptible to regions of bright artefact (Bakshi et al., 2000).

Historically, WMHs have been assessed using a visual rating method such as the Scheltens scale or Fazekas scale (Fazekas et al., 1987, Scheltens et al., 1993). Both methods are highly subjective and are limited in their ability to fully capture information relating to size, location and severity of lesions. Manual segmentation methods are considered the ‘gold standard’ as they are very accurate in delineating WMHs from artefact and allow exact WMHs volumes to be quantified. However this process is still subject to both inter- and intra-rater variability and is time consuming (Wilke et al., 2011). WMH segmentation methods need to be translatable to the large datasets that are increasingly common in AD research, and to volumetric scans that take longer to segment. Research into WMHs is therefore shifting to more automated segmentation techniques. Although faster, automated techniques remain liable to errors relating to the artefacts described above and must therefore be assessed in comparison with a gold standard and quality control procedures put

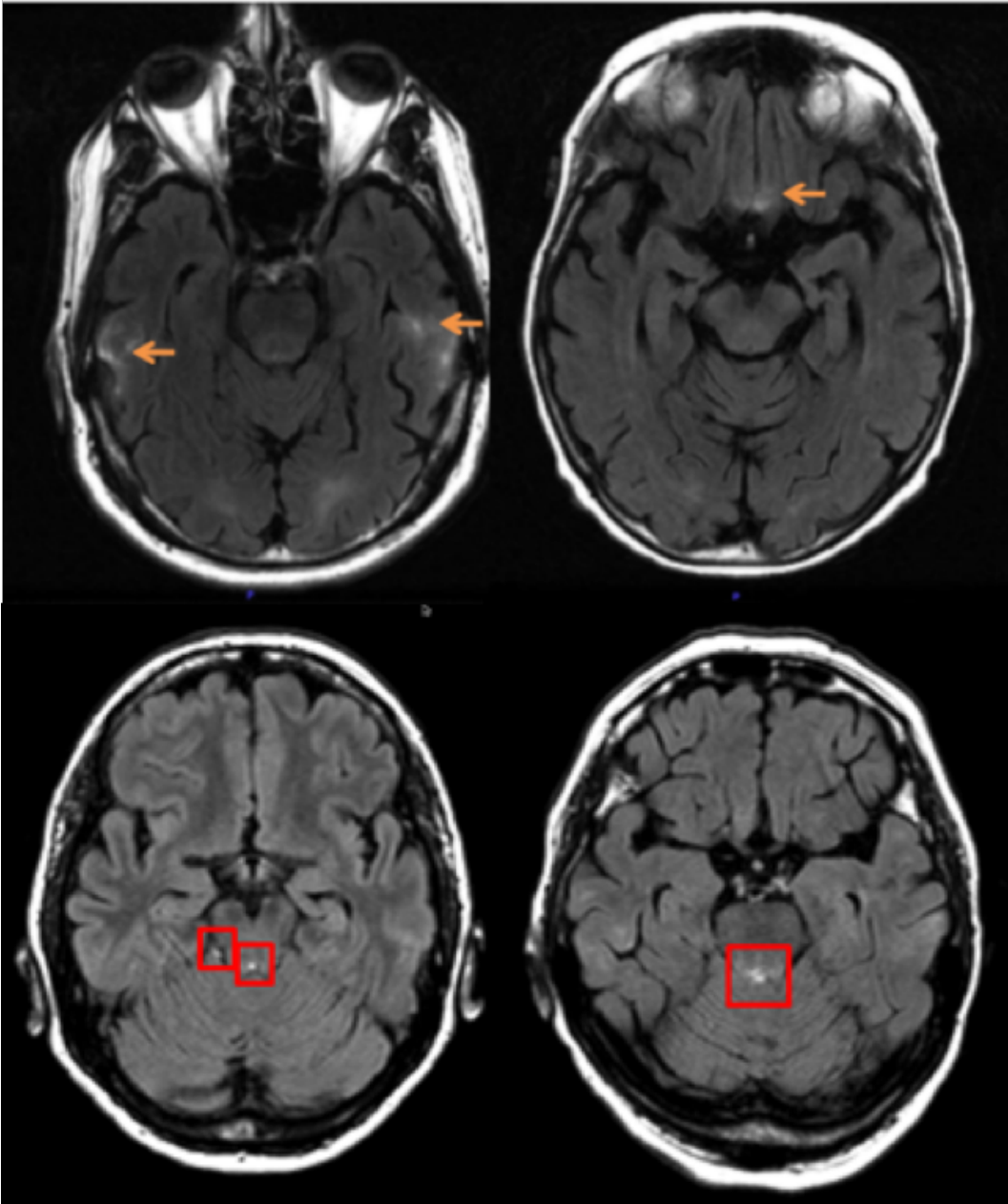


Figure 1.6: Common hyperintense artefact. The orange arrows highlight artefact in the temporal and frontal temporal lobes. The red boxes highlight artefact in the cerebellum and brainstem, which is commonly due to vascular or CSF flow artefact.

in place.

1.6 Thesis rationale

WMHs show great promise as a biomarker in AD; the burden of WMHs is increased in AD and MCI compared to controls (Scheltens et al., 1992, Yoshita et al., 2006),

they can predict controls or MCI patients who will convert to AD (Lopez et al., 2014), they are associated with a greater decline in cognition (De Groot et al., 2002) and WMH burden is increased early on in the disease process (Lee et al., 2016, 2018). However, the hyperintense signal observed on T2-weighted/FLAIR imaging is non-specific and is likely to have a heterogeneous pathological basis (Gouw et al., 2008a). In order for their use as a successful biomarker in AD, a greater understanding of the pathology that WMHs represent is necessary. Although traditionally thought of as a marker of SVD, evidence suggests that the pathological basis could be mixed, and dependent on traits such as location and disease stage (Gouw et al., 2011, McAleese et al., 2017).

Additionally, how WMHs fit in the context of well characterised AD pathology and existing biomarkers is poorly understood. Previous studies have shown associations between WMHs and $A\beta$ (Marnane et al., 2016), but do not cover the entire disease spectrum. The results for tau (Kester et al., 2014, Tosto et al., 2015) and NFL biomarkers (Mattsson et al., 2019, Osborn et al., 2018) are more mixed, with evidence for and against associations with WMHs.

In light of the above, the aims for this thesis are:

1. To investigate associations between WMHs and biomarkers of the hallmark AD pathologies.
 - Chapter 3 - In this chapter I will look at associations of WMHs and CSF $A\beta$, t-tau and p-tau using baseline data from the ADNI cohort.
 - Chapter 4 - In this chapter I will look at associations of WMHs and NFL using baseline data from the ADNI cohort.
2. To investigate WMHs in ADAD and assess the affect of mutation status.
 - Chapter 5 - In this chapter I will look at how WMHs change over time using longitudinal data from the DIAN cohort. I will assess the affect of mutation type on WMHs and look at associations with brain atrophy as quantified using the boundary shift integral (BSI).

3. To investigate the underlying pathology of specific WMHs using *ex vivo* imaging and subsequent histology correlations.

- Chapter 6 - In this chapter I will assess *ex vivo* MRI and subsequent histological investigation as a tool for studying the underlying pathology of WMHs in a small, young onset AD cohort. I will develop and assess the effectiveness of an *ex vivo* MRI, brain sampling and histology pipeline, before testing methodology for the registration of the *in vivo* and *ex vivo* scans, and the *ex vivo* scan and histological sections. I will then assess whether similarities or differences in WMHs between the last *in vivo* MRI and the *ex vivo* scan can be observed, before looking for any pathological changes apparent at the location of WMHs.

Chapter 2

Methods

2.1 Cohorts

2.1.1 ADNI

For the data featured in Chapters 3 and 4, data from ADNI was used. ADNI is a multicentre, longitudinal public-private funded partnership, with the primary goal of using demographic, biomarker, neuropsychological and MRI data to monitor progression of AD. Since 2003, Principle Investigator Michael W. Weiner, MD, has overseen recruitment of healthy controls, MCI and AD subjects from over 50 sites across the United States and Canada. (For up-to-date information, see www.adni-info.org). Participants took part in baseline and follow-up clinical, neuropsychometric and MRI assessments. CSF data was collected from all subjects where possible. Written informed consent was obtained by the Institutional Review Board at each participating centre. The data was downloaded from the ADNI database (<http://adni.loni.usc.edu/>). Detailed information on inclusion and exclusion criteria can be found here <https://adni.loni.usc.edu/wp-content/uploads/2008/07/adni2-procedures-manual.pdf>.

Of importance to the work in this thesis, participants with a score of greater than 4 on the Hachinski scale were excluded (Hachinski et al., 1975), resulting in data that reflects a low prevalence of cerebrovascular disease. Additionally, in order to try and screen out atypical presentations of AD, an amnesic impairment was required in MCI and AD participants. Recruitment into ADNI occurred in several

phases. The first phase, ADNI1, enrolled 200 controls, 400 MCI and 200 mild AD participants. 500 of these controls and MCI subjects continued to be followed up into the ADNIGO and ADNI2 phases. The second phase, ADNIGO, additionally enrolled 200 new early MCI (EMCI) participants. The third phase, ADNI2, newly enrolled 150 normal control, 150 EMCI, 150 late MCI (LMCI) and 200 mild AD. In the work in this thesis, only used data from participants that were newly recruited into the ADNIGO and ADNI2 phases were used.

A diagnosis of MCI was based on a significant memory concern (by participant or informant) and a clinical dementia rating of 0.5, but a Mini-Mental State Examination (MMSE) no lower than 24. Level of MCI (early or late) was determined by the Wechsler Memory Scale Logical Memory II (<https://adni.loni.usc.edu/wp-content/uploads/2008/07/adni2-procedures-manual.pdf>). The significant memory concern (SMC) group was developed by ADNI to bridge the gap between controls and MCI participants, and is characterised by individuals who have self-reported a memory complaint but score within a normal range for cognition.

2.1.2 DIAN

For the work in Chapter 5, data was used from participants that were members of the DIAN cohort, available at the tenth data freeze. Established in 2008, DIAN is the first international collaborative study of individuals carrying *PSEN1*, *PSEN2* and *APP* mutations with the main aim of characterising the progression of disease, especially in presymptomatic periods. Longitudinal clinical, imaging, neuropsychological, and blood and CSF data is collected across 14 centres worldwide. The cohort includes asymptomatic and symptomatic mutation carrier and their non-carrier family members, who serve as a control group. Genotyping was carried out to ascertain the mutation and carrier status of each participant. Ethical approval was obtained by each participating centre and all study participants provided written informed consent. The institutional review board at Washington University (St Louis, MO, USA) provided supervisory review and human studies approval. (For up to date information see <https://dian.wustl.edu>).

Clinical and imaging visits in DIAN are performed every 3 years for asymptomatic individuals until they are within 3 years of their parental age of dementia onset. Assessments switch to annual once an individual is within 3 years of parental age at onset or they become symptomatic. The clinical assessment of participants included evaluation using the Clinical Dementia Rating (CDR) and an estimation of parental age at onset, used as a predictor of participants' expected age at onset. A participant's EYO was subsequently calculated by subtracting the affected parent's symptom onset age from the participant's age at scan visit.

2.2 In vivo MRI acquisition

2.2.1 ADNI

All sites in ADNI use a standardised protocol to obtain MRI data (3T), described in Jack et al. (2015), before undergoing quality control at the Mayo Clinic (Rochester, MN) to assess protocol compliance, image quality and any significant neurological/radiological abnormalities. Further quality control was undertaken at the Dementia Research Centre for motion artefacts. In depth imaging protocols can be found at <http://adni.loni.usc.edu/methods/documents/mri-protocols/>.

2.2.2 DIAN

MRI scans in DIAN were obtained using the standardised ADNI protocol described above in section 2.2.1.

2.3 MRI analysis

2.3.1 WMH segmentation

2.3.1.1 Bayesian Model Selection (BaMoS) WMH segmentation

BaMoS is a novel data modelling framework for segmentation of pathological tissue types (such as WMHs), generated by Dr Carole Sudre (Sudre et al., 2015). This method was used to segment WMHs in Chapters 3 and 4 and was compared to a manual segmentation method in Chapter 5. WMHs were segmented jointly

using T1-weighted and T2-weighted/FLAIR sequences linearly co-registered in T1 space. Images are bias field corrected. BaMoS jointly models healthy and unexpected pathological tissue types by modelling the data as a hierarchical three-level Gaussian mixture model. Each anatomical tissue class (grey matter, white matter, CSF, non-brain) is modelled as a mixture of Gaussians whose number is automatically and dynamically determined using a split and merge strategy and constrained by anatomical probabilistic atlases and neighbourhood constraints. Both skull-stripping and atlases are obtained as a result of the label-fusion Geodesic Information Flows (GIF) framework (Cardoso et al., 2015). Skull stripping was incorporated in the automated segmentation in order to normalise the data as part of the BaMoS pipeline.

Finally, correction for false positives was applied to discard regions of muscle, fat, skin, choroid plexus or other wrongly classified tissue based on clinical knowledge of WMHs. In order to increase sensitivity to smaller WMH lesions with a higher susceptibility to partial volume effect, a two-step two-threshold detection of candidate lesions was adopted. Furthermore, the classification of candidate lesion connected components was performed in two consecutive steps: first with a 6 neighbourhood followed by an 18 neighbourhood definition in order to avoid discarding region of mixed origin (artefacts + true lesion). Only supratentorial WMHs were used.

All WMH segmentations were checked by a trained WMH rater for gross errors. This quality control step was used to further develop robust improvement to the post-processing step, contributing to a better handling of artefacts and their differentiation from true WMHs. The corresponding cases were re-processed with the appropriate modifications. Where there were image duplicates, the best segmentation was chosen.

2.3.1.2 Semi-automated white matter hyperintensity segmentation

The semi-automated WMH segmentation method was developed by Dr Cassy Fiford, described in Fiford et al. (2020). This method was used for the WMH segmentation training described in Chapter 3 and for WMH segmentation in Chapter 5. T1-

weighted scans were registered to the FLAIR scans and segmentation was carried out in FLAIR space. This protocol involves two intensity thresholds for segmentation, whereby a higher threshold was used for WMHs with unclear boundaries and a lower threshold was used for WMHs with definite boundaries. The higher threshold was used in areas where WMHs are likely to be developing, often having a bright core with a diffuse boundary, and in areas that have WMHs that are considered clinically normal such as periventricular caps (Gawne-Cain et al., 1997). The lower threshold was used for lesions that are typically less bright and with defined boundaries. A manual freehand approach was used for specific WMHs that were not identified by the thresholds, but extra care was taken to ensure that abnormal signal was present on both imaging modalities (FLAIR and T1-weighted), and that temporal lobe and vascular flow artefacts were not included.

The high and low thresholds were based on percentages of median whole brain intensity of the FLAIR, which were calculated using brain masks generated using the GIF label fusion framework (Cardoso et al., 2015) on the T1-weighted image and then copied to the co-registered FLAIR image. Threshold values were optimised for the scanner type used, with Siemens and Philips scanners having high and low thresholds of 130% and 120% of median brain intensity and GE scanners having higher thresholds of 140% and 130%. The median whole brain intensity was also used to obtain minimum and maximum viewing intensities, calculated as 15% and 238% of median brain intensity respectively.

Volumes from the two thresholds and any freehand segmentations were added together using `seg_maths` from the NiftySeg platform and the total segmentation volumes were extracted.

For the segmentation of the WMHs in Chapter 5, the protocol was further developed for use with longitudinal data to ensure consistency across the same subject. Two consecutive segmentations were carried out: First a 'separate timepoint' method and secondly a 'multiple timepoint' method.

2.3.1.2.1 ‘Separate timepoint’ Method

Every timepoint from each subject was initially treated as if they were independent scans from separate individuals. A script was created that loaded up images in a random order, to blind the rater. T1-weighted images (registered to the FLAIR images) and the FLAIR images at the required viewing intensity were loaded up side by side in NiftyMIDAS. The values for the high and low segmentation thresholds were coded to appear in the image file name and the thresholds were set prior to each segmentation. The segmentation was then carried out in the manner described above.

2.3.1.2.2 ‘Multiple timepoint’ Method

In a second round of segmentations, the longitudinal nature of the scans were taken into account. This method was to ensure that WMHs from one subject were being consistently included across all timepoints. A script was developed to load all timepoints from each subject into NiftyMIDAS concurrently. Low threshold, high threshold and freehand segmentations from the ‘separate timepoint’ method overlaid onto the FLAIR images, along with the T1-weighted images, were displayed adjacent to each other. In order to ensure the person segmenting was blinded to both subject and timepoint, the script loaded subjects randomly with their timepoints in a random order. WMHs that had not met the threshold for inclusion, but were consistently included across other timepoints, was considered for editing using the following guidelines:

- In higher threshold regions where a definite WMH had been missed, the lower threshold was used. In these subjects, it was common for the other timepoints that had picked up this WMH to not capture the full extent of the lesion (the T1-weighted image was used especially closely as a reference in these instances). The higher threshold was therefore removed and replaced with the lower threshold to be consistent across all timepoints for one subject.
- No freehand segmentations were used in strictly high threshold regions (e.g. in the posterior corona radiata).
- Where WMHs had been missed in regions where the lower threshold would

normally be used, a freehand segmentation was used using the hypointense region on the T1-weighted image as a reference.

2.3.2 Boundary shift integral

In Chapter 5, brain volume loss was calculated using the using the BSI (Freeborough and Fox, 1997). The BSI was used to estimate change directly from pairs of T1-weighted scans, following whole brain segmentation using the whole brain masks calculated from GIF. Pairs of scans were linearly registered (using 12 degrees of freedom). The results of all the pairwise registrations were then averaged to find the midpoint space. Scans were transformed to the midpoint space and underwent differential bias correction. Volume change between baseline scan and each serial scan was then measured using the BSI in the average space (Leung et al., 2012).

2.3.3 Total intracranial volume (TIV)

In many analyses TIV is used as a proxy for prodromal brain size. TIV was estimated using GIF, using T1-weighted images only (Cardoso et al., 2015).

2.4 Pathology

2.4.1 Cases

The brains used in this study were donated to the Queen Square Brain Bank for Neurological Disorders (QSBB; Institute of Neurology, University College London). Ethical approval for the study was obtained from the Local Research Ethics Committee of the National Hospital for Neurology and Neurosurgery.

2.4.1.1 Staging of cases

A neuropathological diagnosis was determined by the neuropathologist, Dr Zane Jaunmuktane, at Queen Square Brain Bank using the three-tiered grading system set out by the National Institute of Aging, Alzheimer's Association guidelines. Firstly, a Thal phase ranging from 0 - 5 was given based on the distribution of $A\beta$ plaques in the neocortex, allocortex and basal ganglia, brain stem and cerebellum (Thal et al., 2002b). Secondly, a Braak and Braak stage of I-VI was given for the distribution of tau pathology throughout the brain (Braak and Braak, 1991). Lastly, the frequencies

of neuritic plaques were staged with a score of 0 - 3 called the CERAD score. The three different scores are then used to determine the overall ABC score (Montine et al., 2012).

The extent and severity of CAA was determined by the neuropathologist, Dr Zane Jaunmuktane, based on a five-tier grading system (Olichney et al., 1996). Score 0 was given to vessels with no amyloid deposition, while score 1 was given to those with traces or scattered distribution of amyloid in leptomeningeal or cortical blood vessels. A score of 2 is indicative of some vessels in the leptomeninges having circumferential amyloid staining. Score 3 represents widespread, circumferential staining of many leptomeningeal and superficial cortical vessels. A score of 4 corresponds to severe amyloid deposition accompanied by projection of amyloid into the adjacent parenchyma or the presence of amyloid deposition in capillaries.

2.4.2 Histological staining

15 μ m thick paraffin sections were dried at 37°C overnight. Sections were placed in three changes of xylene for 3 minutes each in order to deparaffinize them. Sections were then rehydrated in graded alcohol in the order of 100%, 90% and 70%, before washing. For haematoxylin and eosin (H&E) staining, sections were placed in Gill's haematoxylin for 5 mins, followed by washing and differentiation in acid alcohol. Sections were then washed under running tap water. For luxol fast blue (LFB) staining, sections were placed in filtered LFB solution at 60°C overnight. Sections were then washed twice in deionised water, before differentiating in lithium carbonate. Sections were then placed in 70% alcohol, followed by washing in deionised water. Sections were then stained in acidified, filtered cresyl violet solution for 20 minutes at 60°C, before a final wash.

2.4.3 Immunohistochemistry

15 μ m thick paraffin sections were dried at 37°C overnight, before being incubated at 60°C overnight prior to starting the immunohistochemistry protocol. Sections were placed in three changes of xylene for 3 minutes each in order to deparaffinize them. They were then rehydrated in graded alcohol in the order of 100%, 90%

and 70%. The endogenous peroxidase activity was blocked using 0.3% hydrogen peroxide in methanol for 10 minutes and then washed in distilled water for 5 minutes. Sections were then pressure cooked in citrate buffer pH 6.0 for 10 minutes or incubated with proteinase K (MBP antibody). Non-specific protein binding was blocked by incubating the sections for 30 minutes at room temperature in 10% non-fat milk in TBS-Tween. The slides were then incubated in primary antibody for 1 hour at room temperature. The sections were then washed 3 times in TBS-Tween, with 2 minutes between each wash. The sections were then incubated with their respective biotinylated secondary antibodies (rabbit anti-mouse, Dako, 1:200, swine anti-rabbit, Dako, 1:200) for 30 minutes at room temperature followed by washing 3 times in TBS-Tween, with 2 minutes in between each wash. Sections were then incubated in avidin-biotin complex (Dako) for 30 minutes at room temperature, followed by washing 3 times in TBS-Tween, with 2 minutes in between each wash. The antigen-antibody reaction was visualised using diaminobenzidine (DAB, Sigma) as the chromagen. Sections were placed in a TBS-Tween DAB solution, which was activated with 128 μ l of hydrogen peroxide for 4 minutes before checking the intensity of the colour. Sections were then counterstained with Mayer's Haemotoxylin (BDH) for 15 seconds before being washed in warm water. The sections were then dehydrated through graded alcohol concentrations (70%, 90% and 100%) before being cleared in two changes of xylene. The sections were then mounted using Depex (BDH).

2.5 Software

2.5.1 NiftyMIDAS

NiftyMIDAS is a software tool used in this thesis for WMH segmentation. NiftyMIDAS has recently been developed by Centre for Medical Imaging Computing at UCL. NiftyMIDAS enables simultaneous segmentation of multi-modal data, which was used in this work to semi-automatically segment and display FLAIR and T1-weighted images. NiftyMIDAS has recently been made open source as part of NifTK (<https://cmiclab.cs.ucl.ac.uk/CMIC/NifTK>).

2.5.2 Stata

Stata version 16 (Stata Corporation, College Station, TX, USA) was used for all of the statistical analysis in this thesis.

2.5.3 Olympus VS-desktop

VS-desktop (Olympus) is a image analysis tool used in this thesis for the visualisation and extraction of the scanned slides.

2.5.4 ImageJ

ImageJ (<https://imagej.nih.gov/ij/>) is an open source Java image processing program developed at the National Institute of Health. ImageJ was used for the analysis of the immunohistochemical stains.

Chapter 3

Associations of WMHs and CSF biomarkers in sporadic AD

3.1 Introduction

Research studies are now moving toward a more biomarker led approach to AD (Jack et al., 2018), making it important to understand how possible biomarkers are interrelated at different stages of disease. Previous studies have found that WMHs associate with amyloid accumulation, as measured by PET (Kandel et al., 2016, Marnane et al., 2016) and CSF biomarkers (Marnane et al., 2016, Pietroboni et al., 2018). Tau aggregation has also been linked to WMH burden (McAleese et al., 2015, Tosto et al., 2015), although results are somewhat less consistent (Kester et al., 2014, Osborn et al., 2018). The aim of this chapter was to add evidence to further characterise these complex relationships between AD and WMHs, and to extend the current literature by examining these relationships across the full spectrum from normal ageing to AD.

I hypothesised that WMHs would show associations with CSF $A\beta$ 1-42, t-tau, and p-tau biomarkers, reflecting the potential relationships between vascular dysfunction, amyloid deposition, neurodegeneration, and tau deposition. Because WMHs are likely to represent different admixtures of pathology at different disease stages, with recent evidence suggesting in later disease stages WMH associations with tau may be stronger (McAleese et al., 2017) and $A\beta$ 1-42 may be weaker

(Zhou et al., 2009), I also hypothesised that the relationships between $A\beta$ and tau biomarkers and WMHs may change throughout the disease course with stronger associations between tau markers and WMHs at later disease stages, and weaker associations between $A\beta$ 1-42 and WMHs at the more advanced stages.

3.2 Methods

3.2.1 Cohort

All data used for this work was from the ADNI2 and GO database, see section 2.1.1. A proportion of subjects also had available CSF $A\beta$ 1-42, t-tau and p-tau data collected. Controls, SMC, EMCI, LMCI, and AD participants newly recruited into ADNI2 or GO, who had a baseline 3T FLAIR and T1-weighted MRI scan were used in this study.

3.2.2 WMH segmentation

3.2.2.1 WMH segmentation training in a training ADNI dataset

In order to ensure I was proficient in assessing any segmentation of WMHs, I underwent training on the semi-automated segmentation protocol developed by Dr Cassy Fiford and described in section 2.3.1.2. Here my effectiveness at segmenting WMHs was assessed on a training data set, using an expert rater to assess inter-rater reliability. 60 subjects from the ADNI2/GO dataset were segmented by myself and an expert rater (Dr Cassy Fiford). This assessment set were composed of 30 controls and 30 AD patients from each of the three scanner types (Siemens, Philips and GE). T1-weighted images were registered to the FLAIR images. Segmentation was blinded to subject identity, diagnosis and scanner type. The only prior knowledge was the high and low segmentation thresholds, which were calculated as percentage of median brain intensity.

Overall WMH volumes from myself and the expert rater were compared, along with Dice score coefficients. The Dice score coefficient is a measure of spatial overlap between two segmentations. The Dice score is highly dependent on the WMH load, with the same amounts of error between two segmentations affecting

the Dice score of the small volume more than the larger volume. A Dice score of 0.7 or over is widely considered to be good (Caligiuri et al., 2015).

3.2.2.2 Automated segmentation in the full ADNI cohort

The ADNI MRI protocol has been described previously in (Jack et al., 2008a) and in section 2.2.1. WMH segmentation was carried out using BaMoS, described previously in section 2.3.1.1. A visual assessment of all the BaMoS WMH segmentations using NiftyMIDAS was carried out and their performance was graded from 1 - 3, where 1 was a pass, 2 had borderline levels of artefact and 3 had unusable levels of artefact. Information about the artefact location was also noted. 911 participants' scans were reviewed, with 890 graded 1, and only 16 and 5 graded 2 and 3 respectively. The BaMoS algorithm subsequently underwent methodological improvements using the information about the artefact severity and location. The visual assessment was then repeated by Dr Josephine Barnes. In this second visual assessment, an increased number of scans were available from ADNI so that 944 individuals were assessed, and 12 were considered unusable. 3 further individuals were excluded because of lack of demographic/diagnostic information. To calculate the parietal and nonparietal WMHs, Euclidean distance maps from the cortical lobar parcellation obtained from GIF were used to assign each white matter voxel to the closest associated lobe.

3.2.3 CSF measurements

CSF $A\beta$ 1-42, t-tau, and p-tau were measured at the ADNI biomarker core (University of Pennsylvania) using the microbead-based multiplex immunoassay, the INNO-BIA AlzBio3 RUO test (Fujirebio, Ghent, Belgium), on the Luminex platform (Luminex Corp, Austin, TX, USA). The raw, untransformed CSF values were used in all analyses. Additional analyses were carried out on CSF data obtained using the Roche Elecsys cobas e 601 fully automated immunoassay platform at the ADNI biomarker core (University of Pennsylvania).

3.2.4 Statistical analyses

3.2.4.1 Variables used in analyses

The participant information downloaded and used in this study included: age, gender, MMSE scores, *APOE* $\epsilon 4$ status, height and weight, smoking status, history, hypertension history and diabetes history. BMI was calculated from height and weight variables. Smoking status was coded as 1) never smoked, 2) previous smoker, 3) current smoker, using the information downloaded on smoking history.

3.2.4.2 Data transformation

For WMHs, most analyses were performed on \log_e transformed values to reduce skewness. For analyses involving associations between WMH volume and CSF biomarkers, CSF biomarker values were standardised using the pooled within-group standard deviations (SDs) calculated from a linear regression model for each biomarker that allowed for differences in mean levels by group. Because WMH volumes were analysed on a logarithmic scale the resulting coefficients were back-transformed so that they expressed percentage increases or decreases in WMHs for each 1 SD increase in CSF biomarkers.

3.2.4.3 Diagnostic group differences

To estimate differences in means across groups for demographic, imaging, and CSF variables, linear regression models were used for continuous variables. For \log_e WMHs, linear regression models were used with group as the predictor of interest and adjustment for TIV. Differences in untransformed WMH volumes across diagnostic groups were also assessed, using linear regression with adjustment for TIV. Analogous comparisons were performed for categorical variables, with Fisher's exact tests used for gender, *APOE* $\epsilon 4$ status, hypertension and diabetes, and a chi-square test for smoking status.

3.2.4.4 WMH and CSF biomarker relationships with age

Analyses were performed assessing the relationship between age and WMHs using linear regression models with \log_e WMHs being the dependent variable and age and TIV being predictors. This was initially performed in each diagnostic group

separately, with one further model fitted that allowed for an interaction between diagnostic group and age.

To examine relationships between age and CSF variables, linear regression models were initially performed with $A\beta 1-42$ as the dependent variable and age as the predictor, before replacing $A\beta 1-42$ with t-tau and then p-tau.

3.2.4.5 WMH and CSF biomarker relationships

To explore whether CSF $A\beta 1-42$ was associated with WMHs across diagnostic groups, separate diagnostic group-specific linear regression models were fitted with \log_e WMHs as the dependent variable and standardised $A\beta 1-42$ and TIV as predictors. Between-group differences in slope were assessed by fitting a further model in the combined diagnostic groups, with interactions between diagnostic group and $A\beta 1-42$, and carrying out a joint interaction test. All models were also refitted with age at the baseline as an additional covariate. Analyses including age were secondary, since age at the baseline may be on the causal pathway (theoretically a proxy for the number of vascular events that may have happened to an individual and the ability to clear amyloid). Analogous procedures were used with $A\beta 1-42$ values being replaced by t-tau and then by p-tau. Scatter plots of \log_e WMH volume against CSF $A\beta 1-42$, t-tau, or p-tau in each group were also generated to show unadjusted associations.

Further analysis was carried out in the cohort as a whole, adjusting for participant group. A first set of linear regression models explored the $A\beta 1-42$ -WMH relationship adjusting for (1) nothing; (2) TIV; (3) TIV and diagnostic group; (4) TIV, group and age; (5) TIV, group age and *APOE* $\epsilon 4$. This was repeated in a second set of models adding t-tau as a covariate to all models in the set (1) to (5) and in a third set of models by adding p-tau to all models in the set (1) to (5). Partial R^2 values for these potential confounders were also calculated for each covariate from model (5) in each set.

This covariate analysis was then repeated twice for the relationship with t-tau and then p-tau with WMHs, with the second set of models adding in $A\beta 1-42$ as a covariate.

3.2.4.6 Elecsys biomarker analysis

The group specific analyses described above were repeated using the Elecsys biomarker data, where available. Group-specific linear regression models were fitted with \log_e WMHs as the dependent variable and standardised biomarker and TIV as predictors.

3.2.4.7 Vascular risk analysis

To assess the impact of vascular risk factors on the WMH-age relationship, smoking, hypertension, body mass index (BMI), and diabetes were added as covariates into separate diagnostic group-specific models and then in a combined model.

3.2.4.8 Parietal lobe vs whole brain analysis

Associations between CSF biomarkers and parietal lobe WMH volumes versus non-parietal WMHs were also assessed. These analyses used CSF A β 1-42, t-tau, or p-tau as the dependent variable and \log_e transformed parietal and nonparietal WMH volumes as predictor variables.

3.3 Results

3.3.1 WMH segmentation training

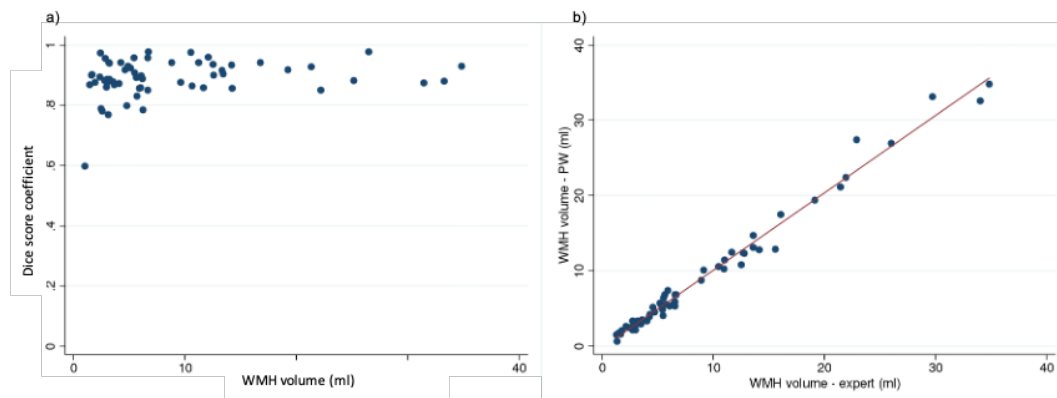


Figure 3.1: Scatter plots showing a) the comparison of the raw WMH volumes segmented using BaMoS and the semi-automated protocol and b) Dice score coefficients demonstrating the degree of overlap.

Figure 3.1 demonstrates the high level of similarity between the semi-automated segmentations carried out by myself and the expert rater on the training set of 60 scans. This is indicated by the volumes (Figure 3.1a) and the Dice score coefficient (Figure 3.1b). The Dice score coefficient demonstrates a high degree of overlap between the trainee and expert, with values of between 0.8 and 1 for most subjects.

3.3.2 Group demographics

There were 929 subjects with useable WMH values and available demographic data. Table 3.1 shows demographic, imaging, and CSF biomarker summary statistics for each diagnostic group. Between-group differences were seen in age, with the AD group being the oldest and the EMCI group being the youngest. Participants differed as expected in terms of MMSE, *APOE* ϵ status, CSF $A\beta$, CSF t-tau, and CSF p-tau with poorer scores, greater $\epsilon 4$ carriage, and CSF biomarkers indicative of more pathology from controls to EMCI to LMCI to AD. Group differences were also seen in WMH volume, driven by the AD group having a significantly higher burden than all groups (Table 3.1, Figure 3.2). In terms of vascular risk factors, differences were only observed between groups in BMI, with a lower BMI observed in the AD group.

Table 3.1: Demographic, imaging and CSF summary statistics

	Controls	SMC	EMCI	LMCI	AD	<i>p</i> value across groups
N (total = 929)	180	107	320	171	151	
Age	73.4 (6.2)	72.3 (5.5)	71.0 (7.5)	72.4 (7.7)	75.0 (8.0)	<0.001
Male (%)	46	43	54	56	56	0.08
MMSE /30	29.0 (1.3)	29.0 (1.3)	28.3 (1.6)	27.6 (1.8)	23.1 (2.1)	<0.001
<i>APOE</i> ϵ 4 positive (%)	33	36	47	60	71	<0.001
TIV (ml)	1403 (134)	1414 (125)	1423 (136)	1436 (132)	1416 (151)	0.2
WMH volume (ml) Median (IQR)	3.4 (4.8)	3.4 (4.4)	3.8 (6.1)	3.7 (8.1)	5.8 (9.0)	0.005^a
Log _e WMHs (ml)	1.3 (0.9)	1.3 (0.9)	1.4 (1.0)	1.4 (1.0)	1.7 (1.0)	0.002^a
CSF A β 1-42 (pg/ml) ^b Median (IQR)	270.5 (80.2)	308.3 (91.2)	251.0 (79.0)	212.0 (77.3)	181.1 (64.3)	<0.001
CSF t-tau (pg/ml) ^c Median (IQR)	62.5 (29.0)	59.6 (24.7)	70.9 (42.3)	93.3 (50.2)	120.1 (56.3)	<0.001
CSF p-tau (pg/ml) ^d Median (IQR)	21.8 (10.0)	21.6 (10.6)	23.0 (11.0)	28.6 (14.3)	34.2 (17.8)	<0.001
History of hypertension (%)	49	47	50	45	52	0.8
Smoking: Never (%)	58	53	39	65	61	
Smoking: Previous (%)	37	45	2	33	34	0.4
Smoking: Current (%)	4	2	10	2	4	
BMI	27.4 (4.6)	28.4 (6.3)	28.2 (5.3)	27.4 (4.9)	26.2 (5.3)	<0.001
History of diabetes	7	10	11	9	15	0.2

Values are mean (SD) unless reported.

^a Adjusted for TIV

^b Available in 138 controls, 92 SMC, 252 EMCI, 144 LMCI, 119 AD

^c Available in 139 controls, 92 SMC, 252 EMCI, 145 LMCI, 119 AD.

^d Available in 143 controls, 92 SMC, 265 EMCI, 149 LMCI, 125 AD.

3.3.3 WMHs and age

Table 3.2 shows the partial regression coefficients for the relationship between WMHs and age in each diagnostic group, and Figure 3.3 shows the corresponding

Table 3.2: Regression model results for the relationship between WMHs and age, by group

WMHs and age	Controls	SMC	EMCI	LMCI	AD
Change in WMHs (ml) per decade increase in age	0.4	0.4	0.7	0.6	0.6
95% confidence intervals	(0.2 to 0.6)	(0.1 to 0.7)	(0.6 to 0.8)	(0.4 to 0.8)	(0.4 to 0.8)
<i>p</i> value	<0.001	<0.001	<0.001	<0.001	<0.001

Between group differences in slope: *p* value = 0.2

Estimates are shown for log_eWMH volume increase, with 95% confidence intervals, for every decade increase in age and all adjusted for TIV.

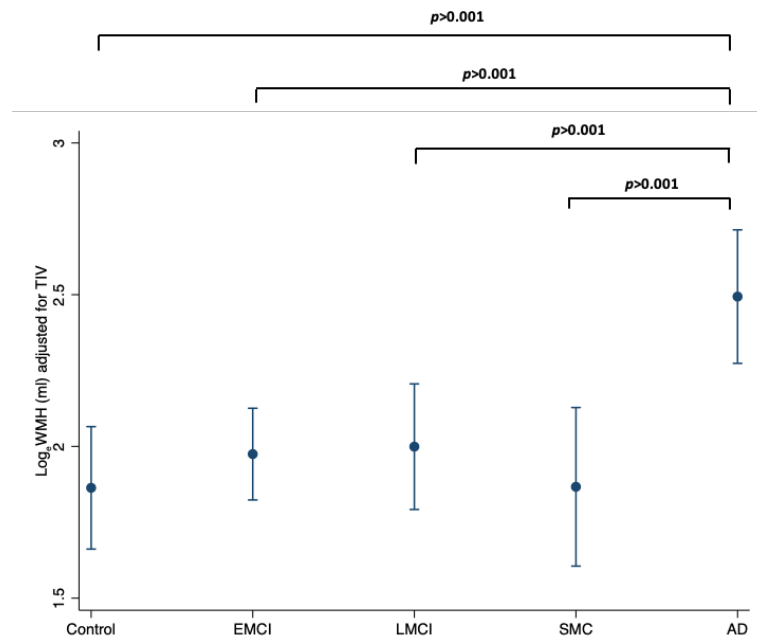


Figure 3.2: Box plot showing WMH volume per group. Values are shown as group means for \log_{10} WMH volume adjusted for TIV, with 95% confidence intervals.

scatter plots. There was strong evidence for a positive association between WMHs and age in each diagnostic group, but no significant interactions between age and diagnostic group were observed.

3.3.4 CSF biomarkers and age

Table 3.3 shows partial regression coefficients for the relationship between CSF biomarkers and age, in each diagnostic group and Figures 3.4, 3.5 and 3.6 show corresponding scatter plots. $A\beta$ 1-42 has an inverse relationship with age in both control and EMCI groups, whereby a 1 year increase in age is associated with a 0.04 and 0.03 SD decrease respectively. T-tau and p-tau demonstrate similar relationships with age, albeit with smaller effect than $A\beta$ 1-42, with the control (0.03 and 0.02 SD change respectively) and EMCI (0.03 and 0.01 SD change respectively) groups positively associated and the AD group showing an inverse relationship (-0.03 and -0.04 SD change respectively). The SMC group also demonstrated a positive association between tau and age (0.02 SD change).

There is a significant overall interaction between $A\beta$ 1-42's relationship with age and diagnostic group. This is driven by the AD group being significantly dif-

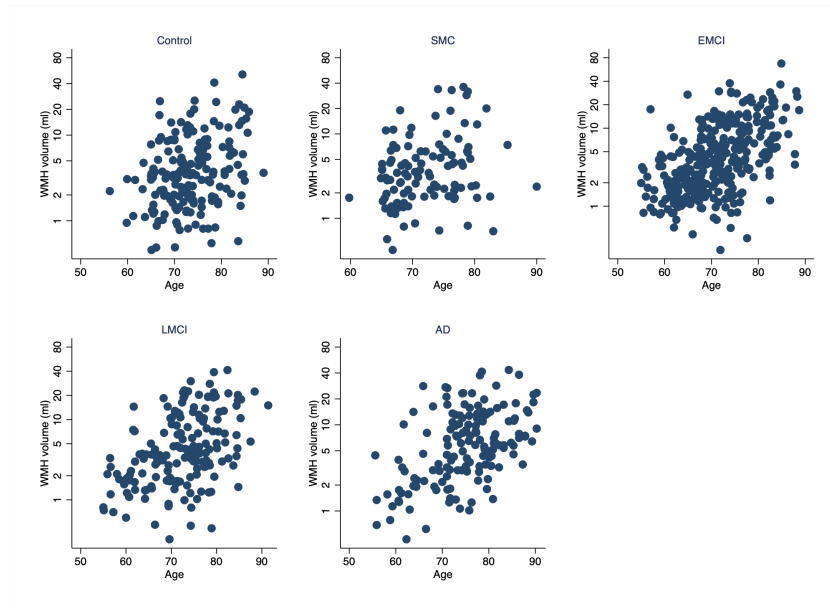


Figure 3.3: Scatter plots showing the relationship between WMHs and age in controls, SMC, EMCI, LMCI and AD groups. WMH volume is shown on a log scale and is unadjusted for any covariates.

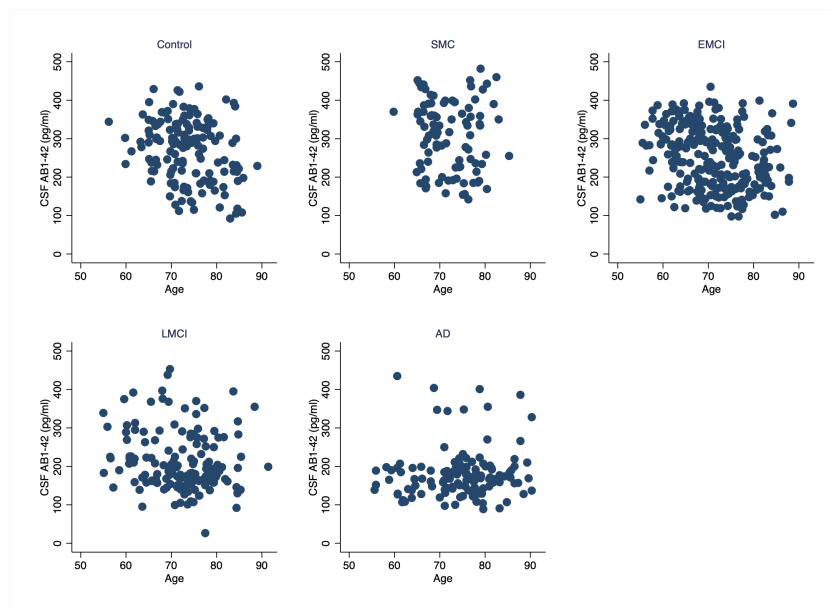


Figure 3.4: Scatter plots showing the relationship between CSF A β 1-42 and age in controls, SMC, EMCI, LMCI and AD groups.

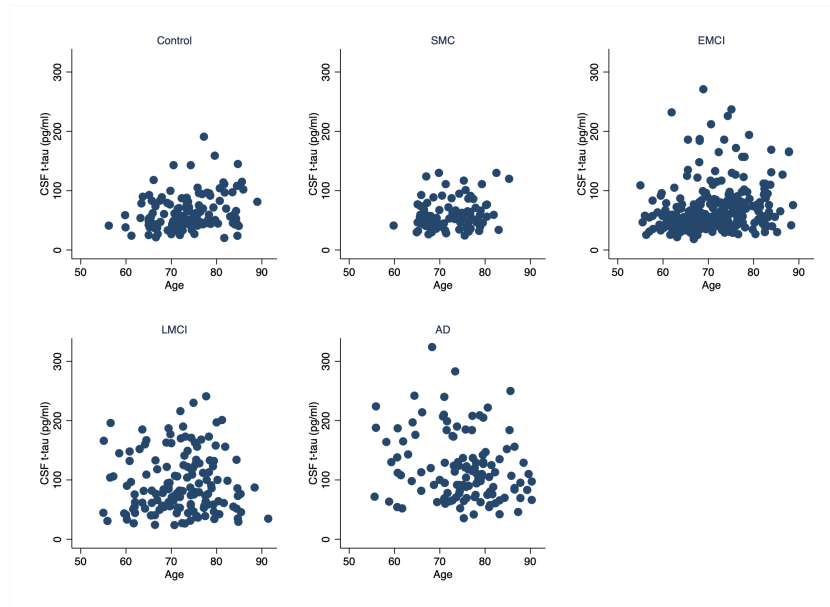


Figure 3.5: Scatter plots showing the relationship between CSF t-tau and age in controls, SMC, EMCI, LMCI and AD groups.

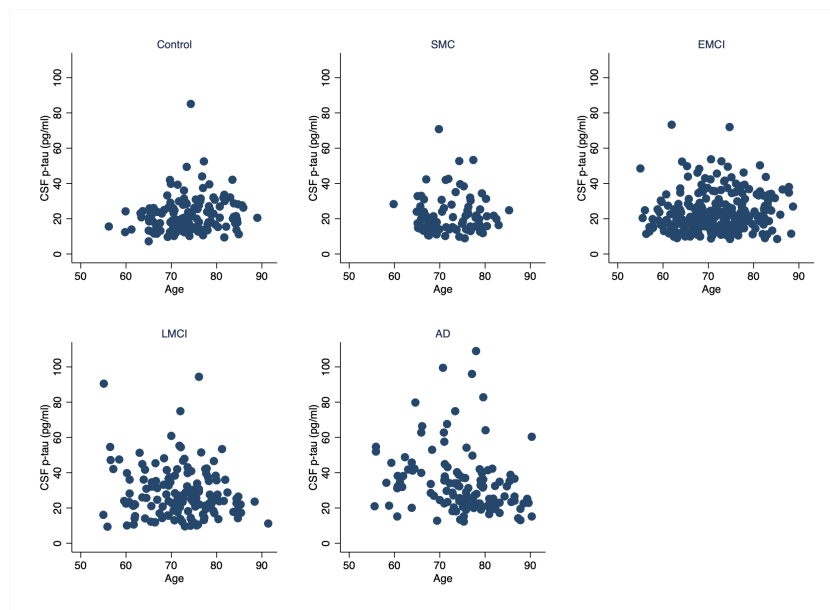


Figure 3.6: Scatter plots showing the relationship between CSF p-tau and age in controls, SMC, EMCI, LMCI and AD groups.

Table 3.3: Regression model results for the relationship between CSF biomarkers and age, by group

	Controls	SMC	EMCI	LMCI	AD
Aβ1-42					
SD change in A β 1-42 per decade increase in age	-0.4	-0.2	-0.3	-0.2	0.08
95% confidence intervals	(-0.7 to -0.2)	(-0.6 to 0.3)	(-0.5 to -0.2)	(-0.4 to 0.1)	(-0.1 to 0.3)
<i>p</i> value	0.001	0.4	< 0.001	0.07	0.4
Between group differences in slope: <i>p</i> value = <0.001					
T-tau					
SD change in t-tau per decade increase in age	0.3	0.2	0.3	-0.02	-0.3
95% confidence intervals	(0.1 to 0.5)	(0.008 to 0.4)	(0.1 to 0.4)	(-0.3 to 0.2)	(-0.6 to -0.06)
<i>p</i> value	0.001	0.04	0.002	0.9	0.02
Between group differences in slope: <i>p</i> value = <0.001					
P-tau					
SD change in t-tau per decade increase in age	0.2	0.05	0.1	-0.2	-0.4
95% confidence intervals	(0.01 to 0.4)	(-0.3 to 0.4)	(0.005 to 0.3)	(-0.4 to 0.03)	(-0.7 to -0.07)
<i>p</i> value	0.04	0.8	0.04	0.09	0.02
Between group differences in slope: <i>p</i> value = <0.001					

Estimates are for SD change in CSF biomarker per decade increase in age. The SD is the pooled within-group SD, calculated from a linear regression model that allowed for differences in mean levels of CSF biomarker by group.

ferent from controls and EMCI, whereby the AD group demonstrates an increase in CSF A β 1-42 with increasing age, compared to the inverse relationship in the other groups. This difference is greater in younger subjects.

There is a significant overall interaction between both t-tau's and p-tau's relationship with age and diagnostic group. For both t-tau and p-tau this is driven by the AD group being significantly different from controls and EMCI, whereby the AD group demonstrates a decrease in tau with increasing age, compared to the opposite relationship in the other groups.

3.3.5 CSF biomarkers and WMHs in each group

Table 3.4: Regression model results for the relationship between WMHs and CSF A β 1-42, by group

WMHs and A β 1-42	Controls	SMC	EMCI	LMCI	AD
TIV adjusted					
% reduction in WMHs (ml) per 1SD change in A β 1-42	30.4	20.0	22.0	14.9	18.0
95% confidence intervals	(20.3 to 39.3)	(6.4 to 31.6)	(12.5 to 30.5)	(-0.5 to 28.0)	(-0.2 to 32.8)
<i>p</i> value	<0.001	0.006	<0.001	0.06	0.05
TIV and age adjusted					
% reduction in WMHs (ml) per 1SD change in A β 1-42	26.7	18.7	12.3	9.4	21.7
95% confidence intervals	(15.7 to 36.2)	(5.2 to 30.2)	(2.5 to 21.0)	(-5.5 to 22.2)	(6.8 to 34.2)
<i>p</i> value	<0.001	0.009	0.02	0.2	0.006
Between group differences in % reductions per 1SD change in Aβ1-42: <i>p</i> value = 0.4 (0.4 with age adjustment)					

Estimates are percentage decrease in WMH volume per one SD change (1 SD = 78.3pg/ml) in A β 1-42. The SD is the pooled within-group SD, calculated from a linear regression model that allowed for differences in mean levels of A β 1-42 by group.

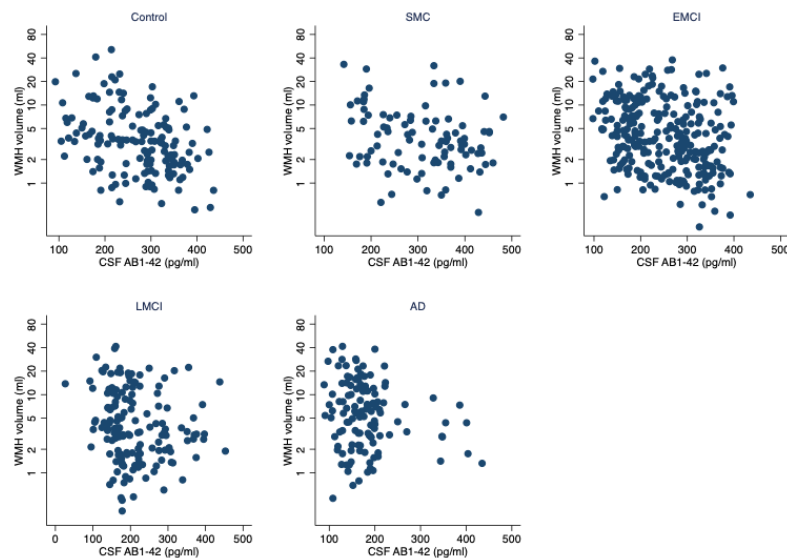


Figure 3.7: Scatter plots showing the relationship between WMHs and CSF A β 1-42 in controls, SMC, EMCI, LMCI and AD groups. WMH volume is shown on a log scale and is unadjusted for any covariates.

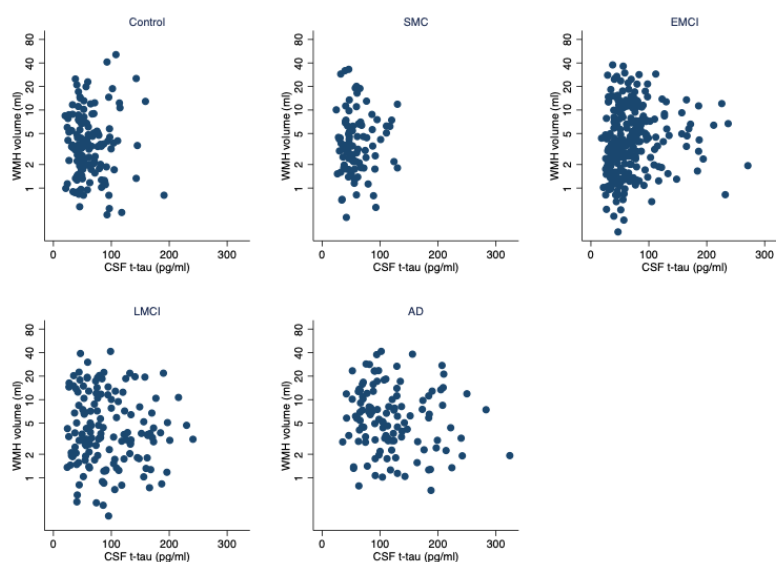
Table 3.4 shows the estimated percentage decreases in WMHs for increases in CSF A β 1-42 after adjustment for TIV and Figure 3.7 shows the corresponding scatter plots. Evidence for an association between CSF A β 1-42 and WMH was observed, whereby an increase in WMHs was associated with a decrease in CSF

Table 3.5: Regression model results for the relationship between WMH and CSF t-tau, by group

WMHs and t-tau	Controls	SMC	EMCI	LMCI	AD
TIV adjusted					
% reduction in WMHs (ml) per 1SD change in t-tau	5.1	3.8	13.2	-4.0	-3.3
95% confidence intervals	(-16.4 to 32.0)	(-24.9 to 43.5)	(0.2 to 27.7)	(-16.9 to 11.1)	(-15.2 to 10.2)
<i>p</i> value	0.7	0.8	0.05	0.6	0.6
TIV and age adjusted					
% reduction in WMHs (ml) per 1SD change in t-tau	-7.3	-5.1	2.4	-3.9	3.6
95% confidence intervals	(-26.6 to 16.3)	(-31.2 to 30.9)	(-8.0 to 14.0)	(-15.7 to 9.5)	(-7.9 to 16.5)
<i>p</i> value	0.5	0.8	0.7	0.6	0.6

Between group differences in % reductions per 1SD change in t-tau: *p* value = 0.4 (0.7 with age adjustment)

Estimates are percentage increase in WMH volume per one SD change (1 SD = 42.8pg/ml) in t-tau. The SD is the pooled within-group SD, calculated from a linear regression model that allowed for differences in mean levels of t-tau by group.

**Figure 3.8:** Scatter plots showing the relationship between WMHs and CSF t-tau in controls, SMC, EMCI, LMCI and AD groups. WMH volume is shown on a log scale and is unadjusted for any covariates.

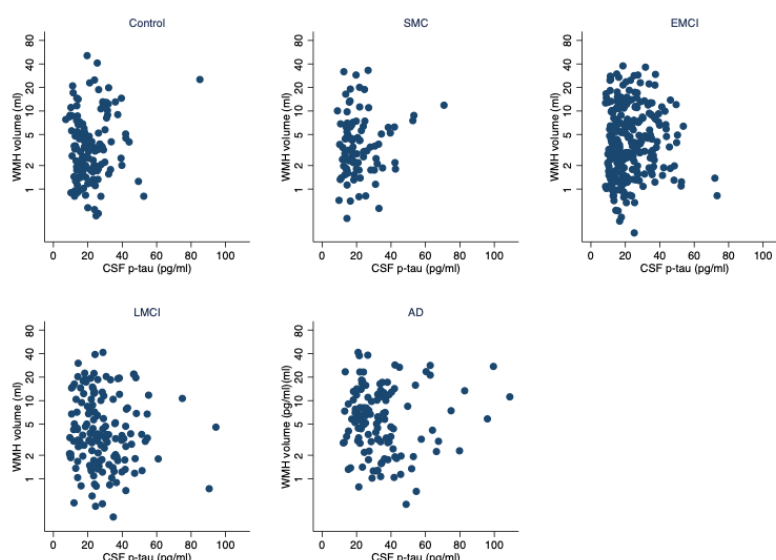
$A\beta$ 1-42. Although the estimated slope of the association in the five diagnostic groups varied somewhat (and was not formally statistically significant in the LMCI and AD groups), 95% confidence intervals were relatively wide and the variability in estimates was consistent with chance (joint tests for differences in slopes among groups were not statistically significant). The effect of CSF $A\beta$ 1-42 on WMHs was

Table 3.6: Regression model results for the relationship between WMHs and CSF p-tau, by group

WMHs and p-tau	Controls	SMC	EMCI	LMCI	AD
TIV adjusted					
% reduction in WMHs (ml) per 1SD change in p-tau	13.6	14.1	3.5	-8.7	0.5
95% confidence intervals	(-6.6 to 38.3)	(-8.8 to 42.8)	(-10.0 to 18.9)	(21.3 to 5.9)	(-10.8 to 13.3)
<i>p</i> value	0.2	0.3	0.6	0.2	0.9
TIV and age adjusted					
% reduction in WMHs (ml) per 1SD change in p-tau	7.3	13.1	-3.9	-3.0	8.0
95% confidence intervals	(-11.3 to 29.9)	(-9.0 to 40.5)	(-14.8 to 8.4)	(-15.3 to 11.1)	(-3.0 to 20.3)
<i>p</i> value	0.5	0.3	0.5	0.7	0.1

Between group differences in % reductions per 1SD change in p-tau: *p* value = 0.4 (0.5 with age adjustment)

Estimates are percentage increase in WMH volume per one SD (1 SD = 12.8pg/ml) change in p-tau. The SD is the pooled within-group SD, calculated from a linear regression model that allowed for differences in mean levels of p-tau by group.

**Figure 3.9:** Scatter plots showing the relationship between WMHs and CSF p-tau in controls, SMC, EMCI, LMCI and AD groups. WMH volume is shown on a log scale and is unadjusted for any covariates.

typically reduced after adjustment for age.

Table 3.5 shows the percentage increases in WMHs for increases in CSF t-tau and Figure 3.8 shows the corresponding scatter plots. With adjustment for TIV, WMH burden was borderline positively associated with t-tau only in the EMCI group. This association was no longer significant after adjusting for age. There was

no evidence for an interaction between t-tau and group.

Table 3.6 shows the percentage increases in WMHs for increases in CSF p-tau and Figure 3.9 shows the corresponding scatter plots. There was no evidence for an association between WMHs and p-tau in any diagnostic group. There no evidence for an interaction between group and p-tau.

3.3.5.1 Elecsys biomarker analysis

Table 3.7: Elecsys CSF summary statistics, by group.

	Controls n=137	SMC n=92	EMCI n=252	LMCI n=143	AD n=119	p value across groups
CSF A β 1-42 (pg/ml)	1252.2 (450.9)	1228.8 (424.7)	1109.8 (440.2)	908.3 (382.8)	693.7 (329.5)	
Median (IQR)	1345.0 (810.1)	1313.5 (825.2)	1085.5 (925.1)	810.6 (440.7)	624.1 (292.4)	<0.001
CSF t-tau (pg/ml)	235.7(91.5)	241.9 (95.2)	255.5 (117.4)	309.9 (137.6)	384.4 (155.7)	
Median (IQR)	210.1 (103.1)	217.8 (133.2)	233.9 (121.7)	283.7 (171.8)	353.7 (177.7)	<0.001
CSF p-tau (pg/ml)	21.7 (9.2)	22.1 (9.8)	24.1 (13.2)	30.3 (13.7)	37.9 (16.2)	
Median (IQR)	19.3 (10.6)	19.3 (11.5)	20.7 (12.8)	27.7 (17.5)	34.3 (20.4)	<0.001

Values are mean (SD) unless reported.

Summary statistics for the subgroup with CSF measures from the Elecsys assay are shown in Table 3.7. The relationships between WMH volumes and these Elecsys measures of CSF A β 1-42, t-tau and p-tau are demonstrated in Tables 3.8 to 3.10. The results from the original assay (Tables 3.4 to 3.6) are not materially changed by the use of this alternative CSF assay.

Table 3.8: Regression model results for the relationship between WMHs and CSF A β 1-42 (Elecsys assay), by group

WMHs and A β 1-42	Controls	SMC	EMCI	LMCI	AD
TIV adjusted					
% reduction in WMHs (ml) per 1SD change in A β 1-42	25.5	30.9	23.4	27.4	20.5
95% confidence intervals	(10.3 to 38.2)	(13.5 to 44.8)	(10.9 to 34.2)	(6.1 to 44.0)	(-3.9 to 39.2)
p value	0.002	0.002	0.001	0.02	0.09
TIV and age adjusted					
% reduction in WMHs (ml) per 1SD change in A β 1-42	22.3	26.4	15.1	19.5	29.1
95% confidence intervals	(6.8 to 35.2)	(7.7 to 41.3)	(2.8 to 25.9)	(-2.2 to 36.6)	(10.5 to 43.8)
p value	0.007	0.008	0.02	0.07	0.004
Between group differences in % reductions per 1SD change in Aβ1-42 p value = 0.9 (0.9 with age adjustment)					

Estimates are percentage decrease in WMH volume per one SD change (1 SD = 413.2pg/ml) in A β 1-42. The SD is the pooled within-group SD, calculated from a linear regression model that allowed for differences in mean levels of A β 1-42 by group.

Table 3.9: Regression model results for the relationship between WMHs and CSF t-tau (Elecsys assay), by group

WMHs and t-tau	Controls	SMC	EMCI	LMCI	AD
TIV adjusted					
% increase in WMHs (ml) per 1SD change in t-tau	1.6	1.3	15.0	-1.4	-4.8
95% confidence intervals	(-17.4 to 24.9)	(-20.5 to 29.2)	(2.0 to 29.7)	(-15.2 to 14.6)	(-16.8 to 9.0)
<i>p</i> value	0.9	0.9	0.02	0.9	0.5
TIV and age adjusted					
% reduction in WMHs (ml) per 1SD change in t-tau	-9.0	-5.5	2.8	-0.8	-0.9
95% confidence intervals	(-25.9 to 11.6)	(-25.7 to 20.2)	(-7.6 to 14.5)	(-13.3 to 13.6)	(-12.1 to 11.7)
<i>p</i> value	0.4	0.6	0.6	0.9	0.9
Between group differences in % reductions per 1SD change in t-tau <i>p</i> value = 0.3 (0.3 with age adjustment)					

Estimates are percentage decrease in WMH volume per one SD change (1 SD = 123.5pg/ml) in t-tau. The SD is the pooled within-group SD, calculated from a linear regression model that allowed for differences in mean levels of t-tau by group.

Table 3.10: Regression model results for the relationship between WMHs and CSF p-tau (Elecsys assay), by group

WMHs and p-tau	Controls	SMC	EMCI	LMCI	AD
TIV adjusted					
% increase in WMHs (ml) per 1SD change in p-tau	8.2	6.0	14.2	-0.5	-3.9
95% confidence intervals	(-13.2 to 34.9)	(-17.9 to 36.7)	(1.7 to 28.1)	(-14.2 to 15.4)	(-16.4 to 10.4)
<i>p</i> value	0.5	0.7	0.03	1.0	0.6
TIV and age adjusted					
% reduction in WMHs (ml) per 1SD change in p-tau	-3.6	-0.6	2.6	0.6	0.9
95% confidence intervals	(-22.7 to 20.3)	(-22.8 to 28.0)	(-7.4 to 13.7)	(-11.9 to 14.9)	(-10.9 to 14.2)
<i>p</i> value	0.7	0.6	0.6	0.9	0.9
Between group differences in % reductions per 1SD change in p-tau <i>p</i> value = 0.3 (0.3 with age adjustment)					

Estimates are percentage decrease in WMH volume per one SD change (1 SD = 13.4pg/ml) in p-tau. The SD is the pooled within-group SD, calculated from a linear regression model that allowed for differences in mean levels of p-tau by group.

3.3.6 CSF biomarkers and WMHs in the full cohort

Table 3.11a shows the percentage reductions in WMHs volume for a 1 SD increase in CSF $A\beta$ 1-42 adjusting for group, age, *APOE* ϵ status, t-tau, and p-tau. The relationship between WMHs and $A\beta$ 1-42 remains significant and materially unchanged (between a 16% and 22% reduction in WMHs per 1 SD change in CSF $A\beta$ 1-42) after progressive adjustment for covariates. This association between CSF $A\beta$ 1-42 and WMHs was also independent of the effects of CSF t-tau and p-tau.

Table 3.11b shows partial R^2 values for all the covariates in each model set. $A\beta$ consistently explained approximately 5% of the variance in WMHs across all models. Age explained the largest variance in WMHs at \sim 15%, compared with tau biomarkers, group, and *APOE* ϵ status, with each only explaining only around 1%.

Table 3.11: Regression model results examining the association between CSF A β 1-42 and WMHs with various covariates

a)

Model set	Covariates	% reduction in WMHs per 1SD change in A β 1-42	95% confidence interval	p value
1	i) None	21.9	17.1 to 26.5	<0.001
	ii) TIV	21.5	16.7 to 26.0	<0.001
	iii) TIV, group	21.6	16.2 to 26.6	<0.001
	iv) TIV, group, age	16.4	11.2 to 21.3	<0.001
	v) TIV, group, age, APOE ϵ 4 status	17.9	12.2 to 23.2	<0.001
2	i) T-tau	24.5	19.2 to 29.5	<0.001
	ii) T-tau, TIV	23.2	17.9 to 28.1	<0.001
	iii) T-tau, TIV, group	23.1	17.5 to 28.3	<0.001
	iv) T-tau, TIV, group, age	18.0	12.6 to 23.1	<0.001
	v) T-tau, TIV, group, age, APOE ϵ 4 status	18.8	13.0 to 24.2	<0.001
3	i) P-tau	24.1	18.7 to 29.1	<0.001
	ii) P-tau, TIV	23.8	18.6 to 28.7	<0.001
	iii) P-tau, TIV, group	23.8	18.2 to 29.0	<0.001
	iv) P-tau, TIV, group, age	17.7	12.2 to 23.0	<0.001
	v) P-Tau, TIV, group, age, APOE ϵ 4 status	18.9	12.9 to 24.4	<0.001

b)

Model set	Covariates from v)	Partial R ²
1	A β 1-42	0.05
	TIV	0.05
	Group	0.003
	Age	0.16
	APOE ϵ 4 status	0.002
2	A β 1-42	0.05
	t-tau	0.005
	TIV	0.06
	Group	0.005
	Age	0.16
3	A β 1-42	0.05
	p-tau	0.003
	TIV	0.06
	Group	0.004
	Age	0.15
	APOE ϵ 4 status	0.001

All models assess associations between WMHs and A β with various covariates, with model 2 additionally adjusting for t-tau and model 3 additionally adjusting for p-tau. In a) estimates are percentage changes in WMH volume per one SD change (1 SD=78.3 pg/mL) in A β . The SD is the pooled within-group SD, calculated from a linear regression model that allowed for differences in mean levels of A β by group. In b) partial R² are shown for each covariate in the fully-adjusted model v) from each of the 3 model sets. R² values are shown to 2 significant figures for values >0.1 and 1 significant figure for values <0.1.

Table 3.12: Regression model results examining the association between CSF t-tau and WMHs with various covariates

a)

Model set	Covariates	% reduction in WMHs per 1SD change in t-tau	95% confidence interval	p value
1	i) None	5.7	-0.9 to 12.7	0.09
	ii) TIV	7.8	1.3 to 14.7	0.02
	iii) TIV, group	2.7	-4.2 to 10.0	0.5
	iv) TIV, group, age	-0.1	-6.1 to 6.3	0.9
	v) TIV, group, age, <i>APOE</i> ϵ 4 status	-1.4	-7.5 to 5.2	0.7
2	i) $A\beta$ 1-42	-6.8	-0.1 to -12.9	0.05
	ii) $A\beta$ 1-42, TIV	-4.3	-10.5 to 2.3	0.2
	iii) $A\beta$ 1-42, TIV, group	-5.9	-12.3 to 1.0	0.09
	iv) $A\beta$ 1-42, TIV, group, age	-6.3	-12.1 to 0.06	0.05
	v) $A\beta$ 1-42, TIV, group, age, <i>APOE</i> ϵ 4 status	-5.9	-11.9 to 0.3	0.06

b)

Model set	Covariates from v)	Partial R ²
1	t-tau	0
	TIV	0.06
	Group	0.006
	Age	0.2
	<i>APOE</i> ϵ 4 status	0.004
2	t-tau	0.005
	$A\beta$ 1-42	0.04
	TIV	0.06
	Group	0.005
	Age	0.2
	<i>APOE</i> ϵ 4 status	0.0007

All models assess associations between WMHs and t-tau with various covariates, with model 2 additionally adjusting for $A\beta$. In a) estimates are percentage changes in WMH volume per one SD change (1 SD=42.8 pg/mL) in t-tau. The SD is the pooled within-group SD, calculated from a linear regression model that allowed for differences in mean levels of t-tau by group. In b) partial R² are shown for each covariate in the fully-adjusted model v) from each of the 3 model sets. R² values are shown to 2 significant figures for values >0.1 and 1 significant figure for values <0.1.

Table 3.13: Regression model results examining the association between CSF p-tau and WMHs with various covariates

a)

Model set	Covariates	% reduction in WMHs per 1SD change in p-tau	95% confidence interval	p value
1	i) None	6.2	-0.6 to 13.4	0.08
	ii) TIV	5.5	-1.1 to 12.5	0.1
	iii) TIV, group	1.4	-5.2 to 8.6	0.7
	iv) TIV, group, age	2.6	-3.5 to 9.0	0.4
	v) TIV, group, age, <i>APOE</i> ϵ 4 status	1.6	-4.7 to 8.2	0.6
2	i) $A\beta$ 1-42	-6.6	-13.0 to 0.3	0.06
	ii) $A\beta$ 1-42, TIV	-7.1	-13.3 to -0.4	0.04
	iii) $A\beta$ 1-42, TIV, group	-8.1	-14.3 to -1.4	0.02
	iv) $A\beta$ 1-42, TIV, group, age	-4.5	-10.5 to 1.8	0.2
	v) $A\beta$ 1-42, TIV, group, age, <i>APOE</i> ϵ 4 status	-4.1	-10.2 to 2.3	0.2

b)

Model set	Covariates from v)	Partial R^2
1	t-tau	0.0005
	TIV	0.05
	Group	0.005
	Age	0.2
	<i>APOE</i> ϵ 4 status	0.003
2	t-tau	0.003
	$A\beta$ 1-42	0.05
	TIV	0.06
	Group	0.004
	Age	0.2
	<i>APOE</i> ϵ 4 status	0.001

All models assess associations between WMHs and p-tau with various covariates, with model 2 additionally adjusting for $A\beta$. In a) estimates are percentage changes in WMH volume per one SD change (1 SD=12.8 pg/mL) in p-tau. The SD is the pooled within-group SD, calculated from a linear regression model that allowed for differences in mean levels of p-tau by group. In b) partial R^2 are shown for each covariate in the fully-adjusted model v) from each of the 3 model sets. R^2 values are shown to 2 significant figures for values >0.1 and 1 significant figure for values <0.1 .

Table 3.12a and Table 3.13a shows the percentage reductions in WMH volume for a 1 SD increase in CSF t-tau and p-tau respectively, independent of group, age, *APOE* $\epsilon 4$, and $A\beta 1-42$. There is evidence for a positive association between t-tau and WMHs, after adjustment for TIV. This association is lost after adjustment for group, age and *APOE* $\epsilon 4$. There was no evidence for an association between p-tau and WMHs in a model with no adjustors, and after adjustment for TIV, group, age and *APOE* $\epsilon 4$. There was some weak and inconsistent evidence for inverse associations of both t-tau and p-tau with WMHs when $A\beta 1-42$ is added to the model.

Both t-tau and p-tau explains a very small proportion of the variance in WMHs, with a partial R^2 in model 1 of 0.03 and 0.5% in model 2 for t-tau (Table 3.12b) and 0.02 and 0.2% for p-tau (Table 3.13b)

3.3.7 Vascular risk analysis

Table 3.14 shows partial regression coefficients for the relationship between WMHs and age in each diagnostic group, adjusting with adjustment for the vascular risk factors of smoking status, a history of hypertension, a history of diabetes and BMI. With separate and combined adjustment for the four vascular risk factors, there was no evidence for a marked attenuation of the association between WMHs and age (shown in Table 3.2) in any disease group. Table 3.15 shows that combined adjustment for the vascular risk factors had minimal effect on the partial regression coefficients for the WMH- $A\beta$ relationship.

3.3.8 Parietal lobe vs whole brain analysis

Table 3.16 shows partial regression coefficients for the association of CSF $A\beta 1-42$, t-tau and p-tau with WMHs in both the parietal lobe and the rest of the brain. There was no evidence that parietal WMHs were a better predictor of any CSF biomarker compared with non-parietal WMHs. However, there was evidence that there was an independent relationship between CSF $A\beta 1-42$ and non-parietal WMH volume, both with and without age adjustment.

Table 3.14: Regression model results for the relationship between WMHs and age by group, adjusting for vascular risk

	Controls	SMC	EMCI	LMCI	AD
a) Adjusted for hypertension					
Change in WMHs (ml) per decade increase in age	0.3	0.4	0.7	0.6	0.6
95% confidence intervals	(0.1 to 0.6)	(0.1 to 0.7)	(0.5 to 0.8)	(0.4 to 0.7)	(0.4 to 0.7)
<i>p</i> value	<0.001	<0.001	<0.001	<0.001	<0.001
b) Adjusted for smoking					
Change in WMHs (ml) per decade increase in age	0.4	0.4	0.7	0.6	0.6
95% confidence intervals	(0.2 to 0.6)	(0.1 to 0.7)	(0.6 to 0.8)	(0.4 to 0.8)	(0.4 to 0.8)
<i>p</i> value	<0.001	<0.001	<0.001	<0.001	<0.001
c) Adjusted for BMI					
Change in WMHs (ml) per decade increase in age	0.4	0.5	0.7	0.6	0.6
95% confidence intervals	(0.2 to 0.7)	(0.2 to 0.8)	(0.6 to 0.8)	(0.4 to 0.7)	(0.4 to 0.8)
<i>p</i> value	<0.001	<0.001	<0.001	<0.001	<0.001
d) Adjusted for diabetes					
Change in WMHs (ml) per decade increase in age	0.4	0.4	0.7	0.6	0.6
95% confidence intervals	(0.2 to 0.6)	(0.1 to 0.8)	(0.6 to 0.8)	(0.4 to 0.8)	(0.4 to 0.8)
<i>p</i> value	<0.001	<0.001	<0.001	<0.001	<0.001
e) Adjusted for hypertension, smoking, BMI and diabetes					
Change in WMHs (ml) per decade increase in age	0.3	0.5	0.7	0.6	0.6
95% confidence intervals	(0.1 to 0.6)	(0.2 to 0.8)	(0.6 to 0.8)	(0.4 to 0.7)	(0.4 to 0.8)
<i>p</i> value	<0.001	<0.001	<0.001	<0.001	<0.001

Estimates are shown for \log_e WMH volume increase, with 95% confidence intervals, for every decade increase in age and all adjusted for TIV. Tables adjusted for a) hypertension, b) smoking, c) BMI d) diabetes e) hypertension, smoking, BMI and diabetes.

Table 3.15: Regression models results for the relationship between WMHs and CSF A β 1-42 with adjustment for smoking status, history of hypertension, history of diabetes and BMI by group

WMHs and CSF Aβ1-42 adjusted for smoking, hypertension, diabetes and BMI (N=820)	Controls	SMC	EMCI	LMCI	AD
SD decrease in A β 1-42 per decade increase in age	28.9	23.7	19.7	13.9	20.1
95% confidence intervals	(18.2 to 38.1)	(9.8 to 35.6)	(9.7 to 28.5)	(-2.2 to 27.5)	(1.4 to 35.2)
<i>p</i> value	<0.001	0.002	<0.001	0.09	0.04

Estimates are percentage decreases in WMH volume per one SD change (1 SD = 78.3pg/ml) in A β 1-42, with 95% confidence intervals and adjustment for TIV. The SD is the pooled within-group SD, calculated from a linear regression model that allowed for differences in mean levels of A β 1-42 by group.

Table 3.16: Regression models of the associations between CSF biomarkers and either the parietal lobe WMHs or the rest of the brain WMHs.

Outcome	Predictors	SD change in biomarker per 1 unit increase in WMH	CI	<i>p</i> value	
A β 1-42	Non-age adjusted	Parietal log _e WMHs	-5.5	-13.9 to 3.8	0.2
		Non-parietal log _e WMHs	-18.1	-29.2 to -5.4	0.007
	Age adjusted	Parietal log _e WMHs	-5.0	-13.5 to 4.3	0.3
		Non-parietal log _e WMHs	-16.2	-27.6 to -2.9	0.02
T-tau	Non-age adjusted	Parietal log _e WMHs	-7.0	-15.7 to 2.6	0.1
		Non-parietal log _e WMHs	14.4	-1.7 to 33.1	0.08
	Age adjusted	Parietal log _e WMHs	-7.4	-16.1 to 2.2	0.1
		Non-parietal log _e WMHs	11.5	-4.5 to 30.1	0.2
P-tau	Non-age adjusted	Parietal log _e WMHs	-2.7	-11.7 to 7.2	0.6
		Non-parietal log _e WMHs	5.8	-8.9 to 22.9	0.5
	Age adjusted	Parietal log _e WMHs	-2.4	-11.4 to 7.6	0.6
		Non-parietal log _e WMHs	7.4	-7.7 to 25.1	0.4

Estimates are for an SD increase in CSF biomarker for every 1 unit increase in WMH volume (ml). The SD is the pooled within-group SD, calculated from a linear regression model that allowed for differences in mean levels of CSF biomarker by group. All are adjusted for TIV and diagnostic group. Results for one predictor are adjusted for the other predictor. Non-parietal WMH is total brain WMH minus the parietal lobe WMH.

3.4 Discussion

This work provides evidence of a consistent association between CSF $A\beta$ and WMHs across the disease spectrum, from normal ageing to AD. Evidence of a decrease in CSF $A\beta$ was associated with an increase in WMHs in control, SMC, EMCI, LMCI and AD groups, and also in the pooled cohort after adjusting for age, diagnostic group, TIV, and *APOE* ϵ status. Importantly, this CSF $A\beta$ -WMH relationship was independent of CSF t-tau and independent of CSF p-tau. Very little evidence was found for a relationship between WMHs and either t-tau or p-tau.

There was no evidence for differing relationships in WMHs and $A\beta$, p-tau, or t-tau between diagnostic groups. WMHs are heterogeneous and are likely to represent multiple pathologies that could potentially vary throughout the disease course. Given the recent evidence that WMHs may be more related to neurodegenerative and tau pathologies in clinical AD (McAleese et al., 2017), it would have been reasonable to propose stronger relationships with tau at later disease stages. Because $A\beta$ levels are thought to be relatively stable in clinical AD stages (Zhou et al., 2009), it could also be expected that there might be less of an association with WMHs in later disease stages. The fact that no differences were found between disease stages suggests that WMH relationships with AD CSF biomarkers actually remain consistent across the disease course.

Age at the baseline was a stronger independent predictor of WMHs than $A\beta$, which likely reflects the contributions of vascular risk factors, vascular events, and comorbidities that accrue with age. Taken together, although this study is purely correlative, these results are compatible with the theory that some WMHs are part of the AD pathological process, and some are the result of an ageing/vascular process (McAleese et al., 2015, 2017). Although there was no evidence for contributions from smoking, hypertension, BMI, and diabetes to the relationship between WMHs and age, or WMH and $A\beta$, a more comprehensive examination of the effects of vascular risk factors, vascular disease, and vascular-related events on the age-WMH relationship may provide greater insight into the potential causes of WMHs associated with age.

In studies of $A\beta$ and WMHs, there have been mixed findings; some have reported a lack of any association (Kalheim et al., 2017, Kester et al., 2014) while several studies confirm these findings that lower CSF $A\beta$ is associated with higher WMHs in both controls and disease groups (Marnane et al., 2016, Pietroboni et al., 2018) Some have reported that lower levels of CSF $A\beta$ were particularly associated with WMHs in AD subjects, as opposed to controls or MCI subjects (Shams et al., 2016, van Westen et al., 2016). Results from amyloid PET studies have also demonstrated significant associations with WMHs in controls (Kandel et al., 2016, Marnane et al., 2016), MCI and AD groups (Zhou et al., 2015). Although a recent systematic review concluded that most studies demonstrate a lack of significant relationship between amyloid PET and WMH burden (Roseborough et al., 2017).

This study adds to the expanding body of literature attempting to characterise the complex relationship between AD and presumed vascular pathology at different disease stages. As well as evidence that both $A\beta$ deposition and WMHs independently predict cognitive impairment or brain atrophy (Barnes et al., 2013, Gordon et al., 2015, Haight et al., 2013, Provenzano et al., 2013), a growing number of studies are suggestive of an additive effect of combined pathology on neurodegeneration (Bos et al., 2017) and/or cognitive decline (Lopez et al., 2014, Vemuri and Knopman, 2016, Vemuri et al., 2015). Several studies have investigated the possibility of an interactive effect between the two pathologies, whereby there is a direct influence of one pathology on the other. One study found that WMHs predicted hippocampal atrophy in preclinical AD subjects with abnormal CSF $A\beta$ (Freeze et al., 2016), and another found that low CSF $A\beta$ predicted greater WMH accrual over time (Scott et al., 2016).

Hypotheses into mechanistic links between $A\beta$ and WMHs have mainly focused on the proposed vascular origin of WMHs and reflect the idea that there may be positive feedback between the two pathologies (Smith and Greenberg, 2009, Zlokovic, 2011). Cerebral amyloid angiopathy (CAA) may be a potential mediator of the relationship between WMHs and $A\beta$, whereby SVD could lead to reduced clearance of $A\beta$ from brain parenchyma, enhancing its deposition in cerebral vessel

walls. This in turn may result in cerebrovascular dysfunction, leading to eventual hypoperfusion and ischemia and subsequent white matter lesions that appear as WMHs (Grinberg and Thal, 2010, Hawkes et al., 2014, Weller et al., 2008). Previous research has demonstrated associations of CAA with WMHs (Ryan et al., 2015) and with CSF $A\beta$ (Renard et al., 2012, Verbeek et al., 2009). A recent paper has shown that WMHs related to $A\beta$ are associated with cerebral microbleeds (a surrogate of CAA pathology) (Graff-Radford et al., 2019). In addition to the vascular origin of WMHs, recent evidence suggests that parietal WMHs could be a result of degenerative axonal loss caused by AD pathology (McAleese et al., 2015, 2017). In this study though, there was no evidence for a stronger association between CSF biomarkers and WMHs in the parietal lobe.

There are comparatively fewer studies regarding the association with tau and WMHs and results are often conflicting. A positive association has been demonstrated neuropathologically (McAleese et al., 2015) and with PET (Vemuri et al., 2017); more direct measures of brain tau load than CSF measures. A positive association has been demonstrated over time in CSF, but the relationship is less clear with baseline measures of tau (Tosto et al., 2015). This study did not find much evidence of a relationship between tau pathology and WMHs, which is in line with several other studies (Guzman et al., 2013, Kester et al., 2014, Osborn et al., 2018).

The fact that age was the strongest predictor of WMHs is consistent with previous studies (de Leeuw et al., 2001b, Raz et al., 2012, Schneider et al., 2009). The association between biomarkers and age was not uniform between diagnostic groups. In controls and EMCI groups, older ages were associated with lower $A\beta$ and higher tau, but in the AD group, younger ages were associated with higher tau. This differential effect of age on CSF biomarkers between AD groups and controls has been previously reported (Mattsson et al., 2012).

Investigations of the associations between AD CSF biomarkers and WMHs in previous studies have either been performed on small samples or in studies with variable acquisition and analysis protocols (Bos et al., 2017, Freeze et al., 2016, Kalheim et al., 2017, Pietroboni et al., 2018, Tosto et al., 2015). Using the ADNI

cohort therefore provides the benefits of a multicentre standardised data acquisition protocol, as well as participants who have been systematically evaluated. This study adds to previous findings using the ADNI cohort (Guzman et al., 2013, Haight et al., 2013, Marnane et al., 2016, Scott et al., 2016), in that data from all diagnostic groups are used and biomarkers for both tau and $A\beta$ are compared with quantitative WMHs. The biomarker and WMH data were also treated as continuous variables; most previous studies have dichotomised variables.

One key limitation to this work, and other such association studies, is that correlation does not mean causation. Therefore it is not possible to determine from the results in this study whether the association observed between $A\beta$ is induced by one biomarker causing change in the other. Further research to reveal such a causal relationship would need to be designed with the Bradford Hill Criteria for causation in mind (Hill, 1965). Other limitations to this work include the selection criteria for the ADNI cohort, meaning any generalisations to the wider population must be made cautiously. ADNI participants tend to be of high socioeconomic status, well-educated and, importantly for this study, free of large amounts of cerebrovascular disease (a score of 4 or lower on the Hachinski Ischemic Scale) (<https://adni.loni.usc.edu/wp-content/uploads/2008/07/adni2-procedures-manual.pdf>). This study was also only carried out using baseline data; longitudinal studies are necessary to characterise the relationship between WMHs and AD biomarkers over time, an approach which will be facilitated by the increasing use of volumetric FLAIR imaging providing more precise measures of change.

There are limitations surrounding the use of CSF biomarkers in this study to investigate AD pathology. CSF biomarkers can now be measured by several different assays, introducing the possibility that these methodological differences may influence study findings. However the analyses carried out using another assay platform, Elecsys, confirm the findings of an associations between CSF biomarkers and WMHs. In addition, despite the benefits of using continuous biomarker variables, it would be interesting to look at associations within biomarker-negative

and biomarker-positive individuals to explore whether associations may be driven by those on the amyloid pathway (Jack et al., 2018) or those who are not. CSF biomarkers are increasingly used to provide information about underlying biochemical changes associated with disease, with $A\beta$ and p-tau well established as markers of AD pathology and t-tau as an established marker of neurodegeneration (Blennow et al., 2010, Jack et al., 2018). While CSF $A\beta$ has shown robust correlations to plaque burden (Strozyk et al., 2003), the relationship of CSF tau to tangle pathology is less clear (Engelborghs et al., 2007) and may account for the lack of association with WMH in this study. However, measures of actual brain $A\beta$ and tau burden and their local distribution, through PET imaging or pathological investigations, were either not available or not used. Only total WMH volume were looked at and therefore no regional associations between NFL and WMH volume were assessed. A detailed assessment of regional WMH associations would be an important future direction.

This study only examined associations between WMHs and the well-established AD biomarkers of CSF $A\beta$, t-tau, and p-tau. The existence of additional co-pathologies in AD suggest that further biomarkers are needed to complement these classical measurements. One biomarker of particular relevance is neurofilament light, a marker of large caliber axonal injury (Skillback et al., 2014). Previous studies of associations between WMHs and neurofilament light have reported mixed results (Mattsson et al., 2019, Osborn et al., 2018, Zetterberg et al., 2016). An analysis of this emerging biomarkers' association with WMHs will be carried out Chapter 4.

A lack of pathological confirmation of cases in the ADNI cohort may, in part, explain the findings in this study. Diagnostic groups may be bimodal in nature; control groups may contain atypical or early stage AD subjects along with the cognitively normal, and a significant proportion of MCI subjects supposedly at high risk for conversion to AD will not have any underlying AD pathology (Jicha et al., 2006, Petersen et al., 2006). Indeed in this study, this may have been a contributing factor to the lack of observed differences in biomarker and WMH relationships

between diagnostic groups. In addition, although the four measures of vascular risk used in this study are among the most notable risk factors, as well as being the most consistently documented for the ADNI cohort, they are unlikely to fully characterise all aspects of SVD and are not direct measures of SVD pathology.

In summary, this study suggests that CSF $A\beta$ is a consistent predictor of WMHs across all diagnostic groups, in a manner that is not dependent on CSF tau. As WMHs are thought to be largely vascular in origin, this study adds to the literature exploring the complex relationship between amyloid and presumed vascular pathologies. Understanding the different relationships between disease markers are important to build more realistic models of biomarkers changes across the full spectrum of normal ageing to AD.

Chapter 4

Associations of WMHs and plasma NFL in sporadic AD

4.1 Introduction

In order to fully investigate AD in vivo, additional biomarkers are needed that complement the classical biomarkers of CSF A β , t-tau and p-tau. NFL is a biomarker of large-calibre axonal injury (Skillback et al., 2014); increases in CSF levels have been demonstrated in AD (Mattsson et al., 2019, Zetterberg et al., 2016), as well as other diseases, such as frontotemporal dementia, amyotrophic lateral sclerosis and MS (Kuhle et al., 2013, Lu et al., 2015, Rohrer et al., 2016, Teunissen and Khalil, 2012). Recent technological developments have also enabled the analysis of NFL in blood (serum and plasma), showing good correlation with CSF levels (Zetterberg and Blennow, 2018).

Links between NFL and white matter changes in AD have previously been demonstrated. There are similarities in the timing of changes in both NFL and WMHs, with recent studies in ADAD reporting elevations in WMHs (Lee et al., 2016) and serum NFL (Preische et al., 2019) in very early disease stages. Studies have also shown direct associations between NFL and WMHs (Osborn et al., 2018, Zetterberg et al., 2016), and NFL and diffusion tensor imaging (DTI) measures (Moore et al., 2018). Other studies however found no evidence of associations between NFL and DTI (Kim et al., 2019) or WMHs (Mattsson et al., 2019).

Here, I sought to investigate whether NFL and WMHs are associated across the full range of normal ageing to AD and whether any relationship was altered with age adjustment. I hypothesise that WMHs would show associations with NFL and that this relationship would change depending on disease stage. This is because WMHs are thought to have a heterogeneous pathological basis (Gouw et al., 2008a) and, although I have shown that WMHs have consistent relationships with CSF A β 1-42 across the disease course from this dataset (Chapter 3 and Walsh et al. (2020)), other studies from other datasets have shown that relationships can vary depending on disease stage (Barnes et al., 2013, Fiford et al., 2017, McAleese et al., 2017, Zhou et al., 2009). Since NFL increases with axonal degeneration, which is likely to become more prominent with the development of AD pathology, I considered the relationship would be stronger at later disease stages. I further considered that the relationship between WMHs and NFL could be mediated by vascular risk factors.

4.2 Methods

4.2.1 Cohort

All data used for this chapter was from the Alzheimer’s Disease Neuroimaging Initiative (ADNI2 and GO) database, see section 2.1.1.

4.2.2 Plasma NFL measurements

Plasma NFL level was measured at the Clinical Neurochemistry Laboratory, University of Gothenburg, Molndal Campus, Molndal, Sweden, using an ultrasensitive enzyme-linked immunosorbent assay on a single molecule array platform (Quanterix Corp).

4.2.3 WMH segmentation

All sites in ADNI use a standardised imaging protocol, described in Jack et al. (2008a) and in section 2.2.1. WMH segmentation was carried out using BaMoS, described previously in section 2.3.1.1. Visual assessment of the BaMoS segmentations and subsequent exclusions is described in Chapter 3. 827 of the 929 subjects in the ADNI cohort used in Chapter 3 had plasma NFL data and therefore made up

the cohort used here. Two subjects had missing information regarding history of diabetes and three subjects had missing information regarding their BMI and were therefore not included in analyses using these variables.

4.2.4 Statistical analyses

4.2.4.1 Variables used in analyses

Demographic and biological data was downloaded from the ADNI database (<http://adni.loni.usc.edu/>). The participant information downloaded and used in this study included: age, gender, MMSE scores, *APOE* ϵ 4 status, plasma NFL values, height and weight, smoking status, hypertension history and diabetes history. BMI was calculated from height and weight variables. Smoking status was coded as 1) never smoked, 2) previous smoker, 3) current smoker, using the information downloaded on smoking history.

4.2.4.2 Data transformation

Analyses involving WMHs were carried out on \log_e transformed values to reduce skewness. NFL values were standardised using the pooled within-group SD, calculated using a linear regression that allowed for differences in mean levels by group. The use of standardised variables enabled comparisons with previous work assessing other CSF-based AD biomarkers to be made. As WMHs were analysed on a logarithmic scale, the coefficients from regression models were back-transformed and expressed as percentage increases or decreases in WMHs for each 1 SD change in plasma NFL.

4.2.4.3 Group demographics and biomarker summary

For estimates of differences in means across control, EMCI, LMCI, SMC and AD groups in demographic, imaging and plasma NFL continuous data, linear regression models were used. For \log_e WMHs, linear regression models were used with group as the predictor of interest and adjustment for TIV. Differences among the five groups were tested with joint Wald tests. Analogous comparisons were performed for categorical variables, with Fisher's exact tests used for gender, *APOE* ϵ 4 status and hypertension, and a chi-square test for smoking status.

4.2.4.4 WMH and NFL relationships

In order to explore the relationships between WMHs and plasma NFL within each diagnostic group, scatter plots of WMHs (on a log scale) against plasma NFL in each group were generated to show unadjusted associations. After inspection of the plots, one outlier from the control group and one from the SMC group with very high plasma NFL were identified and removed from the subsequent main analysis of the NFL-WMH relationship. These outliers were included in a separate sensitivity analysis (see below). The standardisation of NFL values described above was therefore performed twice: once with these two outliers excluded (used in main analyses) and once with the two outliers included (used in sensitivity analyses). Separate linear regression models for each group were then fitted. The dependent variable used in all models was \log_e WMHs, with standardised plasma NFL as the predictor variable of primary interest, and adjusted for TIV. To investigate differences in slope between diagnostic groups, a separate model was fitted to the combined data from all five groups with an interaction term between diagnostic group and plasma NFL. Differences among the five groups were tested with joint Wald tests. All of the above models were then refitted with participant age at baseline as an additional covariate. Analyses including age were secondary, since age at baseline may be on the causal pathway (theoretically a proxy for the number of vascular events that may have happened to an individual and a resultant increase in axonal degeneration).

Partial R^2 values were calculated for the five separate diagnostic group models of \log_e WMHs, and plasma NFL. Partial R^2 values from two models for each diagnostic group were calculated from models adjusting for: i) TIV; ii) TIV and age.

In order to investigate potential mechanisms involved in NFL-WMH relationships, the analysis in each of the separate diagnostic groups was extended to assess the effect of four additional covariates: smoking history; history of hypertension; history of diabetes; and current BMI. The new variables were all added as covariates into a combined linear regression model, as specified above. This allowed an assessment of whether the addition of these vascular risk factors influenced the

NFL-WMH relationship in any manner.

4.2.4.5 NFL and age

In order to assess the relationship between age and plasma NFL, further regression models were fitted with plasma NFL being the dependent variable and age the predictor. This was performed in each diagnostic group separately with an additional model fitted to the combined data including interactions between group and plasma NFL. Scatter plots of plasma NFL against age in each group were also generated.

4.2.4.6 NFL and $A\beta$

To assess the relationship of WMHs and NFL in those who are $A\beta$ positive and negative, the group specific models (as described in 4.2.4.4) were fitted twice more; once in those with a CSF $A\beta$ value of less than 254pg/ml, defined as $A\beta$ positive, and once in those with a value of more than 254pg/ml, defined as $A\beta$ negative (cutpoints defined by ADNI in [https://adni.bitbucket.io/reference/docs/UPENNBIOMK_MASTER/ADNI_Methods_Template_Shaw%20Figurski%20Waligorska%20Trojanowski%20overview%20for%20CSF%20Ab1-42%20tau%20and%20ptau181%20AlzBio3%20immunoassay%20datav3%20\(5\).pdf](https://adni.bitbucket.io/reference/docs/UPENNBIOMK_MASTER/ADNI_Methods_Template_Shaw%20Figurski%20Waligorska%20Trojanowski%20overview%20for%20CSF%20Ab1-42%20tau%20and%20ptau181%20AlzBio3%20immunoassay%20datav3%20(5).pdf)).

4.2.4.7 Sensitivity analysis

A sensitivity analysis was carried out that repeated the regression models assessing the NFL-WMH relationship in each group, but with the inclusion of the one outlier from each of the control and SMC groups respectively. The models were all adjusted for TIV and were carried out with and without age adjustment. Partial R^2 values were again calculated, as above.

4.3 Results

4.3.1 Group demographics and biomarker summary

There were 827 subjects with both useable WMH volumes and available NFL data. Table 4.1 shows demographic, imaging and biomarker summary statistics for each diagnostic group. There were statistically significant ($p < 0.05$) between group dif-

Table 4.1: Demographic and imaging data summary statistics

	Controls	SMC	EMCI	LMCI	AD	<i>p</i> value across groups	
N (total = 827)	163	103	279	152	130		
Age	73.6 (6.2)	72.3 (5.5)	71.2 (7.5)	72.1 (7.6)	74.2 (8.0)	0.005	
Male (%)	47	43	54	55	56	0.1	
MMSE /30	29.0 (1.3)	29.0 (1.2)	28.3 (1.6)	27.5 (1.8)	23.1 (2.1)	<0.001	
<i>APOE</i> ϵ 4 positive (%)	27	34	42	57	68	<0.001	
TIV (ml)	1407 (136)	1414 (126)	1427 (135)	1431 (133)	1422 (153)	0.5	
WMH volume (ml) Median (IQR)	3.4 (4.9)	3.5 (4.4)	3.9 (6.5)	3.7 (8.3)	5.8 (8.3)	0.03^a	
Log _e WMH (ml)	1.2 (0.9)	1.3 (0.9)	1.4 (1.0)	1.4 (1.0)	1.7 (1.0)	0.005^a	
Plasma NFL (pg/ml)	36.6 (24.0)	32.5 (18.2)	36.6 (19.5)	40.3 (20.0)	47.5 (22.7)	<0.001	
History of hypertension (%)	50	47	51	46	45	0.8	
Smoking:	Never (%)	60	51	60	65	62	0.2
	Previous (%)	36	47	38	32	33	
	Current (%)	4	2	2	3	5	
BMI	27.4 (4.5)	28.3 (6.1)	28.2 (5.5)	27.5 (5.0)	26.3 (5.6)	0.01	
History of diabetes (%)	7	10	11	9	14	0.4	

Values are mean (SD) unless reported.

^a Adjusted for TIV

ferences in age, with the youngest participants seen in the EMCI group and the oldest in the AD group. Differences were also seen in MMSE, *APOE* ϵ 4 status and WMH volume with worsening scores, increasing proportion of ϵ 4 carriers, and increasing WMH volumes from controls to EMCI to LMCI though to AD. For BMI the highest values were seen in the SMC and EMCI groups and the lowest values in the AD group. For plasma NFL, the highest levels were seen in the AD group, followed by the LMCI and then EMCI, control and SMC groups.

4.3.2 Plasma NFL and WMHs

Table 4.2a shows percentage increases in WMHs for increases in plasma NFL estimated from diagnostic group specific models and Figure 4.1 shows corresponding scatter plots. After TIV adjustment, significant increases of between 20% and 41% in WMH volume per 1 SD increase in NFL were seen in SMC, EMCI, LMCI and AD groups ($p < 0.004$). There was no evidence for differences in the slopes of the

Table 4.2: Regression model results for the relationship between WMHs and plasma NFL, by group

a)	WMHs and NFL	Controls	SMC	EMCI	LMCI	AD
i)	TIV adjusted					
	% change in WMHs (ml) per 1SD change in NFL	18.2	36.9	29.5	41.1	20.6
	95% confidence intervals	(-1.7 to 42.0)	(-5.2 to 78.1)	(16.8 to 43.6)	(21.9 to 63.4)	(6.2 to 36.8)
	<i>p</i> value	0.08	0.02	<0.001	<0.001	0.004
ii)	TIV and age adjusted					
	% change in WMHs (ml) per 1SD change in NFL	2.0	16.1	4.3	15.5	1.3
	95% confidence intervals	(-16.7 to 24.4)	(-14.8 to 58.1)	(-5.7 to 15.5)	(-1.7 to 35.7)	(-11.0 to 15.5)
	<i>p</i> value	0.9	0.3	0.4	0.08	0.8

Between group differences in % reductions per 1SD change in NFL: *p* value = 0.5 (0.5 with age adjustment)

b)		Controls	SMC	EMCI	LMCI	AD
i)	NFL	0.02	0.05	0.08	0.1	0.06
	TIV	0.07	0.06	0.05	0.09	0.1
ii)	NFL	0.0002	0.009	0.003	0.02	0.0003
	TIV	0.06	0.06	0.05	0.05	0.07
	Age	0.06	0.04	0.2	0.1	0.2

Models assess associations between WMHs and plasma NFL in each diagnostic group, with the addition of TIV (i) and TIV and age (ii) as covariates. In a) estimates are percentage changes in WMH volume per one SD change (1 SD = 18.3pg/ml) in NFL, with 95% confidence intervals. The SD is the pooled within-group SD, calculated from a linear regression model that allowed for differences in mean levels of NFL by group. The results from a model combining all five groups, but with a diagnostic group-NFL interaction is also displayed to investigate between group differences. In b) partial R^2 are shown for each covariate in both models i) and ii).

associations across groups ($p=0.5$). These positive associations between WMHs and NFL were not significant following adjustment for age. Table 4.2b shows partial R^2 values for all covariates from the group-specific models. In model i) with WMHs, NFL and TIV, NFL explained from between 2% to 10% of the variance in WMHs. In model ii) after adjustment for age, a large decrease was observed in the percentage variance explained, with all values less than 2%. Age explained the largest proportion of variance in WMHs in each group, ranging from 4% to 20%.

4.3.3 NFL and age

Table 4.3 shows the relationship between plasma NFL and age in each diagnostic group, with Figure 4.2 showing the corresponding scatter plots. A strong relationship was observed across all groups ($p<0.001$, all groups), but no differences in the slopes of the associations across groups ($p=0.8$)

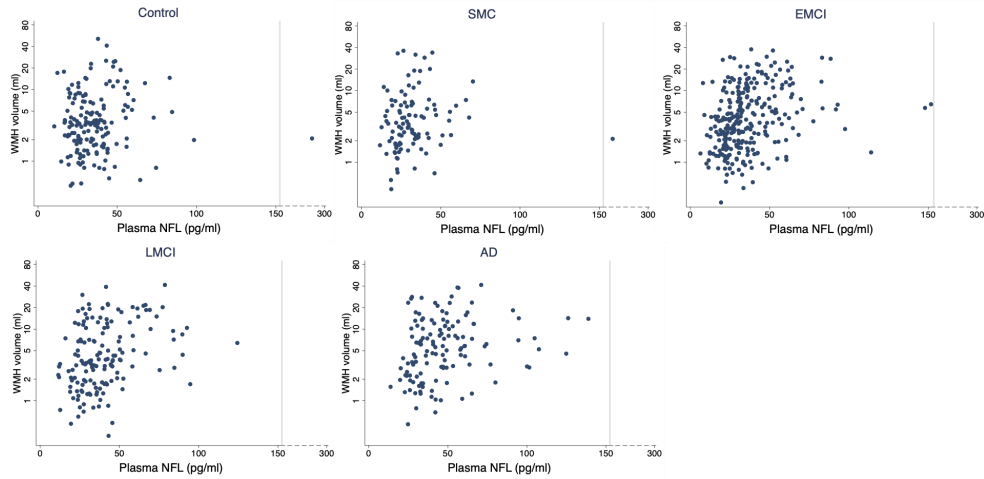


Figure 4.1: Scatter plots showing the relationship between WMHs and plasma NFL in controls, SMC, EMCI, LMCI and AD groups. WMH volume is shown on a log scale and is unadjusted for any covariates. There is an x-axis break to show to show the one NFL outlier in both the control and SMC groups.

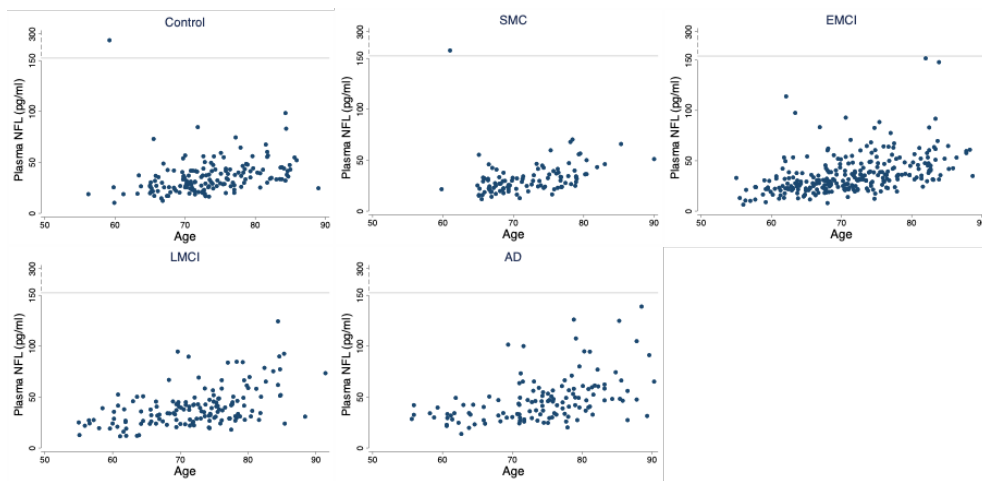


Figure 4.2: Scatter plots showing the relationship between plasma NFL and age in controls, SMC, EMCI, LMCI and AD groups. There is a y-axis break to show to show the one NFL outlier in both the control and SMC groups.

Table 4.3: Regression model results for the relationship between plasma NFL and age, by diagnostic group

NFL and age	Controls	SMC	EMCI	LMCI	AD
SD change in NFL per decade increase in age	0.6	0.7	0.6	0.7	0.7
95% confidence intervals	(0.4 to 0.7)	(0.5 to 0.9)	(0.5 to 0.8)	(0.5 to 0.9)	(0.5 to 1.0)
<i>p</i> value	<0.001	<0.001	<0.001	<0.001	<0.001
Between group differences in slope among all five groups: <i>p</i> value = 0.8					

Estimates are for SD change in NFL per decade increase in age. The SD is the pooled within-group SD, calculated from a linear regression model that allowed for differences in mean levels of NFL by group.

4.3.4 NFL and A β

Table 4.4 shows the relationship between WMHs and NFL in A β positive and A β negative groups. In the A β positive group, a significant relationship was observed in the EMCI, LMCI and AD groups. An approximately 10% greater increase in WMHs per 1 SD change in NFL was observed in these three groups, compared to the results from the full cohort. In the A β negative group, a significant increase in WMHs was only observed in the EMCI group, although all other groups remained directionally consistent with the results in the full cohort.

Table 4.4: Regression model results for the relationship between plasma NFL and WMH, divided into those who are A β positive and A β negative.

WMHs and NFL	Controls	SMC	EMCI	LMCI	AD
A β + N=396	N=59	N=30	N=125	N=109	N=108
% increase in WMHs per 1SD change in NFL	-0.4	13.7	37.7	52.8	27.7
Confidence intervals	(-15.3 to 17.2)	(-33.3 to 93.7)	(12.0 to 69.3)	(25.2 to 86.6)	(7.5 to 51.7)
<i>p</i> value	1.0	0.6	0.003	< 0.001	0.006
A β - N=431	N=104	N=73	N=154	N=43	N=22
% increase in WMHs per 1SD change in NFL	-2.3	8.0	28.9	36.9	22.1
Confidence intervals	(-22.9 to 23.8)	(-13.0 to 34.1)	(11.5 to 49.0)	(-5.8 to 99.0)	(-3.1 to 54.0)
<i>p</i> value	0.8	0.5	0.001	0.1	0.09

Estimates are percentage changes in WMH volume per one SD change (1 SD = 18.3pg/ml) in NFL, with 95% confidence intervals. The SD is the pooled within-group SD, calculated from a linear regression model that allowed for differences in mean levels of NFL by group.

4.3.5 Plasma NFL and WMHs: sensitivity analyses

The analyses presented in Table 4.2 with the addition of one outlier from both the control and SMC groups, are shown in Table 4.5 (outliers visible in Figure 4.1). The addition of these outliers (to the regression analysis and the NFL standardisation) meant that the positive association between NFL and WMHs observed in the SMC group was reduced and was no longer significant (10.6% increase in WMHs for a 1 SD increase in NFL, $p=0.3$). The borderline percentage increase in the control group was also attenuated (5% increase in WMHs for a 1 SD increase in NFL, $p=0.4$). The inclusion of these overly influential outliers lead to a statistically significant difference in the slopes of the associations across all groups ($p=0.007$).

Table 4.5: Regression model results for the relationship between WMHs and plasma NFL by diagnostic group, after the inclusion of two outliers

a)	WMHs and NFL	Controls	SMC	EMCI	LMCI	AD
i)	TIV adjusted					
	% reduction in WMHs (ml) per 1SD change in NFL	5.0	10.6	34.1	47.8	23.7
	95% confidence intervals	(-7.3 to 19.0)	(-9.7 to 35.4)	(19.2 to 50.8)	(25.1 to 74.6)	(7.2 to 42.7)
	<i>p</i> value	0.4	0.3	<0.001	<0.001	0.004
ii)	TIV and age adjusted					
	% reduction in WMHs (ml) per 1SD change in NFL	-0.5	-4.2	4.9	17.8	1.5
	95% confidence intervals	(-12.1 to 12.6)	(-23.6 to 20.1)	(-6.4 to 17.7)	(-1.9 to 41.4)	(-12.4 to 17.7)
	<i>p</i> value	0.9	0.7	0.4	0.08	0.8

Between group differences in % reductions per 1SD increase in NFL: p value = 0.007 (0.2 with age adjustment)

b)		Controls	SMC	EMCI	LMCI	AD
i)	NFL	0.004	0.01	0.08	0.1	0.06
	TIV	0.07	0.06	0.05	0.09	0.1
ii)	NFL	0	0.001	0.003	0.02	0.0003
	TIV	0.06	0.06	0.05	0.05	0.07
	Age	0.08	0.06	0.2	0.1	0.2

Models assess associations between WMHs and plasma NFL in each diagnostic group, with the addition of TIV (i) and TIV and age (ii) as covariates. These models include one outlier from the control group and one from the SMC group. In a) estimates are percentage changes in WMH volume per one SD change (1 SD = 20.7pg/ml) in NFL, with 95% confidence intervals. The SD is the pooled within-group SD, calculated from a linear regression model that allowed for differences in mean levels of NFL by group. The results from a model combining all five groups, but with a diagnostic group-NFL interaction is also displayed to investigate between group differences. In In b) partial R^2 are shown for each covariate in both models i) and ii).

4.3.6 Exploring the WMHs and NFL relationship: the potential role for vascular risk

Table 4.6 shows percentage increases in WMHs for increases in plasma NFL, with adjustment for the vascular risk factors of smoking status, a history of hypertension, a history of diabetes and BMI. With combined adjustment for the four vascular risk factors, there was no evidence for a marked attenuation of the association between NFL and WMHs (shown in Table 4.2) in any disease group.

Table 4.6: Regression models results for the relationship between WMHs and plasma NFL with adjustment for smoking status, history of hypertension, history of diabetes and BMI by group

WMHs and NFL adjusted for smoking, hypertension, diabetes and BMI (N=820)	Controls	SMC	EMCI	LMCI	AD
SD change in NFL per decade increase in age	18.7	43.3	29.1	37.3	20.3
95% confidence intervals	(-2.1 to 44.1)	(8.1 to 90.1)	(13.6 to 39.9)	(17.7 to 60.2)	(5.1 to 37.8)
<i>p</i> value	0.08	0.01	<0.001	<0.001	0.008

Estimates are percentage increases in WMH volume per one SD change (1 SD = 18.3pg/ml) in NFL, with 95% confidence intervals and adjustment for TIV. The SD is the pooled within-group SD, calculated from a linear regression model that allowed for differences in mean levels of NFL by group.

4.4 Discussion

This work provides evidence for an association between plasma NFL and WMHs in those with a significant memory concern, and from the early stages of cognitive impairment through to clinical AD. Baseline participant age had a strong impact on the relationship, accounting for the most variance in WMH volumes and significantly attenuating the relationship between WMHs and NFL when included as a covariate.

These findings suggest that WMHs seen in cognitive impairment are likely to be related to axonal damage, as indicated by plasma NFL, in a manner that is dependent on age. There is previous evidence that supports a relationship between WMHs and plasma NFL. Following injury to large myelinated axons, NFL has been shown to be released into the extracellular space and subsequently into the CSF (Sjogren

et al., 2001). CSF NFL has been shown to be a sensitive biomarker for neurodegeneration in AD, with levels correlating with cognitive decline and brain atrophy (Mattsson et al., 2019, Zetterberg et al., 2016). Recent technological developments have enabled measurement of NFL in blood (Almeida et al., 2015), levels of which are highly correlated with CSF NFL (Zetterberg and Blennow, 2018). Recently it was shown that plasma NFL was more strongly associated with cognitive and neuroimaging outcomes than CSF NFL (Mielke et al., 2019). Given that taking blood samples is less invasive than taking CSF, it may be that plasma NFL has great potential for widespread clinical use.

NFL levels are associated with white matter changes in multiple neurodegenerative diseases, including AD, VaD and MS (Sjogren et al., 2001, Teunissen and Khalil, 2012, Zetterberg et al., 2016). Previous studies have demonstrated associations of NFL with WMHs in cognitively normal and MCI (Osborn et al., 2018), and MCI and AD groups (Zetterberg et al., 2016), and with compromised white matter microstructure using diffusion imaging (Moore et al., 2018). However a recent study by Mattsson et al. (2019) in the ADNI cohort did not find any evidence for an association of WMHs with baseline or longitudinal NFL data. The discrepancy with this study is likely partly due to differing methods used to generate WMH volumes. Additionally, Mattsson et al. combined two ADNI phases with different imaging protocols, which may have affected any associations seen.

WMHs seen in AD are often presumed to be vascular in origin, as a result of cerebral SVD (Wardlaw et al., 2013). Evidence has also suggested that NFL biomarker increases could signify damage related to vascular pathologies (Duering et al., 2018, Gattringer et al., 2017). The positive WMH-NFL relationship may be caused by either traditional Alzheimer's pathologies ($A\beta$ deposited as plaques or in the vasculature as cerebral amyloid angiopathy, and tau) or co-morbid cerebrovascular disease due to conventional risk factors, or both. The association of WMHs with age is well documented (de Leeuw et al., 2001a, Ylikoski et al., 1995), and has been shown in this cohort in Chapter 3 and in Walsh et al. (2020). This relationship could be due to cerebrovascular events, disease and risk factors, which all increase

with age. In this study, however, there was no effect of the vascular risk factors of smoking, hypertension, BMI or diabetes on the relationship between WMHs and NFL. These results could be interpreted as support for the growing body of evidence that WMHs represent core aspects of AD and cannot simply be attributed to concomitant CVD (McAleese et al., 2017). This evidence includes studies of ADAD, where WMH accumulation is seen in presymptomatic disease stages in young mutation carriers without comorbid CVD (Lee et al., 2016, 2018). There is also evidence of elevated NFL in ADAD cohorts (Preische et al., 2019, Weston et al., 2017).

The vascular risk factors included in this study were used as they are some of the most notable (Livingston et al., 2017) and are also consistently recorded in the ADNI cohort. However not all vascular risk factors, vascular disease and vascular-related events will be characterised by these variables collected and a more comprehensive analysis may elucidate more of the NFL-vascular disease relationship. Osborn et al. (2019) recently assessed this relationship between systemic vascular risk and NFL and found that associations are amplified by the presence of $A\beta$ and tau pathology. Interestingly, a previous study from the same group had found that NFL associations with vascular pathology were independent of $A\beta$ (Osborn et al., 2018). Here the relationship of NFL and WMHs was assessed separately in $A\beta$ positive and negative groups. There is some evidence (although not formally tested) that $A\beta$ is exacerbating the relationship between WMHs and NFL, with a significant relationship observed in the $A\beta$ positive group in the three most cognitively impaired groups, compared to only the EMCI group in the $A\beta$ negative group. It is important though to note though that the group size was reduced significantly in several of the groups, which may be a contributing factor in the lack of significance observed. Looking at changes in the percentage increases, it seems that although the presence of $A\beta$ seems to augment the NFL-WMH relationship, it does not appear to be the sole driver, as a positive relationship is still observed in the $A\beta$ negative group.

One potentially major influence on the findings here are the cerebrovascular exclusion criteria in ADNI (a score above 4 on the Hachinski Ischemic

Scale) (<https://adni.loni.usc.edu/wp-content/uploads/2008/07/adni2-procedures-manual.pdf>). For example, the reason why the association between NFL and WMHs was lower in AD than the MCI groups may be due to the exclusion criteria in ADNI, whereby those AD patients with significant cerebrovascular burden (and likely higher WMHs and NFL) may have had a Hachinski score of greater than 4. Indeed, there appears to be a proportion of participants in the AD group with high NFL levels and low WMH volumes, but no participants both with these highest NFL levels and high WMHs (see Figure 4.1). Individuals with higher numbers of vascular risk factors are likely to develop significant cerebrovascular disease and therefore be excluded from this study.

A strong relationship of NFL with age was found, with a highly significant positive relationship in each diagnostic group. The marked reduction in the association between NFL and WMHs after age adjustment also suggests that the relationship between WMHs and NFL is largely due to their associations with age. Results with and without adjustment for age at baseline were presented, to be sensitive to the fact that age can be considered a proxy measure of vascular events and other comorbidities that increase over time and cause resultant degeneration. Adjusting for age cannot simply be considered as removal of the effects of normal ageing on the WMH-NFL relationship. Such an approach could be achieved by the adjustment of the models with the slope of the association in healthy controls, and potentially only using the controls without evidence of amyloid pathology, in attempt to remove the effects of normal ageing.

The strong association between NFL and age is in agreement with previous studies that have demonstrated this positive association in both controls and in AD (Lewczuk et al., 2018, Vagberg et al., 2015). It is unclear what underpins this increase in NFL with age, but it is suggestive of subclinical axonal damage. Whilst the increase could potentially be caused by an increase in cerebrovascular pathology with increasing age (Lewczuk et al., 2018, Vagberg et al., 2015), these results do not support this notion since adjustment for most of the major vascular risk factors had little impact on the NFL and WMH relationship. This hypothesis should not be

entirely discounted since the lack of support for it from this study may have been due to the nature of the vascular variables used here or the selection bias, induced by the Hachinski score cut off, acting on this cohort. Nonetheless, these findings highlight the importance of looking beyond vascular disease and studying the role that other pathological processes may effect upon axonal and white matter health in ageing and in AD.

The highest levels of NFL were observed in the AD group, followed by the LMCI group, with the less cognitively impaired groups having lower levels of NFL. This suggests that NFL differs by disease stage which is a key feature of a biomarker. Further work is needed to understand whether it predicts further WMH development, serves as a good prognostic biomarker, or tracks with disease progression, particularly in the early disease stages. The strong association of NFL with age could have potential implications when considering its use as an AD biomarker. Previous reports found an age-dependent increase in the sensitivity at the cost of a decrease in the specificity, with the most marked effect seen at older ages (Lewczuk et al., 2018, Mattsson et al., 2017). Furthermore, increases in NFL are not specific to the neurodegeneration observed in AD, and have been observed in MS (Kuhle et al., 2013), amyotrophic lateral sclerosis (Lu et al., 2015), frontotemporal dementia (Rohrer et al., 2016) and after traumatic brain injury (Shahim et al., 2018). It may therefore be more plausible for NFL to be used as a screening tool for neurodegeneration, as opposed to a diagnostic test for any condition.

Many of the limitations of this study are the same as in Chapter 3. These include the use of the ADNI cohort, which is largely free of cerebrovascular disease and of higher socioeconomic status. Pathological confirmation of diagnosis is also not available for the ADNI cohort, leaving open the possibility of bimodal disease groups (Jicha et al., 2006, Petersen et al., 2006). Related to this, in the analysis involving $A\beta$, positive individuals were observed in the control groups and negative individuals were observed in the diseased groups. This could provide evidence of bimodal disease groups, or could be the result of using cutoff values. Like in Chapter 3, this study was only carried out using baseline data and so changes over

time in the relationship between NFL and WMHs were not assessed. Again, only total WMH volumes were assessed, so no conclusions about regional distribution can be drawn. Additionally, it is unlikely that all vascular risks will be accounted for in the variables selected. Further, height and weight were collapsed into the commonly-used BMI measure in this analysis, but were not further collapsed over all vascular risk variables to generate a points-based vascular risk score as has been carried out in other studies (D'Agostino et al., 2008, Lane et al., 2019a). There was merit in entering each of these vascular risk factors, given the possibility that they may not all have the same relationship with WMHs or NFL levels.

Only Plasma NFL was used in this study due to CSF NFL not currently being available for ADNI2/GO, but it would have been interesting to compare CSF NFL as differing associations with outcome measures have been reported (Mielke et al., 2019). Only total WMH volume were looked at and therefore no regional associations between NFL and WMH volume were assessed. An important caveat to the study design is that no causality in the WMH-NFL relationship can be inferred. Therefore it is not possible to discern whether the association we observe between NFL and WMHs is induced by each biomarker's strong associations with age, or whether one biomarker causes change in the other. Further research would be necessary to reveal any causal relationship.

In summary, this study is suggestive of an association between plasma NFL and WMHs in MCI and AD, but in a manner that is largely dependent on age. This study adds to our understanding of the ageing brain's vulnerability to damage, such as axonal degeneration. Plasma NFL could offer insight into white matter damage in cognitively impaired individuals in a relatively non-invasive and inexpensive manner.

Chapter 5

Associations of WMHs and brain atrophy in ADAD

5.1 Introduction

WMHs are increasingly recognised as a feature of late-onset sporadic Alzheimer's disease; WMH burden is predictive of AD progression (Brickman et al., 2015, Lopez et al., 2014, van Straaten et al., 2008) and is associated with AD hallmarks such as measures of $A\beta$ (Walsh et al., 2020, Zhou et al., 2015) and tau pathology (McAleese et al., 2015, Tosto et al., 2015) and brain atrophy (Barnes et al., 2013, Fiford et al., 2017, Schmidt et al., 2005). There are very few studies of WMHs in ADAD. One study demonstrated greater WMHs in mutation carriers up to 22 years before symptom onset, suggesting that WMHs are a key feature in AD (Lee et al., 2016). ADAD provides a unique chance to track WMH progression from presymptomatic stages to clinical AD, due to the heritability of age at symptom onset and the virtually complete penetrance of the causative mutations in *PSEN1*, *PSEN2* and *APP* genes. Individuals with ADAD are younger than sporadic AD with a low incidence of comorbidities, enabling an important opportunity to uncover the extent to which WMHs are a core feature of AD, rather than the result of age-related vascular risk factors, vascular events and vascular dysfunction.

In this study, I used the DIAN cohort to assess how WMH change over time differs between non-carriers and *PSEN1*, *PSEN2* and *APP* mutation groups, and

whether WMH burden increases as estimated onset is approached and passed. I also aimed to assess whether WMH and brain atrophy rates are associated features across the disease course. I hypothesised that heterogeneity in WMH accrual may be evident in ADAD, with previous reports showing differences in multiple aspects of the disease according to mutation group (Ryan et al., 2015, Ryan and Rossor, 2010, Shepherd et al., 2009). As indicated from studies in sporadic AD, I hypothesised that brain atrophy and WMHs are associated over the course of the disease (Enzinger et al., 2005, Schmidt et al., 2005).

5.1.1 Cohort

All data used in this chapter was from from the tenth data freeze of the DIAN cohort (see section 2.1.2). Four mutation groups were used in this study: non-carriers, *PSEN1* mutation carriers, *PSEN2* carriers and *APP* carriers. The mutation carrier groups were further classified into three symptom severity groups based on mutation status and global CDR score, similar to a previous study (Kinnunen et al., 2018):

- Presymptomatic (P-Sym): mutation carriers with a global CDR score of 0 at both of their first two visits
- Questionably symptomatic (Q-Sym): mutation carriers with a global CDR score of 0.5 at one or both of their first two visits (the other being 0 or 0.5)
- Symptomatic (Sym): mutation carriers with a global CDR score of 1.0 or greater at one or both of their first two visits

5.1.2 Quality control

221 FLAIR and T1-weighted images with baseline data and at least one follow-up, and with complete clinical data (mutation status, age, CDR score, EYO) were transferred to the Dementia Research Centre, UCL, London. Following visual inspection of T1-weighted and FLAIR images, 20 participants were excluded due to acquisition-related changes between timepoints, lack of clinical information and presence of non-AD pathology (e.g. infarcts, neoplasm). The full cohort consisted

of 201 participants, comprising 72 non-carriers, 95 with *PSEN1* mutations, 7 with *PSEN2* mutations and 27 with *APP* mutations. Of these 201, 26 participants were identified as having imaging artefacts (e.g. motion) that could result in unreliable brain atrophy measures and included in an ‘artefact’ group. For investigations including brain atrophy measures, sensitivity analyses were subsequently performed with and without this ‘artefact’ group.

5.1.3 WMH segmentation

5.1.3.1 Automated segmentation

An automated WMH segmentation was initially carried out by running BaMoS (see section 2.3.1.1) on the serial DIAN scans.

5.1.3.2 Quality control of BaMoS segmentations

BaMoS segmentations from each individual timepoint were visually assessed separately and graded on performance. An improved grading system was introduced from the one used in section 3.2.2.2, whereby the amount of artefact was graded on a 5-point scale for each region commonly associated with artefact (frontal lobe, temporal lobe, cortical, midline), with 1 being very minor and 5 being very severe and unusable. This was to account for the fact that the DIAN BaMoS segmentations appeared to have greater levels of artefact than the ADNI BaMoS segmentations. Scans were flagged up if they had a score of 4 or greater in any one region, or a score of 3 in greater than one region. A substantial proportion of the scans from the 221 participants (35%) were flagged. A decision was therefore taken to undertake further analysis of the effectiveness of the BaMoS segmentation tool in the DIAN cohort.

5.1.3.3 Comparison of automated and semi-automated segmentation in a subset

A subset of participants from the full DIAN cohort were selected to undergo manual segmentation of WMHs, to which the results from BaMoS could be compared. 19 subjects were chosen to reflect the complete range of timepoints and WMH load

Table 5.1: DIAN subset selection

Number of timepoints	Subjects
2	8
3	5
4	4
5	1
6	1
WMH Load	Subjects
High (>5ml)	5
Medium (<1ml,>5ml)	9
Low (<1ml)	5
WMH accrual	Subjects
Stable	9
Accruing	10

present in the full cohort (Table 5.1). Manual segmentation was carried out as described in section 2.3.1.2, using both the 'Separate timepoint' and the 'Multiple timepoint' methods. BaMoS segmentations are run in normally T1 space, whilst the semi-automated segmentations are performed in FLAIR space. To account for this, BaMoS segmentations for this subset were re-run in FLAIR space so that both sets of segmentations would be comparable. A scatter plot was generated to visually confirm that equivalent volumes were obtained from the FLAIR and T1 space BaMoS segmentations.

To examine the agreement between the WMH volumes resulting from BaMoS segmentation and from semi-automated segmentation in this subset, several statistical comparisons were carried out. Firstly, Bland-Altman plots were generated to graphically compare baseline BaMoS WMH estimates with the semi-automated segmentation estimates. Bland-Altman plots are generated by plotting the difference between the volumes from the two techniques against the average of the two volumes. The mean difference between the two techniques and the 95% limits of agreement were also calculated and plotted. Dice score coefficients from WMH

segmentations on baseline scans were then calculated to measure the level of overlap between the two methods.

To assess how the segmentation method affects assessment of WMH change over time, mixed effect modelling was carried out. After testing for fit, a random intercepts model that did not allow rate of change to vary between subjects was selected.

5.1.3.4 Results: Comparison of automated and manual segmentation in subset

There was a high degree of agreement between the BaMoS WMH volumes generated from T1 and those from FLAIR space (Figure 5.1). The decision was therefore made to use the FLAIR space volumes for the remaining DIAN subset analysis, in order to be directly comparable to the manual WMH segmentations.

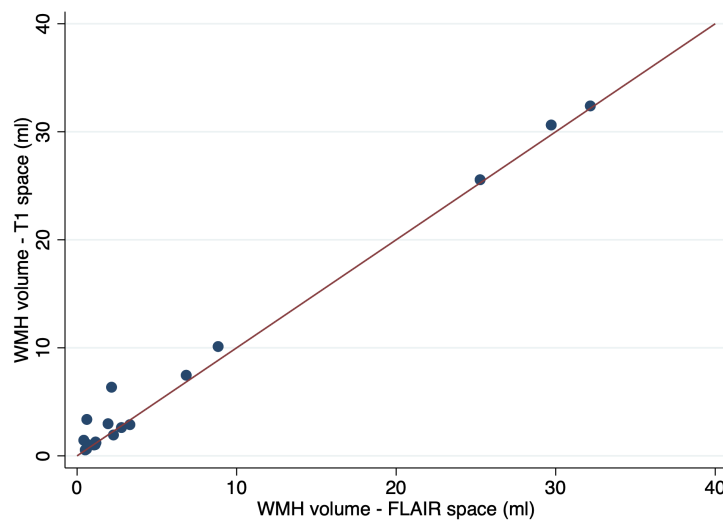


Figure 5.1: A scatter plot demonstrating similarities in the BaMoS generated baseline WMH segmentation volumes from FLAIR and T1 space

When assessing similarities between baseline WMH volumes obtained from BaMoS and the semi-automated method, a moderate degree of agreement was obtained and demonstrated in the Bland-Altman plot in Figure 5.2. The mean difference line is close to zero and the majority of the points fall close to this mean difference line, especially at smaller WMH volumes. At medium and larger WMH vol-

umes, BaMoS tends to overestimate WMH volume compared to the semi-automated method, apart from the largest volume where it has underestimated. In terms of the amount of spatial overlap between the two segmentation methods, the majority of the Dice score coefficients (Figure 5.3) were below the level of 0.7 that is generally considered good in the literature (Caligiuri et al., 2015). The lowest degree of overlap was observed for the smallest WMH volumes, whereas very high degrees of overlap were observed for WMH volumes above 20ml.

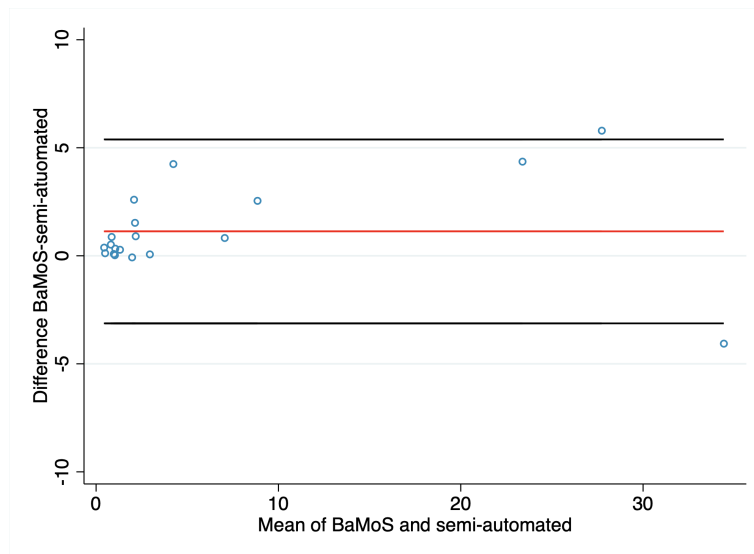


Figure 5.2: Bland-Altman plot of BaMoS generated baseline WMH volumes compared to semi-automated baseline WMH volumes. The difference between the two volumes is plotted on the y axis and the mean of the two volumes is plotted on the x axis. The mean difference between the two volumes is represented by the red line, and the 95% limits of agreement are the black lines

When comparing the two segmentation methods in the assessment of WMH changes over time, the rate of change in the BaMoS volumes was estimated to be over 1.5 times less than the semi-automated volumes (Table 5.2). This suggests that using the BaMoS segmentations results in a flatter estimated trajectory, which is not accompanied by any reduction in within subject variation.

The evidence from both assessing baseline WMHs and WMH change over time suggests that BaMoS is significantly less accurate in segmenting WMHs compared to the semi-automated method. This confirms the original observations from the visual assessment of the BaMoS segmentations in the full cohort, where over 35%

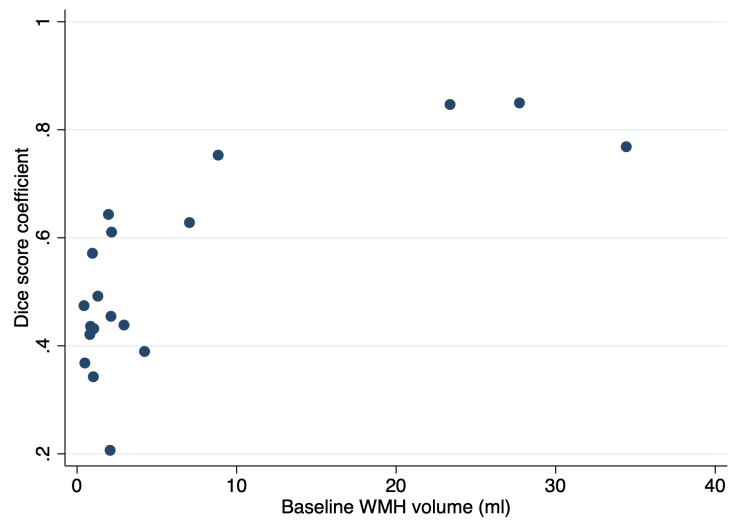


Figure 5.3: A scatter plot showing the Dice score coefficient as a measure of segmentation overlap between the BaMoS and semi-automated volumes, against the mean WMH volume

were flagged as having significant artefact. The decision was therefore taken to proceed with the semi-automated segmentation method on the full cohort.

5.1.4 Brain volume

Brain volume loss was calculate using the BSI, as described in 2.3.2.

5.1.5 Statistical analysis

5.1.5.1 Variable creation and transformation

All statistical analyses were performed on \log_e transformed WMH values to reduce skewness. The resulting coefficients from all linear regression models were back-

Table 5.2: Differences in segmentation methods in assessing WMH change over time from mixed effect modelling

	Semi-automated	BaMoS
Mean intercept	0.99	1.62
Mean rate of change	0.12	0.06
Between subject intercept variation	2.12	1.79
Within subject variation	0.23	0.25

transformed so that they expressed percentage differences in WMHs. Baseline values of TIV for each participant were used as a covariate in all models for WMHs and brain atrophy (unless otherwise stated), allowing rates of change to depend on head size.

5.1.5.2 Analysis of baseline demographic and imaging variables

Fisher's exact test was used to test differences in the distribution of gender, *APOE* $\epsilon 4$ status and symptom severity across mutation groups (non-carrier, *PSEN1*, *PSEN2* and *APP*). For all other variables joint Wald tests of differences amongst groups were performed after fitting a linear regression model with mutation group as a categorical predictor (with adjustment for TIV for \log_e transformed WMHs).

5.1.5.3 WMH Change over time in each mutation group

Line plots showing \log_e WMH volume relative to time from baseline (years) in each subject were generated for each mutation group. To relate changes in \log_e WMH volume to time from baseline, linear mixed models (group-specific model 1) with correlated random slopes and intercepts were fitted in each mutation group separately. Slopes and intercepts were allowed to depend on TIV. Fitted lines (with 95% confidence intervals) for a person having the overall mean TIV were overlaid onto each line plot.

A model (combined model 1) was also fitted to the data from all mutation groups. This model allowed all mean slopes and intercepts, all random effect variances and covariances, and all residual variances, to differ by mutation group. Slopes and intercepts were allowed to depend on TIV, with these dependencies assumed constant across groups. From this (and other later combined models), joint Wald tests of differences amongst the slopes in the non-carriers and three mutation groups were carried out.

To explore whether results were materially affected by baseline age, the above analysis was repeated with slopes and intercepts additionally allowed to depend on age (group-specific model 2 and combined model 2). Fitted slopes (with 95% confidence intervals) for a person of overall mean age and having the overall mean TIV were obtained from the group-specific models.

To explore differences between the non-carriers and the three mutation groups in those without symptoms, group-specific and combined models 1 and 2 were refitted omitting symptomatic and questionably symptomatic individuals. For the non-carrier group, nine individuals with a CDR of 0.5 were omitted from this analysis. To assess potential differences in \log_e WMH change between *PSEN1* carriers with a mutation pre-codon 200 versus those with a mutation post-codon 200, a variant of combined model 1 was fitted in *PSEN1* carriers only. This model (combined model 3) allowed all mean slopes and intercepts, all random effect variances and covariances, and all residual variances, to differ by codon group.

5.1.5.4 WMH Change over time in each symptom group

To explore symptom group differences in WMH change over time, group specific and combined models 1 and 2 were refitted with symptom group instead of mutation group. Line plots were also generated to show \log_e WMH volume relative to time from baseline (years) in each subject for each symptom group. Fitted lines (with 95% confidence intervals) for a person having the overall mean TIV were overlaid onto each line plot.

5.1.5.5 Change based on estimated years to onset

To relate \log_e WMH change to estimated years pre-/post onset (EYO), a mixed-effect model (group-specific model 3) with random slopes but fixed person-specific intercepts (because intercepts did not appear Gaussian with a few clear outliers), was fitted in each mutation group (*PSEN1*, *PSEN2* and *APP*). Slopes were allowed to depend on TIV. A second model (group-specific model 4), with an additional fixed quadratic time term, was also fitted in each mutation group (*PSEN1*, *PSEN2* and *APP*) to assess evidence of an acceleration in WMH change. From this, the mean annualised rates of WMH change from 10 years before onset to 5 years before onset, and in subsequent 5-year periods up to between 10 and 15-years post onset were calculated (with 95% confidence interval). This EYO range was used since most participants were assessed in these intervals. Graphs of \log_e WMHs against EYO for each individual were plotted for each mutation group. Mean fitted lines (with 95% confidence intervals), created by averaging across people, were overlaid

onto each mutation group graph.

5.1.5.6 Associations between brain atrophy and WMH changes

Scatter plots were generated in each mutation group, to show participant-specific rates of change in WMHs and brain volume. For WMHs these rates of change were estimated from participant-specific simple regression models relating log-transformed WMHs to time. For whole brain volume participant-specific regression, models relating each BSI to the time interval over which the BSI was measured without a constant term were used. Crude Pearson correlation coefficients (with p-values and 95% confidence intervals) were calculated for the associations between rate of change in WMHs and brain volume. Partial correlation coefficients adjusting for TIV and an individual's mean follow-up relative to age at expected onset were also calculated.

5.2 Results

5.2.1 Demographic and imaging summary statistics

Table 5.3 shows demographic, imaging and clinical data from the 201 subjects used in this study. No evidence of differences was observed between non-carriers and the three mutation groups in the proportions of males and *APOE* ϵ 4 positive individuals, or in expected years from onset or TIV. Statistically significant differences were seen between baseline \log_e transformed WMH volumes with the largest volumes in the *PSEN2* and *APP* groups and the smallest in the non-carriers. Differences were also observed in the mean length of follow up between mutation groups, with the *PSEN2* group having a longer follow-up interval. There were 31 individuals with a *PSEN1* mutation post-codon 200 and 62 individuals with a mutation pre-codon 200.

Table 5.4 demonstrates that the majority of participants from all groups had no more than two visits in total for this study. As expected, the number of participants declined as the number of visits increased. 5 *PSEN1*, 1 *PSEN2* and 1 *APP* participant had a total of 5 visits, and only 1 *PSEN1* and 1 *APP* participant had a total of 6 visits.

Table 5.3: Demographic and imaging data in each mutation group

	Non-carrier	<i>PSEN1</i>	<i>PSEN2</i>	<i>APP</i>	<i>p</i> value across groups
N (total=201)	72	95	7	27	
Age	38.9 (10.5)	40.0 (10.6)	42.3 (12.6)	42.9 (9.8)	0.4
Male (%)	63	61	43	63	0.8
<i>APOE</i> ϵ 4 positive (%)	25	26	43	26	0.7
EYO ^a	-7.1 (10.7)	-4.5 (9.6)	-7.5 (13.6)	-5.5 (9.4)	0.4
Symptom status:					
P-Sym	-	41 (43%)	5 (71%)	15 (54%)	
Q-Sym	-	34 (36%)	1 (14%)	8 (30%)	0.6
Sym	-	20 (22%)	1 (14%)	4 (14%)	
Length of follow up (years); min, max	2.8 (0.8); 1.9, 5.0	2.6 (1.1); 0.9, 5.2	3.6 (0.5); 3.0, 4.3	2.6 (1.3); 1.0, 5.1	0.008
TIV (ml)	1387 (132)	1378 (136)	1497 (139)	1418 (166)	0.1
WMH (ml)	0.7 (0.7)	0.9 (1.5)	1.5 (4.3)	1.2 (2.1)	
Log _e WMH (ml)	-0.4 (0.9)	-0.05 (1.3)	0.4 (2.1)	0.2 (1.5)	0.004^b

Values are mean (SD) unless reported. White matter hyperintensity values reported as median (IQR).

^a Based on parental age at onset. A negative value of EYO indicates that a participant joined the study prior to expected age of onset; EYO values for non-carriers use parental age at onset (as with carriers). This EYO variable in non-carriers does not indicate that they will develop ADAD.

^b Adjusted for TIV

Table 5.4: Frequency of participants with each maximum visit number, in each mutation group

	Maximum visit number				
	2	3	4	5	6
Non-carrier	55	10	7	0	0
<i>PSEN1</i>	61	25	2	6	1
<i>PSEN2</i>	5	0	1	1	0
<i>APP</i>	17	5	3	1	1
Total	138	40	13	8	2

5.2.2 WMH change over time by mutation group

Table 5.5 shows fitted (for participants with overall mean TIV, and mean age) percentage increases in WMHs over time for non-carriers and each mutation group. Figure 5.4a-d shows these fitted values together with raw data. In Table 5.5a statistically significant increases over time were observed in the non-carrier, *PSEN1* and *APP* mutation groups, with the greatest WMHs increase per year (12.8%) observed in the *APP* group, compared with a 5.5% increase in the *PSEN1* group and a 3.3% increase per year in non-carriers. The mean rate in the *PSEN2* group was close to zero, but the 95% confidence was wide, reflecting the small number of participants in this group. These results were not materially changed with allowance for age. Differences in WMH accrual between groups were formally tested in a combined model and there was evidence for a significant variation amongst the groups ($p=0.01$), driven by the higher rate of accrual in the *APP* group and showing borderline statistical significance after adjustment for age. In Table 5.5b, in models re-

Table 5.5: Regression model results for the mean change in WMHs over time, in each mutation group

		Non-carriers	<i>PSEN1</i>	<i>PSEN2</i>	<i>APP</i>	<i>p</i> value across groups*
a) All participants	Analysis allowing rates of change to depend on TIV					
	% increase in WMHs per year at overall mean TIV	3.3	5.5	-0.1	12.8	0.01
	95% confidence intervals	(0.5 to 6.1)	(1.7 to 9.6)	(-13.1 to 14.8)	(6.9 to 19.0)	
	<i>p</i> value	0.02	0.005	1.0	< 0.001	
	Analysis allowing additional dependency on age					
	% increase in WMHs per year at overall mean TIV	3.6	5.5	-0.1	12.8	0.08
95% confidence intervals	(0.8 to 6.5)	(2.2 to 9.8)	(-10.4 to 14.4)	(6.6 to 17.8)		
<i>p</i> value	0.01	0.002	0.8	< 0.001		
b) Participants without symptoms	Analysis allowing rates of change to depend on TIV	<i>N</i> =63	<i>N</i> =41	<i>N</i> =5	<i>N</i> =15	
	% increase in WMHs per year at overall mean TIV	3.2	-0.8	-9.5	13.3	< 0.001
	95% confidence intervals	(0.3 to 5.8)	(-5.0 to 3.6)	(-21.9 to 4.9)	(8.5 to 18.3)	
	<i>p</i> value	0.01	0.7	0.2	< 0.001	
	Analysis allowing additional dependency on age	<i>N</i> =63	<i>N</i> =41	<i>N</i> =5	<i>N</i> =15	
	% increase in WMHs per year at overall mean TIV	3.2	1.0	-8.4	14.0	< 0.001
95% confidence intervals	(0.5 to 6.1)	(-4.4 to 6.9)	(-27.3 to 15.3)	(9.5 to 18.7)		
<i>p</i> value	0.02	0.7	0.5	< 0.001		

Fitted percentage increases (with 95% confidence intervals and *p*-values) in WMH volume per year. In a) results are assessing WMH change in each group, allowing for dependency of baseline values and rates of change on TIV, and then additionally on age. In b) analogous results are restricted to those without symptoms. The *N* for each group included in each model is as displayed in Table 5.3, unless otherwise stated.)

* Assumes effects of TIV on slopes and intercepts are the same in each mutation group.

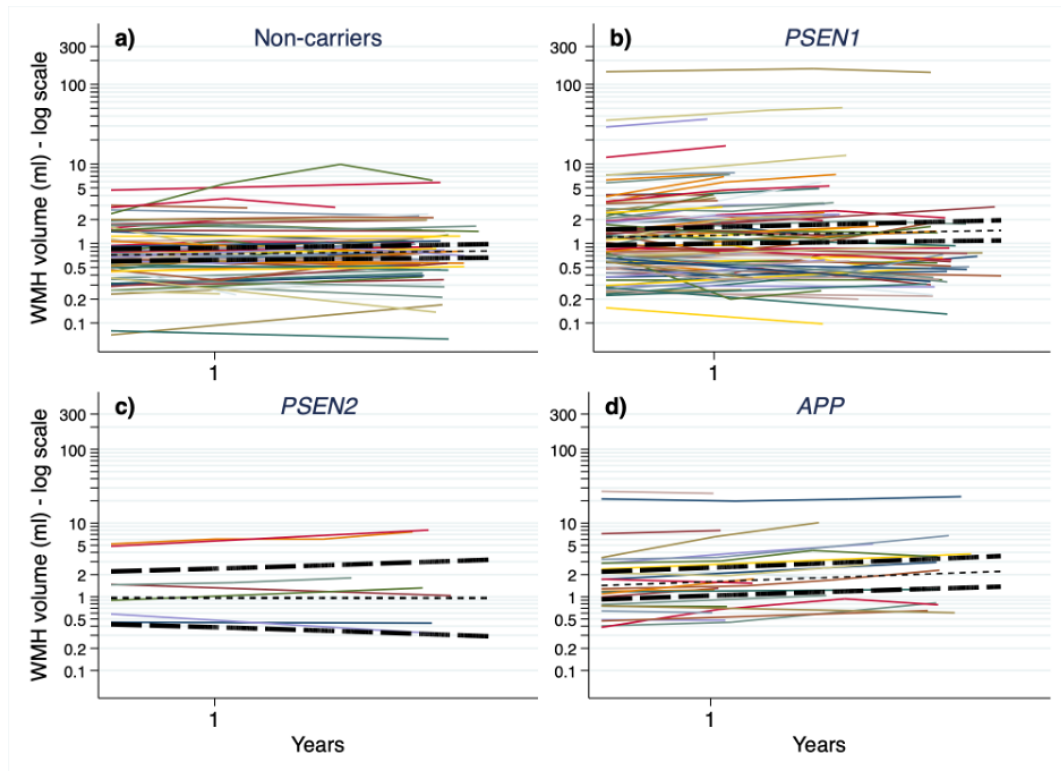


Figure 5.4: Plots showing WMH change over time for each participant (coloured lines) with fitted lines (black) in a) non-carriers, b) *PSEN1*, c) *PSEN2* and d) *APP* mutation groups. Fitted lines (with 95% confidence intervals) are from mixed models relating WMHs to time, for a participant with the overall mean TIV. All graphs have been truncated at 4 years and only the first year is displayed on the axis to ensure anonymity of participants.

stricted to those without symptoms, statistically significant increases were observed in the *APP* group, with a 13.3% increase in WMHs per year. These results were not materially changed with allowance for, and standardisation to the mean, age. Again, there was evidence for a significant variation amongst the groups ($p < 0.001$) that was driven by the higher rate of accrual in the *APP* group and not materially changed with age adjustment. No significant difference was observed in WMH change between the *PSEN1* pre-codon 200 and post-codon 200 mutation groups ($p = 0.4$).

5.2.3 WMH change over time by symptom group

Table 5.6: Regression model results for the mean change in WMHs over time, in each symptom group

	Non-carriers	P-Sym	Q-Sym	Sym	<i>p</i> value across groups*
Analysis allowing rates of change to depend on TIV					
% increase in WMHs per year at overall mean TIV	3.3	2.2	7.8	25.4	<0.001
95% confidence intervals	(0.5 to 6.1)	(-1.4 to 5.9)	(1.2 to 14.8)	(17.3 to 34.3)	
<i>p</i> value	0.02	0.2	0.02	< 0.001	
Analysis allowing additional dependency on age					
% increase in WMHs per year at overall mean TIV	3.6	3.9	6.4	26.7	<0.001
95% confidence intervals	(0.8 to 6.5)	(0.4 to 8.0)	(0.1 to 13.1)	(15.7 to 38.7)	
<i>p</i> value	0.01	0.05	0.05	< 0.001	

Fitted percentage increases (with 95% confidence intervals and *p*-values) in WMH volume per year. Results are assessing WMH change in each symptom group, allowing for dependency of baseline values and rates of change on TIV, and then additionally on age.

* Assumes effects of TIV on slopes and intercepts are the same in each mutation group.

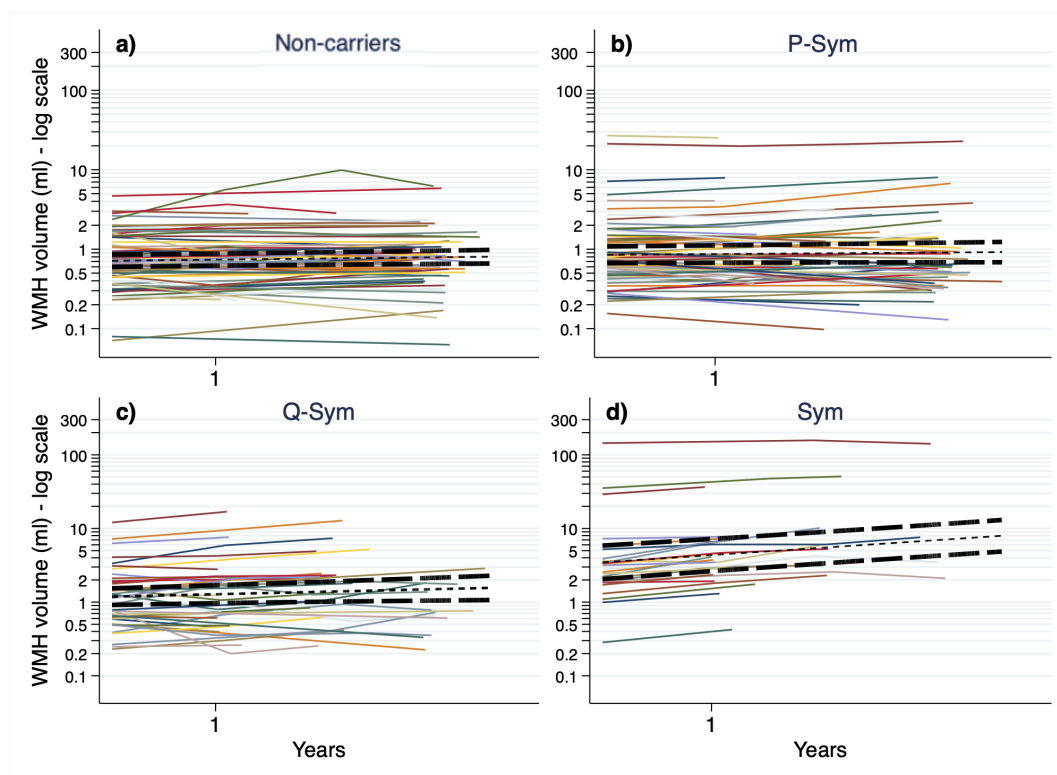


Figure 5.5: Plots showing WMH change over time for each participant (coloured lines) with fitted lines (black) in a) non-carriers, b) P-Sym, c) Q-Sym and d) Sym mutation groups. Fitted lines (with 95% confidence intervals) are from mixed models relating WMHs to time, for a participant with the overall mean TIV. All graphs have been truncated at 4 years and only the first year is displayed on the axis to ensure anonymity of participants.

Table 5.6 demonstrates symptom group differences in WMHs increase per year, with Figure 5.5 showing the corresponding plots. Significant percentage increases in WMHs per year were observed with increasing magnitude across non-carrier (3.2%), Q-Sym (7.8%) and Sym (25.4%) groups, and remain unchanged after adjustment for age. A non-significant association was observed in the P-Sym group, but this reached borderline significance when adjusting for age.

5.2.4 WMH change and associations with estimated years to onset

From models which assumed linear increases in WMH volume with estimated years to onset, statistically significant increases were observed in the *PSEN1* and *APP* groups, with estimated mean increases in WMHs per year (for participants with mean TIV) of 4.6% ($p=0.02$) and 12.7% ($p<0.001$) increase in WMHs per year,

Table 5.7: Regression model results for the relationship between WMHs and estimated years to onset, in each mutation group

	Estimated years to onset	% change in WMHs per 1 year	95% confidence intervals
<i>PSEN1</i>	-10 to -5	2.8	-0.9 to 6.7
	-5 to 0	5.6	1.9 to 9.5
	0 to 5	8.4	3.8 to 13.3
	5 to 10	11.4	5.2 to 17.8
	10 to 15	14.3	6.4 to 22.9
<i>PSEN2</i>	-10 to -5	1.3	-8.5 to 12.2
	-5 to 0	5.7	-5.3 to 17.9
	0 to 5	10.2	-2.8 to 25.0
	5 to 10	15.0	-0.8 to 33.3
	10 to 15	19.9	0.8 to 42.6
<i>APP</i>	-10 to -5	12.2	6.4 to 18.3
	-5 to 0	14.3	8.1 to 21.0
	0 to 5	16.5	8.6 to 25.1
	5 to 10	18.8	8.4 to 30.1
	10 to 15	21.0	7.9 to 35.7

Estimates are shown as % change per year in WMHs for successive 5-year intervals relative to estimated onset, calculated from separate linear mixed models in each mutation group. Estimates are shown at overall mean TIV.

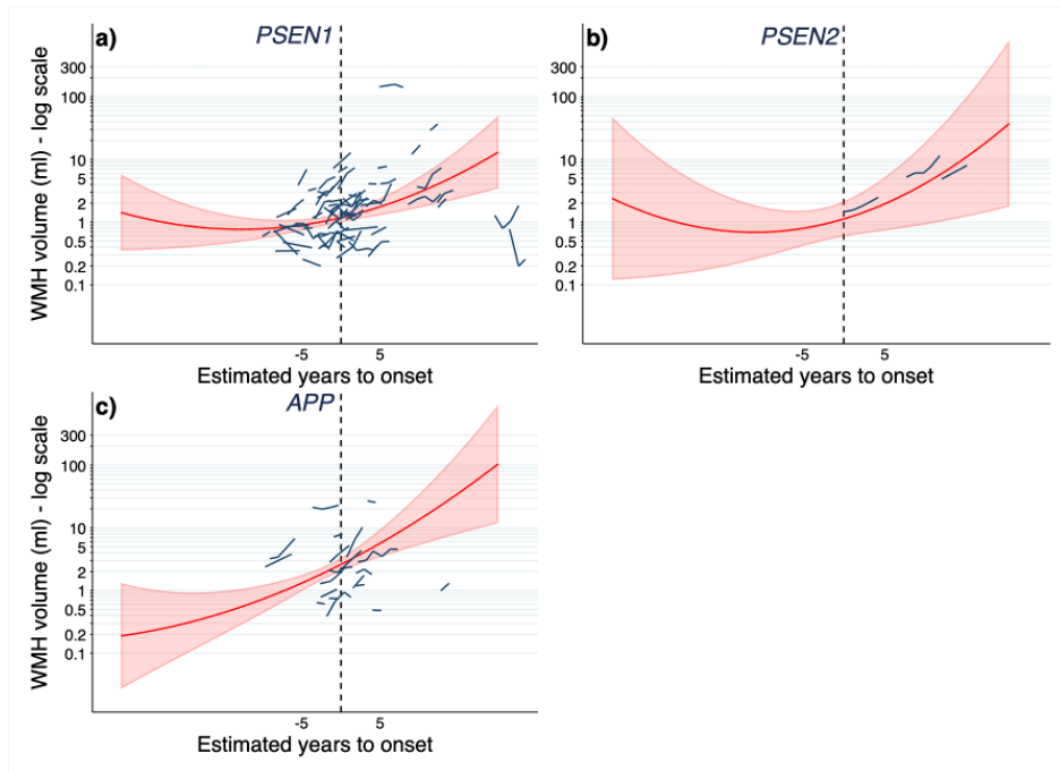


Figure 5.6: Plots of WMH accrual with estimated years to onset in each mutation group. Fitted mean lines from a mixed model (described in text and shown in red, with 95% confidence intervals), are overlaid onto each mutation group graph. Participants with an EYO less than -10 were excluded from these graphs, but not the models, to ensure anonymity.

respectively. From models with quadratic terms, there was also evidence for an acceleration in WMH accrual with increasing EYO in the *PSEN1* ($p=0.005$) and *PSEN2* groups ($p=0.01$) with a non-statistically significant ($p=0.2$), but directionally consistent effect seen in the *APP* group. Annualised percentage increases in WMHs in 5-year EYO intervals were calculated from these models and are displayed in Table 5.7. Because of the estimated acceleration, percentage increases in WMHs became greater every 5 year increase in EYO; in the *PSEN1* group this ranged from a 2.8% average increase per year at 10 to 5 years prior to onset, to a 14.3% increase at 10 to 15 years post onset; in the *PSEN2* group this ranged from a 1.3% average increase per year at 10 to 5 years prior to onset, to a 19.9% increase at 10 to 15 years post onset; in the *APP* group this ranged from a 12.2% average increase per year at 10 to 5 years prior to onset, to a 21.0% increase at 10 to 15 years post onset. Figure

5.6 shows line plots for individual WMH change with estimated years to onset, with fitted lines for each mutation group.

5.2.5 Jointly modelling brain volume and WMH changes

Figure 5.7 shows scatter plots of participant-specific rates of change in WMHs and brain volume for each mutation group, colour coded for symptom group. Correlation coefficients between the rates were between 0.50 and 0.66. After adjusting for time relative to expected onset and for TIV, partial correlation coefficients were calculated at 0.44 ($p<0.001$), 0.55 ($p=0.3$) and 0.48 ($p=0.01$) for *PSEN1*, *PSEN2* and *APP* group respectively. After excluding the 17 participants in the *PSEN1* group, 1 participant in the *PSEN2* group and 8 participants in the *APP* group in the ‘artefact’ group, the correlation coefficients increased to 0.52 ($p<0.001$), 0.82 ($p=0.04$) and 0.70 ($p<0.001$) respectively. The partial correlation coefficients also increased

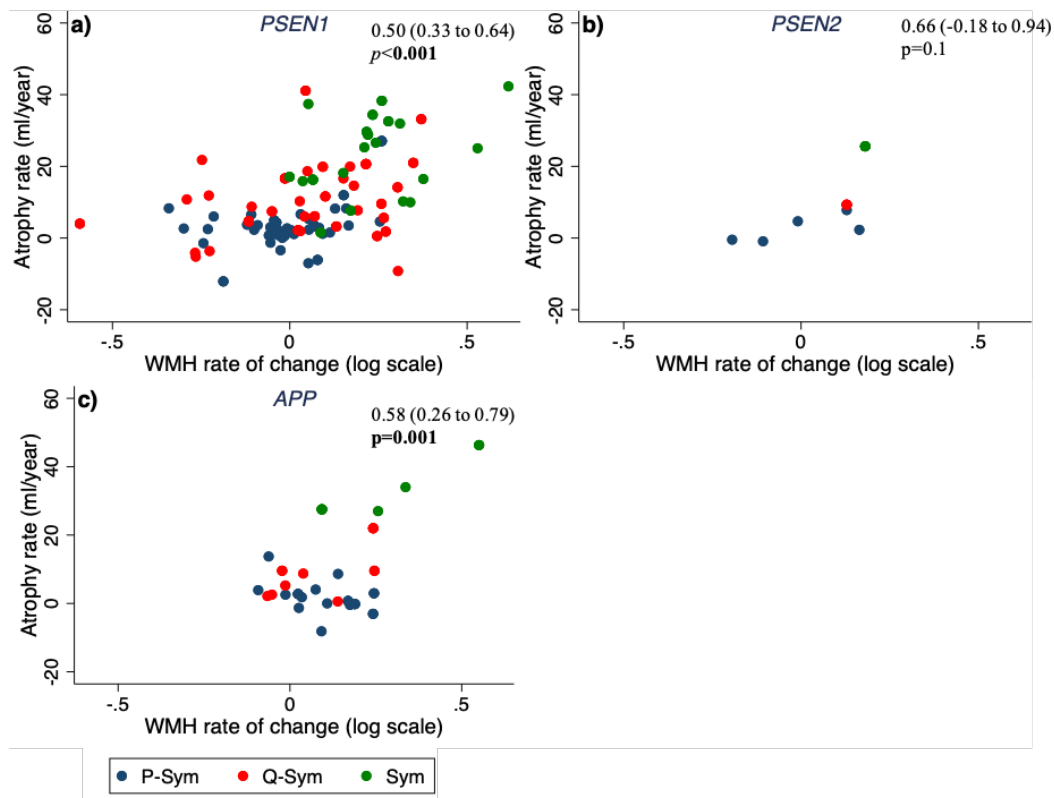


Figure 5.7: Scatter plots showing the crude relationship between atrophy rate and WMH accrual rate for a) *PSEN1*, b) *PSEN2* and c) *APP*, colour coded by symptom status. Displayed on the graph are Pearson correlation coefficients (with 95% confidence intervals and p values).

to 0.47 ($p < 0.001$) and 0.64 ($p = 0.006$) in the *PSEN2* and *APP* respectively, but decreased to 0.36 ($p = 0.6$) in the *PSEN2* group.

5.3 Discussion

This study found that mutation type was an important predictor of WMH accrual in ADAD with individuals with *APP* having the highest rates, even in those without symptoms. There were relationships between WMH volume and distance to estimated age of onset in *PSEN1* and *APP* mutation groups, with evidence of an acceleration as estimated onset is approached and passed in the *PSEN1* and *PSEN2* groups. There was also evidence that WMH accrual is highly associated with progressive brain atrophy, even after allowing for the stage of disease.

The fact that WMHs are associated both with brain atrophy and with EYO in *APP* and *PSEN1* groups, highlights that WMHs accrual is an important biomarker in ADAD that can be tracked throughout the disease course. This is also demonstrated by the large increase in WMHs observed in the symptomatic disease group. This is in agreement with previous studies in late onset sporadic AD that have implicated WMHs as core features of AD, associating with progression of disease and clinical symptoms (Brickman et al., 2015, Prins and Scheltens, 2015, Silbert et al., 2012) and with the hallmark AD pathologies of $A\beta$ (Bos et al., 2017, Walsh et al., 2020), tau (McAleese et al., 2015, Tosto et al., 2015) and brain atrophy (Barnes et al., 2013, Fiford et al., 2017, Schmidt et al., 2005).

There have been very few studies investigating WMHs in ADAD, a younger patient group in whom any changes seen are more likely to be the result of AD pathology and relatively unaffected by age-related co-morbidities. Lee et al. (2016) showed that in a cross-sectional study of the DIAN cohort, mutation carriers had a greater WMH burden than non-carriers, which appeared to increase 6 years before expected symptom onset (22 years in posterior regions). Furthermore, this same research group demonstrated that WMHs in ADAD may be independent of vascular $A\beta$ deposition as CAA (Lee et al., 2018). This was based on their observation that cerebral microbleeds, an imaging marker of CAA, contribute to but do not fully

explain the association between WMH and mutation carrier status. Another smaller cross-sectional study by Ryan et al. (2015) showed increased WMH in symptomatic individuals carrying *PSEN1* mutations located post-codon 200, and demonstrated an association between WMH burden and severity of CAA and cotton wool-type amyloid plaques postmortem. There have been several diffusion imaging studies that have investigated white matter involvement in ADAD (Ringman et al., 2007, Ryan et al., 2013, Sánchez-Valle et al., 2016), of which the largest and most comprehensive showed increases in mean diffusivity 5-10 years before estimated disease onset, with global mean diffusivity correlated with lower levels of A β 1-42 but higher levels of tau, phosphorylated-tau and soluble TREM2 in the CSF (Araque Caballero et al., 2018).

The highest rate of WMH accrual was seen in the *APP* group, which demonstrated faster increases in volume than the non-carrier and *PSEN1* groups, even in those without symptoms. The *APP* group also showed a 12.7% linear increase in WMHs per year increase in EYO, over double that of the *PSEN1* group (4.6%). When allowing for acceleration, this higher rate in the *APP* group is evident at all 5 year intervals of EYO. The acceleration of WMH accrual seen in the *PSEN1* and *PSEN2* mutation groups (but not *APP*) with proximity to estimated disease onset is also suggestive of variability in WMHs development according to mutation type.

Heterogeneity is present in many aspects of ADAD, with differences observed genetically and clinically, but also at a histopathological and molecular level. Along with the characteristic amnesia, patients can present with atypical symptoms such as behavioural and language features, spastic paraparesis, seizures and extra pyramidal and cerebellar signs (Ryan and Rossor, 2010, Ryan et al., 2016). Different mutations influence the production of A β in various ways, with some increasing overall A β 42 deposition, some increasing the ratio of A β 42/40 and some enhancing A β protofibril formation (Nilsberth et al., 2001, Ryan and Rossor, 2010). Pathological findings have also demonstrated variability in neuronal loss, tau tangle load and the type, distribution and size of A β plaques (Maarouf et al., 2008, Shepherd et al., 2009). This considerable heterogeneity within ADAD suggests that many factors

could be influencing the variability in WMH accrual that was observed between mutation groups.

Certain *APP* mutations, particularly those located in the $A\beta$ coding region, typically have severe CAA and can present with haemorrhage as well as dementia, potentially underlying a greater WMH presentation. These mutations include the Arctic (p.Glu693Gly), Dutch (p.Glu693Gln), Flemish (p.Ala692Gly), and Iowa (p.Asp694Asn) mutations (Revesz et al., 2009, Shepherd et al., 2009). In this study there were 11 participants with such *APP* mutations (out of 27 *APP* carriers), however all were in the presymptomatic stages of disease, making it difficult to draw any conclusions about whether the higher rates of WMH accrual over time in the *APP* group is at least in part driven by these mutation carriers. Variability in WMH presentation within *PSEN1* mutation carriers has been demonstrated previously, whereby symptomatic *PSEN1* mutation carriers with a mutation after codon 200 had more severe WMHs (Roks et al., 2000, Ryan et al., 2015, van Rooden et al., 2016). The study by Ryan et al. (2015) had been motivated by an earlier pathology study demonstrating more severe CAA in *PSEN1* mutations located post-codon 200 (Mann et al., 2001). However, I did not find any differences between pre-codon 200 and post-codon 200 *PSEN1* mutation carriers in the accrual of WMHs.

The variability in $A\beta$ pathology with different mutations could be a factor in the WMH accrual heterogeneity seen in this study. I and others have previously described close associations between $A\beta$ and WMHs (Lee et al., 2016, Pietroboni et al., 2018, Walsh et al., 2020, Zhou et al., 2015) and therefore it could be hypothesised that heterogeneity in $A\beta$ pathology could underlie variations in WMHs. One proposed mechanism behind this association is that $A\beta$ deposited in blood vessel walls as CAA could lead to hypoperfusion and ischaemia, resulting in the appearance of white matter lesions (Grinberg and Thal, 2010, Hawkes et al., 2014, Weller et al., 2008). In addition to the vascular origin of WMHs, there is recent evidence to suggest that they could be a result of degenerative axonal loss caused by AD pathology (McAleese et al., 2015, 2017).

In this study, strong correlations between WMH accrual and progressive brain

atrophy were found, suggesting that WMH burden and brain atrophy track together across the disease course. Associations between baseline WMHs and longitudinal atrophy of the whole brain (Barnes et al., 2013, Enzinger et al., 2005, Schmidt et al., 2005) and hippocampus (Fiford et al., 2017) have previously been demonstrated in LOAD. An association between WMH change and longitudinal atrophy has also been shown (Schmidt et al., 2005). There are multiple proposed models that could explain this co-relationship. One possibility is that WMHs and brain atrophy are temporally-associated outcomes of separate pathways; the vascular nature of WMHs is well documented (Prins and Scheltens, 2015, Wardlaw et al., 2013), as is the effect of AD pathology on axonal loss and subsequent atrophy (La Joie et al., 2020, Ossenkoppele et al., 2019, Spillantini and Goedert, 1998). Alternatively, either vascular risk factors or AD pathology could be independently causing both WMHs and brain atrophy. From the vascular perspective, SVD-related hypoperfusion could independently be resulting in lesions in the white matter (visible as WMHs), but also neuronal loss in the grey matter (Zlokovic, 2011). From the perspective of AD pathology, as well as $A\beta$ and tau-related cortical degeneration, it has recently been shown that AD pathology is associated with axonal degeneration in the white matter (McAleese et al., 2015, 2017). An additional possibility is that they occur as serial events, whereby either vascular-related damage to the white matter could result in neuronal degeneration (Erten-Lyons et al., 2013), or neurodegenerative changes secondarily induce WMHs (Ihara et al., 2010). In LOAD, the evidence suggests that both vascular risk factors and degeneration due to AD pathology are important factors in the associations between WMHs and brain atrophy. However, in this study of a young ADAD cohort with likely little age-related vascular co-pathology, it seems more likely that WMHs and brain atrophy increase together as a result of progressive AD pathological processes.

There are several limitations to this study. First, the *PSEN2* group had a very small number of participants, which, although is to be expected due to the very rare nature of *PSEN2* mutations, meant that several analyses were unable to be performed and was probably a significant factor in the non-significant results obtained

in this group. Secondly, only thick-slice FLAIR imaging was available for this cohort and so future improvements to this study may be possible with the use of volumetric FLAIR imaging, which can provide more precise measures of change. Regional changes in WMHs, which may be more sensitive biomarkers than a measure of total WMHs, were also not looked at. Additionally, we did not investigate $A\beta$ and tau levels in this study, and how they may relate to WMHs or brain atrophy change. Although this study demonstrates the tracking of WMHs and brain atrophy over time, the correlation of residual changes may be in part caused by other scanner-related or biological factors affecting both WMHs and atrophy measures but unrelated to the processes of interest. These results also depend upon the accuracy of EYO, which although has previously been shown to be strongly associated with actual age at onset, there can be substantial within-family and within-mutation differences (Ryman et al., 2014). Finally, one statistical limitation surrounds the use of our linear mixed models with quadratic terms to provide evidence of acceleration in the rate of change with time relative to expected age of onset. Addition of quadratic terms to regression models facilitate testing for acceleration (or deceleration) but since all accelerating quadratic curves must have a minimum value they should not be taken to provide evidence of decreasing levels of WMHs many years prior to onset, see Goetghebeur and Pocock (1995) for a discussion of the limitations of quadratic curves in detecting J-shaped relationships.

In conclusion, an increase in WMH burden was observed with increasing proximity to onset and that WMH accrual tracks together with brain atrophy across the disease course. Moreover, this study has demonstrated that mutation type has an impact on WMH accrual, highlighting how mutation differences contribute to the heterogeneity observed in ADAD. Although WMHs are common in normal ageing and are often directly attributed to age-related vascular disease, dysfunction and events, this study in a young ADAD cohort demonstrates that WMHs are a core feature of AD and could be an important biomarker of disease progression.

Chapter 6

Pathological investigations of WMHs using *ex vivo* MRI with histological correlations

6.1 Introduction

MRI markers are often non-specific and can be related to heterogeneous changes in tissue as a result of disease. One such marker are WMHs, where numerous histopathological correlates have been suggested from a relatively small body of literature (Fazekas et al., 1993, Gouw et al., 2008a, 2011, Murray et al., 2012). There is a need to identify the specific pathological underpinnings of any signal change observed on MRI, something which can potentially be achieved through joint MRI-pathology studies.

Ex vivo MRI can provide an essential link between *in vivo* imaging and pathological analysis, as the last available *in vivo* MRI scan may be obtained many years before the patient comes to *post mortem*, during which time the location and severity of brain changes could have changed quite considerably. Additionally, *ex vivo* MRI scanning enables high resolution images in multiple modalities to be obtained, as time limitations for scanning a *post mortem* sample compared to a patient are greatly reduced. There are important considerations though relating to the differences between scanning tissue and scanning a patient in life. The lower temperature

of the *post mortem* brain and the tissue fixation process requires MRI parameters to be adapted accordingly (Birkel et al., 2014, Richardson et al., 2014, Shatil et al., 2018). Further, the tissue can be distorted as a result of extraction from the skull and fixation.

There have been previous MRI-pathology studies of WMHs, but these have used a variety of methodologies and have suggested a broad range of pathological correlates. Due to the large amount of variation in findings from a relatively small number of studies, a systematic literature review has been carried out to better understand the current research landscape and to identify knowledge gaps.

6.1.1 Literature review: *ex vivo* MRI-histology correlations in the study of WMHs

Studies that have correlated *ex vivo* MRI to histopathology of WMHs are summarised in Table 6.1. The older *ex vivo* MRI and histopathology studies are small and descriptive and mainly use histological staining, as opposed to immunohistochemistry. They have proposed a large number of pathological correlates of WMHs in AD, VaD and controls, namely a loss of myelin, axons and oligodendrocytes, astrogliosis, dilation of perivascular spaces, activated macrophages and fibrohyalinotic and arteriosclerotic vessel changes (Awad et al., 1986, Braffman et al., 1988, Fazekas et al., 1991, Mascalchi et al., 1989, Revesz et al., 1989, van Swieten et al., 1991). The degree of neuropathological changes range from mild myelin pallor (without actual loss) likely due to an increase in water content or oedema (Fazekas et al., 1993, Moody et al., 2004, Munoz et al., 1993), to more overt degenerative changes that include loss of myelin, oligodendrocytes and axons (Awad et al., 1986, Mascalchi et al., 1989) with gliosis and infarction in the most severe cases (Marshall et al., 1988). The changes are often reported to be perivascular and surrounded by enlarged perivascular spaces (Fazekas et al., 1991, Revesz et al., 1989).

Table 6.1: Studies using *ex vivo* MRI-histology correlation to characterise WMHs

Reference	Subjects	Histo chemistry	Immuno histochemistry	MRI	Registration technique	Main findings
Awad et al. 1986	7 controls	H&E, LFB	GFAP	1.5T, whole brains	Visual matching guided by anatomy.	WMHs reflect enlarged perivascular spaces, vascular ectasia, axonal degeneration, gliosis.
Englund et al. 1987	21 AD, 19 elderly with infarcts	H&E, LFB	-	0.25T, brain blocks	Brain cut into blocks prior to imaging, allowing sectioning/staining of same overall region	T1 and T2 relaxation times reflect tissue damage in WMH.
Marshall et al. 1988	16 controls	H&E, Congo Red, Alcian Blue, LFB	GFAP, IgG, albumin	0.35T, whole brains	Visual matching guided by anatomy.	WMHs correspond to intermediate and old infarctions: - Intermediate: necrosis, minimal cavitation and gliosis - Old: cavitation, demyelination, fibrohyalinosis, reactive astrocytes (believed to symbolise blood-brain barrier leakage).
Braffman et al., 1988	23 controls with and without neurological symptoms	H&E, Weil, LFB, Bodian	-	1.5T, whole brains	Visual matching guided by anatomy.	WMH pathology ranges from subtle gliosis and demyelination to infarction.

Mascalchi et al. 1989	1 VaD	H&E, Woelke, Congo Red	-	0.5T, whole brains	Visual matching guided by anatomy.	Case report: WMHs reflect demyelination, axonal loss, astrogliosis, oligodendroglial swelling, a few macrophages and slight oedema. Arterial/arteriolar wall changes. Some CAA.
Revesz et al. 1989	4 VaD	H&E, KB, Nissl, Holzer axons, cresyl violet, EvG, Heidenhain's myelin, Bielschowsky, PTAH	-	0.5T, brain slices	Whole scanned slices were stained, so overall regions were the same in both modalities	Vascular wall changes (arteriosclerosis) and enlarged perivascular spaces.
van Swieten et al. 1991	Mixed cohort – 23 cardiovascular disease, 9 infectious disease, 6 cancer in 6, and 2 miscellaneous.	H&E, LFB, Weil, EvG, PTAH, PAS, Congo Red, Bodian	-	1.5T, whole brains	Visual matching guided by anatomy.	WMHs correspond to demyelination, gliosis and arteriosclerotic changes. Arteriolar wall thickening.
Fazekas et al. 1991	2 controls, 4 controls with neurological symptoms	H&E, Masson's trichrome, KB	-	1.5T, whole brains	Brains cut parallel to imaging plane to aid visual matching guided by anatomy.	Spectrum of perivascular damage - fibrohyalinosis, atrophy of neuropil surrounding arteries and demyelination

Grafton et al. 1991	4 controls, 3 AD	LFB-PAS, Holzer astrocytes, Holmes, gallo-cyanin	GFAP	0.15T, whole brains	Use of "miter box" with ferrous localising markers to match MRI and brain slices in the coronal plane.	<ul style="list-style-type: none"> - PWMHs: myelin pallor, gliosis and widened perivascular spaces. - DWMHs: no correlation with any neuropathological measure.
Chimowitz et al. 1992	7 controls	KB, Congo red, desmin	GFAP	1.5T, whole brains	Brains cut in same plane as MRI to aid visual matching guided by anatomy.	<ul style="list-style-type: none"> - PV rims: ependymal loss and subependymal gliosis. - PV caps: myelin pallor. - Punctate DWMHs: widened perivascular spaces.
Fazekas et al. 1993	Mixed cohort - 5 brain tumour, 4 CVD, 1 psychosis, 1 cervical myelopathy.	H&E, Masson's trichrome, KB	-	1.5T, whole brains	Brains cut in same plane as MRI to aid visual matching guided by anatomy.	<ul style="list-style-type: none"> - Smooth PVWMHs: non ischaemic and correlated with demyelination, gliosis and discontinuation of ependymal lining. - Irregular PVWMHs: varying fibre loss, gliosis and cavitation, fibrohyalinosi - Punctate DWMHs: no ischaemic changes, demyelination, atrophic neuropil around fibrohyalintic arterioles and perivenous damage. - Early confluent DWMHs: perivascular rarefaction of myelin, mild-moderate fibre loss, varying gliosis. - Confluent DWMHs: ischaemic tissue damage, irregular areas of incomplete parenchymal destruction

Munoz et al. 1993	2 AD, 13 controls	H&E, chromoxane cyanin, Bielschowsky, Congo red	-	1.5T, Whole brain (minus cerebellum)	Histological regions were chosen on the basis of the MRI measurements in millimeters from the coronal plane	Extensive DWMHs: myelin, axonal and glial cell loss, and spongiosis. No infarction or vascular wall changes. Punctate WMHs: dilated perivascular spaces. - PVWMHs: atherosclerotic changes, vacuolisation of the myelin, neuropil and discontinuous ependymal lining associated with fibrous gliosis. - DWMHs: vacuolated myelin around atherosclerotic arteries/arterioles, widened perivascular spaces with degenerated myelin and recent infarction. PVL/focal DWMHs no clinical consequences, whereas confluent DWMHs are potentially pathological.
Scarpelli et al. 1994	16 controls, 5 with neurological disturbances	H&E, LFB	GFAP	1.0T, whole brains	Visual matching guided by anatomy.	
Scheltens et al. 1995	6 AD, 9 controls	HE, PTAH, KB, Bodian, EvG, Congo Red	-	0.6T, whole brains	Brains cut in same plane as MRI to aid visual matching guided by anatomy.	WMHs associated with loss of myelinated axons, gliosis and denudation of ventricular ependyma. AD group showed more extensive WMHs than controls.
Smith et al. 2000	12 unspecified	LFB	-	Whole brains	Visual matching guided by anatomy.	Extent of PVWMHs on MRI correlates well with extent of WM pathology. PVWMHs appear to be related to myelin loss, not gross evidence of ischemia.

Bronge et al. 2002	6 AD	LFB	-	1.5T, Whole brains (left hemisphere in one case)	Brains cut in same plane using same slice thickness as MRI to aid visual matching guided by anatomy.	Regions of WM pathology, but no WMHs: lower myelin density, loose but intact fibre network, normal glial density. Regions of WM pathology and WMHs: myelin/ axonal loss, irregular and fragmented axons, vacuolation, decreased cell density, dilated perivascular spaces, smooth muscle degeneration. No gliosis/ infarction.
Englund et al. 2004	2 AD	LFB	-	3.0T, QMRI, whole brains	Visual matching guided by anatomy.	<i>ex vivo</i> DTI is feasible in fixated brain specimens. DTI measures in WMH correlates with severity of myelin loss.
Moody et al. 2004	21 controls	Alkaline phosphatase, Congo red, Masson trichrome,	-	1.5 T, frontal brain slice	Whole scanned slices were stained, so overall regions were the same in both modalities	WMH correlates with decreased vascular density (arteries/arterioles/capillaries).
Fernando and Ince 2004	16 controls, 17 AD + VaD	HE, LFB/Loyez method	CD68, collagen-IV, 1.0T ICAM-1	1.0T, One hemisphere cut into slices in a slice stack	Whole scanned slices were stained, so overall regions were the same in both modalities	MRI at 1.0- tends to underestimate mildly the prevalence of WM changes demonstrated by histology

Fernando et al. 2006	99 demented, 108 controls	H&E, LFB	CD68, Col IV, ICAM1, HIF1 $\alpha/2\alpha$, MMP7, Ngb, NMBR, VE-FGR2, β A4	1.0T, One hemisphere cut into slices in a slice stack box	Whole scanned slices were stained, so overall regions were the same in both modalities	<p>Vascular changes in WMHs: wall thickening, dilated perivascular spaces.</p> <p>- PVWMHs: Denudation of ventricular lining in WMHs related to increased fluid accumulation.</p> <p>- DWMHs: higher capillary network density, microglial activation, upregulation of hypoxia factors.</p> <p>- Both DWMHs and PVL: upregulation of MMP7. No differences demented and non-demented subjects.</p>
Larsson et al. 2004	1 FTD	H&E, LFB		3.0T, QMRI, whole brains	Visual matching guided by anatomy.	<p>The area of DTI changes was more extensive than WMH areas on conventional MRI. WMHs correlates with gliosis and demyelination.</p>
Simpson et al. 2007a	Tissue blocks (14 PV WMHs from 12 cases, 15 DWMHs from 12 cases and 15 NAWM), with a mixture of diagnoses	H&E, LFB	MBP, GFAP, CD68, PDGF α R, MAP-2, fibrinogen	1.0T, coronal slices	Visual matching guided by anatomy.	<p>PV and DWMHs have severe myelin loss and increased microglia (CD68). Plasma-todendritic astrocytosis, positive for serum proteins suggesting BBB dysfunction</p> <p>- PVWMHs: Denudation of ependymal lining. Severe myelin loss and reactive astrocytes beneath ependymal lining. Attempts at remyelination with OPC response.</p> <p>- DWMHs: Higher microglial response.</p>

Simpson et al. 2007b	Tissue blocks	-	HLA-DR, B7-2, CD40, Mcm2, PCNA, Ki67	1.0T, coronal slices	Visual matching guided by anatomy.	Microglial responses: - PVWMHs: more MHCII positive microglia and costimulatory B7-2 and CD40, suggesting a more proliferative/immune re-active environment. Could be as a result BBB disruption. -DWMHs: amoeboid microglia for phagocytosis of myelin breakdown products.
Young et al. 2008	20 subjects with mixed diagnoses	H&E, PAS, Weil	dMBP, CD31, GFAP, 3.0T hGLUT-5, APP, HLA-DR, P-gp, IgG	3.0T, whole brains	Visual matching guided by anatomy.	Loss of vascular integrity and a loss of BBB in WMH areas. No single pathological correlate corresponds to WMH severity (e.g. myelin, microglia)
Gouw et al. 2008a	11 AD, 7 controls	H&E, LFB-CV, Bodian	GFAP, HLA-DR	1.5T, QMRI, One hemisphere cut into slices in a slice stack box	Brain slices were cut until halfway to reveal the centre of the imaged plane on which the ROIs were defined. This way, the brain slices could be reliably matched to the MR images.	WMHs have loss of myelin and axons and astrogliosis in both groups. WMHs in AD group also has more microglia activation. Quantitative MRI: Distinguishes WMHs from AD and control and correlates with severity of changes. Axonal density predicts FA in DTI, axon/myelin density and microglial activation predicts T1 relaxation.

Polvikoski et al. 2010	15 controls, 34 borderline AD, 30 AD, 18 AD+, 35 other pathology	H&E, Bielschowsky	α -syn	Whole brains	No registration (cortical pathology burden assessed)	Frontal WMHs associated with Braak and CERAD score. Infarcts associated with DWMHs, but not PVWMHs.
Murray et al. 2012	4 controls	H&E, LFB	MBP, phosphorylated neurofilament, GFAP, IBA1 and collagen.	3.0T, QMRI, left hemispheres	Overlaid FLAIR slices and autopsy photographs to identify WMH ROI on FLAIR slice and histological section	Vacuolation, myelin loss and SVD underlie both PVWMHs and DWMHs. PVWMHs also had higher astrogliosis, axonal loss and oligodendrocyte loss, and dilated perivascular spaces.
McAleese et al. 2015	23 AD, 13 controls	H&E	AT8, A β	4.7T, right hemisphere	No registration (cortical pathology burden assessed)	Tau pathology predicted severity of WMHs in frontal, temporal and parietal regions. More WMHs in AD compared to controls, but no differences in severity of SVD suggesting SVD is not underlying cause for WMHs in AD.
Hainsworth et al. 2017	47 controls, 69 dementia, 10 undetermined	-	Fibrinogen, IgG, CD68, smooth muscle actin, CD34	1.0T, One hemisphere cut into slices in a slice stack	Whole scanned slices were stained, so overall regions were the same in both modalities	Extent of fibrinogen labeling was not significantly associated with white matter abnormalities defined either by MRI or by histopathology.

Woollacott et al. 2018	1 FTD	H&E, LFB, Perl	TDP-43, AT8, A β , α -syn, SMI31, GFAP, CD68, CR3/43, Iba1	1.5T, cadaveric	Visual matching guided by anatomy.	Severe WMHs correlated with severity of demyelination and white matter gliosis. No significant axonal loss in WMH regions. Minimal vascular pathology observed - WMHs in GRN carriers are not secondary to vascular pathology.
Arfanakis et al. 2020	178 controls, 154 MCI, 271 dementia	Bielschowsky, H&E	TDP-43, A β	3.0T, one hemisphere	No registrations - overall burden of pathologies assessed.	A β plaques/arteriosclerosis/infarcts associated with higher WMHs burden across all groups, but only vascular pathologies associated in control groups. WMH burden associated with decline in perceptual speed. Longer interval between <i>in vivo</i> and <i>ex vivo</i> assessment associated with higher burden of WMHs in <i>ex vivo</i>
Roseborough et al. 2020	1 control, 1 AD, 1 CVD, 1 AD+CVD	H&E, LFB	Neurofilament	7.0T, one frontal coronal slice	Landmark registration of histological slices and scanned images	WMHs on 7T MRI reflects underlying pathology of myelin and axon density. Myelin content and a diagnosis of CVD were the most significant predictors of MRI white matter intensity.

Key: α -syn, alpha synuclein; APP, amyloid precursor protein; CD31, vascular integrity; CD40 and CD40 ligand, immune costimulatory molecules; DWMH, deep white matter hyperintensities; EVG, Elastic van Gieson; FTD, frontotemporal dementia; GFAP, glial fibrillary acidic protein; H&E, haematoxylineosin; hGLUT-5, human glucose transporter-5; HIF, hypoxia inducible factor; HL-A-DR, human leucocyte antigen-DR; ICAM1, intercellular adhesion molecule; IgG, immunoglobulin; KB, Klüver-Barrera; LFB, Luxol Fast Blue; LFB-PAS, Luxol Fast Blue/periodic acid-Schiff; MAP-2 +13, microtubule associated protein 2 expressing exon 13; MBP, myelin basic protein; Mcm2, MMP7, matrix metalloproteinase 7; NAWM, normal appearing white matter; Ngb, neuroglobin; NMBR, neuromedin B receptor; PCNA and Ki67, cell proliferation related molecules; PDGFR α , platelet derived growth factor receptor; P-gp, P-glycoprotein; PTAH, phosphotungstic acid haematoxylin; PVWMH, periventricular white matter hyperintensities; QMRI, (quantitative) MRI; VEGFR2, vascular endothelial growth factor receptor 2

Several studies have classified WMHs into different types based on their location in the periventricular region or deep white matter (Fazekas et al., 1993, Fernando et al., 2006, Grafton et al., 1991, Murray et al., 2012, Polvikoski et al., 2010, Simpson et al., 2007a, Young et al., 2008). Periventricular WMHs correspond with ependymal lining disruption in controls and/or AD (Fernando et al., 2006, Scarpelli et al., 1994, Scheltens et al., 1995, Simpson et al., 2007a); subependymal gliosis in controls (Chimowitz et al., 1992, Murray et al., 2012); widened perivascular spaces in controls and/or AD (Grafton et al., 1991, Murray et al., 2012); myelin pallor or loss in controls, AD and cohorts with multiple diagnoses (Scarpelli et al., 1994, Simpson et al., 2007a); and more MHCII positive microglia suggesting a more proliferative and immune reactive environment in a cohort with multiple diagnoses, including controls, AD, cardiovascular disease, cancer, and Parkinson's disease (Simpson et al., 2007b). In general, periventricular WMHs were less associated with ischaemic changes (Smith et al., 2000), although some studies have suggested a pathological distinction between smaller ventricular caps and the larger irregular periventricular WMHs that extend into the deep white matter (Chimowitz et al., 1992, Fazekas et al., 1993). It has been proposed that smaller and smooth periventricular caps are likely to be non-ischaemic and are caused by milder changes to the ependymal layer, whereas the latter correspond to more severe pathology such as complete myelin loss and reactive gliosis, sometimes in combination with fibrohyalinotic and arteriosclerotic vessels. Similarly, deep WMHs were suggested to be on a spectrum of tissue change, with punctate WMHs being associated with less severe damage than confluent WMHs (Fazekas et al., 1993, Scarpelli et al., 1994). Punctate, deep WMHs were suggested to be mild and related to enlarged perivascular spaces, whereas more confluent WMHs were associated with loss of myelin, axons and oligodendrocytes, astrogliosis and complete infarcts (Chimowitz et al., 1992, Fazekas et al., 1993).

Ex vivo MRI studies are often in small and mixed cohorts, making it difficult to draw conclusions about the pathological differences of WMHs in different disease groups. Studies commonly found WMHs to be more extensive in AD groups com-

pared to controls (McAleese et al., 2015, Polvikoski et al., 2010, Scheltens et al., 1995). The type of pathological correlate has reported to be comparable in some studies (Fernando et al., 2006, Scheltens et al., 1995), although some have reported that the resulting tissue changes are more severe in AD compared to controls (Scheltens et al., 1995). Pathological differences have been reported by some, with Gouw et al. (2008a) showing more microglia activation and distinct quantitative MRI measures (lower FA and higher T1 relaxation time) in the WMHs in AD compared to controls. The histopathological profile of WMHs was found to be comparable between AD and VaD patients (Englund, 1998) leading some to suggest that the two diseases are part of a pathological continuum (Fernando et al., 2006, Gouw et al., 2011).

More recently, studies have examined the pathogenic mechanisms that lead to the histological alterations described above. Combining *ex vivo* MRI with quantitative assessments of immunohistochemical staining, often in larger cohorts, has enabled more detailed investigations of the pathological basis of WMHs. An ischaemic hypothesis has been assessed by Fernando et al. (2006) where markers of hypoxia and alterations to vessel walls were found to be associated with WMHs. This agrees with previous studies demonstrating arteriolar tortuosity, arteriosclerotic changes to vessel walls and decreased vascular density (Fazekas et al., 1993, Moody et al., 2004, Revesz et al., 1989), supportive of an ischaemic pathogenesis of WMHs especially in the deep white matter.

Blood-brain barrier dysfunction has also been shown to underlie a proportion of WMHs. The presence of clasmotodendritic astrocytes that stain positive for the serum protein fibrinogen (Marshall et al., 1988, Simpson et al., 2007a) and the decrease in markers of vascular and blood-brain barrier integrity (Young et al., 2008) collectively suggests leakage of the blood-brain barrier. However a recent study by Hainsworth et al. (2017) of 126 control and dementia cases found that the extent of fibrinogen labelling was not significantly associated with WMHs. Several studies have also provided evidence that a disruption of the brain-CSF barrier is a potential mechanism of some WMHs. Loss of the ependymal lining of the ven-

tricles has been demonstrated to underlie periventricular WMHs, leading to severe subependymal myelin loss and dense gliosis (Fernando et al., 2006, Simpson et al., 2007a).

A number of *ex vivo* MRI studies have also assessed the role of cortical A β and tau deposition in WMH formation. McAleese et al. (2015) has demonstrated that tau pathology is predictive of WMHs. A very recent and very large study by Arfanakis et al. (2020) has demonstrated that A β plaques were associated with higher WMH burden in 603 control, MCI and AD cases. Although, the use of non-standardised pathology systems and the use of total (as opposed to regional) cortical pathology to assess associations with WMH, should be recognised as limitations to this study. Interestingly, both these studies found that vascular pathologies were less likely to be associated with WMHs in AD subjects.

The study by Arfanakis et al. (2020) also carried out an assessment of the differences between WMH detection on *in vivo* and *ex vivo* MRI, finding that a longer interval between scans was associated with higher burden of WMHs *post mortem*. This highlights the value of *ex vivo* MRI scans in elucidating the underlying pathology of WMHs, as it provides the most current picture of the intact brain. *In vivo* MRI-pathology studies have however provided useful insights into the pathology of WMHs, especially where the most recent *in vivo* scan was taken close to time of death. Moreover these studies often include greater numbers of subjects due to the more routine nature of conducting *in vivo* MRI in large cohorts and the ethical, logistical and image acquisition complexities of performing scans on either cadavers or brain tissue.

In vivo studies have been supportive of a loss of myelin (Erten-Lyons et al., 2013, Iordanishvili et al., 2019) and axons (Ryan et al., 2015) as a contributing factor to WMHs. Several studies have also provided evidence of a vascular origin, with associations of WMHs demonstrated with arteriosclerosis and other markers of CVD (Alosco et al., 2018, Erten-Lyons et al., 2013). Similarly to the regional differences demonstrated by the *ex vivo* MRI studies, microinfarcts and haemorrhages were shown to associate most strongly with deep WMHs (Shim et al., 2015). CAA

has also been demonstrated as a possible underlying cause of WMHs in individuals with ADAD (Ryan et al., 2015) and in patients admitted to hospital with intracerebral hemorrhage (Charidimou et al., 2016). Blood-brain barrier dysfunction has also been proposed as a core mechanism of WMH formation in *in vivo* MRI-pathology studies (Todd et al., 2018, Wardlaw et al., 2017). Multiple studies have suggested a role for ependymal dysfunction in the formation of periventricular WMHs (Anderson et al., 2014, Iordanishvili et al., 2019, Shim et al., 2015, Todd et al., 2018). In the most comprehensive investigation, Todd et al. (2018) recently demonstrated a link between lateral ventricle volume and periventricular WMHs, relating ventricular expansion to the replacement of the ependymal layer with astrocytic gliosis. Associations between the burden of AD pathology and WMHs have also been demonstrated (Alosco et al., 2018, Erten-Lyons et al., 2013), with several studies proposing the observed link is due to Wallerian degeneration of myelinated axons caused by AD pathology (Erten-Lyons et al., 2013, McAleese et al., 2017). Finally, an inflammatory basis has been proposed by Swardfager et al. (2017), whereby an increase in the peripheral inflammatory markers IL-1 β , IL-21, IL-10, IL-23 and TNF- α were shown to be associated with WMHs.

The *ex vivo* MRI studies described here have used a range of methodologies for matching up the WMHs seen on imaging to the corresponding region on the histological sections. Older studies have typically matched hyperintense regions of interest on the *ex vivo* MRI to histological sections using anatomical landmarks (Awad et al., 1986, Braffman et al., 1988, Marshall et al., 1988, Mascalchi et al., 1989, van Swieten et al., 1991). Brains are often cut in the same plane as the MRI slices and using the same slice thickness to aid alignment (Bronje et al., 2002, Chirmowitz et al., 1992, Fazekas et al., 1991, 1993). Some studies have used externally added visual markers to aid in the registration (Grafton et al., 1991, Munoz et al., 1993), or have used purpose built containers for scanning and subsequent coronal sectioning (Munoz et al., 1993). Other studies have carried out MRI scanning after the brain cutting procedure, so that the scanned brain slices could be sectioned for staining and therefore requiring no further registration (Fernando and Ince, 2004,

Fernando et al., 2006, Moody et al., 2004, Revesz et al., 1989). Murray et al. (2012) used autopsy photographs as an intermediate modality to which both MRI slices and brain slices could be registered. This method is an early iteration of the more complex registration techniques that are being developed with the assistance of sophisticated registration software to provide precise matching of histological sections to MRI images (Iglesias et al., 2018, Mancini et al., 2019, Pallegage-Gamarallage et al., 2018, Pichat et al., 2018). Several of the larger *ex vivo* MRI studies have not directly examined the pathology of specific white matter hyperintensities, instead assessing associations between the overall burden of WMHs and pathology (Arfanakis et al., 2020, McAleese et al., 2015), similar to the approach used in the majority of the *in vivo* MRI-histology studies (Alosco et al., 2018, Erten-Lyons et al., 2013, McAleese et al., 2017).

6.1.2 Gaps in the literature

The MRI-pathology studies described above demonstrated a large number of pathological correlates of WMHs. The cohorts were often small and only considered a limited number of pathologies each, meaning there was often little overlap in the markers assessed between studies. Additionally, the methodologies employed for *ex vivo* scanning and registration were variable and could further exacerbate discrepancies. Moreover, the registration techniques were generally not sophisticated enough to enable exact matching and full registration of the *in vivo* imaging, *ex vivo* imaging and histology was not carried out. It may be that the homogeneous signal on MRI scans is the result of such heterogeneous pathology, meaning that it is very difficult to conclusively find patterns in the data. It is clear then that there is a need to gain a greater understanding of whether any features of WMH appearance and/or location can pinpoint a particular pathological process.

6.1.3 Aims

With the above unmet needs in mind, this work will act as the first step towards the ultimate goal of being able to predict the underlying pathology of WMHs based on their appearance on clinical imaging. This ultimate goal would require the align-

ment of *in vivo* MRI, *ex vivo* MRI and histopathological images to elucidate whether there are distinct features of WMHs seen during life that translate to underlying pathology.

As this is a novel area of research, the work presented here can be considered a pilot study that was developed with scalability in mind. An in depth *ex vivo* MRI-histology pipeline was developed with the aim of answering the following questions:

- Question 1: Can high quality *ex vivo* MRI images be obtained?
- Question 2: Is registration of *in vivo* and *ex vivo* MRI scans possible?
- Question 3: Is registration of histological sections to *ex vivo* MRI images possible?
- Question 4: Can similarities or differences in WMHs between the last *in vivo* MRI and the *ex vivo* scan be observed?
- Question 5: Can any pathological changes be observed in regions of WMHs?

6.2 Methods

Due to the novelty of this work and the necessary involvement of multiple disciplines and collaborators in this project, a detailed pipeline was first developed to carefully coordinate the process of brain donation, *ex vivo* MRI scanning, brain sampling and histological staining, WMH segmentation, registration of the multiple modalities and analysis of histological staining. The finalised pipeline is displayed in Figure 6.1 and described below. The research outcomes of the pipeline that pertain to each of the questions listed above in section 6.1.3 are labelled on Figure 6.1 in red. The MRI imaging part of the pipeline was carried out in all five cases, however the brain sampling and histology protocol was only developed for the final four cases.

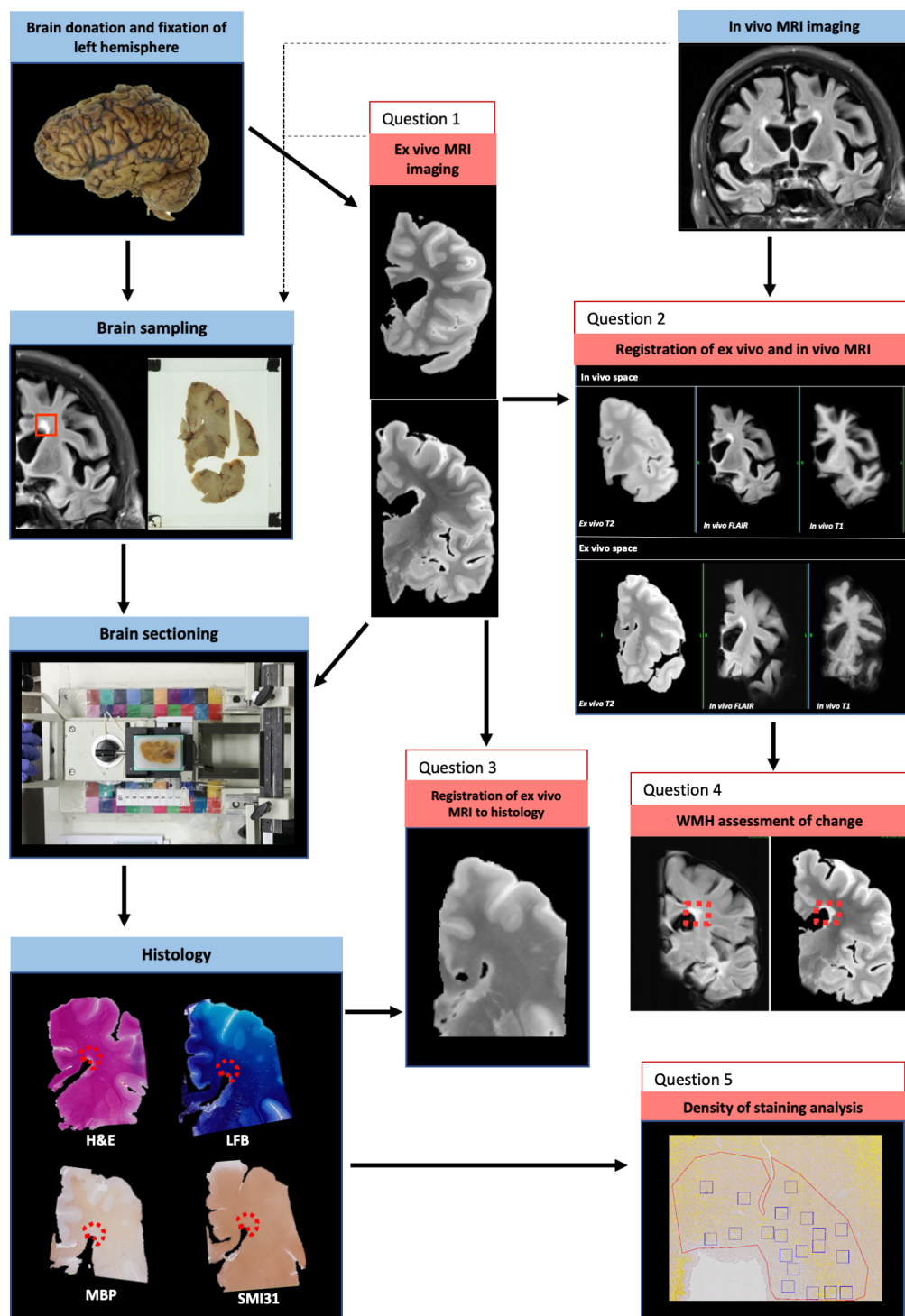


Figure 6.1: The full pipeline for the correlation of *ex vivo* imaging and histology

6.2.1 *In vivo* MRI imaging

Existing *in vivo* MRI imaging was used for all subjects in this study. These were obtained using the same 3 T Siemens TIM Trio scanner with a 32-channel phased array head-coil. A sagittal 3D MP-RAGE T1- weighted volumetric MRI (echo time/repetition time/inversion time = 2.9/2200/900 ms, dimensions of 256 x 256 x 208, voxel size of 1.1 x 1.1 x 1.1 mm) and a coronal T2 FLAIR sequence (echo time/repetition time/inversion time = 87/9000/2500 ms, voxel size of 0.9375 x 0.9375 x 5 mm) were acquired.

6.2.2 Brain donation

Five individuals with a diagnosis of AD, an *in vivo* FLAIR image and T1-weighted image, and who had chosen to donate their brains to Queen Square Brain Bank for Neurological Disorders (QSBB), were used for this study. No specific case selection criteria was used, as brains were a convenience sample of those donated to QSBB during the time frame of this study. The majority of those who donate their brains to QSBB are likely to be younger in onset due to the nature of clinical referrals. Upon receiving each brains, the right hemisphere was frozen and the left hemisphere was fixed in 10% formalin. The diagnosis of AD was pathologically confirmed using a vibratome section and $A\beta$ and tau immunohistochemistry prior to *ex vivo* imaging.

6.2.3 *Ex vivo* MRI imaging

After approximately 4 weeks in formalin, each fixed left hemisphere was washed and placed in Fluorinert (FC-3283, a stable fluorocarbon based fluid). This fluid is similar in susceptibility to brain tissue but has no MRI signal resulting in distortion-free images with a very low signal background. Due to the fact that small air bubbles can cause signal artefacts on the MRI scan, the protocol was updated for the final case to include the massaging the submerged brain to remove any air bubbles.

The fixed hemispheres were scanned on a Siemens Magnetom Prisma 3T MRI scanner. A high-resolution imaging protocol, including T2-weighted, diffusion weighted and SWI scans, was used with the following parameters:

- T2-weighted: 3D long echo train fast spin echo (SPACE) sequence; Voxel

size: 0.5 x 0.5 x 0.5 mm; TR 500 ms; TE 69 ms; echo train duration 200ms; N_{av} 5

- SWI: 3D multi-echo gradient echo; Voxel size: 0.5 x 0.5 x 0.5 mm; TR: 31 ms; 5 TEs: 7.2, 13.4, 19.6, 25.8 ms; Flip angle: 17°; N_{av} 2
- Diffusion weighted imaging: SSFP sequence with diffusion gradients (40); Voxel size 0.85 x 0.85 x 0.85 mm; EPI factor 3; TR: 30ms; TE 22ms; flip angle: 35°; 25 diffusion-weighting directions; q value: 300 cm⁻¹ (approx. equivalent to b=5000 s/mm²)

6.2.3.1 Image processing

In order to improve the signal to noise ratio, multiple acquisitions of the T2-weighted scans were obtained so that acquisitions could be averaged together. Brain regions of the five T2-weighted images were delineated using NiftyMIDAS. Using these brain regions as masks, an average intensity-normalised *ex vivo* T2-weighted image was created using the `reg_aladin` command from NiftyReg. Testing was carried out to determine the optimal number of acquisitions for the greatest benefit to the signal to noise ratio. Two acquisitions were initially averaged, before sequentially increasing by one acquisition until all five acquisitions were averaged. The mean and standard deviation for each number of acquisitions was obtained using `seg_analysis`. As well as assessing the average signal intensity across the whole brain region, 10 equal sized square regions of grey matter and then white matter were also evaluated for the optimum number of acquisitions.

6.2.4 Brain sampling

Prior to the brain cutting procedure, regions of interest were identified from the MRI scans. The *in vivo* FLAIR scan was initially assessed slice by slice, and a lesion code was assigned for each appearance of a lesion on each slice. This means that some larger lesions spanning multiple slices were assigned multiple codes. The *ex vivo* T2-weighted scan was then assessed for any new lesions that were not identified from the FLAIR scan and also given a code. Regions of normal appearing white

matter (NAWM) were selected from white matter regions with no apparent lesion. Where possible, one NAWM region was selected per lobe for each case.

In Case 3, the lesions were further subcategorised due to macroscopic differences in lesion appearance identified at the brain cut by the neuropathologist. These differences in appearance are likely due to the dual MS and ADAD diagnosis in this case. Lesions were classified by the neuropathologist into three groups based on visibility on brain tissue:

- Type 1: Not macroscopically visible (only visible on MRI)
- Type 2: Macroscopically visible and well circumscribed
- Type 3: Macroscopically visible and not well circumscribed

All lesions that were not visible macroscopically on the brain tissue were classified as type 1 lesions. These type of lesions were only visible on the MRI scan, as was typical for all lesions from the other cases in this study. Lesions that were classified as macroscopically visible and well circumscribed were typical in appearance of MS plaques (Type 2 lesions). During the brain cut procedure, several areas of white matter were identified macroscopically by the neuropathologist as being diffusely discoloured, but without a defined boundary. These lesions were therefore classified as type 3 lesions, macroscopically visible and not well circumscribed.

Each brain was cut into 5mm slices and numbered in ascending order from front to back. Photographs were taken of the anterior and posterior of each numbered slice within a glass frame with coloured black markers. Slices containing regions of interest were cut into blocks, making sure to preserve the lesion. These blocks, along with the remaining tissue not sampled, were then re-photographed (again on both sides). All blocks were then processed and embedded in wax for assessment.

6.2.5 Brain sectioning and histology

Tissue from each block was sectioned on a sledge microtome at 15 μ m. 50 serial sections were obtained, and photographs were taken of the block face before

each section was cut. Several blocks from each case were selected to take forward for immunohistochemical staining in this study. Blocks with the most prominent WMHs were selected, with NAWM blocks chosen from corresponding lobes where possible.

For this pilot study, four of the 50 sections were used per block for histological or immunohistochemical staining. The histological stains of hematoxylin and eosin (H&E) and luxol fast blue (LFB) were used, as well as immunohistochemical stains for myelin basic protein (MBP, Abcam 1:200) and SMI31 for axons (Sternberger Monoclonals, 1:5000). Immunohistochemical and histological staining was carried out as described in section 2.4.3.

6.2.6 Staining analysis

All stained sections were scanned using an Olympus slide scanner at 20x magnification and a digital image was then stored.

6.2.6.1 Qualitative analysis

The H&E and LFB stains were initially assessed by a neuropathologist to identify any abnormalities to the overall tissue structure and to the myelin. Using the H&E staining, the atrophy of the ventricular ependyma of the periventricular lesions was assessed using a rating scale of 0 - 3 (Figure 6.2). 0 signified no apparent loss of ependymal cells, 1 signified mild ependymal loss and 2 signified major ependymal loss accompanied by loss to the underlying parenchyma.

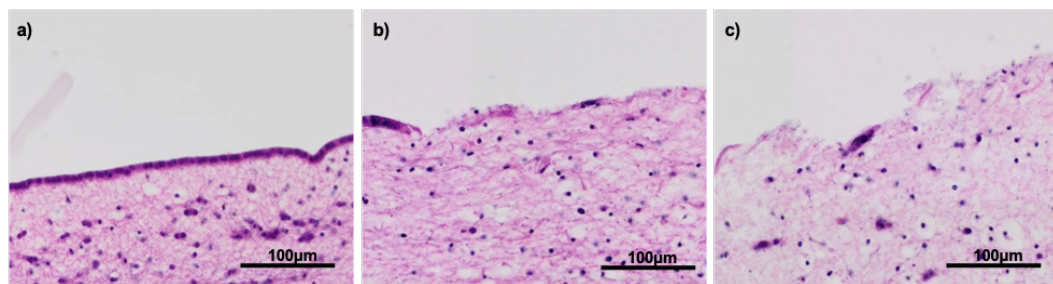


Figure 6.2: Grading of the ventricular ependymal lining. Examples are shown in a) of a grade 0, in b) of a grade 1 and c) of a grade 2.

6.2.6.2 Quantitative analysis

Olympus VS-Desktop was used to view the images and extract the rough area of interest. The extracted images were loaded up individually into ImageJ (<https://imagej.nih.gov/ij/>) and a macro used, developed by a collaborator (Dr Dale Moulding, Institute of Child Health, UCL), to generate 20 random squares of 1000x1000 pixels from each region of interest. The boundaries for the regions of interest were guided by the *in vivo* FLAIR (or *ex vivo* T2-weighted image if not visible on the *in vivo* FLAIR), unless the lesion boundaries were visible macroscopically on the slide. Where lesions were visible macroscopically on the slide, the H&E and LFB staining were used as a guide to the lesion boundary. A threshold was then set to select all the brown chromagen from the 20 random squares and to give a percentage for the area stained. As well as the NAWM regions described in section 6.2.4, a region of NAWM was also selected from every section containing a WMH. This region was to act as an internal control, accounting for variability in staining intensity between different sections.

The percentages for the 20 random squares were averaged together to give one percentage for each region of interest. To assess differences in staining between the WMHs and either the NAWM from the same section and the NAWM from a different section/block, mixed effect linear regression models were used. These models allowed correlations between sections from the same case, and allowed the two types of NAWM to be included in one model. Two separate mixed effect models were used, first with MBP as the dependent variable and then with SMI31. Region of interest (WMH, NAWM - same section, NAWM - different section) was used as the dependent variable, with WMHs as the group to which the NAWM groups were compared. A Kenwood-Roger correction for small sample size was included in each of the models. Scatter plots were created for each immunohistochemical stain, where percentages for each pair of WMH and NAWM from the same section were displayed above each other to highlight any differences.

For Case 3, only WMHs of type 1 (not clearly visible macroscopically on brain tissue and so less typical of MS plaques) were included in the models and the initial

scatter plots. Separate scatter plots were created for the type 2 and 3 lesions for each immunohistochemical stain.

6.2.7 MRI image registration

The registration of the imaging modalities was carried out as detailed in Figure 6.3 and below, after discussion with registration experts. Registration of the *in vivo* T1-weighted and FLAIR images to the *ex vivo* T2-weighted image was carried out first. This meant all images could be visualised in the *ex vivo* T2-weighted image space. To visualise images in the *in vivo* space, the calculated transformations were inverted to allow all images to be seen in the *in vivo* FLAIR space. Initially the registrations were carried out in one case (Case 5), in order to test multiple parameters for the non-linear registration. Once the optimal parameters were selected, the process was repeated for the remainder of the cases.

6.2.7.1 Registration of *in vivo* MRI to *ex vivo* space

Firstly the *in vivo* T1-weighted and FLAIR images were converted into NIFTI format, before brain masks were semi-automatically created for the *in vivo* T1-weighted, FLAIR and *ex vivo* T2-weighted images. For the *in vivo* images, left sided supra-tentorial brain regions were semi-automatically segmented. As the cerebellum does not maintain its position in relation to the brain when not *in situ*, it was not included in either the *in vivo* or *ex vivo* masks. Each mask was then dilated by two voxels and then smoothed over the next voxel, before being multiplied with their respective image to remove the majority of non-brain voxels, the cerebellum and the right hemisphere. FLAIR images were segmented and processed in a similar way.

The T1-weighted and FLAIR images were then reoriented. There were considerable differences in orientation of the *ex vivo* image compared to the *in vivo* images, largely due to the optimum orientation that the hemisphere fitted into the scanning container being different to the orientation of an *in vivo* brain in the scanner. In order to reorient the *ex vivo* image so that it appears in the same orientation as the *in vivo* images, the `reg_aladin` command in the NiftyReg platform was used to

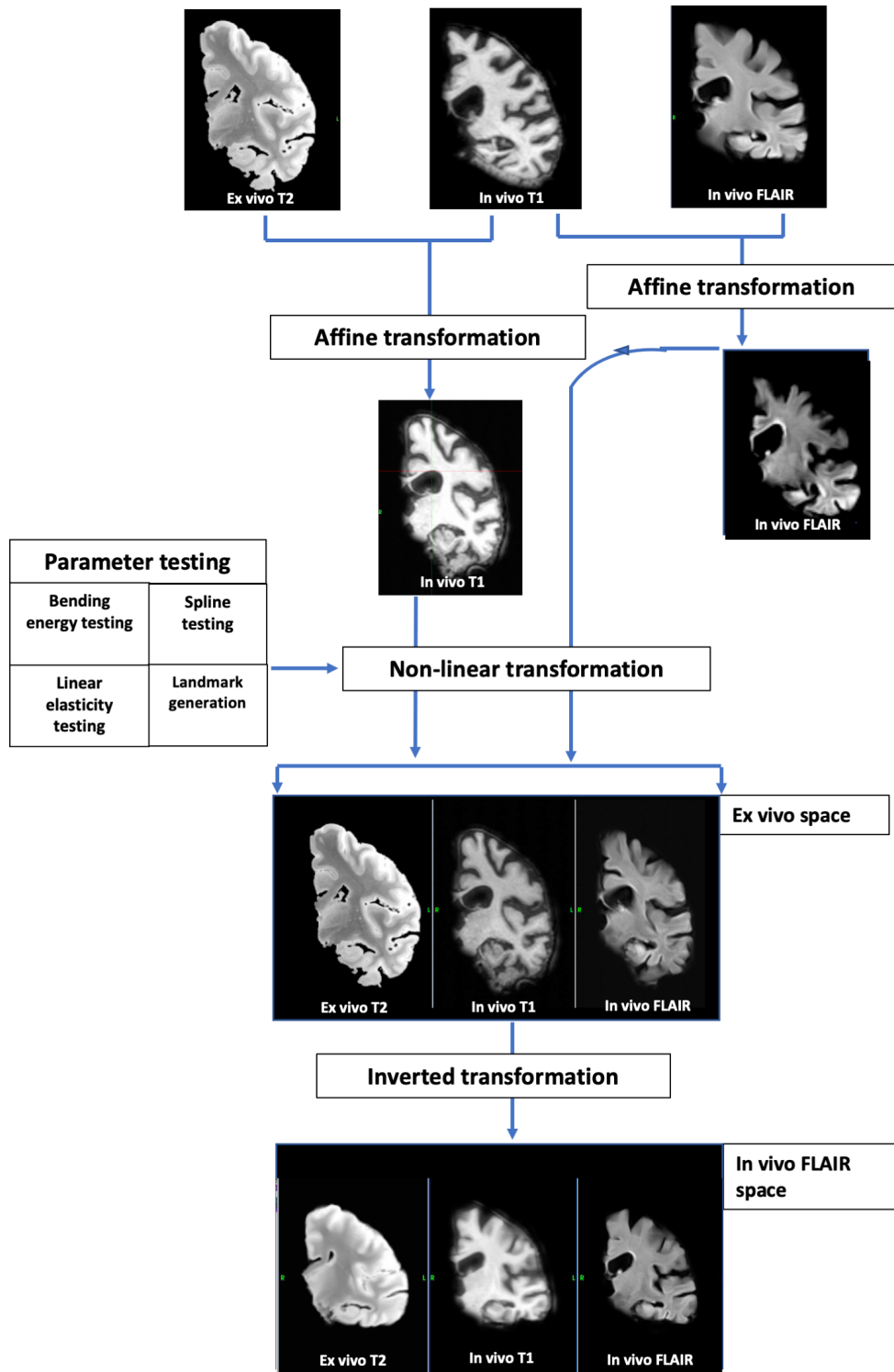


Figure 6.3: The pipeline for the registration of the *ex vivo* T2-weighted and *in vivo* T1-weighted and FLAIR images

change the s-form of the image and mask. This reoriented *ex vivo* image and mask was then standardised using `fsloreorient2std`.

Initially, an affine registration of the *in vivo* T1-weighted and *ex vivo* T2-weighted image was carried out using the `reg_transform` command. A non-linear registration using the `reg_f3d` command was then carried out, where multiple parameters were tested to optimise the registration. Parameters were varied individually, using the default `f3d` settings for all other parameters. The following parameters were tested and then visually assessed:

- Weights of linear elasticity penalty term at default (0.01) and at 0.
- Weights of the bending energy in multiples of 10 between 0.0001 and 0.1.
- Spline options for control points at grid spacings of 3, 5, 10, 15 and 20mm along the the x, y and z axis.

In order to try and improve the non-linear registration, corresponding landmarks on the *in vivo* T1-weighted and *ex vivo* scans were identified. Landmarks were chosen in areas that were particularly challenging to register, such as periventricular regions affected by collapsing ventricles. Landmark weighting was varied between 0.1 to 1.

Once the optimal combination of parameters was selected, the deformation required for the registration was outputted for use in the FLAIR registration. The *in vivo* FLAIR image was initially registered to the *in vivo* T1-weighted image using an affine registration in `reg_aladin`. The *in vivo* FLAIR image was then transformed using `reg_transform`, using the composed `f3d` matrix from the *in vivo* T1-weighted to *ex vivo* T2-weighted, and the *in vivo* FLAIR to T1-weighted affine transformations in a single step. This prevented multiple interpolations of the FLAIR image. `Reg_resample` was then used to resample the *in vivo* FLAIR into the *ex vivo* space.

6.2.7.2 Registration of *ex vivo* MRI to *in vivo* space

In order to register the *ex vivo* T2-weighted image into in the vivo FLAIR space, the transforms from the registrations described above were inverted using `reg_transform` and the *ex vivo* image was resampled into *in vivo* FLAIR space using `reg_resample`.

6.2.8 Registration of *ex vivo* MRI and histological sections

For the registration of the histological sections to the *ex vivo* MRI scan, registration software developed by a collaborator (Dr Eugenio Iglesias) was used (Iglesias et al., 2018, Mancini et al., 2019). This software was originally developed in order to reconstruct the brain in its entirety from histological sections. This would require the whole brain to be sampled and sectioned, before reconstruction could take place. Full brain reconstruction using the software initially involves the organisation of stacks of section photos so they represent full blocks, before registering these blocks to the *ex vivo* MRI image. The MRI image is then resampled into the space of individual blocks. For each block, the stack of resampled MRI images can be registered to a stack of histological sections. The software is designed to minimise errors between sections and blocks to then reconstruct the whole brain. Due to the fact that only specific regions of the brain are sampled in this project, the software needed to be adapted accordingly. Stained sections (four per block) were registered to the brain slice photographs taken during the brain cutting procedure. The *ex vivo* MRI images were also registered to these photographs, which then enabled the resampling of the MRI image into the space of a histological section.

6.2.9 WMH segmentation and assessment of WMH change

WMH segmentation was carried out on FLAIR images in their native space. Segmentation was carried out using the semi-automated protocol described in section 2.3.1.2. WMH volumes were extracted from the segmentations for each half hemisphere.

In order to assess the WMHs on the *ex vivo* T2-weighted scan, an initial attempt was made to transform the segmentations into the *ex vivo* space using the calculated deformations from the registration of the images. However it became apparent that, although useful as a guide to the location of corresponding regions, the registration was not good enough for voxel to voxel correspondence, as would be required in the assessment of the WMH segmentations (Figure 6.4).

In order to assess whether similarities or differences in WMHs can be observed between the *in vivo* and *ex vivo* scan, a more qualitative approach was adopted.

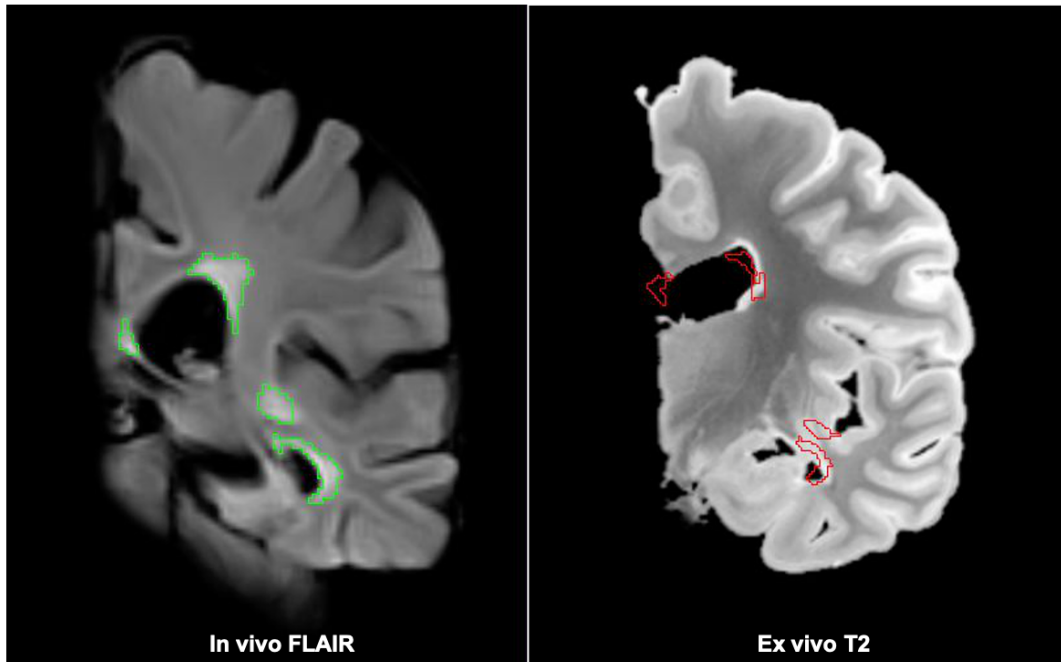


Figure 6.4: A demonstration of the imperfect alignment achieved when the *in vivo* WMH segmentation is transformed to the *ex vivo* space.

Each coded WMH (see section 6.2.4) was viewed on both the *in vivo* FLAIR and side-by-side. This was carried out initially in FLAIR space and then in *ex vivo* space. Where a lesion could be observed on one scan, but not at the corresponding registered location on the other, adjacent slices were checked. This was to ensure that any inaccuracies in the registration was not resulting in corresponding lesions being missed. Where a lesion was identified in this way, careful attention was paid to its shape and location in relation to other anatomical structures to ensure that it was indeed the same lesion.

Lesions were graded according to their appearance between scans, with a 1 given to those that appeared similar, a 2 given to those that appeared smaller or had disappeared on the *ex vivo* scan and a 3 given to those that had increased or newly appeared on the *ex vivo* scan.

Table 6.2: Clinical, imaging and pathological information

Case	Sex	Age at onset	Age at death	Clinical diagnoses	AD clinical presentation	Vascular risk score	Disease duration (years)	APOE- $\epsilon 4$ status	Time between scans (years)	WMH volume (ml)	Brain weight (g)	Post-mortem delay (h:m:s)	Fixation time* (days)	Braak stage	CERAD Thal Phase	ABC score	CAA
1	M	54	66	AD, Epilepsy	Amnesic	0	12	44	9.2	1.1	1089	34:25:00	40	6	5	A3B3C3	3
2	M	45	59	AD	PCA	0	14	33	8.3	2.0	1338	90:45:00	51	6	5	A3B3C3	3
3	M	38	52	ADAD (PSEN1 E280G), MS	Behavioural	0	14	34	4.2	6.7	1251	34:25:00	54	6	5	A3B3C3	3
4	F	44	58	AD	Amnesic	0	14	33	8.3	1.1	1075	58:50:00	19	6	5	A3B3C2	3
5	F	51	68	AD	PCA	0	17	33	7.3	4.7	965	49:45:00	35	6	5	A3B3C3	2

WMH volumes are reported for the left hemisphere. The presence or absence of hypertension, diabetes, hyperlipidaemia, stroke, transient ischaemic attack and coronary artery disease was assessed to create a composite score for vascular risk that was the sum of the factors present, ranging from 0 to 6 (DeCarli et al., 2004)

* Fixation time prior to *ex vivo* scanning.

6.3 Results

6.3.1 Demographics

Table 6.2 shows the clinical, imaging and pathology data for the cases used in this study. Five individuals clinically diagnosed with AD were used in this study, consisting of two with typical amnesic presentations of AD, two PCA and one ADAD (*PSEN1* E280G mutation). The ADAD case, Case 5, also had a clinical and pathological diagnosis of MS. All cases had an early age at onset, ranging from 38 in the ADAD case to 54 years. Age at death ranged between 52 and 68 years, with disease duration therefore ranging from 12 to 17 years. The presence or absence of hypertension, diabetes, hyperlipidaemia, stroke, transient ischaemic attack and coronary artery disease was assessed to create a composite score for vascular risk that was the sum of the factors present, ranging from 0 to 6 (DeCarli et al., 2004). All cases had a vascular risk score of 0, indicative of a low vascular risk. The time between the *in vivo* and *ex vivo* scan ranged from 4.2 years in Case 5 to 9.2 in Case 1. The *post mortem* delay was ranged from over 90 hours in Case 2 to 34 hours in Cases 1 and 3. Fixation time prior to *ex vivo* scanning ranged from 19 days in Case 4 to 54 days in Case 3. All cases had an ABC score of A3B3C3 signifying end stage disease, apart from Case 4 with a score of A3B3C2. All cases had a CAA score of 3, apart from Case 5 with a CAA score of 2. A further assessment of vascular pathology was carried out by the neuropathologist, revealing mild atherosclerosis in Case 1 and mild hyaline arteriosclerosis only in the subcortical white matter in Cases 2 and 4. Case 5 demonstrated both mild atherosclerosis and mild hyaline arteriosclerosis, as well as a subdural haemorrhage. Case 3 demonstrated no additional vascular pathology above the frequent CAA.

6.3.2 White matter hyperintensities

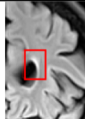
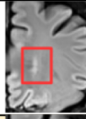
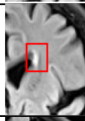

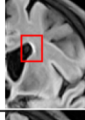

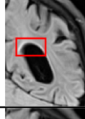
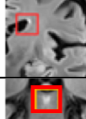
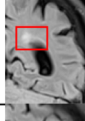
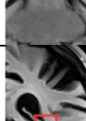
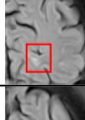
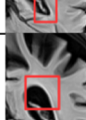


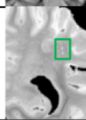
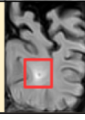

6.3.2.1 General overview

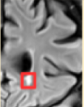

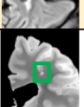
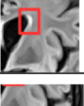

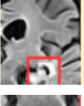





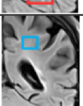
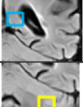
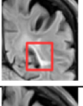
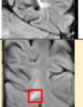
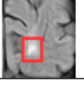



The cases in this small cohort demonstrated variability in WMH load on the *in vivo* FLAIR scans. WMH volumes were highest in Case 3 (who had a dual diagnosis of ADAD and MS), with a volume of 6.7ml in the left hemisphere, followed by Case 5

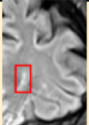
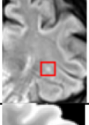
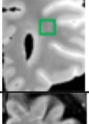
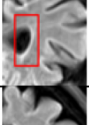
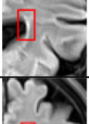
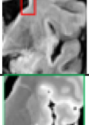



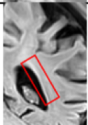

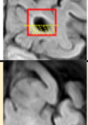

with 4.7ml. Low WMH volumes of between 1.1 and 2.0ml were observed in Cases 1, 2 and 4.

In Case 1 (amnesic AD), WMHs were restricted to small ventricular caps that were observed in the frontal, parietal and occipital lobes of the brain. In Case 2 (PCA), WMHs were again largely only apparent as small caps on the ventricles throughout the brain, apart from one lesion in the brainstem and one small subcortical parietal lesion observed only on the *ex vivo* scan. Case 3 had the highest WMH load with large periventricular WMHs, especially in the parietal and temporal lobes. Although the majority of WMHs were again periventricular, there were a few juxtacortical and deep WMHs in the parietal lobe. The low WMH burden in Case 4 (amnesic AD) was largely made up of frontal and occipital ventricular caps, along with one juxtacortical and one deep WMH in the frontal lobe. An area of temporal WMH was also identified only on the *ex vivo* MRI scan. In Case 5 (PCA), Large periventricular WMHs were observed in the frontal lobe and at the parieto-temporal junction.

6.3.2.2 Lesion coding

Case 1			Case 2		
Lesion code	Notes	Image	Lesion code	Notes	Image
1.1	Frontal Periventricular		2.1	Frontal Periventricular	
1.2	Frontal Periventricular		2.2	Frontal Periventricular	
1.3	Frontal Periventricular		2.3	Frontal Periventricular	
1.4	Parietal Periventricular		2.4	Frontal Periventricular	
1.5	Parietal Periventricular		2.5	Brainstem	
1.6	Occipital Periventricular		2.6	Inferior parietal Periventricular	
1.7	Occipital Periventricular		2.7	Parietal Periventricular	
			2.8	Parieto-occipital Periventricular	
			2.9	Parietal Juxtacortical	
			2.10	Occipital Periventricular	

Case 3			
Lesion code	Notes	Lesion classification	Image
3.1	- Frontal - Periventricular - Macroscopically visible and well circumscribed	Type 2	
3.2	- Frontal - Periventricular - Macroscopically normal	Type 1	
3.3	- Frontal - Juxtacortical - Macroscopically visible and well circumscribed	Type 2	
3.4	- Frontal - Juxtacortical - Identified from ex vivo scan	Type 2	
3.5	- Frontal - Periventricular - Macroscopically normal	Type 1	
3.6	- Temporal - Periventricular - Macroscopically visible and well circumscribed	Type 2	
3.7	- Parietal - Juxtacortical - Macroscopically normal	Type 1	
3.8	- Upper medial temporal - Periventricular	Type 2	
3.9	- Lower pons - Macroscopically visible and well circumscribed	Type 2	
3.10	- Parietal - Periventricular - Macroscopically normal	Type 1	
3.11	- Temporal - Periventricular and juxtacortical - Macroscopically visible and well circumscribed	Type 2	
3.12	- Inferior parietal (junction with temporal lobe) - Macroscopically visible and well circumscribed	Type 2	
3.13	- Parietal - Macroscopically visible and not well circumscribed	Type 3	
3.14	- Midline/cingulate - Macroscopically visible and well circumscribed	Type 2	
3.15	- Cerebellum	Type 2	
3.16	- Parieto-occipital - Periventricular - Macroscopically visible and not well circumscribed	Type 3	
3.17	- Parietal - Deep WM lesion - Macroscopically visible and well circumscribed	Type 2	
3.18	- Occipital - Periventricular	Type 1	
3.19	- Occipital - Macroscopically visible and not well circumscribed	Type 3	

Case 4		
Lesion code	Notes	Image
4.1	- Frontal - Periventricular	
4.2	- Frontal - Deep WMH	
4.3	- Frontal - Juxtacortical - Identified from ex vivo scan	
4.4	- Frontal - Periventricular	
4.5	- Frontal - Periventricular	
4.6	- Frontal - Periventricular	
4.7	- Temporal - Periventricular - Identified from ex vivo scan	
4.8	- Temporal - Periventricular lesion - Identified from ex vivo scan	
4.9	- Frontal - Periventricular	
4.10	- Parieto-temporal - Periventricular	
4.11	- Parieto-occipito - Periventricular - Identified from ex vivo scan	
4.12	- Occipito-temporal - Periventricular	
4.13	- Occipital - Periventricular	

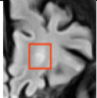

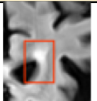
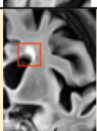
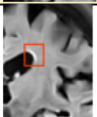

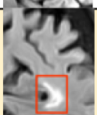

Case 5		
Lesion code	Notes	Image
5.1	- Frontal - Periventricular	
5.2	- Frontal - Periventricular	
5.3	- Frontal - Periventricular	
5.4	- Frontal - Periventricular	
5.5	- Frontal - Periventricular	
5.6	- Temporal - Periventricular	
5.7	- Parieto-temporal - Periventricular	
5.8	- Parieto-temporal - Periventricular	

Figure 6.5: Lesion guide for Cases 1-5. Lesions highlighted in yellow were selected for immunohistochemical staining. The lesions in the red boxes were identified on the *in vivo* FLAIR, lesions in the green box were identified on the *ex vivo* T2-weighted image and lesions in the blue boxes were identified on the brain tissue during the brain cutting procedure. For Case 3 (with dual ADAD-MS) type 1 lesions are defined as not macroscopically visible (only visible on MRI), type 2 lesions are defined as macroscopically visible on brain tissue and well circumscribed and type 3 lesions are defined as macroscopically visible and not well circumscribed

Figures 6.5 display the lesions identified for each case. In Case 2, 10 lesion blocks and two NAWM blocks were identified and sampled. Two WMH lesions, 2.2 and 2.10, were selected for inclusion in the first round of immunohistochemical staining and analysis. For Case 4, 13 lesions blocks and four NAWM regions were sampled into blocks. Three WMH lesions, 4.1, 4.11 and 4.13, and two NAWM regions were selected for immunohistochemical staining. For Case 5, eight lesion blocks and four NAWM blocks were sampled, with three lesion blocks (5.2, 5.4 and 5.7) and two NAWM blocks selected for staining.

In Case 3, 19 lesions and five NAWM regions were identified and sampled into blocks. Five lesions were classified as type 1 (not macroscopically visible), 11 lesions were classified as type 2 (macroscopically visible and well circumscribed), and three lesions were classified as type 3 (macroscopically visible and not well circumscribed). Seven lesion blocks were selected for immunohistochemical staining (lesions 3.1, 3.2, 3.3, 3.7, 3.8, 3.10, 3.18), along with two NAWM blocks.

6.3.3 Question 1: Can high quality *ex vivo* MRI images be obtained?

The implementation of the pipeline enabled *ex vivo* scanning to be successfully carried out for all five cases in this study. *Ex vivo* T2-weighted scans were obtained for all subjects, with five acquisitions taken and averaged per case. Figures 6.6, 6.8 and 6.7 show the effect of increasing the number of acquisitions on the coefficient of variation (a measure of relative variability) for the whole brain regions and the 10 grey and 10 white matter regions, in all cases. For the full brain region, a large decrease in the coefficient of variation is observed from one acquisition to two acquisitions in all cases. The decreases in the coefficient of variation were smaller with the addition of three, four and five acquisitions. Some reduction in the coefficient of variation was still seen with the fourth and fifth additions. Similar overall patterns were observed with the grey and white matter regions. Figure 6.9 confirms that an increase in image quality is observed with the addition of each acquisition. The averaging of the five T2-weighted acquisitions together resulted in high quality imaging in each case, demonstrated by the example slices shown for Case 5 in

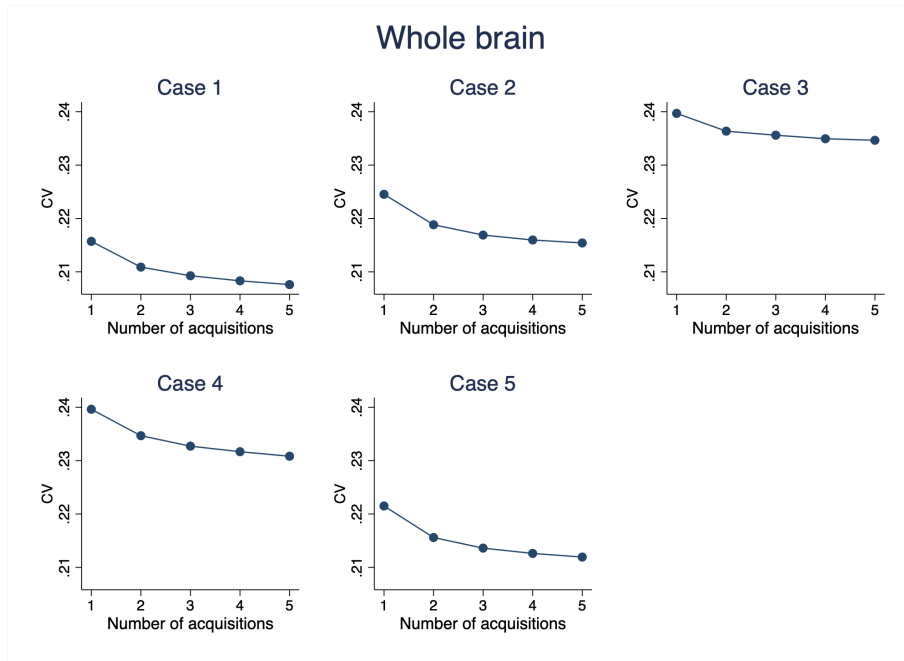


Figure 6.6: Plots showing the coefficient of variation for the whole brain region with the addition of each subsequent acquisition for all Cases 1-5

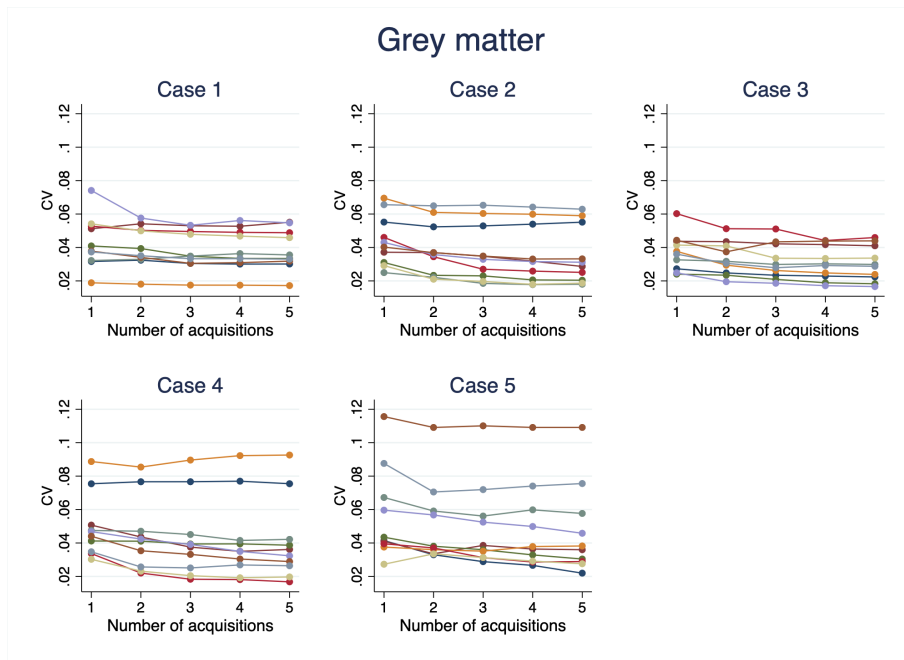


Figure 6.7: Plots showing the coefficient of variation for the 10 grey matter regions with the addition of each subsequent acquisition for all Cases 1-5.

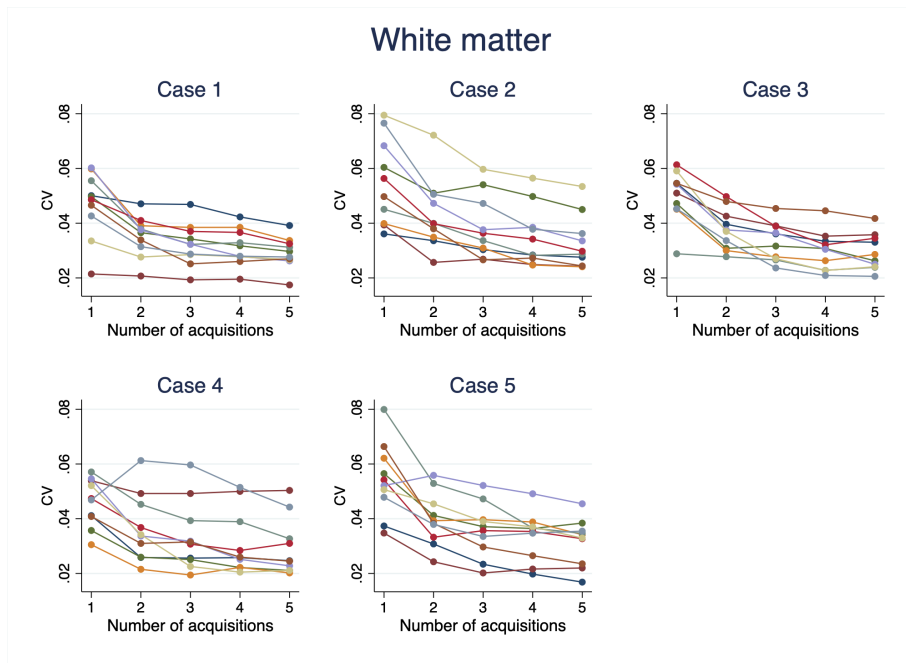


Figure 6.8: Plots showing the coefficient of variation for the 10 white matter regions with the addition of each subsequent acquisition for all Cases 1-5.

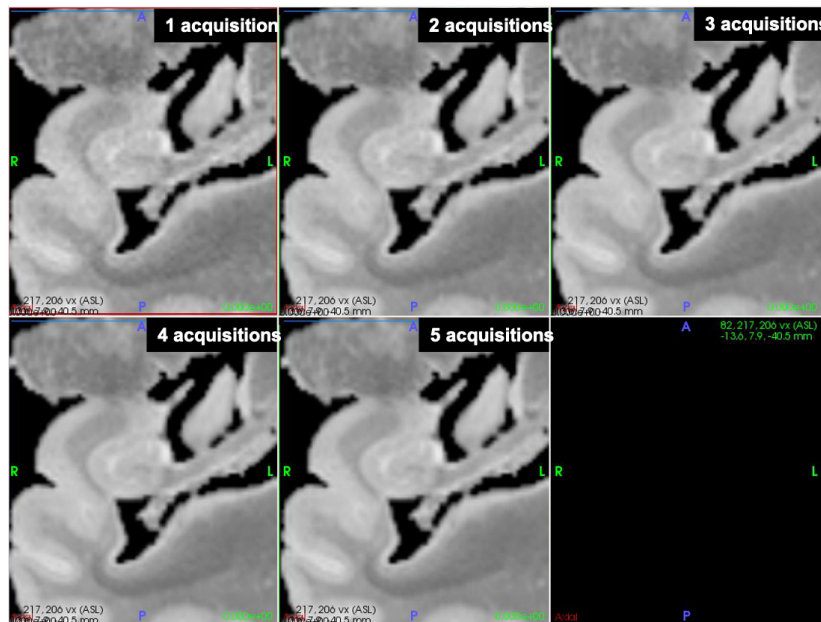


Figure 6.9: Images demonstrating the hippocampus on the *ex vivo* T2-weighted images for Case 5, with the addition of each acquisition.

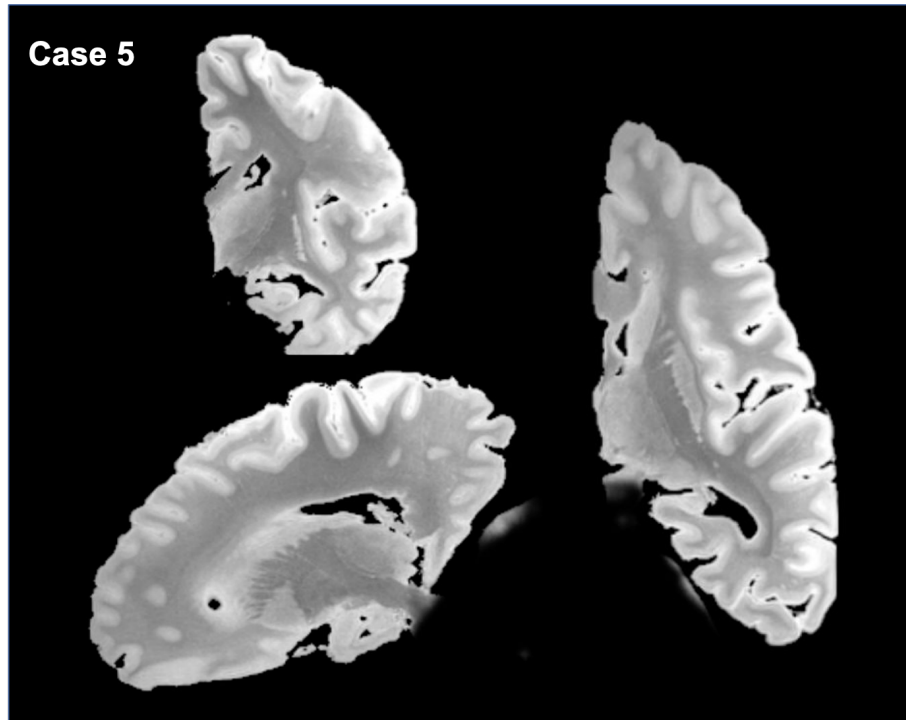


Figure 6.10: Example coronal, sagittal and axial slices of the *ex vivo* MRI T2-weighted scan (an average of all five acquisitions) for Case 5.

Figures 6.10.

6.3.4 Question 2: Is registration of *in vivo* and *ex vivo* MRI scans possible?

6.3.4.1 Non-linear registration parameters

The testing of multiple parameters enabled the optimisation of the non-linear registration. Figure 6.11 demonstrates that there was negligible improvement in the registration quality by using a linear elasticity of zero compared to the default. However a value of zero was selected in order that the other parameters could be manipulated. A much improved registration was seen with the use of control points at 15mm and 20mm (Figure 6.12). A spacing of 15mm was selected due to a marginally greater correspondence with the *ex vivo* scan.

Figure 6.13 shows that a bending energy of 0.1 gives the best registration when the other parameters of f3d are kept at default. However, a value of 0.1 is quite rigid and therefore a bending energy of 0.01 was also tested, whilst keeping the the linear

elasticity and control point parameters at their optimised values. Although there was a high degree of similarity in the registration, a higher level of correspondence was observed around the ventricles. As this is a highly important region in terms of WMH formation, the decision was made to proceed with a bending energy of 0.01.

In order to try and improve the registration further, coordinates of corresponding landmarks on the *ex vivo* and *in vivo* T1-weighted image were included in the registration. However, this did not improve the registration, instead resulting in substantial warping in the location the landmark, as seen in Figure 6.14. The decision was made to therefore proceed without the use of landmarks.

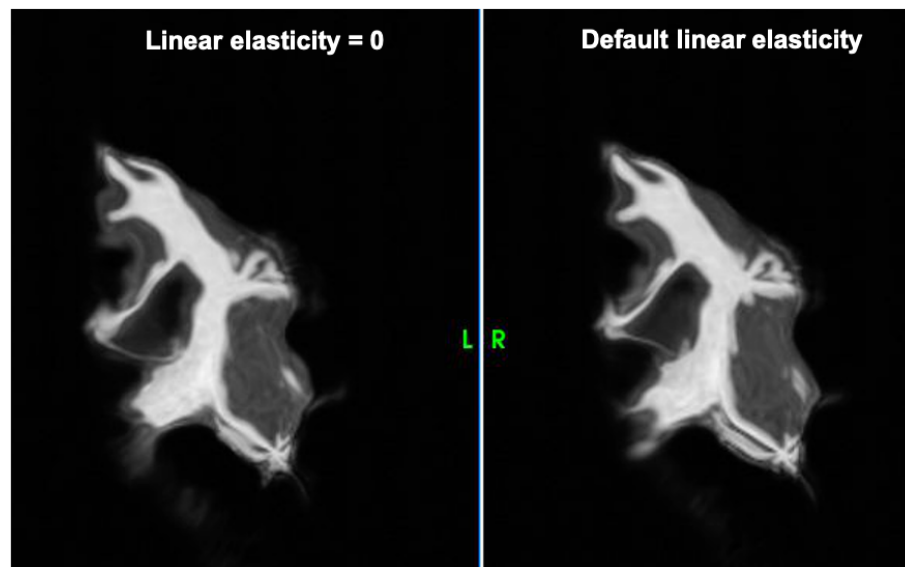


Figure 6.11: T1-weighted images for Case 5, in which the f3d non-linear registration was carried out with the default linear elasticity of 0.01 and then with a linear elasticity of 0.

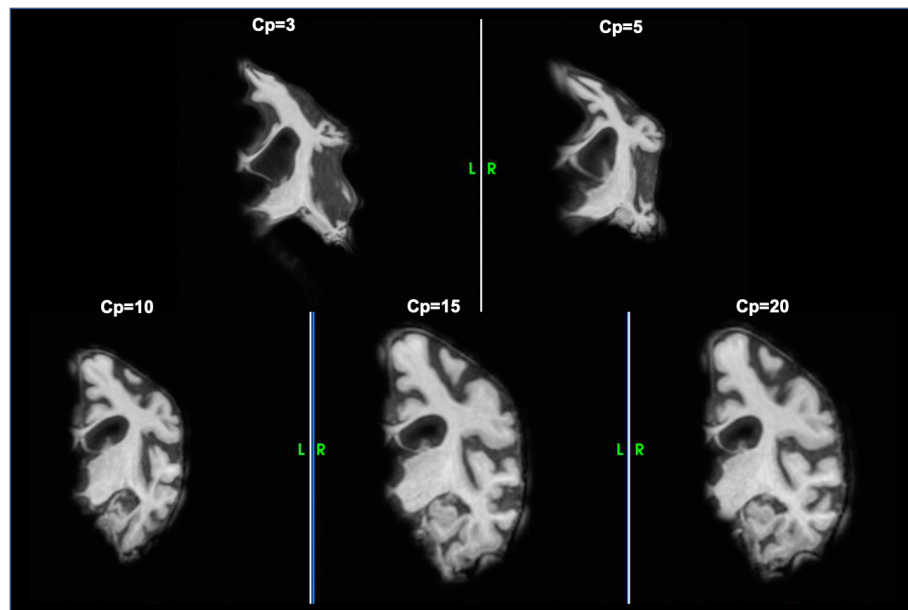


Figure 6.12: T1-weighted images for Case 5, in which the spline options were varied to give control points at 3, 5, 10 and 15mm spacings.

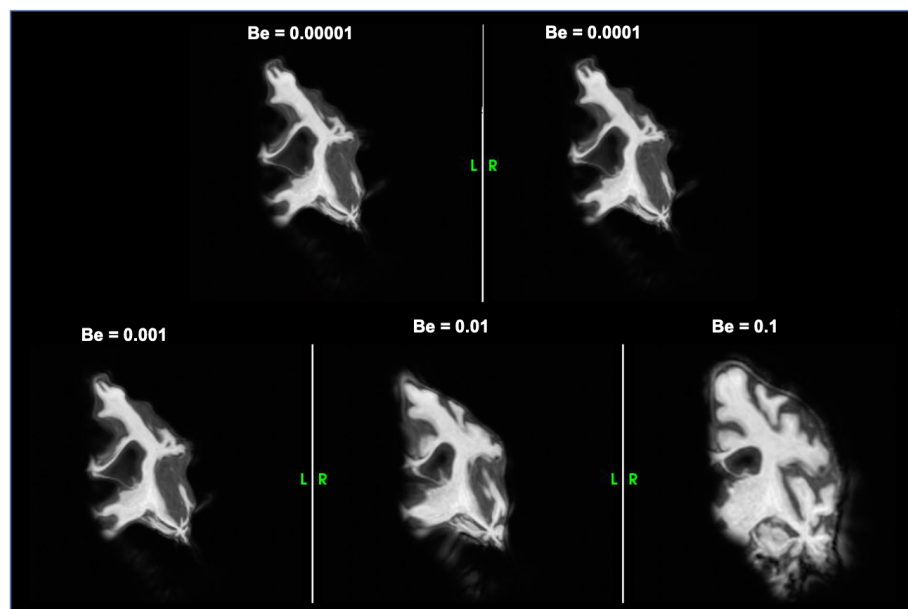


Figure 6.13: T1-weighted images for Case 5, in which the bending energy was varied between 0.00001 and 0.1.

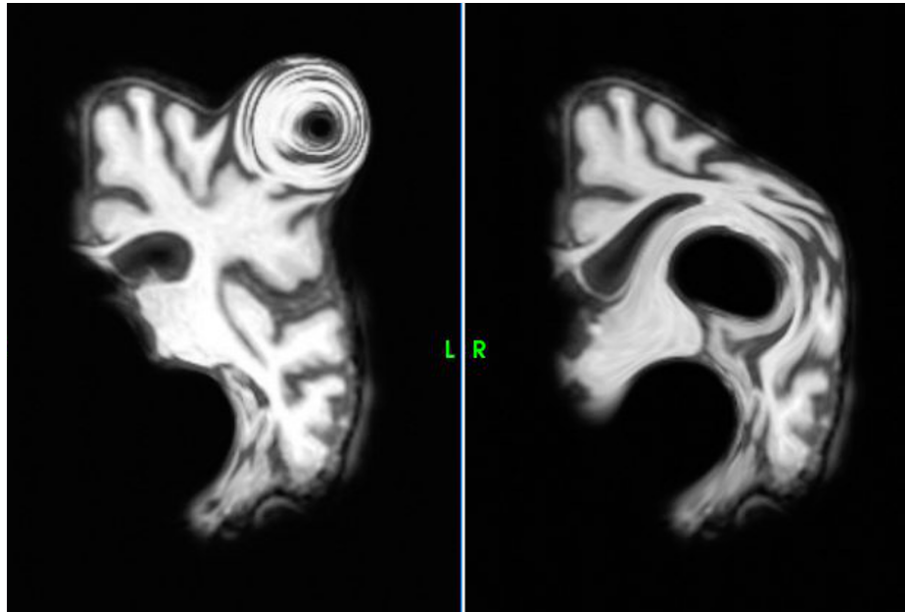


Figure 6.14: Unsuccessfully registered T1-weighted images for Case 5, where landmarks were used to try and improve the registration.

6.3.4.2 Final non-linear registrations

Figures 6.15 to 6.19 show the final non-linear registrations in both the *ex vivo* T2-weighted image space and *in vivo* FLAIR space. Successful registration was achieved, with a good level of correspondence demonstrated in all cases. The *post mortem* brain has undergone considerable deformation meaning that the registration in particular areas was challenging. One of the areas most affected was the ventricles, which tend to collapse in the fixed *post mortem* brain. The correspondence between the *in vivo* and *ex vivo* scans in the ventricular and surrounding regions was therefore less accurate. This ventricular collapse was particularly apparent in Case 5 (Figure 6.19), where the structures superior to the ventricles such as the corpus callosum are not well registered. Overall, the registration achieved is effective in providing a guide to corresponding regions on the *ex vivo* and *in vivo* scans, but is not accurate enough for voxel to voxel correspondence.

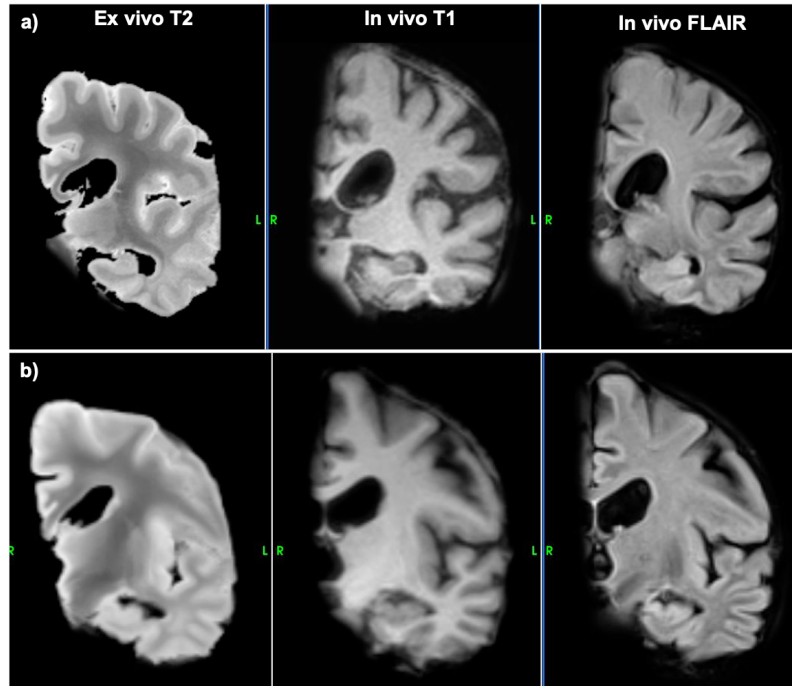


Figure 6.15: Non-linearly registered *ex vivo* T2, *in vivo* T1-weighted and *in vivo* FLAIR images in a) *ex vivo* T2-weighted image space and b) *in vivo* FLAIR space, for Case 1.

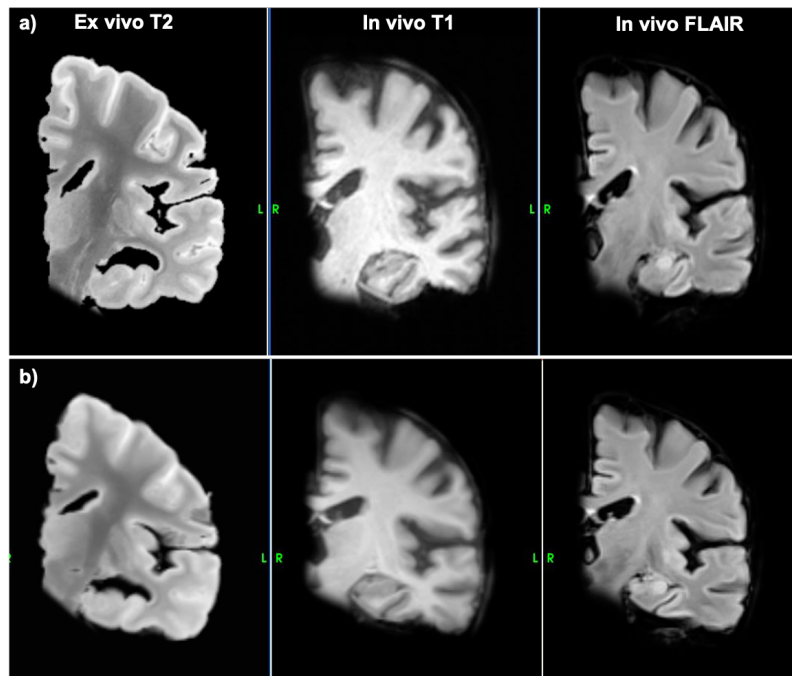


Figure 6.16: Non-linearly registered *ex vivo* T2, *in vivo* T1-weighted and *in vivo* FLAIR images in a) *ex vivo* T2-weighted image space and b) *in vivo* FLAIR space, for Case 2.

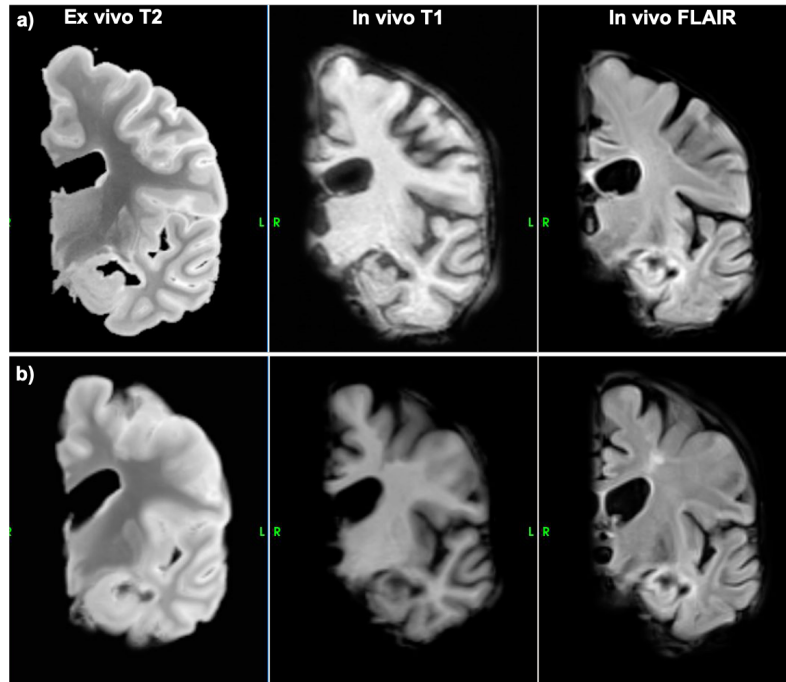


Figure 6.17: Non-linearly registered *ex vivo* T2, *in vivo* T1-weighted and *in vivo* FLAIR images in a) *ex vivo* T2-weighted image space and b) *in vivo* FLAIR space, for Case 3.

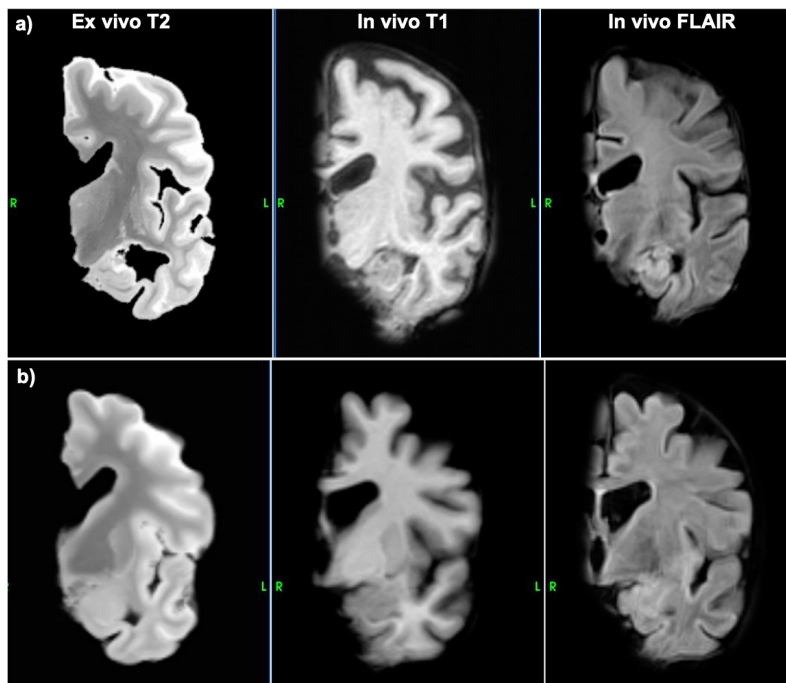


Figure 6.18: Non-linearly registered *ex vivo* T2, *in vivo* T1-weighted and *in vivo* FLAIR images in a) *ex vivo* T2-weighted image space and b) *in vivo* FLAIR space, for Case 4.

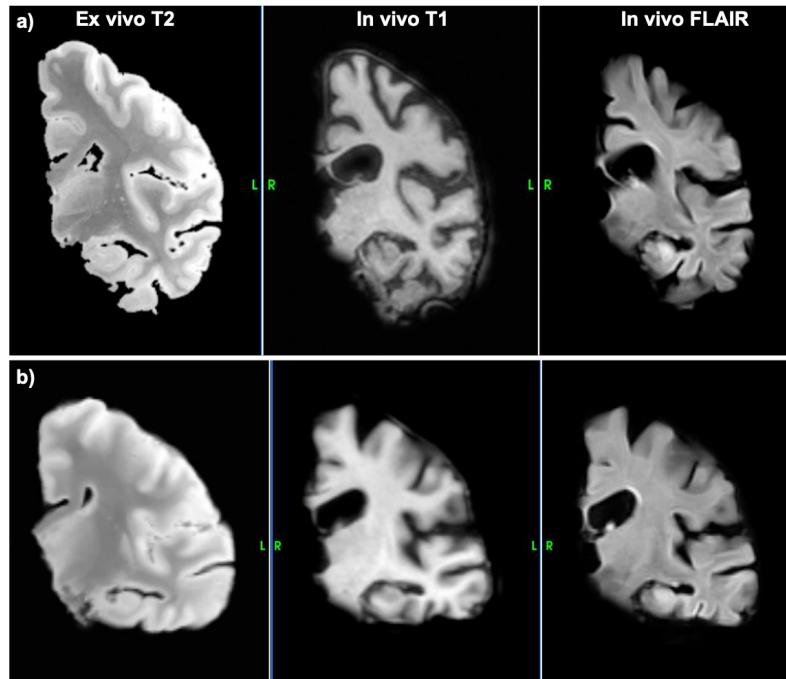


Figure 6.19: Non-linearly registered *ex vivo* T2, *in vivo* T1-weighted and *in vivo* FLAIR images in a) *ex vivo* T2-weighted image space and b) *in vivo* FLAIR space, for Case 5.

6.3.5 Question 3: Is registration of histological sections to *ex vivo* MRI images possible?

Several issues were encountered with the registration of the histological sections and the *ex vivo* MRI scans. The overarching issue for this registration stems from the fact that Dr Eugenio Iglesias' pipeline was developed for use when the entire brain has been sampled into blocks and sectioned. This pipeline works to minimise errors between each block when they are reconstructed into a full brain. A simplified version of the registration pipeline was used for this study, but due to the large gaps between each sampled brain region, the accumulation of errors was often too great for the pipeline to resolve.

Figure 6.20 shows the *ex vivo* T2-weighted scans registered into the space of the histological section from five of the brain blocks sampled for Case 5; the case in which the best results were achieved. Registration was also achieved for some stains for some of the blocks for Case 3 (Figure 6.21).

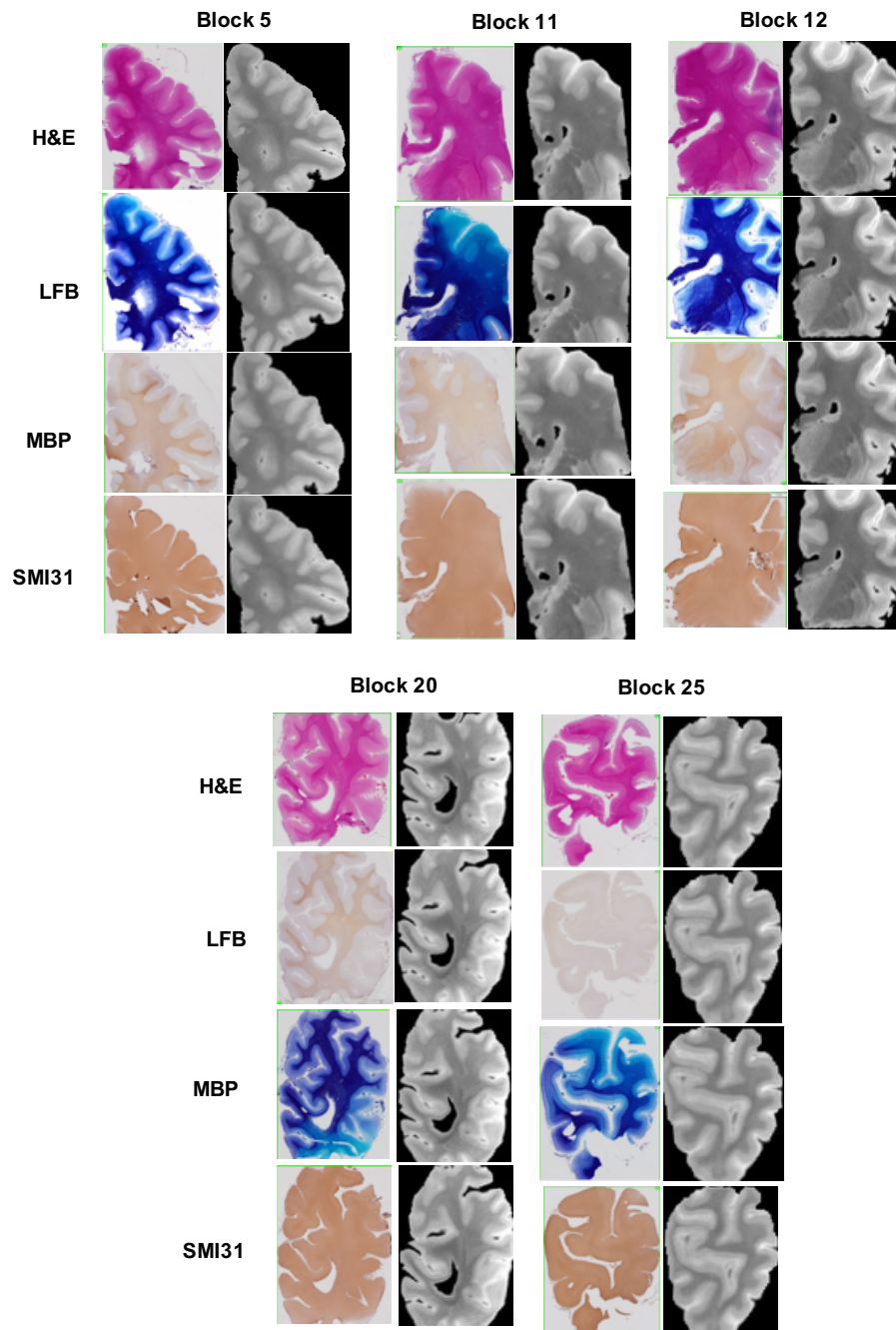


Figure 6.20: *Ex vivo* T2-weighted scans for Case 5 registered into the space of the histological section, shown with the corresponding H&E, LFB, MBP and SMI31 stained sections.

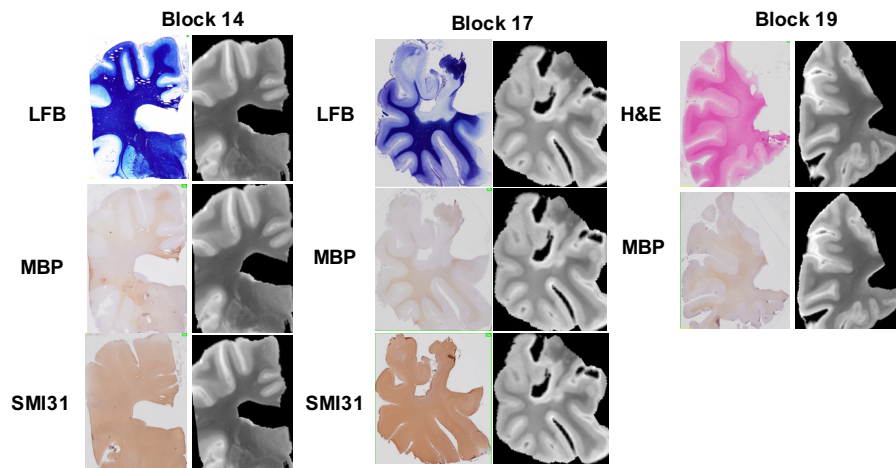


Figure 6.21: *Ex vivo* T2-weighted scans for Case 3 registered into the space of the histological section, shown with the corresponding stained sections. Note that not all of the stained sections are present for each brain block.

6.3.6 Question 4: Can similarities or differences in WMHs between the last *in vivo* MRI and the *ex vivo* scan be observed?

The large majority of lesions from all cases appeared on both *in vivo* and *ex vivo* scans and were graded a 1 or a 1a, for similarly appearing WMHs. The grade 1a was introduced to account for the fact that there were a large number of lesions that appeared bright with well defined boundaries on the *in vivo* scan, but were fainter or more diffuse on the *ex vivo* scan, despite being of a similar size. Examples of these type 1a graded lesions are lesion 1.3 in Figure 6.22 and lesion 5.2 in Figure 6.26. Although initially these lesions appeared to have shrunk or disappeared on the

Table 6.3: Grade of lesion change.

Case	Grade 1	Grade 1a	Grade 2	Grade 3
1 (n=7)	2	5	0	0
2 (n=10)	7	2	0	1
3 (n=14)	11	2	0	1
4 (n=13)	5	3	1	4
5 (n=8)	1	7	0	0

Grade 1 was given to those that appeared similar between *in vivo* and *ex vivo* scans, grade 1a was given to those that appeared fainter/diffuse but of the same size on the *ex vivo* scan, grade 2 was given to those that appeared smaller or had disappeared on the *ex vivo* scan and a grade 3 was given to those that had increased or newly appeared on the *ex vivo* scan.

ex vivo scan, a grade 1a was given when on closer inspection a faint hyperintensity was visible over a roughly similar area. This reduction in brightness from the *in vivo* to the *ex vivo* scan was not always the case though, with lesions occasionally appearing brighter on the *ex vivo* scan (Figure 6.24).

One lesion in Case 4 did that appeared on the *in vivo* scan, did not appear on the *ex vivo* scan and was graded a 2. Six lesions had newly appeared or increased on the *ex vivo* scan and were graded a 3, four of which were in Case 4. Examples of lesions from each of the five cases are shown in Figures 6.22 to 6.26.

All lesions on the *ex vivo* scan were much more clearly visible in native space as opposed to *in vivo* space, due to the higher resolution of the *ex vivo* image compared to the *in vivo* image. Lesions that were newly appearing or appeared to have increased substantially between scans were often only visible (or much more clearly visible) on the *ex vivo* image in its native space (see lesions 3.4 on Figure 6.24 and 4.11 on Figure 6.25). It may be the case therefore that the lesions that seem to be newly appearing on the *ex vivo* scan, may in fact just not have been visible on the low resolution *in vivo* imaging. Many of these grade 3 lesions were small and punctate and so could have easily been missed by thick slice FLAIR.

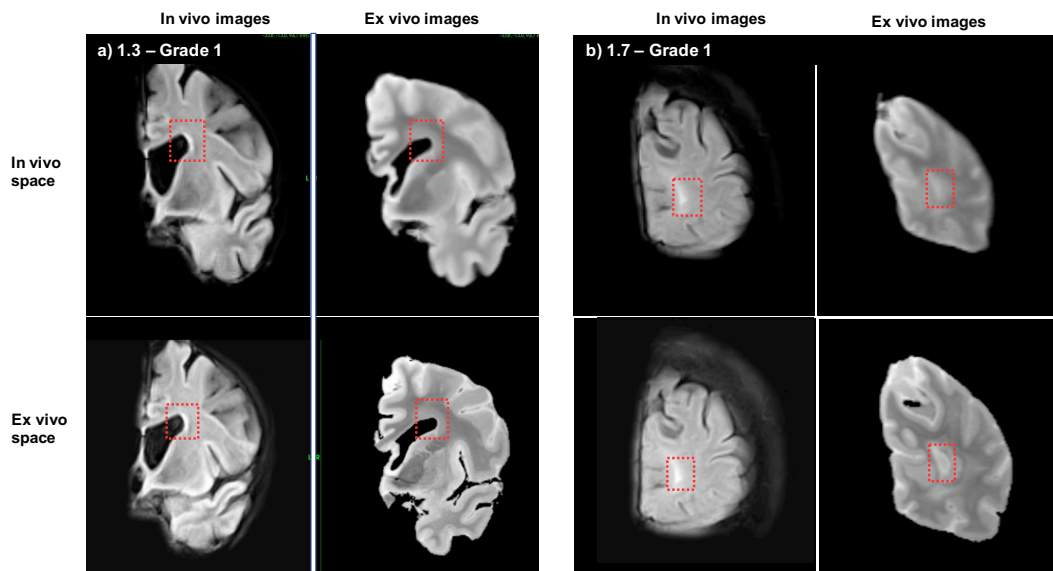


Figure 6.22: Example lesions from Case 1. Lesions are shown on *in vivo* and *ex vivo* images in both *in vivo* space and *ex vivo* space.

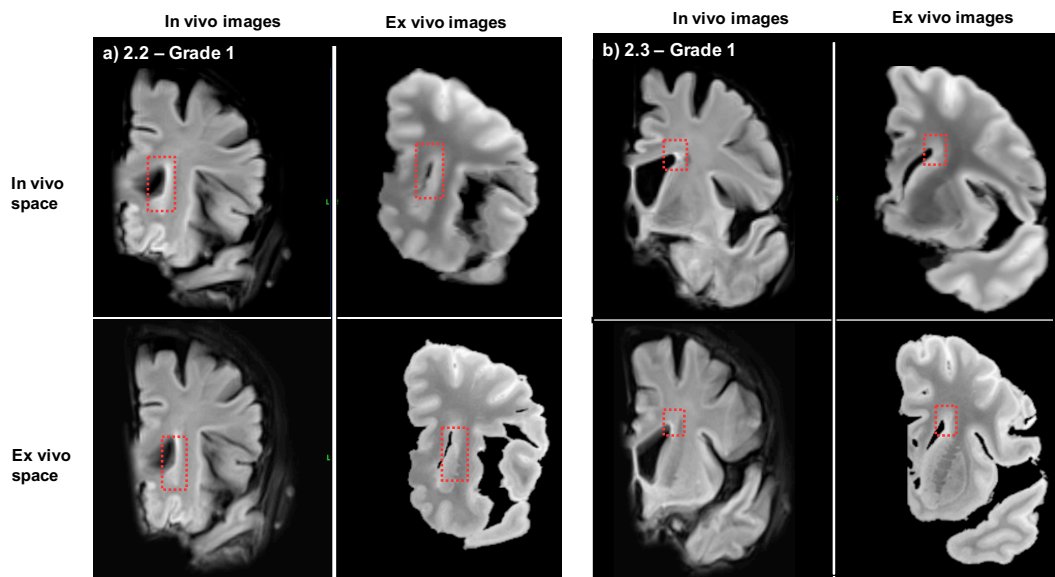


Figure 6.23: Example lesions from Case 2. Lesions are shown on *in vivo* and *ex vivo* images in both *in vivo* space and *ex vivo* space.

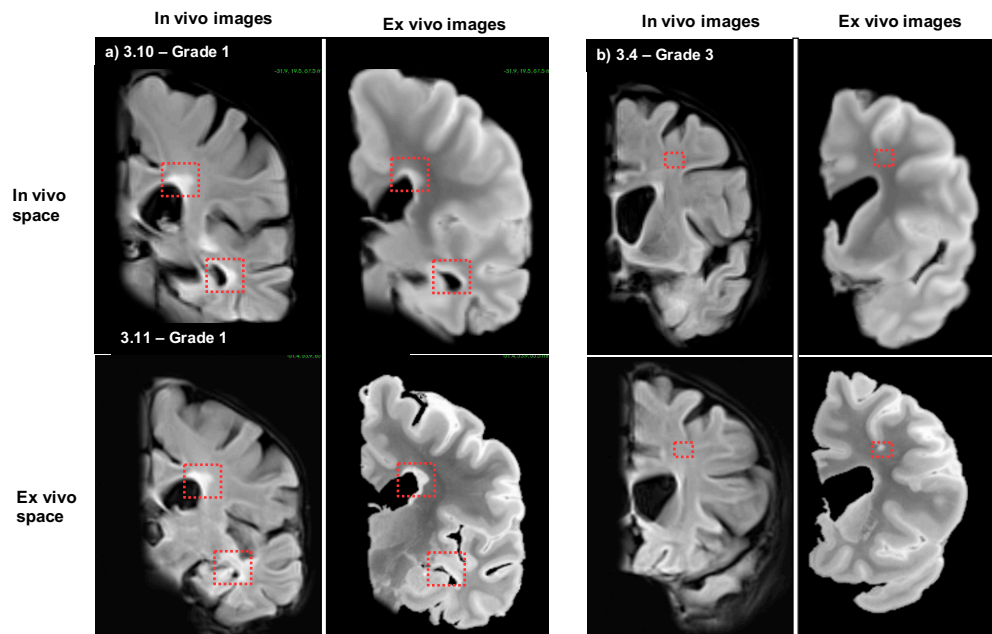


Figure 6.24: Example lesions from Case 3. Lesions are shown on *in vivo* and *ex vivo* images in both *in vivo* space and *ex vivo* space.

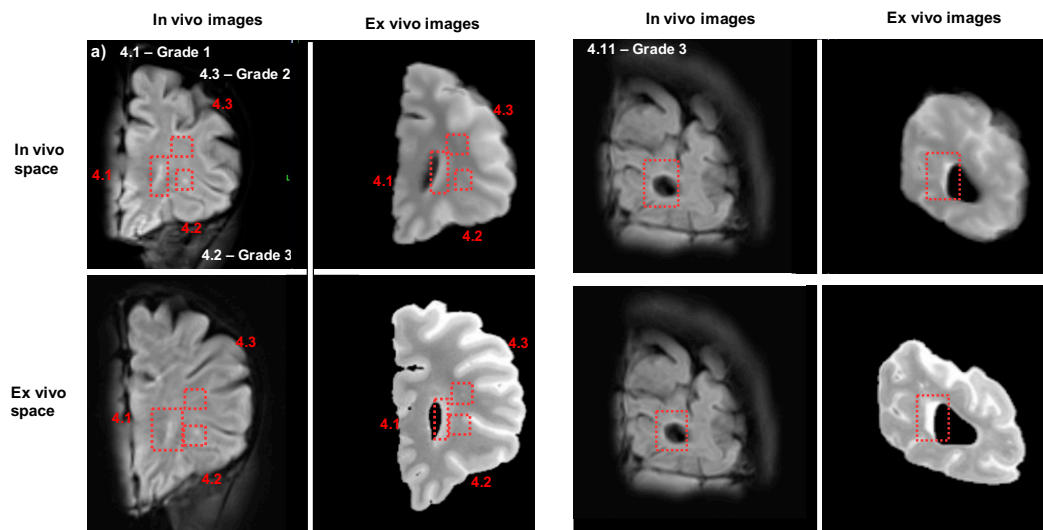


Figure 6.25: Example lesions from Case 4. Lesions are shown on *in vivo* and *ex vivo* images in both *in vivo* space and *ex vivo* space.

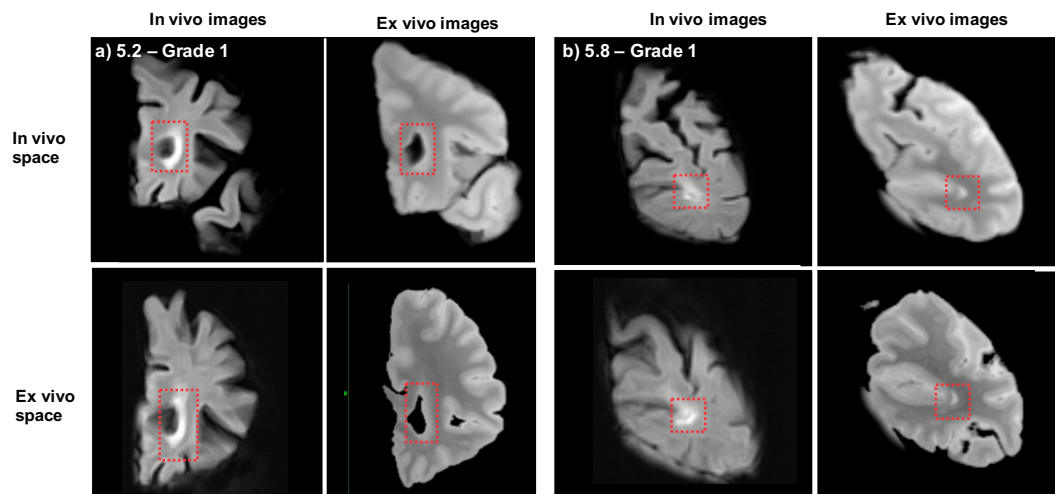


Figure 6.26: Example lesions from Case 5. Lesions are shown on *in vivo* and *ex vivo* images in both *in vivo* space and *ex vivo* space.

6.3.7 Question 5: Can any pathological changes be observed in regions of WMHs?

6.3.7.1 Quantitative assessment of WMH pathology

Results from the mixed effect models showed significant differences in staining of MBP, a marker of myelination, with a reduction in the percentage area stained of 12.5% from NAWM from the same section ($p < 0.001$) and 7.5% ($p = 0.008$) from NAWM from a different section (Table 6.4). No significant differences in the percentage area of staining between the regions of WMH and NAWM were observed in the axonal marker, SMI31. Figure 6.27 shows the difference between the WMHs and NAWM regions in the MBP and SMI31 staining. In type 1 lesions from Case 3 (those that are not macroscopically visible on the brain tissue and so are less typical

Table 6.4: Regression results for difference in percentage area of MBP staining in NAWM vs WMHs

MBP	NAWM	NAWM
	Same section	Different section
Difference in MBP % area stained	12.5	7.5
95% confidence interval	7.6 to 17.5	2.1 to 12.8
<i>p</i> value	<0.001	0.008

Estimates are shown for the % change in area stained by MBP in NAWM regions from region of WMHs. Estimates are shown for NAWM in the same section and in a different section, with 95% confidence intervals. WMH lesions assessed were from four different cases, with two from Case 2, three from Case 3, three from Case 4 and three from Case 5 included in the models.

Table 6.5: Regression results for the percentage area of SMI31 staining in WMHs vs NAWM

SMI31	NAWM	NAWM
	Same section	Different section
Difference in SMI31 % area stained	-0.7	-2.5
95% confidence interval	-4.7 to 3.3	-6.9 to 1.8
<i>p</i> value	0.7	0.2

Estimates are shown for the % change in area stained by SMI31 in NAWM regions from region of WMH. Estimates are shown for NAWM in the same section and in a different section, with 95% confidence intervals. WMH lesions assessed were from four different cases, with two from Case 2, three from Case 3, three from Case 4 and three from Case 5 included in the models.

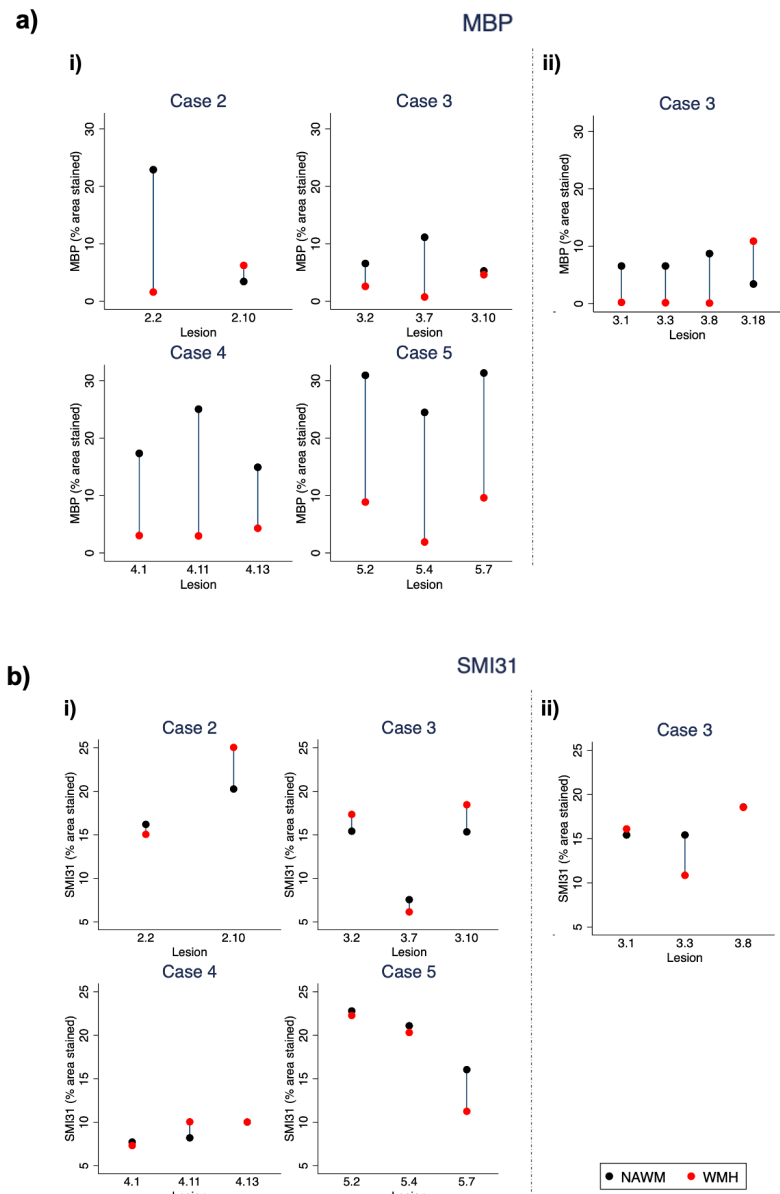


Figure 6.27: Graphs to show the difference in % area of a) MBP and b) SMI31 staining between regions of WMHs and NAWM within the same section. WMHs are labelled according to the lesion guide. In i), the lesions from case 3 are ones classified as not being macroscopically visible at brain cut (type 1, see 6.3.2.2) and therefore less typical of MS plaques. In ii), the lesions from case 3 are classified as macroscopically visible at brain cut (type 2 and 3) and therefore more typical of MS plaques/discolouration.

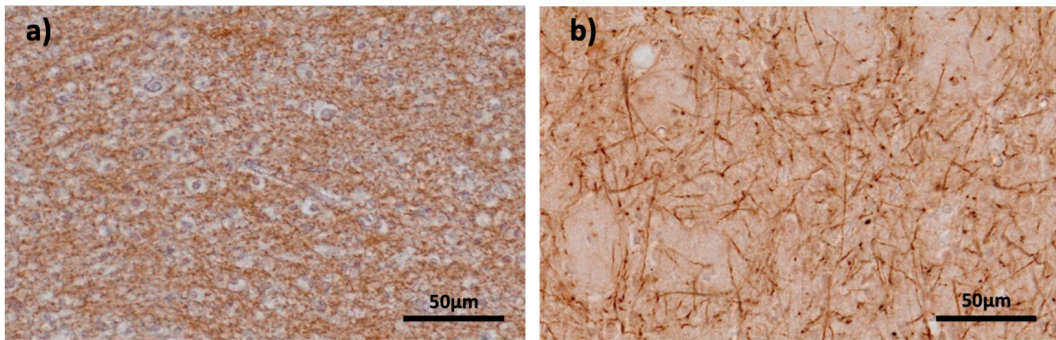


Figure 6.28: Immunohistochemical staining example for the a) MBP and b) SMI31 antibodies. Scale bar represents 50µm.

of MS lesions), generally smaller differences in percentage area stained with MBP between WMHs and NAWM were observed than the other cases, although this was not formally tested. In type 2 and 3 lesions from Case 3, a small decrease in MBP was observed in the majority of lesions, but this was not formally tested due to very small sample size. Examples of the MBP and SMI31 immunohistochemical staining are shown in Figure 6.28.

6.3.7.2 Qualitative assessment of WMH pathology

A general assessment of the H&E and LFB staining highlighted regions of pallor of varying extents. These will be discussed in relation to their appearances on MRI below. The more specific assessment of the ventricular ependyma on the H&E staining in the periventricular WMHs revealed that mild loss (grade 1) was apparent in the vast majority of lesions. One WMH from Case 5, lesion 5.2, demonstrated severe ependymal loss (grade 2) and one WMH from Case 3, lesion 3.8, had an

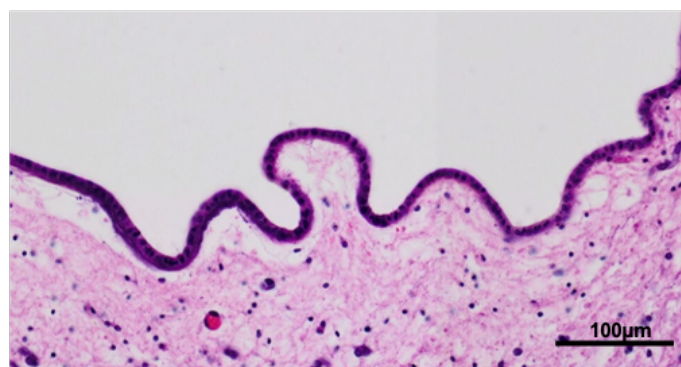


Figure 6.29: A tortuous ependymal layer.

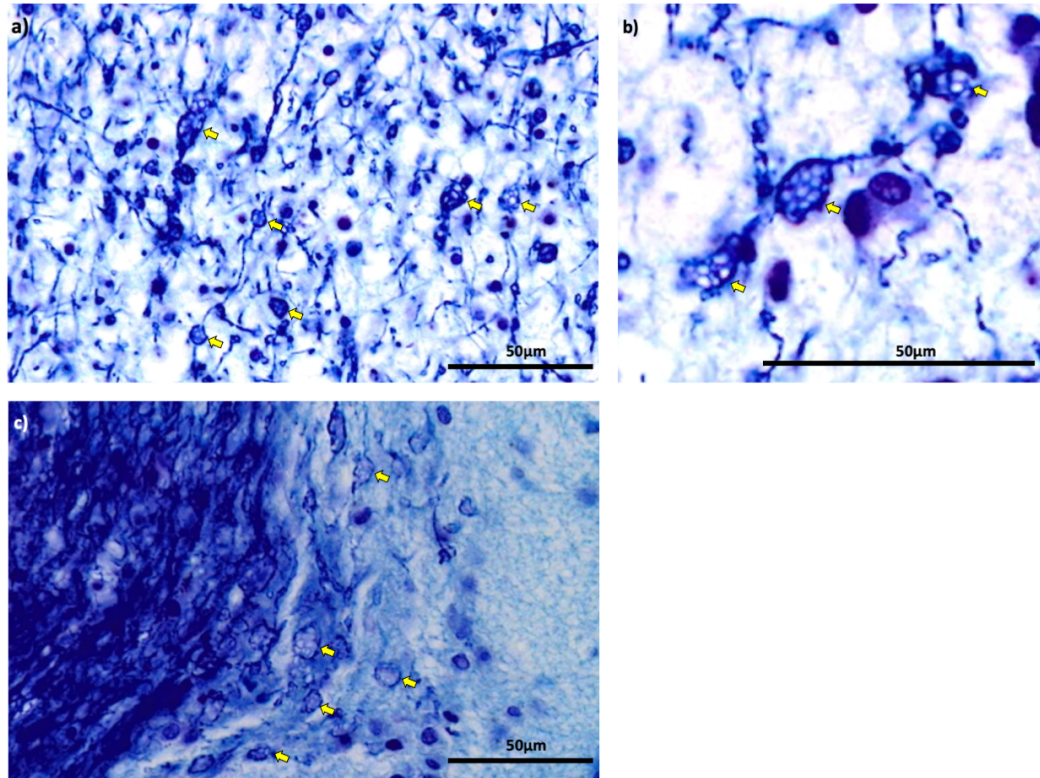


Figure 6.30: Segmental intramyelin oedema in Case 5 (lesion 5.2) in a) and b) and a type 3 lesion from Case 3 (lesion 3.10) in c). Case 5 showed extensive oedema across the large region of myelin pallor, whereas Case 3 showed only a few very localised areas of oedema on the border of the small area of pallor in this lesion.

intact ependyma (grade 0). Some of the periventricular WMHs that were given a grading of 1, also demonstrated an ventricular lining that was tortuous (Figure 6.29). This was most often apparent in regions of the ventricular lining where the ependymal cells had not been lost.

The assessment by the neuropathologist, Dr Zane Jaunmuktane, of the LFB staining in particular revealed an interesting finding. Vacuoles located within the myelin were identified on the LFB staining in some of the periventricular, but not deep, WMHs (Figure 6.30). There appeared to be a spectrum of severity across the cases, with Case 5 demonstrating a very high prevalence of this segmental intramyelin oedema in most of the periventricular WMHs assessed. A few areas of oedema were observed in lesions from Cases 2 and 4, but none were observed in the majority of WMHs from Case 3, the dual MS/ADAD case. A small number of

areas of segmental intramyelin oedema were located in one of the type 1 lesions (not visible macroscopically) from this case, lesion 3.10. The areas of segmental intramyelin oedema were most apparent in large areas of myelin pallor, although this may be due to the density of the myelin staining in other areas masking their appearance. It is worth noting that Case 5 with the highly prevalent oedema, also had the most marked ependymal loss in one of the lesions (the only one to be graded a 2).

General patterns across modalities

Whilst analysing all of the WMHs from this cohort across the *in vivo* MRI, *ex vivo* MRI and histology, differences in the way the lesions appeared across the modalities were observed. Although initially there seemed to be a fair amount of variation in the pathological changes, some broad patterns were observed and are described below and shown in Figures 6.31a-j.

Amongst the sporadic AD cases (Cases 2, 4, 5), there appeared to be a spectrum of pathology in the periventricular WMHs. Some periventricular WMHs presented with a small region of pallor of H&E and LFB staining that was markedly smaller than the lesion observed on the *in vivo* scan. These lesions often also appeared fainter on the *ex vivo* T2-weighted scan. Examples are:

- Case 2, lesion 2.10 (Figure 6.31a). Periventricular WMH at the occipital horn of the lateral ventricle. There is no substantial area of pathological change, but there is a small area of pallor in the H&E and LFB staining restricted to just around the ventricle. WMH is visible on the *ex vivo* scan, but appears less bright (graded 1a, see section 6.3.6). There were very few, if any, segmental intramyelin oedema present.
- Case 5, lesion 5.7 (Figure 6.31b). Periventricular WMH at the occipital horn of the lateral ventricle. There is a small area of pallor of H&E and LFB staining just around the ventricle. The WMH appears less bright on the *ex vivo* scan (graded 1a). Very few segmental intramyelin oedema were observed.

There were some periventricular WMHs that appeared to have more severe

pathological changes. In these lesions, a large region of pallor in H&E and LFB staining with diffuse boundaries was common. These lesions either appeared fairly consistently on the *in vivo* FLAIR and *ex vivo* T2-weighted scans or were fainter (graded 1 or 1a). Examples are:

- Case 2, lesion 2.2 (Figure 6.31c). Periventricular WMH at the frontal horn of the lateral ventricle. There is a large region of pallor in the H&E and LFB staining with a diffuse boundary that is similar in size to the WMH on the *in vivo* MRI. The WMH appearance is similar on the *ex vivo* scan is similar to the *in vivo* scan (graded 1). A few segmental intramyelin oedema were observed. There was tortuosity and some mild loss of the ventricular ependyma.
- Case 5, lesion 5.2 (Figure 6.31d). Periventricular WMH at the frontal horn of the lateral ventricle. There is a large area of pallor in the H&E and LFB staining with a diffuse boundary that is similar in size to the lesion on the *in vivo* MRI scan. The WMH appears less bright and more diffuse on the *ex vivo* scan (graded 1a). There was a very high prevalence of segmental intramyelin oedema and marked ependymal cell loss.

Within Case 3, marked variation in the appearance of WMHs was observed. A proportion of WMHs in this case had very little evidence of pathological change, or a very small region of pallor of H&E and LFB staining that was considerably smaller than the lesion observed on the *in vivo* scan. Some of these lesions appeared similar on the *ex vivo* scan to the *in vivo* scan, but one in particular appeared very bright with a well defined boundary. Additionally these lesions were categorised as type 1 (not visible macroscopically at brain cut). Examples are:

- Case 3, lesion 3.2 (Figure 6.31e). Periventricular WMH at the frontal horn of the lateral ventricle. There is a small region of pallor in the H&E and LFB staining, smaller in area than the WMH observed on the *in vivo* scan. The WMH appears similar on the *in vivo* and *ex vivo* MRI. This lesion was not macroscopically visible at brain cut. There were very few, if any, segmental intramyelin oedema and mild loss of the ependymal lining.

- Case 3, lesion 3.10 (Figure 6.31f). Periventricular WMH in the parietal lobe. Perhaps the most striking WMH of this type as it appears very bright and very well defined on the *ex vivo* scan, more so than any other lesion from any case. However there were minimal pathological changes, with just a small region of pallor in the H&E and LFB staining, and in a much smaller area than the WMH on the scans. Some intramyelin oedema were observed and mild loss of the ependymal lining.

In Case 3, WMHs with very visible pallor and well demarcated boundaries in the H&E and LFB staining were also observed. These were lesions that also had clearly demarcated boundaries on the *ex vivo* scan and categorised as type 2 at brain cut (clearly demarcated visible lesions), Examples are:

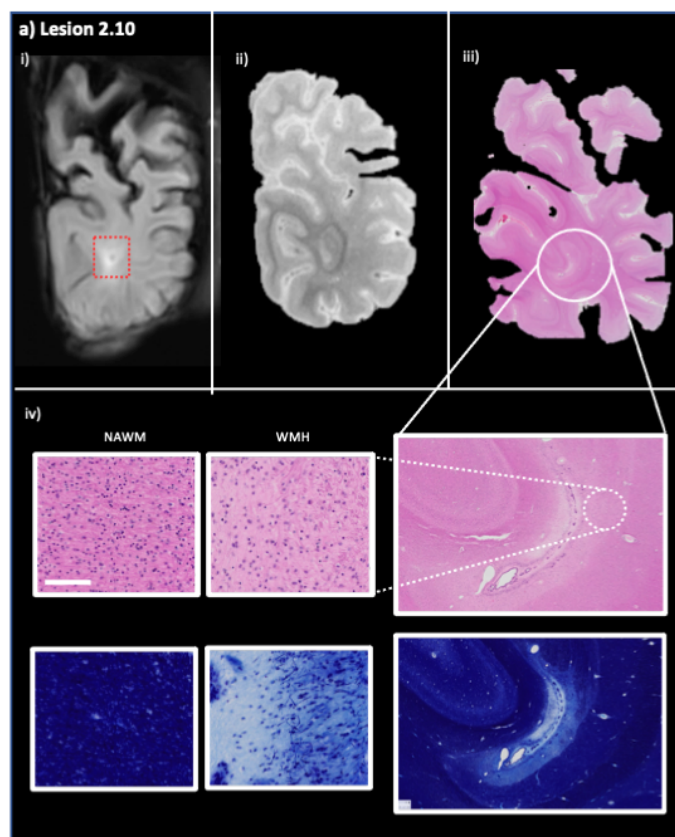
- Case 3, lesion 3.1 (Figure 6.31e). Periventricular WMH at the frontal horn of the lateral ventricle. The lesion is well demarcated on the *ex vivo* MRI scan and on the H&E and LFB staining. This WMH was also macroscopically visible at brain cut and typical of an MS plaque. There was no segmental intramyelin oedema observed and mild loss of the ependymal cells.
- Case 3, lesion 3.8 (Figure 6.31g). Periventricular WMH at the temporal horn of the lateral ventricle. The lesion is very well demarcated on the H&E and LFB staining, similar in appearance on the *ex vivo* MRI scan to the *in vivo* scan, and macroscopically visible at brain cut, resembling an MS plaque. There were no segmental intramyelin oedema observed and the ependymal lining was intact.

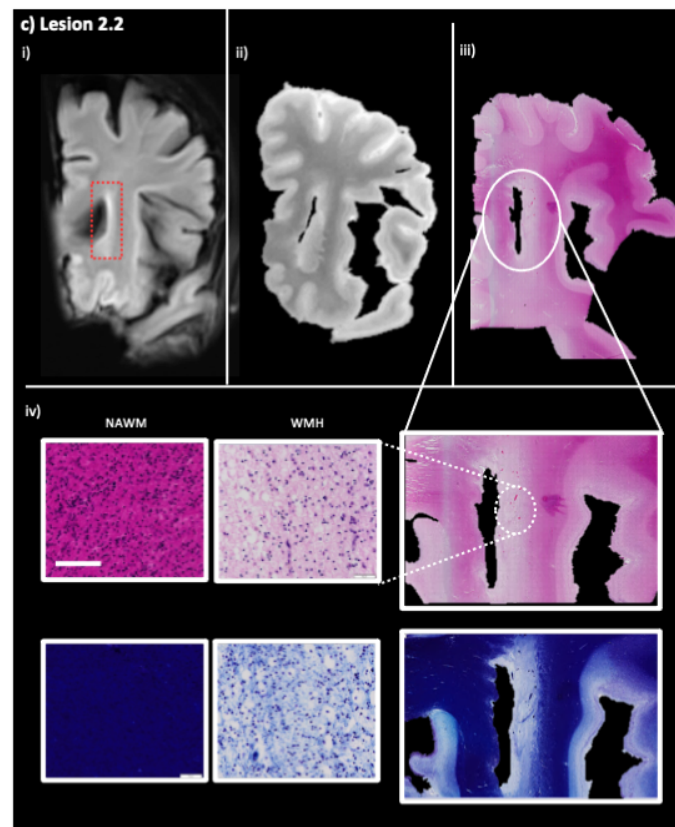
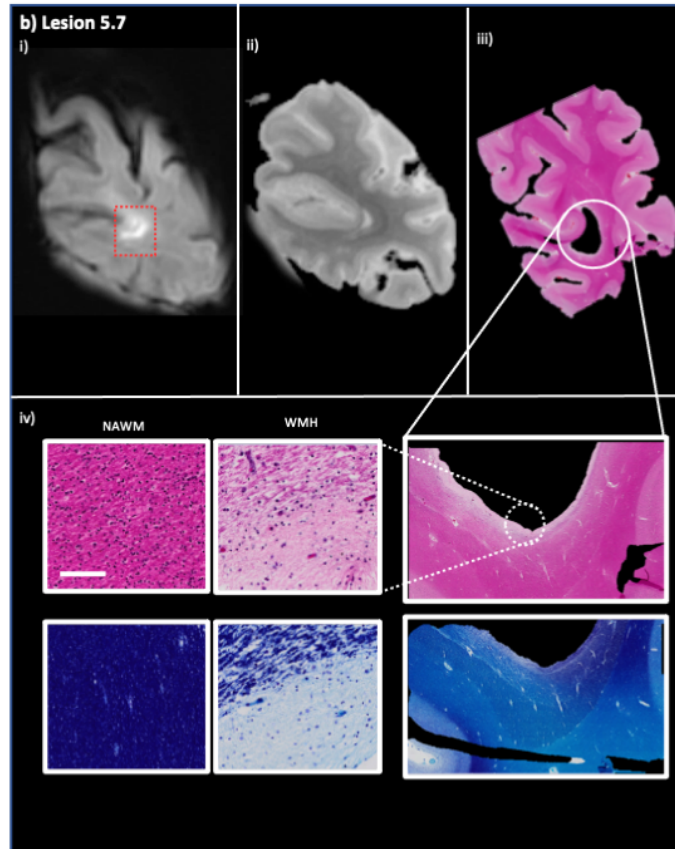
Case 3 also had two of the very few non-periventricular lesions observed in our small cohort, and the only two to be assessed pathologically. It is hard to identify any patterns from these lesions as one was classified as type 2 and so typical of an MS plaque, and one was not macroscopically visible and so classified as type 1.:

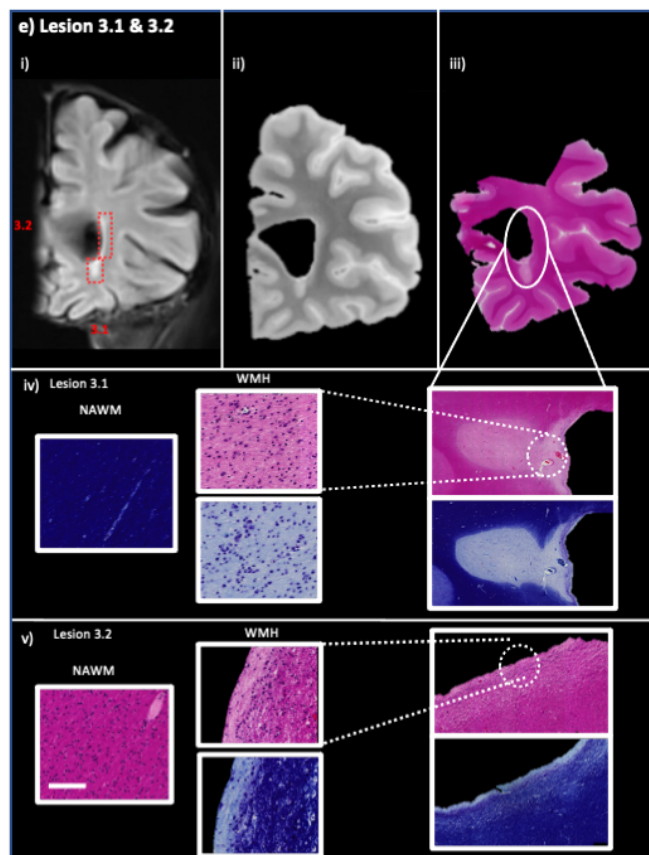
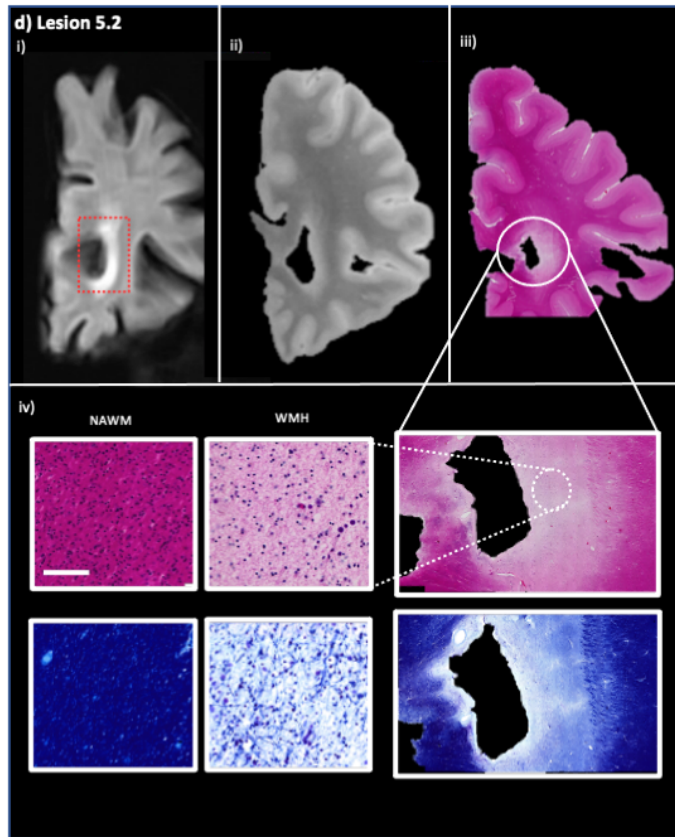
- Case 3, lesion 3.3 (Figure 6.31h). Juxtacortical WMH in the frontal lobe, classified as type 2. Lesion is very well demarcated on the H&E and LFB

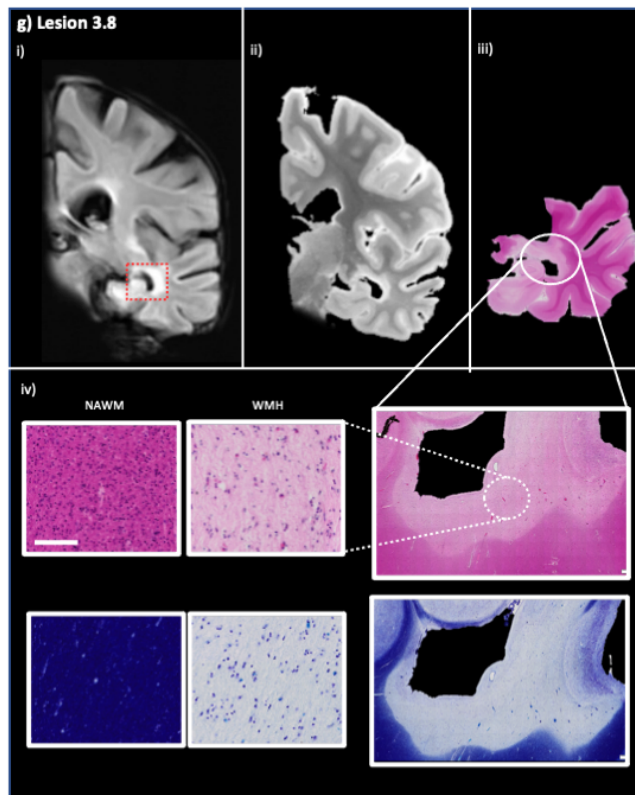
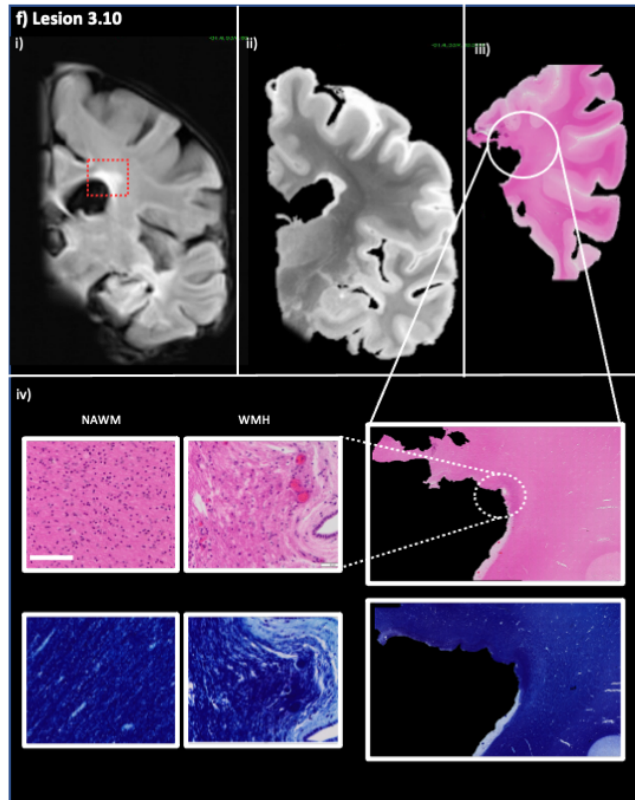
stains, similar in appearance on the *ex vivo* MRI scan to the *in vivo* scan, and macroscopically visible at brain cut, resembling an MS plaque. There were no segmental intramyelin oedema.

- Case 3, lesion 3.7 (Figure 6.31j). Juxtacortical WMH in the parietal lobe, classified as type 1. There appears to be no changes to the H&E and LFB stains in the region of the WMH, with no evidence of segmental intramyelin oedema. The WMH appears similar on the *in vivo* and *ex vivo* MRI.









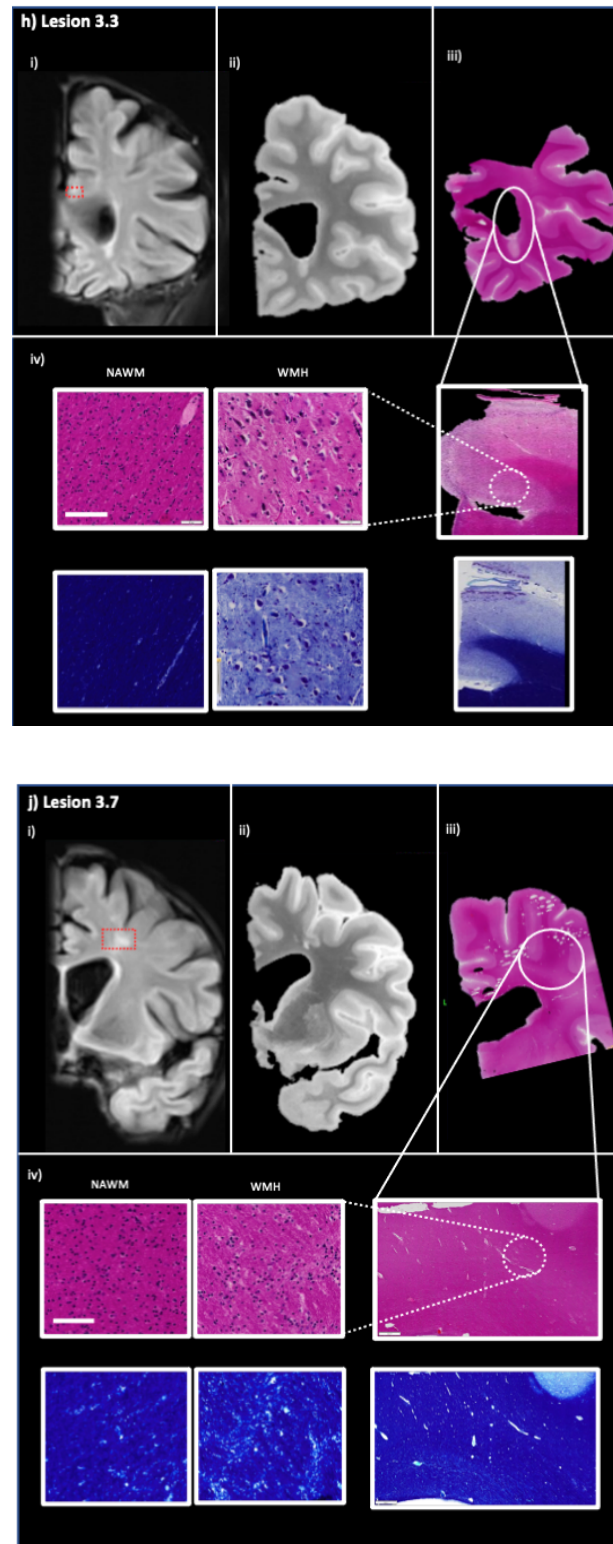


Figure 6.31: In vivo MRI, *ex vivo* MRI and histological staining for example lesions. In i) the *in vivo* FLAIR is shown with the WMH outlined in red, registered to the *ex vivo* T2-weighted image in ii). The corresponding H&E stained section is in iii), with magnified areas of H&E and LFB staining shown in iv). Scale bar represents $100\mu\text{m}$.

6.4 Discussion

In this work an *ex vivo* MRI and histology pipeline was developed to answer several methodological and biological questions surrounding the visualisation of WMHs both in life and after death, and to determine the pathological basis of WMHs. This study demonstrated that such a pipeline was successfully designed and implemented, enabling high quality *ex vivo* MRI images to be obtained that could then be registered with the *in vivo* imaging. Although WMHs identified on *in vivo* scans were generally evident on *ex vivo* MRI, they often appeared less bright with more diffuse boundaries. Difficulties were encountered with the registration of the histopathological images and *ex vivo* images, whereby the difference in sampling technique from which the software was designed for, lead to the accumulation of multiple errors. Registration was possible in some sections though, indicating the potential of this method with further optimisation. The quantitative work here provides evidence to suggest that the pathological basis of WMHs may be more related to myelin loss than axonal degeneration. This was the case for both WMHs that were typical of MS plaques and WMHs that did not resemble MS lesions, in the case with dual MS and AD pathology. However on qualitative examination of individual lesions, different patterns were observed in WMH appearance on each of the image modalities. Varying degrees of myelin pallor were observed amongst periventricular WMHs, and a more detailed assessment revealed the presence of segmental intramyelin oedema in Case 5 in particular. There was also some evidence of disruption to the ependymal lining of the ventricle. Distinct imaging and pathological observations were made in the unusual case with the dual ADAD/MS diagnosis, whereby very clearly demarcated lesions on *ex vivo* MRI could be accompanied either with or without corresponding myelin pallor.

WMHs are MRI signatures commonly observed on *in vivo* imaging, a method that does not provide information on their histopathological basis. Pathological confirmation of WMHs is only possible with *post mortem* investigations, often years after the most recent *in vivo* scan and by which time the whole brain, including any WMHs, may have changed quite considerably. *Ex vivo* MRI can also offer more

beyond just validation, with the opportunity to scan for longer periods and with new sequences, enabling the acquisition of higher resolution images that have the potential to uncover more subtle pathological changes. You can also obtain different types of images (such as quantitative imaging), which can tell you more about the underlying tissue structure.

It is important to compare the appearance of WMHs on *in vivo* MRI images, *ex vivo* MRI images and on histochemically/immunohistochemically stained sections, in order to provide the best possible chance at uncovering their pathological basis. Very little research has been carried out assessing the appearance of WMHs on both *in vivo* and *ex vivo* imaging (Arfanakis et al., 2020), with no study registering together the images from all three modalities in order to accurately assess what pathological changes underlie specific hyperintense MRI signals. The design of the pipeline used in this study, in particular the brain sampling protocol, will enable the future registration of *in vivo*, *ex vivo* and histopathological images.

Although previous studies of WMHs that have combined *in vivo* imaging, *ex vivo* imaging and histology are extremely rare, there is a small body of literature that has assessed histopathological correlates of either *ex vivo* or *in vivo* imaging. A large proportion of the work using both *ex vivo* MRI and histology to look at the pathological underpinnings of WMHs has been carried out over 20 years ago, when both MRI and histological techniques were not as advanced as they are now. Studies often used very small and mixed cohorts, only used low field MRI, included no immunohistochemistry and only used very basic and crude registration techniques. These studies found an extensive range of pathological correlates relating to WMHs, including a loss of myelin, axons and oligodendrocytes, astrogliosis, dilation of perivascular spaces, activated macrophages and fibrohyalinotic and arteriosclerotic vessel changes (Awad et al., 1986, Braffman et al., 1988, Fazekas et al., 1991, Mascalchi et al., 1989, Revesz et al., 1989, van Swieten et al., 1991).

Previous studies have tended to either assess *ex vivo* imaging and its pathological correlates (Fernando and Ince, 2004, McAleese et al., 2015, Young et al., 2008) or have looked at *in vivo* imaging and its pathological correlates (Alosco et al.,

2018). The novelty of this study is the use of *ex vivo*, *in vivo* and histopathological images of WMHs to more accurately establish the relationship of pathological findings to *in vivo* imaging. This study used both the *in vivo* and *ex vivo* images to locate the WMHs of interest and then additionally carried out alignment of the two modalities using a systematic registration approach. Additionally this study attempted registration of the *ex vivo* MRI scan and the histopathological images using a sophisticated automated tool, as opposed to the crude matching used in previous studies. This work had the aim to develop an integrated, single pipeline to move closer to the ultimate goal of developing an entirely novel software tool to predict the underlying pathology associated with WMH seen on *in vivo* imaging.

6.4.1 Question 1: Can high quality *ex vivo* MRI images be obtained?

The careful coordination of the brain donation, brain fixation and MRI scanning processes set out by the detailed pipeline, enabled the high quality *ex vivo* T2-weighted images to be obtained for all cases in this study. A voxel size of 0.5mm^3 , combined with the averaging of all five T2-weighted scans together meant that the image resolution was excellent, and superior to the *in vivo* FLAIR images. Although the largest increase in image quality was observed with the addition of two acquisitions together, an increase in image quality was still observed with the addition of the fifth acquisition. Increasing the number of acquisitions above five to assess for any further benefit to image quality was not tested, largely due to the important aim of this study to be reproducible and scalable to a larger study. Five T2-weighted acquisitions meant that the structural imaging protocol fit into one hour of scanning time. This enables the addition of other imaging modalities within a sensible scanning time frame, such as the diffusion weighted imaging and the SWI obtained (but not analysed) in this study. There have been previous *ex vivo* imaging studies that have used long MRI protocols, including those with a total scan time of up to 48 hours (Pallebage-Gamarallage et al., 2018). Along with the question of feasibility posed by that length of scan time for a large number of cases, the study presented here used a busy hospital scanner meaning that long scanning slots were simply not

available. Indeed, several of the imaging sessions used for the cases in this study were split across multiple days.

6.4.2 Question 2: Is registration of *in vivo* and *ex vivo* MRI scans possible?

Very few, if any, previous studies have attempted the registration of *in vivo* and *ex vivo* brain MR images. Previous studies using registrations of this nature have often been in animal models (Holmes et al., 2017) or in non-brain tissue such as the prostate (Orczyk et al., 2012). Where human brain has been used, this has only been on surgically resected brain specimens (Goubran et al., 2015) or on the hippocampal region (Wisse et al., 2016). A recent study by (Maranzano et al., 2020) carried out *ex vivo* imaging with the brain in situ, which enabled registration of both *in vivo* and *ex vivo* images to the same standard neuroanatomical template.

In this project a reasonable registration of *in vivo* and *ex vivo* scans was achieved using a non-linear registration in both the *ex vivo* and *in vivo* spaces. Although the registration was not accurate enough to enable voxel to voxel correspondence between scans, it was good enough as a guide to corresponding regions. Before registration, matching up analogous areas on both images was highly challenging; something that had implications for the assessment of WMH change and also the identification of corresponding landmarks for the registration parameter optimisation.

There are considerable challenges faced when registering *in vivo* and *ex vivo* images largely due to the significant deformations caused by the processes of removal and fixation of the *post mortem* brain. The most common deformation that occurs is the collapse of the ventricles due to the lack of pressure that was previously provided by the CSF and supporting structures. This ventricular collapse leads to structures in the surrounding areas to also become deformed, something that could be problematic in studies of WMHs where periventricular locations are highly important. Additionally the long interval between the *in vivo* and *ex vivo* scans, ranging from 4 to over 9 years in this cohort, means that considerable atrophy could have occurred and could further complicate the registration.

There are various ways in which the difficulties in registering *in vivo* and *ex vivo* imaging could be overcome. To minimise the need for much registration at all, imaging of brains *in situ* could be carried out. This could be in the form of cadaveric imaging (Woollacott et al., 2018) or imaging of fixed and transected heads (Maranzano et al., 2020). However the scalability of this type of imaging is questionable due to the techniques being more logistically challenging than current brain banking donation protocols. Alternatively more localised registrations could be carried out, focusing on a particular areas of interest in order to give much better correspondence in those regions. As was carried out for hippocampal registrations in Wisse et al. (2016), local registrations could be a possibility to improve correspondence in periventricular areas. If the landmark-based registration attempted in this study could be optimised, the use of landmarks in a more focused periventricular area may provide a more accurate registration, in which the collapsed ventricles on the *ex vivo* scan could be opened up to match the *in vivo* scan.

6.4.3 Question 3: Is registration of histological sections to *ex vivo* MRI images possible?

An even greater challenge than registering *in vivo* and *ex vivo* MRI, is the registration of histological sections to MRI scans due to the substantial differences between the two techniques. Compared to the microscopic detail provided by histology, MRI enables a more general overview of the brain. It is this difference that not only holds great potential for understanding global brain changes on a microscopic level, but presents several registration challenges. Firstly, there is a large difference in resolution between MRI images and histological images, due in part to the considerable difference in slice thickness between the typically $<15\mu\text{m}$ histological sections and the thick MRI slices (typically $>0.5\text{ mm}$). The partial volume effects in the MRI images makes directly comparing heterogeneous tissues challenging. Another related issue is that MRI slices are usually contiguous, whereas the process of sampling *post mortem* brain into blocks results in large sampling gaps between histological sections. A further issue with the precise matching of MRI and histology is the tissue deformations that occur as a result of histology analysis. Histological sections

become distorted due to the cutting, processing, sectioning and mounting procedures, complicating the registration to the *ex vivo* MRI image further.

In the majority of the literature assessing the pathology of WMHs using *ex vivo* MRI and histology correlations, manual registration techniques of the two modalities involving the matching up of anatomical landmarks is most commonly used (Awad et al., 1986, Braffman et al., 1988, Marshall et al., 1988, Mascalchi et al., 1989, van Swieten et al., 1991). Although simple, this method can be very time consuming and has issues with accuracy and reproducibility, meaning the application to larger datasets may not be feasible. Other techniques have minimised any necessary registration steps either by carrying out MRI of small segmented regions that are then directly sectioned and stained, or by carrying out whole slice histology (Fernando and Ince, 2004, Fernando et al., 2006, Gouw et al., 2008a, Moody et al., 2004, Revesz et al., 1989). However imaging the whole brain (or hemisphere) is more beneficial than small regions, not only because of the increased efficiency and ease of a single scan, but the preservation of landmarks within the context of the brain enables better region of interest identification. Additionally, fewer artefacts related to brain tissue edges will be present on a whole brain MRI scan, compared to multiple MRI scans of small regions. The disadvantage to using whole slice histology is the increased cost and labour intensity, meaning it would not be feasible on a large dataset.

In recent years, technological advances have enabled a move towards more automated approaches to registration of histology and *ex vivo* MRI images (Iglesias et al., 2018, Mancini et al., 2019, Pallegage-Gamarallage et al., 2018, Pichat et al., 2018). These more complex methodologies typically involve using an intermediate modality, commonly blockface photographs, to which both the histological and *ex vivo* images can be registered using dedicated software.

The registration software used in this study was designed for a dataset where more complete coverage is achieved through the sampling of histological sections throughout the entire brain (Iglesias et al., 2018, Mancini et al., 2019). This minimises gaps in the data, both between brain blocks and within the stacks of sections

that make up the brain blocks. It is hugely time consuming and labour intensive to sample the brain in this way and so, with both the time constraints of this project and the scalability to a larger dataset in the future in mind, only a few sections from each region of interest block were sampled. An adapted version of the software therefore had to be used in this study, but this simplification was unable to account for variations in the histological data. Slight deviations in slice thickness or parallelity, or the fact that the histological sections were not obtained from the exact top of the block resulted in errors accumulating quickly, and in some cases more than others.

Successful registrations of the *ex vivo* MRI images into the space of the histological sections were achieved for Case 5 and some blocks from Case 3. This demonstrates that, with further optimisation, registration of a dataset of this nature using this pipeline is feasible. Registration of the *ex vivo* image into the histology space allows precise matching of anatomical regions, so the pathological changes underlying the exact area of hyperintensity identified on the MRI scan can be identified. Similarly, any pathological changes identified on the histological sections can be assessed for any difference in signal in the exact same region on the MRI scan. Although only the *ex vivo* scan was registered in this study, an important next step would be to register the *in vivo* MRI image to the histology. By aligning *in vivo*, *ex vivo* and histopathological images, the relationship of pathological findings to *in vivo* imaging can be more accurately established. This will aid in the understanding of how distinct features of WMHs seen during life translate to underlying pathology.

6.4.4 Question 4: Can similarities or differences in WMHs between the last *in vivo* MRI and the *ex vivo* scan be observed?

Very few studies have compared the appearance of WMHs on *in vivo* and *ex vivo* images. Arfanakis et al. (2020) demonstrated that the majority of WMHs had the same Fazekas score on both scans, with a sizeable minority demonstrating an increase in

WMH burden on the *ex vivo* scan and no lesions demonstrating a decrease. Similarly in this study, the large majority of the WMHs were visible over a similar area on both the *in vivo* and *ex vivo* scans in all of the five cases. Six lesions were newly appearing or had increased on the *ex vivo* scan compared to the *in vivo* scan and only one lesion had disappeared.

A relatively small number of WMHs were found to have newly appeared or increased over time. With the large time intervals between the *in vivo* and *ex vivo* scans for the cases in this study, more progression in WMH burden may have been expected. Indeed, Arfanakis et al. (2020) showed an association of increased WMH burden with longer time intervals between the *in vivo* and *ex vivo* scans. A major contributing factor to this difference may be the significantly younger age of individuals in this study; between 52 to 68 compared to an average age of ~ 90 in the study by Arfanakis et al. (2020), as the progression of WMHs has been demonstrated to be associated with increasing age (van Dijk et al., 2008, van Leijssen et al., 2017b). Additionally, a higher baseline lesion load has also shown to be a predictor of a greater WMH progression (Sachdev et al., 2007, van Leijssen et al., 2018). In general, the cases in this study had a relatively low WMH burden, which may account for the lack of progression seen.

In this study, a large number of WMHs appeared much fainter on the *ex vivo* scan. There are a number of possibilities as to why this was the case, ranging from methodological to biological. An important consideration is the inherent differences between scanning *post mortem* tissue and scanning a patient in life. Formalin fixation of *post mortem* tissue to prevent degradation can cause various structural changes and tissue distortions (Fox et al., 1985). Fixation has also been shown to alter various MRI properties such as shortening T1 and T2 relaxation times, and on DTI parameters (Richardson et al., 2014, Shatil et al., 2018). Temperature is also a factor in tissue properties important for MRI; the $\sim 15^{\circ}\text{C}$ difference between the body temperature of a living person and a *post mortem* sample at room temperature means adaptations of MRI protocols are necessary (Birkel et al., 2014). Any of number of these factors could therefore result in WMHs on *ex vivo* scans appear-

ing differently to those on *in vivo* scans. Additionally, the brighter appearance of WMHs on the *in vivo* scans especially in periventricular areas, could be due to edge artefact that is not apparent on the higher quality *ex vivo* scan.

Some WMHs though, for example lesion 3.10 on Figure 6.24 and lesion 4.11 on Figure 6.25 appear brighter on the *ex vivo* scans, demonstrating that *ex vivo* scanning does not result in uniformly fainter lesions. Indeed, the fainter-appearing WMHs were by far the most common in two of the cases, with 70% of lesions appearing fainter in Case 1 and 88% on Case 5 (13 - 23% on other three cases). As the *ex vivo* T2-weighted scanning protocol was kept the same for all cases, this variability between cases could potentially be due to those differences in tissue properties caused by a longer *post mortem* delay or fixation time (Shatil et al., 2018). However since the *post mortem* delay times and the fixation times were among the shortest for Case 1 and 5, and the fact there was still some within-case variability in faintness, this is unlikely to be the case.

The difficulty of assessing WMH change over time in this study is the lack of characterisation of the differences in WMH appearance on *ex vivo* and *in vivo* MRI imaging, and how much of this is attributable to methodological factors. In the literature on longitudinal *in vivo* studies, the most widely accepted view is that WMHs gradually increase over time without resolving. Numerous studies have shown WMH increases over time, with values ranging 0.1 to 2.2ml/year (van Leijssen et al., 2017b). The regression of WMHs is less well documented, with some studies reporting decreases in volume over time, but then either not commenting on the relevance or attributing the reductions to measurement error (Gouw et al., 2008b, Sachdev et al., 2007, van Leijssen et al., 2017b). Recently, several studies have more directly considered reductions in WMHs over time. Regression of WMHs has been reported in longitudinal imaging studies of the elderly (van Leijssen et al., 2017a) and AD patients (Ramirez et al., 2016), with studies of stroke patients demonstrating WMH regression in up to a third of patients (Cho et al., 2015, Wardlaw et al., 2017). Some studies have assessed the clinical relevance of WMH regression with mixed findings; van Leijssen et al. (2019) found no difference

in cognitive decline between individuals with stable and regressing WMH regression, whereas Al-Janabi et al. (2019) found that WMH regression is associated with decreased brain atrophy and improved cognition compared to WMH progression.

Several mechanisms have been proposed as underlying WMH regression. The observed decline could be methodological and due to registration or segmentation errors. Similarly, there could be a radiological explanation, whereby partial volume effects in thick slice FLAIR imaging could result in WMHs being missed. Alternatively, WMH regression could be a real biological phenomenon, such as the result of a tissue oedema that then reduces or due to improved control of vascular risk factors (Wardlaw et al., 2015). An apparent decrease in WMH volume could also be a result of generalised atrophy occurring throughout the brain.

6.4.5 Question 5: Can any pathological changes be observed in regions of WMHs?

In the quantitative analysis of myelin loss, significant differences were observed in the amount of MBP staining between regions of WMHs and NAWM. This is in agreement with the previous literature on the pathology underlying WMHs, where myelin changes were a very common finding (Awad et al., 1986, Fazekas et al., 1993, Mascalchi et al., 1989, McAleese et al., 2017, Moody et al., 2004, Munoz et al., 1993, Murray et al., 2012, Roseborough et al., 2017). Both deep and periventricular WMHs have been shown to be related to loss of myelin, although some studies have suggested that loss of myelin is more severe in periventricular WMHs (Murray et al., 2012). Myelin loss has been reported to be on a spectrum, ranging from mild myelin pallor thought to be related to oedema (Fazekas et al., 1993, Moody et al., 2004, Munoz et al., 1993), to complete loss of myelin (Awad et al., 1986, Mascalchi et al., 1989). A spectrum of myelin loss was evident in the cases investigated here, with some periventricular WMHs only showing very small areas of mild pallor of the LFB and MBP stains, compared to a much larger and more complete loss in others.

In a more detailed assessment of myelin pathology, segmental intramyelin oedema were identified within regions of myelin pallor in Case 5 in particular.

Although this finding does not seem to be well characterised in humans, similar findings are detailed in one study by Cognat et al. (2014) in a mouse model of Cerebral Autosomal Dominant Arteriopathy with Subcortical Infarcts and Leukoencephalopathy (CADASIL) with prominent white matter pathology. This study used electron microscopy to identify vacuoles within the myelin sheath, typically in the innermost layer (see Figure 6.32). They found no apparent association with blood brain barrier dysfunction, and the changes in myelin were hypothesised to occur prior to axonal degeneration or oligodendrocyte loss. The authors proposed a mechanism relating to a failure in water homeostasis, leading to an accumulation of water and ion between the myelin lamellae. Supportive of this theory is the fact that ion channel disorders present with white matter oedema in vacuoles within myelin sheaths (Depienne et al., 2013, van der Knaap et al., 2012). Others have theorised the oedemas in the myelin could be an unknown consequence of demyelination (Duering et al., 2018), or alternatively a failure of clearance mechanisms such as the glymphatic system (Mestre et al., 2017). In light of the findings here and elsewhere (Fernando et al., 2006, Scarpelli et al., 1994, Scheltens et al., 1995, Shim et al., 2015, Simpson et al., 2007a) of a role for ependymal cell disruption in periventricular WMHs, CSF infiltration through the damaged ventricular lining is also a consideration. This could account for the considerably more prevalent intramyelin oedema in Case 5, which also demonstrated the greatest degree of ependymal destruction. Alternatively the more marked presentation in this case may be due to a more advanced myelin loss or abnormality than the other cases. Indeed (outside of the unusual Case 3) this case had the highest WMH burden and the most marked myelin pallor, both in the quantitative and descriptive analysis.

Those periventricular WMHs on the lower end of the severity spectrum, where pallor on H&E and LFB staining was evident in a smaller area than on the *in vivo* scan, often also appeared less bright on the *ex vivo* scan. It is possible that these lesions may be showing signs of regression, which would also be of importance for all the lesions that appear fainter on the *ex vivo* scan compared to the *in vivo* scan (discussed in section 6.4.4) as it could signify a biology rather than methodological

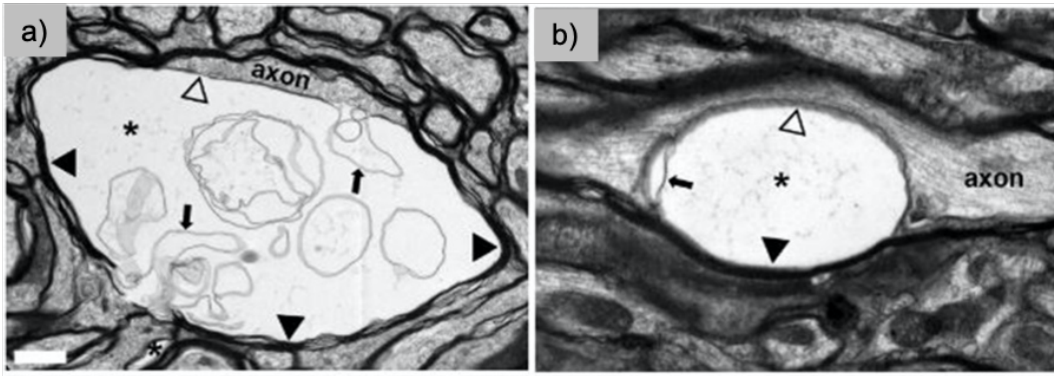


Figure 6.32: Figure from (Cognat et al., 2014) showing segmental intramyelin oedema using electron microscopy. In a) a typical vacuole (star) in the innermost layer of the myelin sheath is shown. The vacuole separates the axon from its myelin sheath (black arrowheads) and contains multiple aberrant myelin sheets (arrows). Note the thin myelin sheet (empty arrowhead) at the interface between the axon and the vacuole. In b) a longitudinal section of a myelinated fiber containing a vacuole in the innermost layer of the myelin sheath is shown. Note how the axon is squashed against one side of the sheath and separated from the vacuole by a thin layer of myelin. Scale bar represents a) $0.5\mu\text{m}$ and b) $1.3\mu\text{m}$.

phenomenon. However, this is not always the case for WMHs that appear fainter with more diffuse boundaries on the *ex vivo* scan; lesion 5.2 from Case 5 appears less bright and with a more diffuse boundary compared to the *in vivo* scan, but it accompanied with a large region of pallor in the H&E, LFB and MBP staining, indicating myelin loss.

It should be noted that the periventricular WMHs that appeared on the lower end of the severity spectrum in terms of the pathology assessed, were most commonly found to be at the occipital horn of the lateral ventricle. Those that had more extensive pathology, were often found to be at the frontal horn of the lateral ventricle. Although the number of cases and brain regions used in this study is too small to be able to draw any conclusions, regional variations in WMHs have been previously reported. McAleese et al. (2017) demonstrated a role of Wallerian degeneration in the pathogenesis of parietal WMHs, triggered by AD pathology. In non-demented patients, WMHs are more prevalent in the frontal region and more likely to be due to CVD (Tullberg et al., 2004). There is also evidence to suggest that CAA could be a factor in posterior presentations of WMHs (Ryan et al., 2015).

Differences in WMHs between periventricular regions versus deep has been well documented, with suggestions that periventricular WMHs were more likely to be due to breakdown of the ependymal lining (Fernando et al., 2006, Scarpelli et al., 1994, Scheltens et al., 1995, Shim et al., 2015, Simpson et al., 2007a) compared to deep WMHs that were more likely to be ischaemic (Gouw et al., 2011, Moody et al., 2004, Smith et al., 2000). However, findings were often not as clear cut with the suggestion that the severity of WMHs is more important than location in terms of pathological similarities, with larger diffuse periventricular WMHs and confluent deep WMHs corresponding to more severe tissue changes of ischaemic origin (Chimowitz et al., 1992, Fazekas et al., 1993). It was hard to assess any such regional differences in this study, as pathological investigations were carried out mainly into periventricular WMHs, with only two deep WMHs assessed from the dual ADAD/MS case. However ependymal lining dysfunction was evident in the vast majority of the periventricular WMHs assessed and could potentially be accounting for the small (or large in some lesions) area of pallor commonly observed adjacent to the ventricle in H&E and LFB staining. Indeed, ependymal lining dysfunction has shown associations with demyelination in previous studies (Chimowitz et al., 1992, Fernando et al., 2006, Simpson et al., 2007a). Further staining with immunohistochemical ependymal markers to assess dysfunction would be helpful to investigate this further.

There is a considerable amount of variation observed in the WMHs within Case 3, with a diagnosis of both ADAD and MS. Whether this is because the WMHs are a result of two different disease processes is unclear and would be very difficult to uncover with any degree of certainty. On the one hand, there are lesions that appear more similar to the other sporadic AD/PCA cases, whereby there is very little pathological change underlying the WMH location on MRI and they do not appear macroscopically on the brain tissue. Some of these lesions appear similarly faint in nature and with diffuse boundaries on the *ex vivo* scan, but one lesion in particular appears brighter on the *ex vivo* scan and with very well demarcated boundaries. It is unclear as to the pathological basis of this lesion, as the histological and immuno-

histochemical markers used in this study are clearly not reflecting the underlying pathology. As this WMH appears so different on the *ex vivo* scan to any of the other lesions in this or the other cases, a shared pathogenesis with lesions in the sporadic AD/PCA cases is maybe less likely.

On the other hand there are those lesions in Case 3 that were macroscopically visible and well circumscribed, with very clearly demarcated H&E and LFB pal-lor. These lesions were identified by the neuropathologist as being typical of MS plaques. The characteristic pathological hallmark of MS is inflammatory lesions that result in demyelinating plaques. Axons are relatively preserved in the early stages, but become irreversibly damaged as the disease progresses (Dobson and Giovannoni, 2019).

Although the well demarcated lesions in Case 3 appear to have MS aetiology, the origin of WMH formation in the remainder of the lesions is unclear. Although myelin loss seems to be a key contributing factor in the appearance of WMHs, multiple pathogenic mechanisms could be responsible for tissue changes of this nature. The young age, low vascular risk and low level of vascular pathology in the cohort used in this study means that a vascular origin becomes less likely. However the majority of the cases had a CAA score of 3, which should be taken into consideration given previously reported associations with WMHs (Ryan et al., 2015). As discussed above, there is some evidence in this cohort for the ependymal lining dysfunction previously reported as a mechanism of periventricular WMHs. The segmental intramyelin oedema described in some of the WMHs here could be related to this breakdown of the ventricular lining or could be a result of other proposed mechanisms such as dysfunctional water and ion homeostasis (Cognat et al., 2014). Further investigations into the mechanisms underlying the myelin changes, and more generally, are clearly required and will be discussed in section 6.6.

6.5 Limitations

The novelty of this work combined with the time constraints of the project, required complex decisions to be taken efficiently and without the chance to test and optimise

methodologies first. This work is therefore considered a pilot study on which future studies of this nature can be based. As a result, there are several limitations to this particular work and decisions that would be made differently for future work.

The cohort used in this study is very small, which is largely due to the time taken to complete the entire pipeline for each case and was dependent on brain donations. Now that the pipeline has been developed and optimised, it will be easier to increase the number of cases for a future study. Additionally, although the cohort used here all had a diagnosis of young onset AD, a variety of phenotypic presentations were present. Whilst this was beneficial in assessing a wide range of WMH presentations, it made it hard for any disease specific trends to be revealed. As this study was reliant upon which individuals came to *post mortem* and underwent brain donation in the study time frame, control over the cohort demographics and diagnoses was not possible. A longer and larger study would therefore also be beneficial to this end.

There are several limitations related to the MRI scanning of the *post mortem* brains. Firstly the brains were not always put into the scanning container in exactly the same way, meaning that the orientation in which they were scanned did vary. This was rectified with reorientation of the images, but it meant that our registration pipeline had to undergo some case specific adaptation. Scanning time restrictions on the hospital MRI scanner required that scanning had to be undertaken over two separate sessions. Although this increased the chance of variability within cases, steps were taken to ensure that each brain was returned to the scanner in the same orientation and the brain remained in the container during the time between the scans. This should not affect the results presented in this study, as all of the structural T2-weighted imaging was undertaken in one session.

The process of registering the *ex vivo* and *in vivo* images also comes with limitations. Only alterations to a limited number of parameters were tested, and also not all parameters were tested. A more fine-grained approach could be adopted whereby small adjustments slightly above and below each of the seemingly optimal parameters, whilst holding all other parameters constant, could be tested. Furthermore the

issues experienced with the landmark-based registration were not resolved during the course of this study and would be something that could improve the registration further.

Although a good level of correspondence was achieved between the *in vivo* and *ex vivo* scans in this study, the registration was such that voxel-to-voxel comparisons could not be made. This had implications for the comparison of WMHs between the scans, in that the segmentations carried out on the *in vivo* FLAIR scans could not be transformed effectively to *ex vivo* space. The more qualitative approach adopted was accompanied with limitations, mainly relating to the lack of understanding of how WMHs appear on *ex vivo* scans in relation to *in vivo* scans. Before accurate assessments of WMH increase or decrease across *in vivo* and *ex vivo* scans, it is clear that a better characterisation of their appearance on *ex vivo* scans is necessary. It would be highly useful to have *in vivo* imaging close to time of death or within a time frame where WMHs are unlikely to have changed between scans, even just for one or a very small number of cases. This information could then be used to understand the changes in the appearance of WMHs likely due to effects inherent to imaging *post mortem* tissue, as opposed to biological alterations to the WMHs themselves. The last *in vivo* scan in this study was a long time prior to death in all cases (~4 - 9 years), during which time considerable atrophy is likely to have occurred. This likely played a role in the difficulties faced both in the registration of the images and the assessment of WMH change between them. A further limitation to the comparison of WMHs between the *in vivo* and *ex vivo* scans is the difference in resolution between the two. Partial volume effects are much more likely on the *in vivo* thick slice FLAIR, that could result in lesions being falsely reported as newly appearing.

There are several limitations relating to the sampling of the brains in this study. Firstly, Case 1 was mainly used for optimisation of the *ex vivo* scanning protocols and was not sampled in the same way as the other brains. The brain sampling pipeline using the slice photographs was not developed at this stage, so this brain was not taken forward for immunohistochemical staining. There was also an issue

with the brain sampling of Case 4 due to a breakdown in communication meaning the brain was sampled without the slice photographs being taken. Photographs were taken retrospectively, but the slices had already been cut into blocks. Although reconstruction of the full slices was attempted, it is likely this has an impact on the MRI-histology registrations. A further limitation relates again to the long time period between *in vivo* scanning and death. Although an assessment of the *ex vivo* images was made to check for any new WMHs, the *in vivo* MRI was used as the main guide to WMH locations on the brain tissue that existed on the *ex vivo* scan. This sometimes meant that, even for a trained neuropathologist, matching of the brain region on the *in vivo* scan image to the region on the physical tissue was challenging due to atrophy and other changes that had occurred. A further limitation relates to the assessment of the ependymal lining, in that its location at the tissue edge is particularly prone to tearing during the brain cutting and processing procedure. It is therefore possible that the ependymal lining loss observed was artefactual as opposed to pathological. A more in depth assessment of the ependymal lining with a focus on the directly underlying parenchyma, may be useful in determining whether the cell loss is a technical artefact.

Study limitations relating to the histological techniques include the fact that not all of the WMHs sampled at the brain cut were able to be taken forward for staining due to time constraints. The selection process for which WMHs would be sampled in this study could have been more methodical, as it was mainly based on the WMHs that were the brightest or just most striking. This often meant that WMHs were not selected from each lobe of the brain or from both periventricular and deep regions, which would have enabled better identification of regional trends. Some issues were encountered with the immunohistochemistry that was carried out, whereby a lot of background staining was seen with the SMI31 stain. This could mean that any differences in staining intensity may have been masked. The opposite was true for the MBP antibody, which appeared quite faint in some sections. Although the use of the internal control region would have helped to reduce the effect of this, occasionally the MBP staining appeared slightly patchy within a section and so even

the internal control may have been affected. The results from the SMI31 and MBP staining should therefore be interpreted with caution. Due to laboratory closures caused by the COVID-19 pandemic, it was not possible to rectify the issues with immunohistochemical stains as would have normally have been done. Additionally this impacted plans to stain a second wave of sampled WMH regions.

The limitations relating to the registration of histological sections and *ex vivo* MRI images, both in general terms and specifically the technique used in this study are discussed in detail in section 6.4.3.

6.6 Future directions of study

In the short term, there are a number of steps that can be taken to improve the utility of this pilot study to a larger study. It is clear that the histological staining used in this study has not fully captured the underlying pathology of all lesions. Several lesions, for example lesion 3.10, have a large and bright area of WMH on the MRI scans but no change of corresponding scale in the markers assessed. In order to try and understand the changes that are occurring in the underlying tissue and the mechanisms behind them, it would be useful to carry out an increased panel of staining, such as that shown in Table 6.6. This would include markers of vascular dysfunction, such as endothelial markers and collagen, markers of blood brain barrier dysfunction and markers of inflammation such as microglial and astrocytic markers. Once an increased panel of antibodies has been optimised, staining analysis could then be carried out to assess which markers are of interest. It would then be useful to carry out staining of the selected markers on an increased number of WMHs in this cohort (see the lesion guide in Figure 6.5). This would not only increase the power of this study, but aid in assessing any regional patterns in the pathology of WMHs.

As well as the T2-weighted imaging used in this study, diffusion weighted and SWI protocols were included as part of the *ex vivo* imaging. It would therefore be of interest to utilise these modalities as part of any further work. Previous studies have demonstrated altered diffusion weighted metrics, such as decreased FA and

Table 6.6: Increased panel of staining

Investigations	Markers
Morphology	H&E
Pathology	A β Tau
Collagen	Masson's trichrome stain Collagen type 1
Endothelial	ICAM VEGF LYVE-1
Axonal	SMI31 Neurofilament cocktail MAP2
Myelin	MBP LFB
Iron	Perl's
Oligodendrocytes	Olig2
Blood brain barrier dysfunction	Fibrinogen COL4 Claudin-5 CD68
Inflammation	CD3/43 Iba1 GFAP

increased MD, are predictive of WMHs (Maillard et al., 2013, Silva et al., 2016, van Leijssen et al., 2018), as well as showing differences between periventricular and deep WMHs (Griffanti et al., 2018), and being reflective of the underlying pathology (Gouw et al., 2008a). SWI imaging can be used to assess certain types of vascular pathologies, such as microbleeds and structural abnormalities like tortuous vessels (Halefoglu and Yousem, 2018).

Another area of short-term work is to optimise the registration of the *in vivo* and *ex vivo* MRI images. An area of focus would be the landmark-based registration, for which it may be necessary to consult with a registration expert in order to

resolve the current issues. If the landmark registration could be successfully implemented, more localised registrations could be carried out in specific areas of interest such as the periventricular region.

Another possible line of future work would be to carry out more detailed analysis of Case 3, the dual ADAD/MS case. This is an extremely rare combined diagnosis of two diseases, both with links to white matter changes. It therefore provides a unique opportunity to investigate in a single individual how two distinct pathologies may result in very similar WMHs on MRI, whilst also offering a chance to gain insights into any potential interplay between between the disease aetiologies.

It is important to also carry out a better characterisation of the segmental intramyelin oedema observed in some of the WMHs. There is very little description of such a finding in humans and so carrying out an electron microscopy study, similar to the one carried out in a mouse model by Cognat et al. (2014), would be pertinent. Alternatively, double immunostaining could also be carried out with markers to axons/myelin and also to myelin/oligodendrocytes to uncover the exact location of the oedema. It would also be interesting examine a larger number of juxtacortical and deep WMHs for the presence of intramyelin oedema, in order to assess whether they are only linked to periventricular lesions.

An important consideration in the development of the pipeline was the ability to scale this pilot study up to a larger study. The ultimate goal of such a study would be to develop a tool to predict white matter lesion pathology for use in the clinic. The aims of this prospective study are detailed below and would be undertaken with the expertise of multiple collaborators:

- To carry out *ex vivo* scanning hemispheres from approximately 30 individuals over the course of three years, acquiring T2-weighted, SWI and diffusion-weighted imaging.
- To whether any changes in an increased panel of antibodies (see Table 6.6) underlie WMHs.
- To improve the registration pipelines to enable accurate matching of the *in*

vivo and *ex vivo* MRI images.

- To register the histological sections into the space of both *ex vivo* image and then the *in vivo* image.
- To assess whether any features of WMHs visible on *in vivo* imaging are associated with underlying pathology. An ultimate goal is to develop a machine learning system to predict the pathology of each lesion based on size, shape, texture and location.
- To assess whether 7T scans enable higher resolution and a great number of quantitative images compared with 3T.

6.7 Conclusions

In conclusion, this project has demonstrated the successful development and implementation of a pipeline that combines high resolution T2-weighted *ex vivo* structural brain imaging with histological investigations. In the small cohort used in this study, myelin changes were found to be an important pathological correlate of WMHs. With further optimisation of the registration protocols, it would be entirely feasible to be able align *in vivo*, *ex vivo* and histological sections together to accurately establish the relationship of pathological findings to *in vivo* MRI. This study is an important first step toward the ultimate goal of being able to predict the underlying pathology of WMHs based on appearance and location, for use in a clinical setting.

Chapter 7

General Discussion

Biomarkers are a hugely important evolving area of research in the AD field, with the potential to provide an accurate preclinical diagnosis and predictions about conversion to more advanced disease stages, as well as acting as inclusion criteria and outcome measures in clinical trials. Biomarkers are also instrumental to uncovering the different pathological changes that occur in AD and how they relate to each other along the continuum of disease. There is a need to extend the core AD biomarkers of $A\beta$, tau, and measures of brain atrophy and metabolism (Jack et al., 2018) in order to encompass the multifactorial nature of the disease.

WMHs are a potential biomarker of interest, demonstrating an increased burden in AD (Scheltens et al., 1992, Yoshita et al., 2006), predicting those who convert to clinical disease (Lopez et al., 2014) and appearing early in the disease process (Lee et al., 2016, Silbert et al., 2012). Despite their apparent importance in AD, a clear pathological basis of WMHs remains to be uncovered. Heterogeneous neuropathological substrates resulting from a wide range of pathogenic mechanisms appear likely, despite being traditionally thought of only as a marker of SVD.

Although WMHs have been shown to associate with existing biomarkers of AD (Enzinger et al., 2005, Marnane et al., 2016, Tosto et al., 2015, Zhou et al., 2015), results are often mixed (Kester et al., 2014, Osborn et al., 2018) and do not assess relationships across the full disease course. Less is known about how WMHs interact with newer and emerging AD biomarkers such as NFL, with studies again demonstrating mixed results. Even less is known about WMHs and their associations

with other biomarkers in ADAD, a rare form of AD in typically younger individuals with a lower risk of SVD.

With this in mind, the work in this thesis revolved around two overarching aims:

1. To investigate the relevance of WMHs as a biomarker in cohorts of sporadic and ADAD patients, examining their associations with other existing biomarkers.
2. To investigate the pathological basis of WMHs in order to better understand how certain imaging characteristics are represented in pathology.

7.1 Summary of main findings

7.1.1 Chapter 3

In Chapter 3 I assessed the relationships between WMHs and CSF $A\beta$ 1-42, t-tau and p-tau in control, SMC, EMCI, LMCI and AD groups from the ADNI cohort. Evidence for a strong association between WMHs and $A\beta$ was found across the AD disease spectrum, whereby an increase in WMHs corresponded to a decrease in CSF $A\beta$. I observed no differences in the $A\beta$ -WMH relationship between disease groups, but a highly significant relationship remained in the pooled cohort after adjustment for age, diagnostic group, TIV and APOE ϵ status. No evidence was found for a relationship between WMHs and either t-tau or p-tau. Moreover the WMH-CSF $A\beta$ relationship was found to independent of both t-tau and p-tau. I found no effect of the vascular risk factors of smoking, hypertension, diabetes and BMI on the WMH-age or WMH- $A\beta$ relationship. Although the relationship remained after adjustment for age, age was found to be the strongest independent predictor of WMHs.

As WMHs are largely thought to be representative of vascular pathology, my work here adds to the literature exploring the complex relationship between AD and SVD. However evidence in the literature and now from this thesis has indicated that not all WMHs are related to atherosclerotic SVD, with suggestions of a degenerative basis as a consequence of AD pathology (McAleese et al., 2017), among others.

Although age was highly predictive of WMHs, the strong WMH-CSF A β relationship combined with the lack of contribution from vascular risk factors, is compatible with the theory that some WMHs are part of the AD pathological process and some are the result of an ageing/vascular process.

7.1.2 Chapter 4

In Chapter 4, I added to the work in Chapter 3 by investigating the relationship between WMHs and the axonal degeneration marker of plasma NFL in the same ADNI cohort. I found evidence for a positive association between WMHs and NFL from the early stages of cognitive impairment through to clinical AD. This WMH-NFL relationship was highly dependent on participant age. Age also accounted for the most variance in WMHs. Like in Chapter 3, no effect of adjusting for vascular risk on the relationship between NFL and WMHs was seen.

My results here suggest that WMHs in the cognitively impaired are likely to be related to axonal degeneration, in a manner that is dependent on age. This positive relationship maybe caused by AD pathologies and/or comorbid CVD. However the fact that no effect of the vascular risk factors tested on the relationship between NFL and WMHs was observed, adds to the growing body of evidence that WMH are part of core AD process and not simply attributed to concomitant CVD.

7.1.3 Chapter 5

I carried out an assessment of WMHs in ADAD in Chapter 5, looking at the effect of mutation group on WMH change over time in the DIAN cohort. Whether WMH burden increases as estimated onset is approached and passed was also assessed, as was the relationship between WMHs and brain atrophy. I found mutation type to be an important predictor of WMH accrual, with *APP* mutation carriers having the highest rates. Increases in WMH volumes with estimated years to onset was observed in the *APP* and *PSEN1* mutation groups, with evidence of an acceleration in the *PSEN1* and *PSEN2* groups. I also found WMH accrual to be highly associated with brain atrophy, even after allowing for disease stage.

My work here in a younger patient group with lower risk of age-related vascu-

lar comorbidities, demonstrates that WMHs are likely to be a core feature of AD. The fact that WMH burden increases with EYO and tracks together with brain atrophy across the disease course, suggests WMHs are an important biomarker of disease progression. Among other factors, the observed heterogeneity between mutation groups could be being driven by the large number of Dutch and Flemish mutation carriers in the *APP* group with typically higher WMH burden.

7.1.4 Chapter 6

In Chapter 6, I focused on the development of a novel MRI-histology pipeline in a small cohort in order to answer key questions relating to the visualisation of WMHs in life and after death, and their underlying pathology. The majority of this work was methodological, testing and optimising protocols for *ex vivo* MRI acquisition and the registration of the *ex vivo* images to the *in vivo* MRI and histological sections. I then carried out an assessment of changes in WMHs between the last *in vivo* and *ex vivo* scans. Finally quantitative and qualitative analyses of stains for myelin (LFB and MBP), axons (SMI31) and tissue morphology (H&E) were performed.

The successful implementation of the pipeline enabled high quality *ex vivo* T2-weighted images to be obtained that were subsequently registered to the *in vivo* imaging with a good level of correspondence. Some issues were encountered with the *ex vivo* MRI-histology registration, whereby an accumulation of multiple errors meant that registration was not possible in some cases.

I found evidence for a role of myelin loss in WMHs, with results from a mixed model demonstrating a significant decrease in myelin staining compared to the NAWM in the WMHs of this small group of patients with young onset AD. More qualitatively, different patterns were observed in WMH appearance across the *in vivo* imaging, *ex vivo* imaging and histology. Lesions ranged from appearing more faintly on the *ex vivo* scan to appearing more brightly, and with varying degrees of underlying pathological change. Among the periventricular WMHs from the sporadic AD/PCA cases, I observed a spectrum in the degree of myelin pallor. Also in these cases, an interesting and novel finding of segmental intramyelin oedema was observed within the lesion area. There was considerable variation in

lesion appearance within the case with a dual diagnosis of ADAD-MS, with some lesions that appeared similar to the other sporadic cases with smaller areas of pallor and less well defined boundaries and those that were very clearly demarcated on the histological staining, MRI images and on the brain tissue itself, consistent with MS plaques.

The overarching aim of this work was to optimise the pipeline to be scalable to a larger study in the future. My pilot study was an important first step in achieving the long-term goal of a tool to predict the underlying pathology of WMHs based on appearance and location, for eventual use in a clinical setting.

7.2 Importance of this work

With respect to the first overarching aim, this thesis has provided a comprehensive investigation into the relevance of WMHs as a biomarker. Chapters 3 and 4 have outlined strong relationships between WMHs and the AD biomarker of $A\beta$ and the axonal degeneration biomarker of NFL, suggesting that WMHs are an intrinsic part of the AD disease process and not just a benign consequence of ageing. Chapter 5 may even be considered as more robust evidence for this important role of WMHs in AD pathogenesis, whereby a strong relationship between WMHs and brain atrophy over the disease course was demonstrated in individuals with ADAD mutations, who were typically young and lacking significant vascular risk factors. Moreover, the fact that WMH burden increases with proximity to estimated age at symptom onset suggests that they could be an important biomarker of disease progression, even in the presymptomatic phase.

WMHs have long been considered a marker of SVD and have been proposed as a candidate biomarker for the vascular component of AD. Although not disputing the evidence that a large proportion of WMHs seen in the elderly have a vascular basis, the work in this thesis adds to the growing evidence that they are not uniformly associated with conventional vascular risk factors. Chapters 3 and 4 are evidence of this in that ADNI cohort is of low vascular risk by design, as a result of their exclusion criteria. Similarly in Chapter 5, the young age of the DIAN cohort means

that incidence of vascular comorbidities is likely to be low.

The strong relationship of WMHs with the traditional AD biomarkers of CSF $A\beta$ and brain atrophy implies that WMHs are representative of aspects of pathology beyond CVD. What is not clear though, is what WMHs do represent. The strong association between WMHs and brain atrophy could imply that they are measurements of the same pathway, meaning that WMHs are just a surrogate measure for brain atrophy. However the lack of complete correlation is evidence against this and a lesser degree of overlap is more likely. Having an additional marker for a shared pathological process is useful, not just as confirmatory, but to reduce the sample size in future studies or clinical trials. It may be that WMHs can be considered a general marker of brain health; a proxy measure for multiple deleterious pathological processes such as amyloid accumulation, axonal degeneration, brain atrophy and vascular pathology. What is clear is that WMHs increase throughout the AD disease course and are strongly associated with several damaging pathways, so investigations into WMHs, such as in this thesis, are highly pertinent.

It is important though to uncover exactly what WMHs represent and in a way that will be useful clinically in the future. Chapter 6 of this thesis is a critical first step in identifying the seemingly heterogeneous pathological bases of this uniformly appearing MRI signal. Perhaps this is best epitomised by Case 3 in this study, where the homogeneous hyperintense signal is likely underpinned by the two distinct disease processes of ADAD and MS. Being able to predict the pathology underlying specific WMH based on their location, size and shape would be a hugely powerful tool and one for which there is a clear unmet clinical need.

Chapter 8

Contributions

8.1 Chapters 3 & 4

The BaMoS WMH segmentation tool was developed and run by Dr Carole Sudre. Dr Jo Barnes carried out the second round of visual inspections of all the WMH segmentations. Dr Cassidy Fiford developed the semi-automated WMH segmentation protocol. Professor Chris Frost provided statistical support.

8.2 Chapter 5

The BaMoS WMH segmentation tool was run by Dr Carole Sudre. Dr Jo Barnes and Dr Emily Manning assisted with the blinding for the segmentations. Dr David Cash, Tom Veale and Dr Emily Manning helped in generating BSI measures. Dr Natalie Ryan assisted in interpretation of clinical measures. Dr Chris Frost and Dr Jo Barnes provided statistical support.

8.3 Chapter 6

Professor Tammarn Lashley, Dr Jo Barnes and Dr Natalie Ryan assisted in the pipeline development. MRI scanning was carried out by radiographers at The National Hospital for Neurology and Neurosurgery, Queen Square. *Ex vivo* MRI protocol development and technical support was provided by Dr David Thomas. Assistance with the brain sampling protocol was provided by Shauna Crampsie and Nellie Robinson. Brain cutting and qualitative assessments of the H&E and LFB sections were carried out by the pathologist, Dr Zane Zaubmuktane. Professor Dale

Moulding provided the macro for the stained image analysis. Statistical support was provided by Dr Jennifer Nicholas. Dr Jo Barnes, Dr Ian Malone and Dr Jamie McClelland provided support with *in vivo* and *ex vivo* MRI image registration. Dr Eugenio Iglesias developed and ran the MRI-histology registration pipeline.

Chapter 9

Publications

Publications that have arisen to date as a direct result of the work in this thesis:

P. Walsh, C. H. Sudre, C. M. Fiford, N. S. Ryan, T. Lashley, C. Frost, and J. Barnes. Csf amyloid is a consistent predictor of white matter hyperintensities across the disease course from ageing to alzheimer's disease. *Neurobiology of Aging*, 2020

P. Walsh, C. H. Sudre, C. M. Fiford, N. S. Ryan, T. Lashley, C. Frost, and J. Barnes. The age-dependent associations of white matter hyperintensities and neurofilament light in early- and late-stage alzheimer's disease. *Neurobiol Aging*, 97:10–17, 2021

Papers in preparation:

P. Walsh, C. H. Sudre, E. N. Manning, T. Veale, D. M. Cash, N. S. Ryan, T. Lashley, C. Frost, N. C. Fox and J. Barnes. White matter hyperintensity increases are a feature of dominantly inherited Alzheimer's disease and are associated with increased brain atrophy.

Bibliography

- J. Acosta-Cabronero, S. Alley, G. B. Williams, G. Pengas, and P. J. Nestor. Diffusion tensor metrics as biomarkers in alzheimer's disease. *PLoS One*, 7(11): e49072, 2012.
- O. M. Al-Janabi, C. E. Bauer, L. B. Goldstein, R. R. Murphy, A. A. Bahrani, C. D. Smith, D. M. Wilcock, B. T. Gold, and G. A. Jicha. White matter hyperintensity regression: Comparison of brain atrophy and cognitive profiles with progression and stable groups. *Brain sciences*, 9(7):170, 2019.
- R. P. Almeida, S. A. Schultz, B. P. Austin, E. A. Boots, N. M. Dowling, C. E. Gleason, B. B. Bendlin, M. A. Sager, B. P. Hermann, H. Zetterberg, C. M. Carlsson, S. C. Johnson, S. Asthana, and O. C. Okonkwo. Effect of cognitive reserve on age-related changes in cerebrospinal fluid biomarkers of alzheimer disease. *JAMA Neurology*, 72:699–706, 2015.
- M. L. Alosco, M. A. Sugarman, L. M. Besser, Y. Tripodis, B. Martin, J. N. Palmisano, N. W. Kowall, R. Au, J. Mez, C. DeCarli, T. D. Stein, A. C. McKee, R. J. Killiany, and R. A. Stern. A clinicopathological investigation of white matter hyperintensities and alzheimer's disease neuropathology. *J Alzheimers Dis*, 63(4):1347–1360, 2018.
- V. C. Anderson, J. T. Obayashi, J. A. Kaye, J. F. Quinn, P. Berryhill, L. P. Riccelli, D. Peterson, and W. D. Rooney. Longitudinal relaxographic imaging of white matter hyperintensities in the elderly. *Fluids and barriers of the CNS*, 11:24–24, 2014.

- M. A. Araque Caballero, M. Suarez-Calvet, M. Duering, N. Franzmeier, T. Benzinger, A. M. Fagan, R. J. Bateman, C. R. Jack, J. Levin, M. Dichgans, M. Jucker, C. Karch, C. L. Masters, J. C. Morris, M. Weiner, M. Rossor, N. C. Fox, J. H. Lee, S. Salloway, A. Danek, A. Goate, I. Yakushev, J. Hassenstab, P. R. Schofield, C. Haass, and M. Ewers. White matter diffusion alterations precede symptom onset in autosomal dominant alzheimer's disease. *Brain*, 141(10):3065–3080, 2018.
- K. Arfanakis, A. M. Evia, S. E. Leurgans, L. F. C. Cardoso, A. Kulkarni, N. Alqam, L. F. Lopes, D. Vieira, D. A. Bennett, and J. A. Schneider. Neuropathologic correlates of white matter hyperintensities in a community-based cohort of older adults. *Journal of Alzheimer's Disease*, 73:333–345, 2020.
- J. Attems and K. A. Jellinger. The overlap between vascular disease and alzheimer's disease—lessons from pathology. *BMC Med*, 12:206, 2014.
- I. A. Awad, P. C. Johnson, R. F. Spetzler, and J. A. Hodak. Incidental subcortical lesions identified on magnetic resonance imaging in the elderly. ii. postmortem pathological correlations. *Stroke*, 17(6):1090–7, 1986.
- R. Bakshi, S. D. Caruthers, V. Janardhan, and M. Wasay. Intraventricular csf pulsation artifact on fast fluid-attenuated inversion-recovery mr images: Analysis of 100 consecutive normal studies. *American Journal of Neuroradiology*, 21(3): 503, 2000.
- J. Barnes, O. T. Carmichael, K. K. Leung, C. Schwarz, G. R. Ridgway, J. W. Bartlett, I. B. Malone, J. M. Schott, M. N. Rossor, G. J. Biessels, C. DeCarli, N. C. Fox, and I. Alzheimer's Disease Neuroimaging. Vascular and alzheimer's disease markers independently predict brain atrophy rate in alzheimer's disease neuroimaging initiative controls. *Neurobiol Aging*, 34(8):1996–2002, 2013.
- R. J. Bateman, P. S. Aisen, B. De Strooper, N. C. Fox, C. A. Lemere, J. M. Ringman, S. Salloway, R. A. Sperling, M. Windisch, and C. Xiong. Autosomal-dominant alzheimer's disease: a review and proposal for the prevention of alzheimer's disease. *Alzheimer's Research and Therapy*, 3(1):1, 2011.

- R. J. Bateman, C. Xiong, T. L. Benzinger, A. M. Fagan, A. Goate, N. C. Fox, D. S. Marcus, N. J. Cairns, X. Xie, T. M. Blazey, D. M. Holtzman, A. Santacruz, V. Buckles, A. Oliver, K. Moulder, P. S. Aisen, B. Ghetti, W. E. Klunk, E. McDade, R. N. Martins, C. L. Masters, R. Mayeux, J. M. Ringman, M. N. Rossor, P. R. Schofield, R. A. Sperling, S. Salloway, and J. C. Morris. Clinical and biomarker changes in dominantly inherited alzheimer's disease. *N Engl J Med*, 367(9):795–804, 2012.
- T. L. S. Benzinger, T. Blazey, C. R. Jack, R. A. Koeppe, Y. Su, C. Xiong, M. E. Raichle, A. Z. Snyder, B. M. Ances, R. J. Bateman, N. J. Cairns, A. M. Fagan, A. Goate, D. S. Marcus, P. S. Aisen, J. J. Christensen, L. Ercole, R. C. Hornbeck, A. M. Farrar, P. Aldea, M. S. Jaszec, C. J. Owen, X. Xie, R. Mayeux, A. Brickman, E. McDade, W. Klunk, C. A. Mathis, J. Ringman, P. M. Thompson, B. Ghetti, A. J. Saykin, R. A. Sperling, K. A. Johnson, S. Salloway, S. Correia, P. R. Schofield, C. L. Masters, C. Rowe, V. L. Villemagne, R. Martins, S. Ourselin, M. N. Rossor, N. C. Fox, D. M. Cash, M. W. Weiner, D. M. Holtzman, V. D. Buckles, K. Moulder, and J. C. Morris. Regional variability of imaging biomarkers in autosomal dominant alzheimer's disease. *Proceedings of the National Academy of Sciences*, 110(47):E4502, 2013.
- A. Biffi and S. M. Greenberg. Cerebral amyloid angiopathy: a systematic review. *J Clin Neurol*, 7(1):1–9, 2011.
- C. Birkl, C. Langkammer, J. Haybaeck, C. Ernst, R. Stollberger, F. Fazekas, and S. Ropele. Temperature-induced changes of magnetic resonance relaxation times in the human brain: a postmortem study. *Magn Reson Med*, 71(4):1575–80, 2014.
- S. Black, F. Gao, and J. Bilbao. Understanding white matter disease: imaging-pathological correlations in vascular cognitive impairment. *Stroke*, 40(3 Suppl): S48–52, 2009.
- K. Blennow, H. Hampel, M. Weiner, and H. Zetterberg. Cerebrospinal fluid and plasma biomarkers in alzheimer disease. *Nat Rev Neurol*, 6(3):131–44, 2010.

- L. M. Bloudek, D. E. Spackman, M. Blankenburg, and S. D. Sullivan. Review and meta-analysis of biomarkers and diagnostic imaging in alzheimer's disease. *J Alzheimers Dis*, 26(4):627–45, 2011.
- I. Bos, F. R. Verhey, I. Ramakers, H. I. L. Jacobs, H. Soinen, Y. Freund-Levi, H. Hampel, M. Tsolaki, A. K. Wallin, M. A. van Buchem, A. Oleksik, M. M. Verbeek, M. Olde Rikkert, W. M. van der Flier, P. Scheltens, P. Aalten, P. J. Visser, and S. J. B. Vos. Cerebrovascular and amyloid pathology in predementia stages: the relationship with neurodegeneration and cognitive decline. *Alzheimers Res Ther*, 9(1):101, 2017.
- P. A. Boyle, L. Yu, S. Nag, S. Leurgans, R. S. Wilson, D. A. Bennett, and J. A. Schneider. Cerebral amyloid angiopathy and cognitive outcomes in community-based older persons. *Neurology*, 85(22):1930–6, 2015.
- P. A. Boyle, L. Yu, R. S. Wilson, S. E. Leurgans, J. A. Schneider, and D. A. Bennett. Person-specific contribution of neuropathologies to cognitive loss in old age. *Ann Neurol*, 83(1):74–83, 2018.
- H. Braak and E. Braak. Neuropathological staging of alzheimer-related changes. *Acta Neuropathol*, 82(4):239–59, 1991.
- B. H. Braffman, R. A. Zimmerman, J. Q. Trojanowski, N. K. Gonatas, W. F. Hickey, and W. W. Schlaepfer. Brain mr: pathologic correlation with gross and histopathology. 2. hyperintense white-matter foci in the elderly. *AJR Am J Roentgenol*, 151(3):559–66, 1988.
- C. Brayne, K. Richardson, F. E. Matthews, J. Fleming, S. Hunter, J. H. Xuereb, E. Paykel, E. B. Mukaetova-Ladinska, F. A. Huppert, A. O'Sullivan, T. Denning, and C. Cambridge City Over-75s Cohort Cc75c Study Neuropathology. Neuropathological correlates of dementia in over-80-year-old brain donors from the population-based cambridge city over-75s cohort (cc75c) study. *J Alzheimers Dis*, 18(3):645–58, 2009.

- A. M. Brickman, L. B. Zahodne, V. A. Guzman, A. Narkhede, I. B. Meier, E. Y. Griffith, F. A. Provenzano, N. Schupf, J. J. Manly, Y. Stern, J. A. Luchsinger, and R. A. M. Mayeux. Reconsidering harbingers of dementia: progression of parietal lobe white matter hyperintensities predicts alzheimer's disease incidence. *Neurobiol Aging*, 36(1):27–32, 2015.
- L. Bronge, N. Bogdanovic, and L. O. Wahlund. Postmortem mri and histopathology of white matter changes in alzheimer brains. a quantitative, comparative study. *Dement Geriatr Cogn Disord*, 13(4):205–12, 2002.
- P. Buchhave, L. Minthon, H. Zetterberg, A. K. Wallin, K. Blennow, and O. Hansson. Cerebrospinal fluid levels of β -amyloid 1-42, but not of tau, are fully changed already 5 to 10 years before the onset of alzheimer dementia. *Archives of General Psychiatry*, 69(1):98–106, 2012.
- K. Buerger, M. Ewers, T. Pirttila, R. Zinkowski, I. Alafuzoff, S. J. Teipel, J. DeBernardis, D. Kerkman, C. McCulloch, H. Soininen, and H. Hampel. Csf phosphorylated tau protein correlates with neocortical neurofibrillary pathology in alzheimer's disease. *Brain*, 129(Pt 11):3035–41, 2006.
- M. E. Caligiuri, P. Perrotta, A. Augimeri, F. Rocca, A. Quattrone, and A. Cherubini. Automatic detection of white matter hyperintensities in healthy aging and pathology using magnetic resonance imaging: A review. *Neuroinformatics*, 13(3):261–76, 2015.
- M. J. Cardoso, M. Modat, R. Wolz, A. Melbourne, D. Cash, D. Rueckert, and S. Ourselin. Geodesic information flows: Spatially-variant graphs and their application to segmentation and fusion. *IEEE Trans Med Imaging*, 34(9):1976–88, 2015.
- A. Charidimou, G. Boulouis, K. Haley, E. Auriel, E. S. van Etten, P. Fotiadis, Y. Reijmer, A. Ayres, A. Vashkevich, Z. Y. Dipucchio, K. M. Schwab, S. Martinez-Ramirez, J. Rosand, A. Viswanathan, S. M. Greenberg, and M. E. Gurol. White

- matter hyperintensity patterns in cerebral amyloid angiopathy and hypertensive arteriopathy. *Neurology*, 86(6):505–11, 2016.
- M. I. Chimowitz, M. L. Estes, A. J. Furlan, and I. A. Awad. Further observations on the pathology of subcortical lesions identified on magnetic resonance imaging. *Archives of Neurology*, 49(7):747–752, 1992.
- A. H. Cho, H. R. Kim, W. Kim, and D. W. Yang. White matter hyperintensity in ischemic stroke patients: it may regress over time. *J Stroke*, 17(1):60–6, 2015.
- H. Cho, J. Y. Choi, M. S. Hwang, J. H. Lee, Y. J. Kim, H. M. Lee, C. H. Lyoo, Y. H. Ryu, and M. S. Lee. Tau pet in alzheimer disease and mild cognitive impairment. *Neurology*, 87(4):375–83, 2016.
- L. Chávez-Gutiérrez, L. Bammens, I. Benilova, A. Vandersteen, M. Benurwar, M. Borgers, S. Lismont, L. Zhou, S. Van Cleynenbreugel, H. Esselmann, J. Wiltfang, L. Serneels, E. Karran, H. Gijzen, J. Schymkowitz, F. Rousseau, K. Broersen, and B. De Strooper. The mechanism of γ -secretase dysfunction in familial alzheimer disease. *Embo j*, 31(10):2261–74, 2012.
- E. Cognat, S. Cleophax, V. Domenga-Denier, and A. Joutel. Early white matter changes in cadasil: evidence of segmental intramyelinic oedema in a pre-clinical mouse model. *Acta Neuropathol Commun*, 2(49), 2014.
- S. J. Crutch, M. Lehmann, J. M. Schott, G. D. Rabinovici, M. N. Rossor, and N. C. Fox. Posterior cortical atrophy. *Lancet Neurol*, 11(2):170–8, 2012.
- E. Cuyvers and K. Sleegers. Genetic variations underlying alzheimer’s disease: evidence from genome-wide association studies and beyond. *Lancet Neurol*, 15(8):857–868, 2016.
- S. D’Agostino, R. B., R. S. Vasan, M. J. Pencina, P. A. Wolf, M. Cobain, J. M. Massaro, and W. B. Kannel. General cardiovascular risk profile for use in primary care: the framingham heart study. *Circulation*, 117(6):743–53, 2008.

- M. R. D'Andrea and R. G. Nagele. Morphologically distinct types of amyloid plaques point the way to a better understanding of alzheimer's disease pathogenesis. *Biotech Histochem*, 85(2):133–47, 2010.
- J. C. De Groot, F. E. De Leeuw, M. Oudkerk, J. Van Gijn, A. Hofman, J. Jolles, and M. M. Breteler. Periventricular cerebral white matter lesions predict rate of cognitive decline. *Ann Neurol*, 52(3):335–41, 2002.
- F. E. de Leeuw, J. C. de Groot, E. Achten, M. Oudkerk, L. M. Ramos, R. Heijboer, A. Hofman, J. Jolles, J. van Gijn, and M. M. Breteler. Prevalence of cerebral white matter lesions in elderly people: a population based magnetic resonance imaging study. the rotterdam scan study. *J Neurol Neurosurg Psychiatry*, 70(1):9–14, 2001a.
- F. E. de Leeuw, J. C. de Groot, and J. van Gijn. [cerebral white matter lesions in the elderly: vascular risk factors and cognitive consequences]. *Ned Tijdschr Geneeskd*, 145(43):2067–71, 2001b.
- M. J. de Leon, A. Convit, O. T. Wolf, C. Y. Tarshish, S. DeSanti, H. Rusinek, W. Tsui, E. Kandil, A. J. Scherer, A. Roche, A. Imossi, E. Thorn, M. Bobinski, C. Caraos, P. Lesbre, D. Schlyer, J. Poirier, B. Reisberg, and J. Fowler. Prediction of cognitive decline in normal elderly subjects with 2-[(18)f]fluoro-2-deoxy-d-glucose/positron-emission tomography (fdg/pet). *Proc Natl Acad Sci U S A*, 98(19):10966–71, 2001.
- S. Debette and H. S. Markus. The clinical importance of white matter hyperintensities on brain magnetic resonance imaging: systematic review and meta-analysis. *Bmj*, 341:c3666, 2010.
- C. DeCarli, D. Mungas, D. Harvey, B. Reed, M. Weiner, H. Chui, and W. Jagust. Memory impairment, but not cerebrovascular disease, predicts progression of mci to dementia. *Neurology*, 63(2):220–7, 2004.
- C. DeCarli, G. B. Frisoni, C. M. Clark, D. Harvey, M. Grundman, R. C. Petersen, L. J. Thal, S. Jin, J. Jack, C. R., and P. Scheltens. Qualitative estimates of medial

- temporal atrophy as a predictor of progression from mild cognitive impairment to dementia. *Arch Neurol*, 64(1):108–15, 2007.
- C. Depienne, M. Bugiani, C. Dupuits, D. Galanaud, V. Touitou, N. Postma, C. van Berkel, E. Polder, E. Tollard, F. Darios, A. Brice, C. E. de Die-Smulders, J. S. Vles, A. Vanderver, G. Uziel, C. Yalcinkaya, S. G. Frints, V. M. Kalscheuer, J. Klooster, M. Kamermans, T. E. Abbink, N. I. Wolf, F. Sedel, and M. S. van der Knaap. Brain white matter oedema due to *clc-2* chloride channel deficiency: an observational analytical study. *Lancet Neurol*, 12(7):659–68, 2013.
- B. DeStrooper and E. Karran. The cellular phase of alzheimer’s disease. *Cell*, 164(4):603–615, 2016.
- K. Dhiman, K. Blennow, H. Zetterberg, R. N. Martins, and V. B. Gupta. Cerebrospinal fluid biomarkers for understanding multiple aspects of alzheimer’s disease pathogenesis. *Cell Mol Life Sci*, 2019.
- R. Dobson and G. Giovannoni. Multiple sclerosis - a review. *Eur J Neurol*, 26(1):27–40, 2019.
- B. Dubois, M. Chupin, H. Hampel, S. Lista, E. Cavedo, B. Croisile, G. Louis Tisserand, J. Touchon, A. Bonafe, P. J. Ousset, A. Ait Ameer, O. Rouaud, F. Ricolfi, A. Vighetto, F. Pasquier, C. Delmaire, M. Ceccaldi, N. Girard, C. Dufouil, S. Lehericy, I. Tonelli, F. Duveau, O. Colliot, L. Garnero, M. Sarazin, and D. Dormont. Donepezil decreases annual rate of hippocampal atrophy in suspected prodromal alzheimer’s disease. *Alzheimers Dement*, 11(9):1041–9, 2015.
- M. Duering, M. J. Konieczny, S. Tiedt, E. Baykara, A. M. Tuladhar, E. V. Leijssen, P. Lyrer, S. T. Engelter, B. Gesierich, M. Achmuller, C. Barro, R. Adam, M. Ewers, M. Dichgans, J. Kuhle, F. E. de Leeuw, and N. Peters. Serum neurofilament light chain levels are related to small vessel disease burden. *J Stroke*, 20(2):228–238, 2018.
- S. Engelborghs, K. Sleegers, P. Cras, N. Brouwers, S. Serneels, E. De Leenheir, J.-J. Martin, E. Vanmechelen, C. Van Broeckhoven, and P. P. De Deyn. No association

- of csf biomarkers with apoe ϵ 4, plaque and tangle burden in definite alzheimer's disease. *Brain*, 130(9):2320–2326, 2007.
- E. Englund. Neuropathology of white matter changes in alzheimer's disease and vascular dementia. *Dement Geriatr Cogn Disord*, 9 Suppl 1:6–12, 1998.
- E. Englund, A. Brun, and B. Persson. Correlations between histopathologic white matter changes and proton mr relaxation times in dementia. *Alzheimer Dis Assoc Disord*, 1(3):156–70, 1987.
- E. Englund, M. Sjöbeck, S. Brockstedt, J. Lätt, and E. M. Larsson. Diffusion tensor mri post mortem demonstrated cerebral white matter pathology. *J Neurol*, 251(3):350–2, 2004.
- C. Enzinger, F. Fazekas, P. M. Matthews, S. Ropele, H. Schmidt, S. Smith, and R. Schmidt. Risk factors for progression of brain atrophy in aging: six-year follow-up of normal subjects. *Neurology*, 64(10):1704–11, 2005.
- D. Erten-Lyons, R. Woltjer, J. Kaye, N. Mattek, H. H. Dodge, S. Green, H. Tran, D. B. Howieson, K. Wild, and L. C. Silbert. Neuropathologic basis of white matter hyperintensity accumulation with advanced age. *Neurology*, 81(11):977–983, 2013.
- M. M. Esiri, Z. Nagy, M. Z. Smith, L. Barnetson, and A. D. Smith. Cerebrovascular disease and threshold for dementia in the early stages of alzheimer's disease. *Lancet*, 354(9182):919–20, 1999.
- M. M. Esiri, C. Joachim, C. Sloan, S. Christie, G. Agacinski, L. R. Bridges, G. K. Wilcock, and A. D. Smith. Cerebral subcortical small vessel disease in subjects with pathologically confirmed alzheimer disease: a clinicopathologic study in the oxford project to investigate memory and ageing (optima). *Alzheimer Dis Assoc Disord*, 28(1):30–5, 2014.
- K. Farid, A. Charidimou, and J.-C. Baron. Amyloid positron emission tomography

- in sporadic cerebral amyloid angiopathy: A systematic critical update. *NeuroImage. Clinical*, 15:247–263, 2017.
- F. Fazekas. Incidental periventricular white matter hyperintensities revisited: what detailed morphologic image analyses can tell us. *AJNR Am J Neuroradiol*, 35(1): 63–4, 2014.
- F. Fazekas, J. B. Chawluk, A. Alavi, H. I. Hurtig, and R. A. Zimmerman. Mr signal abnormalities at 1.5 t in alzheimer’s dementia and normal aging. *AJR Am J Roentgenol*, 149(2):351–6, 1987.
- F. Fazekas, R. Kleinert, H. Offenbacher, F. Payer, R. Schmidt, G. Kleinert, H. Radner, and H. Lechner. The morphologic correlate of incidental punctate white matter hyperintensities on mr images. *AJNR Am J Neuroradiol*, 12(5):915–21, 1991.
- F. Fazekas, R. Kleinert, H. Offenbacher, R. Schmidt, G. Kleinert, F. Payer, H. Radner, and H. Lechner. Pathologic correlates of incidental mri white matter signal hyperintensities. *Neurology*, 43(9):1683–9, 1993.
- M. S. Fernando and P. G. Ince. Vascular pathologies and cognition in a population-based cohort of elderly people. *J Neurol Sci*, 226(1-2):13–7, 2004.
- M. S. Fernando, J. E. Simpson, F. Matthews, C. Brayne, C. E. Lewis, R. Barber, R. N. Kalaria, G. Forster, F. Esteves, S. B. Wharton, P. J. Shaw, J. T. O’Brien, and P. G. Ince. White matter lesions in an unselected cohort of the elderly: molecular pathology suggests origin from chronic hypoperfusion injury. *Stroke*, 37(6): 1391–8, 2006.
- C. M. Fiford, E. N. Manning, J. W. Bartlett, D. M. Cash, I. B. Malone, G. R. Ridgway, M. Lehmann, K. K. Leung, C. H. Sudre, S. Ourselin, G. J. Biessels, O. T. Carmichael, N. C. Fox, M. J. Cardoso, and J. Barnes. White matter hyperintensities are associated with disproportionate progressive hippocampal atrophy. *Hippocampus*, 27(3):249–262, 2017.

- A. S. Fleisher, K. Chen, Y. T. Quiroz, L. J. Jakimovich, M. Gutierrez Gomez, C. M. Langois, J. B. Langbaum, A. Roontiva, P. Thiyyagura, W. Lee, N. Ayutyanont, L. Lopez, S. Moreno, C. Muñoz, V. Tirado, N. Acosta-Baena, A. M. Fagan, M. Giraldo, G. Garcia, M. J. Huentelman, P. N. Tariot, F. Lopera, and E. M. Reiman. Associations between biomarkers and age in the presenilin 1 e280a autosomal dominant alzheimer disease kindred: a cross-sectional study. *JAMA Neurol*, 72(3):316–24, 2015.
- H. M. Fonteijn, M. Modat, M. J. Clarkson, J. Barnes, M. Lehmann, N. Z. Hobbs, R. I. Scahill, S. J. Tabrizi, S. Ourselin, N. C. Fox, and D. C. Alexander. An event-based model for disease progression and its application in familial alzheimer’s disease and huntington’s disease. *Neuroimage*, 60(3):1880–9, 2012.
- C. H. Fox, F. B. Johnson, J. Whiting, and P. P. Roller. Formaldehyde fixation. *J Histochem Cytochem*, 33(8):845–53, 1985.
- N. C. Fox, R. S. Black, S. Gilman, M. N. Rossor, S. G. Griffith, L. Jenkins, and M. Koller. Effects of abeta immunization (an1792) on mri measures of cerebral volume in alzheimer disease. *Neurology*, 64(9):1563–72, 2005.
- P. A. Freeborough and N. C. Fox. The boundary shift integral: an accurate and robust measure of cerebral volume changes from registered repeat mri. *IEEE Trans Med Imaging*, 16(5):623–9, 1997.
- W. M. Freeze, H. I. Jacobs, E. H. Gronenschild, J. F. Jansen, S. Burgmans, P. Aalten, L. Clerx, S. J. Vos, M. A. Van Buchem, F. Barkhof, W. M. Van Der Flier, M. M. Verbeek, M. O. Rikkert, W. H. Backes, and F. R. Verhey. White matter hyperintensities potentiate hippocampal volume reduction in non-demented older individuals with abnormal amyloid- β . *Journal of Alzheimer’s Disease*, 55: 333–342, 2016.
- R. Frikke-Schmidt, B. G. Nordestgaard, D. Thudium, M. L. Moes Gronholdt, and A. Tybjaerg-Hansen. Apoe genotype predicts ad and other dementia but not ischemic cerebrovascular disease. *Neurology*, 56(2):194–200, 2001.

- L. Gao, Z. Jiang, Z. Cai, M. Cai, Q. Zhang, Y. Ma, G. Li, F. Zhao, and Q. Ma. Brain iron deposition analysis using susceptibility weighted imaging and its association with body iron level in patients with mild cognitive impairment. *Mol Med Rep*, 16(6):8209–8215, 2017.
- E. Garde, E. Lykke Mortensen, E. Rostrup, and O. B. Paulson. Decline in intelligence is associated with progression in white matter hyperintensity volume. *J Neurol Neurosurg Psychiatry*, 76(9):1289–91, 2005.
- T. Gatttringer, D. Pinter, C. Enzinger, T. Seifert-Held, M. Kneihsl, S. Fandler, A. Pichler, C. Barro, S. Grobke, M. Voortman, L. Pirpamer, E. Hofer, S. Ropele, R. Schmidt, J. Kuhle, F. Fazekas, and M. Khalil. Serum neurofilament light is sensitive to active cerebral small vessel disease. *Neurology*, 89(20):2108–2114, 2017.
- M. L. Gawne-Cain, N. C. Silver, I. F. Moseley, and D. H. Miller. Fast flair of the brain: the range of appearances in normal subjects and its application to quantification of white-matter disease. *Neuroradiology*, 39(4):243–9, 1997.
- G. G. Glenner and C. W. Wong. Alzheimer’s disease: initial report of the purification and characterization of a novel cerebrovascular amyloid protein. *Biochem Biophys Res Commun*, 120(3):885–90, 1984.
- A. Goate, M. C. Chartier-Harlin, M. Mullan, J. Brown, F. Crawford, L. Fidani, L. Giuffra, A. Haynes, N. Irving, L. James, and et al. Segregation of a missense mutation in the amyloid precursor protein gene with familial alzheimer’s disease. *Nature*, 349(6311):704–6, 1991.
- A. K. Godbolt, L. Cipolotti, H. Watt, N. C. Fox, J. C. Janssen, and M. N. Rossor. The natural history of alzheimer disease: a longitudinal presymptomatic and symptomatic study of a familial cohort. *Arch Neurol*, 61(11):1743–8, 2004.
- E. J. T. Goetghebeur and S. J. Pocock. Detection and estimation of j-shaped risk-response relationship. *Journal of the Royal Statistical Society. Series A (Statistics in Society)*, 158(1):107–121, 1995.

- B. A. Gordon, S. Najmi, P. Hsu, C. M. Roe, J. C. Morris, and T. L. Benzinger. The effects of white matter hyperintensities and amyloid deposition on alzheimer dementia. *NeuroImage: Clinical*, 8:246–252, 2015.
- B. A. Gordon, T. M. Blazey, J. Christensen, A. Dincer, S. Flores, S. Keefe, C. Chen, Y. Su, E. M. McDade, G. Wang, Y. Li, J. Hassenstab, A. Aschenbrenner, R. Hornbeck, C. R. Jack, B. M. Ances, S. B. Berman, J. R. Brosch, D. Galasko, S. Gauthier, J. J. Lah, M. Masellis, C. H. van Dyck, M. A. Mintun, G. Klein, S. Ristic, N. J. Cairns, D. S. Marcus, C. Xiong, D. M. Holtzman, M. E. Raichle, J. C. Morris, R. J. Bateman, and T. L. S. Benzinger. Tau pet in autosomal dominant alzheimer’s disease: relationship with cognition, dementia and other biomarkers. *Brain*, 142(4):1063–1076, 2019.
- M. Goubran, S. de Ribaupierre, R. R. Hammond, C. Currie, J. G. Burneo, A. G. Parrent, T. M. Peters, and A. R. Khan. Registration of in-vivo to ex-vivo mri of surgically resected specimens: a pipeline for histology to in-vivo registration. *J Neurosci Methods*, 241:53–65, 2015.
- A. A. Gouw, A. Seewann, H. Vrenken, W. M. van der Flier, J. M. Rozemuller, F. Barkhof, P. Scheltens, and J. J. Geurts. Heterogeneity of white matter hyperintensities in alzheimer’s disease: post-mortem quantitative mri and neuropathology. *Brain*, 131(Pt 12):3286–98, 2008a.
- A. A. Gouw, W. M. van der Flier, E. C. van Straaten, L. Pantoni, A. J. Bastos-Leite, D. Inzitari, T. Erkinjuntti, L. O. Wahlund, C. Ryberg, R. Schmidt, F. Fazekas, P. Scheltens, and F. Barkhof. Reliability and sensitivity of visual scales versus volumetry for evaluating white matter hyperintensity progression. *Cerebrovasc Dis*, 25(3):247–53, 2008b.
- A. A. Gouw, A. Seewann, W. M. van der Flier, F. Barkhof, A. M. Rozemuller, P. Scheltens, and J. J. Geurts. Heterogeneity of small vessel disease: a systematic review of mri and histopathology correlations. *J Neurol Neurosurg Psychiatry*, 82(2):126–35, 2011.

- J. Graff-Radford, E. M. Arenaza-Urquijo, D. S. Knopman, C. G. Schwarz, J. Brown, Robert D., A. A. Rabinstein, J. L. Gunter, M. L. Senjem, S. A. Przybelski, T. Lesnick, C. Ward, M. M. Mielke, V. J. Lowe, R. C. Petersen, W. K. Kremers, K. Kantarci, J. Jack, Clifford R., and P. Vemuri. White matter hyperintensities: relationship to amyloid and tau burden. *Brain*, 2019.
- S. T. Grafton, S. M. Sumi, G. K. Stimac, J. Alvord, E. C., C. M. Shaw, and D. Nochlin. Comparison of postmortem magnetic resonance imaging and neuropathologic findings in the cerebral white matter. *Arch Neurol*, 48(3):293–8, 1991.
- L. Griffanti, M. Jenkinson, S. Suri, E. Zsoldos, A. Mahmood, N. Filippini, C. E. Sexton, A. Topiwala, C. Allan, M. Kivimäki, A. Singh-Manoux, K. P. Ebmeier, C. E. Mackay, and G. Zamboni. Classification and characterization of periventricular and deep white matter hyperintensities on mri: A study in older adults. *Neuroimage*, 170:174–181, 2018.
- L. T. Grinberg and D. R. Thal. Vascular pathology in the aged human brain. *Acta Neuropathologica*, 119:277–290, 2010.
- I. Grundke-Iqbal, K. Iqbal, M. Quinlan, Y. C. Tung, M. S. Zaidi, and H. M. Wisniewski. Microtubule-associated protein tau. a component of alzheimer paired helical filaments. *J Biol Chem*, 261(13):6084–9, 1986.
- V. A. Guzman, O. T. Carmichael, C. Schwarz, G. Tosto, M. E. Zimmerman, and A. M. Brickman. White matter hyperintensities and amyloid are independently associated with entorhinal cortex volume among individuals with mild cognitive impairment. *Alzheimer's and Dementia*, 9:S124–S131, 2013.
- V. C. Hachinski, L. D. Iliff, E. Zilhka, G. H. Du Boulay, V. L. McAllister, J. Marshall, R. W. Russell, and L. Symon. Cerebral blood flow in dementia. *Arch Neurol*, 32(9):632–7, 1975.
- T. J. Haight, S. M. Landau, O. Carmichael, C. Schwarz, C. DeCarli, and W. J.

- Jagust. Dissociable effects of alzheimer disease and white matter hyperintensities on brain metabolism. *JAMA Neurology*, 70:1039–1045, 2013.
- A. H. Hainsworth, T. Minett, J. Andoh, G. Forster, I. Bhide, T. R. Barrick, K. Elderfield, J. Jeevahan, H. S. Markus, and L. R. Bridges. Neuropathology of white matter lesions, blood-brain barrier dysfunction, and dementia. *Stroke*, 48(10):2799–2804, 2017.
- A. M. Halefoglou and D. M. Yousem. Susceptibility weighted imaging: Clinical applications and future directions. *World journal of radiology*, 10(4):30–45, 2018.
- J. A. Hardy and G. A. Higgins. Alzheimer’s disease: the amyloid cascade hypothesis. *Science*, 256(5054):184–5, 1992.
- Y. Hase, K. Horsburgh, M. Ihara, and R. N. Kalaria. White matter degeneration in vascular and other ageing-related dementias. *J Neurochem*, 144(5):617–633, 2018.
- C. A. Hawkes, N. Jayakody, D. A. Johnston, I. Bechmann, and R. O. Carare. Failure of perivascular drainage of β -amyloid in cerebral amyloid angiopathy. *Brain Pathology*, 24:396–403, 2014.
- A. B. Hill. The environment and disease: Association or causation? *Proceedings of the Royal Society of Medicine*, 58(5):295–300, 1965.
- C. Holmes. Genotype and phenotype in alzheimer’s disease. *British Journal of Psychiatry*, 180(2):131–134, 2002.
- H. E. Holmes, N. M. Powell, D. Ma, O. Ismail, I. F. Harrison, J. A. Wells, N. Colgan, J. M. O’Callaghan, R. A. Johnson, T. K. Murray, Z. Ahmed, M. Heggenes, A. Fisher, M. J. Cardoso, M. Modat, M. J. O’Neill, E. C. Collins, E. M. C. Fisher, S. Ourselin, and M. F. Lythgoe. Comparison of in vivo and ex vivo mri for the detection of structural abnormalities in a mouse model of tauopathy. *Frontiers in Neuroinformatics*, 11(20), 2017.

- L. S. Honig, B. Vellas, M. Woodward, M. Boada, R. Bullock, M. Borrie, K. Hager, N. Andreasen, E. Scarpini, H. Liu-Seifert, M. Case, R. A. Dean, A. Hake, K. Sundell, V. Poole Hoffmann, C. Carlson, R. Khanna, M. Mintun, R. DeMattos, K. J. Selzler, and E. Siemers. Trial of solanezumab for mild dementia due to alzheimer's disease. *New England Journal of Medicine*, 378(4):321–330, 2018.
- C. Iadecola and R. F. Gottesman. Cerebrovascular alterations in alzheimer disease. *Circulation Research*, 123(4):406–408, 2018.
- J. E. Iglesias, M. Lorenzi, S. Ferraris, L. Peter, M. Modat, A. Stevens, B. Fischl, and T. Vercauteren. Model-based refinement of nonlinear registrations in 3d histology reconstruction, 2018.
- M. Ihara, T. M. Polvikoski, R. Hall, J. Y. Slade, R. H. Perry, A. E. Oakley, E. Englund, J. T. O'Brien, P. G. Ince, and R. N. Kalaria. Quantification of myelin loss in frontal lobe white matter in vascular dementia, alzheimer's disease, and dementia with lewy bodies. *Acta neuropathologica*, 119(5):579–589, 2010.
- M. D. Ikonomic, W. E. Klunk, E. E. Abrahamson, C. A. Mathis, J. C. Price, N. D. Tsopelas, B. J. Lopresti, S. Ziolk, W. Bi, W. R. Paljug, M. L. Debnath, C. E. Hope, B. A. Isanski, R. L. Hamilton, and S. T. DeKosky. Post-mortem correlates of in vivo pib-pet amyloid imaging in a typical case of alzheimer's disease. *Brain : a journal of neurology*, 131(Pt 6):1630–1645, 2008.
- E. Iordanishvili, M. Schall, R. Loução, M. Zimmermann, K. Kotetishvili, N. J. Shah, and A. M. Oros-Peusquens. Quantitative mri of cerebral white matter hyperintensities: A new approach towards understanding the underlying pathology. *Neuroimage*, 202:116077, 2019.
- N. Itoh, H. Arai, K. Urakami, K. Ishiguro, H. Ohno, H. Hampel, K. Buerger, J. Wiltfang, M. Otto, H. Kretschmar, H. J. Moeller, M. Imagawa, H. Kohno, K. Nakashima, S. Kuzuhara, H. Sasaki, and K. Imahori. Large-scale, multicenter study of cerebrospinal fluid tau protein phosphorylated at serine 199 for the antemortem diagnosis of alzheimer's disease. *Ann Neurol*, 50(2):150–6, 2001.

- C. R. Jack, M. A. Bernstein, B. J. Borowski, J. L. Gunter, N. C. Fox, P. M. Thompson, N. Schuff, G. Krueger, R. J. Killiany, C. S. DeCarli, A. M. Dale, O. W. Carmichael, D. Tosun, and M. W. Weiner. Update on the magnetic resonance imaging core of the alzheimer's disease neuroimaging initiative. *Alzheimer's and Dementia*, 6(3):212–220, 2010a.
- C. R. Jack, D. A. Bennett, K. Blennow, M. C. Carrillo, B. Dunn, S. B. Haeberlein, D. M. Holtzman, W. Jagust, F. Jessen, J. Karlawish, E. Liu, J. L. Molinuevo, T. Montine, C. Phelps, K. P. Rankin, C. C. Rowe, P. Scheltens, E. Siemers, H. M. Snyder, R. Sperling, C. Elliott, E. Masliah, L. Ryan, and N. Silverberg. Nia-aa research framework: Toward a biological definition of alzheimer's disease. *Alzheimer's and Dementia*, 14:535–562, 2018.
- J. Jack, C. R., M. A. Bernstein, N. C. Fox, P. Thompson, G. Alexander, D. Harvey, B. Borowski, P. J. Britson, L. W. J, C. Ward, A. M. Dale, J. P. Felmlee, J. L. Gunter, D. L. Hill, R. Killiany, N. Schuff, S. Fox-Bosetti, C. Lin, C. Studholme, C. S. DeCarli, G. Krueger, H. A. Ward, G. J. Metzger, K. T. Scott, R. Mallozzi, D. Blezek, J. Levy, J. P. Debbins, A. S. Fleisher, M. Albert, R. Green, G.artzokis, G. Glover, J. Mugler, and M. W. Weiner. The alzheimer's disease neuroimaging initiative (adni): Mri methods. *J Magn Reson Imaging*, 27(4):685–91, 2008a.
- J. Jack, C. R., V. J. Lowe, M. L. Senjem, S. D. Weigand, B. J. Kemp, M. M. Shiung, D. S. Knopman, B. F. Boeve, W. E. Klunk, C. A. Mathis, and R. C. Petersen. 11c pib and structural mri provide complementary information in imaging of alzheimer's disease and amnesic mild cognitive impairment. *Brain*, 131(Pt 3): 665–80, 2008b.
- J. Jack, C. R., D. S. Knopman, W. J. Jagust, L. M. Shaw, P. S. Aisen, M. W. Weiner, R. C. Petersen, and J. Q. Trojanowski. Hypothetical model of dynamic biomarkers of the alzheimer's pathological cascade. *Lancet Neurol*, 9(1):119–28, 2010b.
- J. Jack, Clifford R., J. Barnes, M. A. Bernstein, B. J. Borowski, J. Brewer, S. Clegg,

- A. M. Dale, O. Carmichael, C. Ching, C. DeCarli, R. S. Desikan, C. Fennema-Notestine, A. M. Fjell, E. Fletcher, N. C. Fox, J. Gunter, B. A. Gutman, D. Holland, X. Hua, P. Insel, K. Kantarci, R. J. Killiany, G. Krueger, K. K. Leung, S. Mackin, P. Maillard, I. B. Malone, N. Mattsson, L. McEvoy, M. Modat, S. Mueller, R. Nosheny, S. Ourselin, N. Schuff, M. L. Senjem, A. Simonson, P. M. Thompson, D. Rettmann, P. Vemuri, K. Walhovd, Y. Zhao, S. Zuk, and M. Weiner. Magnetic resonance imaging in alzheimer's disease neuroimaging initiative 2. *Alzheimer's and dementia : the journal of the Alzheimer's Association*, 11(7):740–756, 2015.
- J. T. Jarrett, E. P. Berger, and J. Lansbury, P. T. The carboxy terminus of the beta amyloid protein is critical for the seeding of amyloid formation: implications for the pathogenesis of alzheimer's disease. *Biochemistry*, 32(18):4693–7, 1993.
- A. L. Jefferson, A. S. Beiser, J. J. Himali, S. Seshadri, C. J. O'Donnell, W. J. Manning, P. A. Wolf, R. Au, and E. J. Benjamin. Low cardiac index is associated with incident dementia and alzheimer disease: the framingham heart study. *Circulation*, 131(15):1333–9, 2015.
- K. A. Jellinger and J. Attems. Prevalence and impact of cerebrovascular pathology in alzheimer's disease and parkinsonism. *Acta Neurol Scand*, 114(1):38–46, 2006.
- G. A. Jicha, J. E. Parisi, D. W. Dickson, K. Johnson, R. Cha, R. J. Ivnik, E. G. Tangalos, B. F. Boeve, D. S. Knopman, H. Braak, and R. C. Petersen. Neuropathologic outcome of mild cognitive impairment following progression to clinical dementia. *Arch Neurol*, 63(5):674–81, 2006.
- K. A. Johnson, M. Gregas, J. A. Becker, C. Kinnecom, D. H. Salat, E. K. Moran, E. E. Smith, J. Rosand, D. M. Rentz, W. E. Klunk, C. A. Mathis, J. C. Price, S. T. Dekosky, A. J. Fischman, and S. M. Greenberg. Imaging of amyloid burden and distribution in cerebral amyloid angiopathy. *Ann Neurol*, 62(3):229–34, 2007.
- K. A. Johnson, N. C. Fox, R. A. Sperling, and W. E. Klunk. Brain imaging in

- alzheimer disease. *Cold Spring Harbor perspectives in medicine*, 2(4):a006213–a006213, 2012.
- K. A. Johnson, A. Schultz, R. A. Betensky, J. A. Becker, J. Sepulcre, D. Rentz, E. Mormino, J. Chhatwal, R. Amariglio, K. Papp, G. Marshall, M. Albers, S. Mauro, L. Pepin, J. Alverio, K. Judge, M. Philiossaint, T. Shoup, D. Yokell, B. Dickerson, T. Gomez-Isla, B. Hyman, N. Vasdev, and R. Sperling. Tau positron emission tomographic imaging in aging and early alzheimer disease. *Ann Neurol*, 79(1):110–9, 2016.
- R. N. Kalaria. The pathology and pathophysiology of vascular dementia. *Neuropharmacology*, 134(Pt B):226–239, 2018.
- L. F. Kalheim, A. Bjørnerud, T. Fladby, K. Vegge, and P. Selnes. White matter hyperintensity microstructure in amyloid dysmetabolism. *Journal of Cerebral Blood Flow and Metabolism*, 37:356–365, 2017.
- B. M. Kandel, B. B. Avants, J. C. Gee, C. T. McMillan, G. Erus, J. Doshi, C. Davatzikos, and D. A. Wolk. White matter hyperintensities are more highly associated with preclinical alzheimer’s disease than imaging and cognitive markers of neurodegeneration. *Alzheimer’s and Dementia: Diagnosis, Assessment and Disease Monitoring*, 4:18–27, 2016.
- A. Kapasi, C. DeCarli, and J. A. Schneider. Impact of multiple pathologies on the threshold for clinically overt dementia. *Acta Neuropathol*, 134(2):171–186, 2017.
- M. I. Kester, J. D. Goos, C. E. Teunissen, M. R. Benedictus, F. H. Bouwman, M. P. Wattjes, F. Barkhof, P. Scheltens, and W. M. Van Der Flier. Associations between cerebral small-vessel disease and alzheimer disease pathology as measured by cerebrospinal fluid biomarkers. *JAMA Neurology*, 71:855–862, 2014.
- W. H. Kim, A. M. Racine, N. Adluru, S. J. Hwang, K. Blennow, H. Zetterberg, C. M. Carlsson, S. Asthana, R. L. Kosciak, S. C. Johnson, B. B. Bendlin, and

- V. Singh. Cerebrospinal fluid biomarkers of neurofibrillary tangles and synaptic dysfunction are associated with longitudinal decline in white matter connectivity: A multi-resolution graph analysis. *Neuroimage Clin*, 21:101586, 2019.
- K. M. Kinnunen, D. M. Cash, T. Poole, C. Frost, T. L. S. Benzinger, R. L. Ahsan, K. K. Leung, M. J. Cardoso, M. Modat, I. B. Malone, J. C. Morris, R. J. Bateman, D. S. Marcus, A. Goate, S. P. Salloway, S. Correia, R. A. Sperling, J. P. Chhatwal, R. P. Mayeux, A. M. Brickman, R. N. Martins, M. R. Farlow, B. Ghetti, A. J. Saykin, J. Jack, C. R., P. R. Schofield, E. McDade, M. W. Weiner, J. M. Ringman, P. M. Thompson, C. L. Masters, C. C. Rowe, M. N. Rossor, S. Ourselin, and N. C. Fox. Presymptomatic atrophy in autosomal dominant alzheimer's disease: A serial magnetic resonance imaging study. *Alzheimers Dement*, 14(1):43–53, 2018.
- W. E. Klunk. Amyloid imaging as a biomarker for cerebral β -amyloidosis and risk prediction for alzheimer dementia. *Neurobiology of aging*, 32 Suppl 1(Suppl 1): S20–S36, 2011.
- E. S. Korf, L. O. Wahlund, P. J. Visser, and P. Scheltens. Medial temporal lobe atrophy on mri predicts dementia in patients with mild cognitive impairment. *Neurology*, 63(1):94–100, 2004.
- J. Kuhle, K. Plattner, J. P. Bestwick, R. L. Lindberg, S. V. Ramagopalan, N. Norgren, A. Nissim, A. Malaspina, D. Leppert, G. Giovannoni, and L. Kappos. A comparative study of csf neurofilament light and heavy chain protein in ms. *Mult Scler*, 19(12):1597–603, 2013.
- R. La Joie, A. V. Visani, S. L. Baker, J. A. Brown, V. Bourakova, J. Cha, K. Chaudhary, L. Edwards, L. Iaccarino, M. Janabi, O. H. Lesman-Segev, Z. A. Miller, D. C. Perry, J. P. O'Neil, J. Pham, J. C. Rojas, H. J. Rosen, W. W. Seeley, R. M. Tsai, B. L. Miller, W. J. Jagust, and G. D. Rabinovici. Prospective longitudinal atrophy in alzheimer's disease correlates with the intensity and topography of baseline tau-pet. *Sci Transl Med*, 12(524), 2020.

- C. A. Lane, J. Barnes, J. M. Nicholas, C. H. Sudre, D. M. Cash, I. B. Malone, T. D. Parker, A. Keshavan, S. M. Buchanan, S. E. Keuss, S. N. James, K. Lu, H. Murray-Smith, A. Wong, E. Gordon, W. Coath, M. Modat, D. Thomas, M. Richards, N. C. Fox, and J. M. Schott. Associations between vascular risk across adulthood and brain pathology in late life: Evidence from a british birth cohort. *JAMA Neurol*, 77(2):1–9, 2019a.
- C. A. Lane, J. Barnes, J. M. Nicholas, C. H. Sudre, D. M. Cash, T. D. Parker, I. B. Malone, K. Lu, S.-N. James, A. Keshavan, H. Murray-Smith, A. Wong, S. M. Buchanan, S. E. Keuss, E. Gordon, W. Coath, A. Barnes, J. Dickson, M. Modat, D. Thomas, S. J. Crutch, R. Hardy, M. Richards, N. C. Fox, and J. M. Schott. Associations between blood pressure across adulthood and late-life brain structure and pathology in the neuroscience substudy of the 1946 british birth cohort (insight 46): an epidemiological study. *The Lancet Neurology*, 18(10):942–952, 2019b.
- E. M. Larsson, E. Englund, M. Sjöbeck, J. Lätt, and S. Brockstedt. Mri with diffusion tensor imaging post-mortem at 3.0 t in a patient with frontotemporal dementia. *Dement Geriatr Cogn Disord*, 17(4):316–9, 2004.
- L. J. Launer, G. W. Ross, H. Petrovitch, K. Masaki, D. Foley, L. R. White, and R. J. Havlik. Midlife blood pressure and dementia: the honolulu-asia aging study. *Neurobiol Aging*, 21(1):49–55, 2000.
- E. Lavdas, I. Tsougos, S. Kogia, G. Gratsias, P. Svolos, V. Roka, I. V. Fezoulidis, and E. Kapsalaki. T2 flair artifacts at 3-t brain magnetic resonance imaging. *Clin Imaging*, 38(2):85–90, 2014.
- S. Lee, F. Viqar, M. E. Zimmerman, A. Narkhede, G. Tosto, T. L. Benzinger, D. S. Marcus, A. M. Fagan, A. Goate, N. C. Fox, N. J. Cairns, D. M. Holtzman, V. Buckles, B. Ghetti, E. McDade, R. N. Martins, A. J. Saykin, C. L. Masters, J. M. Ringman, N. S. Ryan, S. Förster, C. Laske, P. R. Schofield, R. A. Sperling, S. Salloway, S. Correia, C. Jack, M. Weiner, R. J. Bateman, J. C. Morris,

- R. Mayeux, and A. M. Brickman. White matter hyperintensities are a core feature of alzheimer's disease: Evidence from the dominantly inherited alzheimer network. *Annals of Neurology*, 79:929–939, 2016.
- S. Lee, M. E. Zimmerman, A. Narkhede, S. E. Nasrabady, G. Tosto, I. B. Meier, T. L. S. Benzinger, D. S. Marcus, A. M. Fagan, N. C. Fox, N. J. Cairns, D. M. Holtzman, V. Buckles, B. Ghetti, E. McDade, R. N. Martins, A. J. Saykin, C. L. Masters, J. M. Ringman, S. Frster, P. R. Schofield, R. A. Sperling, K. A. Johnson, J. P. Chhatwal, S. Salloway, S. Correia, J. Jack, C. R., M. Weiner, R. J. Bateman, J. C. Morris, R. Mayeux, and A. M. Brickman. White matter hyperintensities and the mediating role of cerebral amyloid angiopathy in dominantly-inherited alzheimer's disease. *PLoS One*, 13(5):e0195838, 2018.
- K. K. Leung, G. R. Ridgway, S. Ourselin, and N. C. Fox. Consistent multi-time-point brain atrophy estimation from the boundary shift integral. *Neuroimage*, 59(4):3995–4005, 2012.
- A. Leuzy, K. Chiotis, L. Lemoine, P. G. Gillberg, O. Almkvist, E. Rodriguez-Vieitez, and A. Nordberg. Tau pet imaging in neurodegenerative tauopathies-still a challenge. *Mol Psychiatry*, 24(8):1112–1134, 2019.
- E. Levy-Lahad, W. Wasco, P. Poorkaj, D. M. Romano, J. Oshima, W. H. Pettingell, C. E. Yu, P. D. Jondro, S. D. Schmidt, K. Wang, and et al. Candidate gene for the chromosome 1 familial alzheimer's disease locus. *Science*, 269(5226):973–7, 1995.
- P. Lewczuk, N. Ermann, U. Andreasson, C. Schultheis, J. Podhorna, P. Spitzer, J. M. Maler, J. Kornhuber, K. Blennow, and H. Zetterberg. Plasma neurofilament light as a potential biomarker of neurodegeneration in alzheimer's disease. *Alzheimers Res Ther*, 10(1):71, 2018.
- H. Lin, C. Satizabal, Z. Xie, Q. Yang, T. Huan, R. Joehanes, C. Wen, P. J. Munson, A. Beiser, D. Levy, and S. Seshadri. Whole blood gene expression and white matter hyperintensities. *Molecular Neurodegeneration*, 12(1):67, 2017.

- G. Livingston, A. Sommerlad, V. Orgeta, S. G. Costafreda, J. Huntley, D. Ames, C. Ballard, S. Banerjee, A. Burns, J. Cohen-Mansfield, C. Cooper, N. Fox, L. N. Gitlin, R. Howard, H. C. Kales, E. B. Larson, K. Ritchie, K. Rockwood, E. L. Sampson, Q. Samus, L. S. Schneider, G. Selbaek, L. Teri, and N. Mukadam. Dementia prevention, intervention, and care. *Lancet*, 390(10113):2673–2734, 2017.
- G. Livingston, J. Huntley, A. Sommerlad, D. Ames, C. Ballard, S. Banerjee, C. Brayne, A. Burns, J. Cohen-Mansfield, C. Cooper, S. G. Costafreda, A. Dias, N. Fox, L. N. Gitlin, R. Howard, H. C. Kales, M. Kivimäki, E. B. Larson, A. Ogunniyi, V. Orgeta, K. Ritchie, K. Rockwood, E. L. Sampson, Q. Samus, L. S. Schneider, G. Selbæk, L. Teri, and N. Mukadam. Dementia prevention, intervention, and care: 2020 report of the *lancet* commission. *The Lancet*, 396(10248):413–446, 2020.
- O. L. Lopez, W. E. Klunk, C. Mathis, R. L. Coleman, J. Price, J. T. Becker, H. J. Aizenstein, B. Snitz, A. Cohen, M. Ikonovic, E. McDade, S. T. DeKosky, L. Weissfeld, and L. H. Kuller. Amyloid, neurodegeneration, and small vessel disease as predictors of dementia in the oldest-old. *Neurology*, 83(20):1804–11, 2014.
- S. Love, J. A. Nicoll, A. Hughes, and G. K. Wilcock. Apoe and cerebral amyloid angiopathy in the elderly. *Neuroreport*, 14(11):1535–6, 2003.
- S. Love, K. Chalmers, P. Ince, M. Esiri, J. Attems, K. Jellinger, M. Yamada, M. McCarron, T. Minett, F. Matthews, S. Greenberg, D. Mann, and P. G. Kehoe. Development, appraisal, validation and implementation of a consensus protocol for the assessment of cerebral amyloid angiopathy in post-mortem brain tissue. *Am J Neurodegener Dis*, 3(1):19–32, 2014.
- C. H. Lu, C. Macdonald-Wallis, E. Gray, N. Pearce, A. Petzold, N. Norgren, G. Giovannoni, P. Fratta, K. Sidle, M. Fish, R. Orrell, R. Howard, K. Talbot, L. Green-smith, J. Kuhle, M. R. Turner, and A. Malaspina. Neurofilament light chain: A

- prognostic biomarker in amyotrophic lateral sclerosis. *Neurology*, 84(22):2247–57, 2015.
- C. L. Maarouf, I. D. Daus, S. Spina, R. Vidal, T. A. Kokjohn, R. L. Patton, W. M. Kalback, D. C. Luehrs, D. G. Walker, E. M. Castaño, T. G. Beach, B. Ghetti, and A. E. Roher. Histopathological and molecular heterogeneity among individuals with dementia associated with presenilin mutations. *Molecular Neurodegeneration*, 3(1):20, 2008.
- P. Maillard, O. Carmichael, D. Harvey, E. Fletcher, B. Reed, D. Mungas, and C. DeCarli. Flair and diffusion mri signals are independent predictors of white matter hyperintensities. *AJNR Am J Neuroradiol*, 34(1):54–61, 2013.
- M. Mancini, S. Crampsie, D. L. Thomas, Z. Jaunmuktane, J. L. Holton, and J. E. Iglesias. Hierarchical joint registration of tissue blocks with soft shape constraints for large-scale histology of the human brain. In *2019 IEEE 16th International Symposium on Biomedical Imaging (ISBI 2019)*, pages 666–669, 2019. ISBN 1945-8452. doi: 10.1109/ISBI.2019.8759396.
- D. M. A. Mann, S. M. Pickering-Brown, A. Takeuchi, and T. Iwatsubo. Amyloid angiopathy and variability in amyloid β deposition is determined by mutation position in presenilin-1-linked alzheimer’s disease. *The American Journal of Pathology*, 158(6):2165–2175, 2001.
- J. Maranzano, M. Dadar, A. Bertrand-Grenier, E. M. Frigon, J. Pellerin, S. Plante, S. Duchesne, C. L. Tardif, D. Boire, and G. Bronchti. A novel ex vivo, in situ method to study the human brain through mri and histology. *J Neurosci Methods*, 345:108903, 2020.
- M. Marnane, O. O. Al-Jawadi, S. Mortazavi, K. J. Pogorzelec, B. W. Wang, H. H. Feldman, and G. Y. R. Hsiung. Periventricular hyperintensities are associated with elevated cerebral amyloid. *Neurology*, 86:535–543, 2016.
- V. G. Marshall, J. Bradley, W. G., C. E. Marshall, T. Bhoopat, and R. H. Rhodes.

- Deep white matter infarction: correlation of mr imaging and histopathologic findings. *Radiology*, 167(2):517–22, 1988.
- M. Mascalchi, D. Inzitari, G. Dal Pozzo, N. Taverni, and A. L. Abbamondi. Computed tomography, magnetic resonance imaging and pathological correlations in a case of binswanger’s disease. *Canadian Journal of Neurological Sciences / Journal Canadien des Sciences Neurologiques*, 16(2):214–218, 1989.
- C. L. Masters, R. Bateman, K. Blennow, C. C. Rowe, R. A. Sperling, and J. L. Cummings. Alzheimer’s disease. *Nat Rev Dis Primers*, 1:15056, 2015.
- N. Mattsson, E. Rosen, O. Hansson, N. Andreasen, L. Parnetti, M. Jonsson, S. K. Herukka, W. M. van der Flier, M. A. Blankenstein, M. Ewers, K. Rich, E. Kaiser, M. M. Verbeek, M. Olde Rikkert, M. Tsolaki, E. Mulugeta, D. Aarsland, P. J. Visser, J. Schroder, J. Marcusson, M. de Leon, H. Hampel, P. Scheltens, A. Wallin, M. Eriksdotter-Jonhagen, L. Minthon, B. Winblad, K. Blennow, and H. Zetterberg. Age and diagnostic performance of alzheimer disease csf biomarkers. *Neurology*, 78(7):468–76, 2012.
- N. Mattsson, P. S. Insel, S. Palmqvist, E. Portelius, H. Zetterberg, M. Weiner, K. Blennow, and O. Hansson. Cerebrospinal fluid tau, neurogranin, and neurofilament light in alzheimer’s disease. *EMBO Mol Med*, 8(10):1184–1196, 2016.
- N. Mattsson, U. Andreasson, H. Zetterberg, and K. Blennow. Association of plasma neurofilament light with neurodegeneration in patients with alzheimer disease. *JAMA Neurol*, 74(5):557–566, 2017.
- N. Mattsson, N. C. Cullen, U. Andreasson, H. Zetterberg, and K. Blennow. Association between longitudinal plasma neurofilament light and neurodegeneration in patients with alzheimer disease. *JAMA Neurol*, 76(7):791–799, 2019.
- K. E. McAleese, M. Firbank, M. Dey, S. J. Colloby, L. Walker, M. Johnson, J. R. Beverley, J. P. Taylor, A. J. Thomas, J. T. O’Brien, and J. Attems. Cortical tau load is associated with white matter hyperintensities. *Acta neuropathologica communications*, 3:60, 2015.

- K. E. McAleese, I. Alafuzoff, A. Charidimou, J. De Reuck, L. T. Grinberg, A. H. Hainsworth, T. Hortobagyi, P. Ince, K. Jellinger, J. Gao, R. N. Kalara, G. G. Kovacs, E. Kovari, S. Love, M. Popovic, O. Skrobot, R. Taipa, D. R. Thal, D. Werring, S. B. Wharton, and J. Attems. Post-mortem assessment in vascular dementia: advances and aspirations. *BMC Med*, 14(1):129, 2016.
- K. E. McAleese, L. Walker, S. Graham, E. L. Moya, M. Johnson, D. Erskine, S. J. Colloby, M. Dey, C. Martin-Ruiz, J. P. Taylor, A. J. Thomas, I. G. McKeith, C. De Carli, and J. Attems. Parietal white matter lesions in alzheimer's disease are associated with cortical neurodegenerative pathology, but not with small vessel disease. *Acta Neuropathologica*, 134:459–473, 2017.
- E. McDade, G. Wang, B. A. Gordon, J. Hassenstab, T. L. S. Benzinger, V. Buckles, A. M. Fagan, D. M. Holtzman, N. J. Cairns, A. M. Goate, D. S. Marcus, J. C. Morris, K. Paumier, C. Xiong, R. Allegri, S. B. Berman, W. Klunk, J. Noble, J. Ringman, B. Ghetti, M. Farlow, R. A. Sperling, J. Chhatwal, S. Salloway, N. R. Graff-Radford, P. R. Schofield, C. Masters, M. N. Rossor, N. C. Fox, J. Levin, M. Jucker, and R. J. Bateman. Longitudinal cognitive and biomarker changes in dominantly inherited alzheimer disease. *Neurology*, 91(14):e1295–e1306, 2018.
- G. McKhann, D. Drachman, M. Folstein, R. Katzman, D. Price, and E. M. Stadlan. Clinical diagnosis of alzheimer's disease: report of the nincds-adrda work group under the auspices of department of health and human services task force on alzheimer's disease. *Neurology*, 34(7):939–44, 1984.
- G. M. McKhann, D. S. Knopman, H. Chertkow, B. T. Hyman, J. Jack, C. R., C. H. Kawas, W. E. Klunk, W. J. Koroshetz, J. J. Manly, R. Mayeux, R. C. Mohs, J. C. Morris, M. N. Rossor, P. Scheltens, M. C. Carrillo, B. Thies, S. Weintraub, and C. H. Phelps. The diagnosis of dementia due to alzheimer's disease: recommendations from the national institute on aging-alzheimer's association workgroups on diagnostic guidelines for alzheimer's disease. *Alzheimers Dement*, 7(3):263–9, 2011.

- Medical Research Council. Maximising the value of uk population cohorts mrc strategic review of the largest uk population cohort studies. Report, 2014. URL <http://www.mrc.ac.uk/news-events/publications/maximising-the-value-of-uk-population-cohorts/>.
- H. Mestre, S. Kostrikov, R. I. Mehta, and M. Nedergaard. Perivascular spaces, glymphatic dysfunction, and small vessel disease. *Clin Sci (Lond)*, 131(17):2257–2274, 2017.
- M. M. Mielke, P. B. Rosenberg, J. Tschanz, L. Cook, C. Corcoran, K. M. Hayden, M. Norton, P. V. Rabins, R. C. Green, K. A. Welsh-Bohmer, J. C. Breitner, R. Munger, and C. G. Lyketsos. Vascular factors predict rate of progression in alzheimer disease. *Neurology*, 69(19):1850–8, 2007.
- M. M. Mielke, C. E. Hagen, J. Xu, X. Chai, P. Vemuri, V. J. Lowe, D. C. Airey, D. S. Knopman, R. O. Roberts, M. M. Machulda, J. Jack, C. R., R. C. Petersen, and J. L. Dage. Plasma phospho-tau181 increases with alzheimer’s disease clinical severity and is associated with tau- and amyloid-positron emission tomography. *Alzheimers Dement*, 14(8):989–997, 2018.
- M. M. Mielke, J. A. Syrjanen, K. Blennow, H. Zetterberg, P. Vemuri, I. Skoog, M. M. Machulda, W. K. Kremers, D. S. Knopman, J. Jack, C., R. C. Petersen, and S. Kern. Plasma and csf neurofilament light: Relation to longitudinal neuroimaging and cognitive measures. *Neurology*, 93(3):e252–e260, 2019.
- T. J. Montine, C. H. Phelps, T. G. Beach, E. H. Bigio, N. J. Cairns, D. W. Dickson, C. Duyckaerts, M. P. Frosch, E. Masliah, S. S. Mirra, P. T. Nelson, J. A. Schneider, D. R. Thal, J. Q. Trojanowski, H. V. Vinters, and B. T. Hyman. National institute on aging-alzheimer’s association guidelines for the neuropathologic assessment of alzheimer’s disease: a practical approach. *Acta Neuropathol*, 123(1):1–11, 2012.
- D. M. Moody, C. R. Thore, J. A. Anstrom, V. R. Challa, C. D. Langefeld, and W. R.

- Brown. Quantification of afferent vessels shows reduced brain vascular density in subjects with leukoaraiosis. *Radiology*, 233(3):883–90, 2004.
- E. E. Moore, T. J. Hohman, F. S. Badami, K. R. Pechman, K. E. Osborn, L. M. Y. Acosta, S. P. Bell, M. A. Babicz, K. A. Gifford, A. W. Anderson, L. E. Goldstein, K. Blennow, H. Zetterberg, and A. L. Jefferson. Neurofilament relates to white matter microstructure in older adults. *Neurobiol Aging*, 70:233–241, 2018.
- L. Mosconi, W. H. Tsui, K. Herholz, A. Pupi, A. Drzezga, G. Lucignani, E. M. Reiman, V. Holthoff, E. Kalbe, S. Sorbi, J. Diehl-Schmid, R. Perneczky, F. Clerici, R. Caselli, B. Beuthien-Baumann, A. Kurz, S. Minoshima, and M. J. de Leon. Multicenter standardized 18f-fdg pet diagnosis of mild cognitive impairment, alzheimer’s disease, and other dementias. *J Nucl Med*, 49(3):390–8, 2008.
- N. Mukadam, A. Sommerlad, J. Huntley, and G. Livingston. Population attributable fractions for risk factors for dementia in low-income and middle-income countries: an analysis using cross-sectional survey data. *The Lancet Global Health*, 7(5):e596–e603, 2019.
- D. G. Munoz, S. M. Hastak, B. Harper, D. Lee, and V. C. Hachinski. Pathologic correlates of increased signals of the centrum ovale on magnetic resonance imaging. *Arch Neurol*, 50(5):492–7, 1993.
- M. E. Murray, P. Vemuri, G. M. Preboske, M. C. Murphy, K. J. Schweitzer, J. E. Parisi, J. Jack, C. R., and D. W. Dickson. A quantitative postmortem mri design sensitive to white matter hyperintensity differences and their relationship with underlying pathology. *J Neuropathol Exp Neurol*, 71(12):1113–22, 2012.
- A. Nakamura, N. Kaneko, V. L. Villemagne, T. Kato, J. Doecke, V. Doré, C. Fowler, Q.-X. Li, R. Martins, C. Rowe, T. Tomita, K. Matsuzaki, K. Ishii, K. Ishii, Y. Arahata, S. Iwamoto, K. Ito, K. Tanaka, C. L. Masters, and K. Yanagisawa. High performance plasma amyloid- β biomarkers for alzheimer’s disease. *Nature*, 554(7691):249–254, 2018.

- P. T. Nelson, I. Alafuzoff, E. H. Bigio, C. Bouras, H. Braak, N. J. Cairns, R. J. Castellani, B. J. Crain, P. Davies, K. Del Tredici, C. Duyckaerts, M. P. Frosch, V. Haroutunian, P. R. Hof, C. M. Hulette, B. T. Hyman, T. Iwatsubo, K. A. Jellinger, G. A. Jicha, E. Kovari, W. A. Kukull, J. B. Leverenz, S. Love, I. R. Mackenzie, D. M. Mann, E. Masliah, A. C. McKee, T. J. Montine, J. C. Morris, J. A. Schneider, J. A. Sonnen, D. R. Thal, J. Q. Trojanowski, J. C. Troncoso, T. Wisniewski, R. L. Woltjer, and T. G. Beach. Correlation of alzheimer disease neuropathologic changes with cognitive status: a review of the literature. *J Neuropathol Exp Neurol*, 71(5):362–81, 2012.
- C. Nilsberth, A. Westlind-Danielsson, C. B. Eckman, M. M. Condron, K. Axelman, C. Forsell, C. Stenh, J. Luthman, D. B. Teplow, S. G. Younkin, J. Naslund, and L. Lannfelt. The 'arctic' app mutation (e693g) causes alzheimer's disease by enhanced abeta protofibril formation. *Nat Neurosci*, 4(9):887–93, 2001.
- R. J. O'Brien and P. C. Wong. Amyloid precursor protein processing and alzheimer's disease. *Annu Rev Neurosci*, 34:185–204, 2011.
- A. O'Connor, T. K. Karikari, T. Poole, N. J. Ashton, J. Lantero Rodriguez, A. Khatun, I. Swift, A. J. Heslegrave, E. Abel, E. Chung, P. S. J. Weston, I. M. Pavisic, N. S. Ryan, S. Barker, M. N. Rossor, J. M. Polke, C. Frost, S. Mead, K. Blennow, H. Zetterberg, and N. C. Fox. Plasma phospho-tau181 in presymptomatic and symptomatic familial alzheimer's disease: a longitudinal cohort study. *Mol Psychiatry*, 2020.
- Office for National Statistics. Deaths registered in england and wales: 2018, 2020.
- J. M. Olichney, L. A. Hansen, D. Galasko, T. Saitoh, C. R. Hofstetter, R. Katzman, and L. J. Thal. The apolipoprotein e epsilon 4 allele is associated with increased neuritic plaques and cerebral amyloid angiopathy in alzheimer's disease and lewy body variant. *Neurology*, 47(1):190–6, 1996.
- B. Olsson, R. Lautner, U. Andreasson, A. Öhrfelt, E. Portelius, M. Bjerke, M. Hölttä, C. Rosén, C. Olsson, G. Strobel, E. Wu, K. Dakin, M. Petzold,

- K. Blennow, and H. Zetterberg. Csf and blood biomarkers for the diagnosis of alzheimer's disease: a systematic review and meta-analysis. *Lancet Neurol*, 15 (7):673–684, 2016.
- T. T. Olsson, O. Klementieva, and G. K. Gouras. Prion-like seeding and nucleation of intracellular amyloid- β . *Neurobiology of Disease*, 113:1–10, 2018.
- C. Orczyk, A. Mikheev, A. B. Rosenkrantz, J. Melamed, S. S. Taneja, and H. Rusinek. Imaging of prostate cancer: a platform for 3d co-registration of in-vivo mri ex-vivo mri and pathology. *Proc SPIE Int Soc Opt Eng*, 8316:83162m, 2012.
- K. E. Osborn, D. Liu, L. R. Samuels, E. E. Moore, F. E. Cambroner, L. M. Y. Acosta, S. P. Bell, M. A. Babicz, E. A. Gordon, K. R. Pechman, L. T. Davis, K. A. Gifford, T. J. Hohman, K. Blennow, H. Zetterberg, and A. L. Jefferson. Cerebrospinal fluid beta-amyloid42 and neurofilament light relate to white matter hyperintensities. *Neurobiol Aging*, 68:18–25, 2018.
- K. E. Osborn, J. M. Alverio, L. Dumitrescu, K. R. Pechman, K. A. Gifford, T. J. Hohman, K. Blennow, H. Zetterberg, and A. L. Jefferson. Adverse vascular risk relates to cerebrospinal fluid biomarker evidence of axonal injury in the presence of alzheimer's disease pathology. *J Alzheimers Dis*, 2019.
- R. Ossenkoppele, D. R. Schonhaut, M. Scholl, S. N. Lockhart, N. Ayakta, S. L. Baker, J. P. O'Neil, M. Janabi, A. Lazaris, A. Cantwell, J. Vogel, M. Santos, Z. A. Miller, B. M. Bettcher, K. A. Vessel, J. H. Kramer, M. L. Gorno-Tempini, B. L. Miller, W. J. Jagust, and G. D. Rabinovici. Tau pet patterns mirror clinical and neuroanatomical variability in alzheimer's disease. *Brain*, 139(Pt 5):1551–67, 2016.
- R. Ossenkoppele, R. Smith, T. Ohlsson, O. Strandberg, N. Mattsson, P. S. Insel, S. Palmqvist, and O. Hansson. Associations between tau, $a\beta$, and cortical thickness with cognition in alzheimer disease. *Neurology*, 92(6):e601, 2019.

- S. Ostrowitzki, R. A. Lasser, E. Dorflinger, P. Scheltens, F. Barkhof, T. Nikolcheva, E. Ashford, S. Retout, C. Hofmann, P. Delmar, G. Klein, M. Andjelkovic, B. Dubois, M. Boada, K. Blennow, L. Santarelli, P. Fontoura, and S. R. I. for the. A phase iii randomized trial of gantenerumab in prodromal alzheimer's disease. *Alzheimer's Research and Therapy*, 9(1):95, 2017.
- N. P. Oxtoby and D. C. Alexander. Imaging plus x: multimodal models of neurodegenerative disease. *Curr Opin Neurol*, 30(4):371–379, 2017.
- N. P. Oxtoby, A. L. Young, D. M. Cash, T. L. S. Benzinger, A. M. Fagan, J. C. Morris, R. J. Bateman, N. C. Fox, J. M. Schott, and D. C. Alexander. Data-driven models of dominantly-inherited alzheimer's disease progression. *Brain*, 141(5):1529–1544, 2018.
- M. Pallegage-Gamarallage, S. Foxley, R. A. L. Menke, I. N. Huszar, M. Jenkinson, B. C. Tandler, C. Wang, S. Jbabdi, M. R. Turner, K. L. Miller, and O. Ansorge. Dissecting the pathobiology of altered mri signal in amyotrophic lateral sclerosis: A post mortem whole brain sampling strategy for the integration of ultra-high-field mri and quantitative neuropathology. *BMC Neurosci*, 19(1):11, 2018.
- I. M. Pavisic, J. M. Nicholas, A. Connor, H. Rice, K. Lu, N. C. Fox, and N. S. Ryan. Disease duration in autosomal dominant familial alzheimer disease. *Neurology Genetics*, 6(5):e507, 2020.
- R. C. Petersen, J. E. Parisi, D. W. Dickson, K. A. Johnson, D. S. Knopman, B. F. Boeve, G. A. Jicha, R. J. Ivnik, G. E. Smith, E. G. Tangalos, H. Braak, and E. Kokmen. Neuropathologic features of amnesic mild cognitive impairment. *Arch Neurol*, 63(5):665–72, 2006.
- J. Pichat, J. E. Iglesias, T. Yousry, S. Ourselin, and M. Modat. A survey of methods for 3d histology reconstruction. *Med Image Anal*, 46:73–105, 2018.
- A. M. Pietroboni, M. Scarioni, T. Carandini, P. Basilico, M. Cadioli, G. Giulietti, A. Arighi, M. Caprioli, L. Serra, C. Sina, C. Fenoglio, L. Ghezzi, G. G. Fuma-

- galli, M. A. De Riz, A. Calvi, F. Triulzi, M. Bozzali, E. Scarpini, and D. Galimberti. Csf β -amyloid and white matter damage: A new perspective on alzheimer's disease. *Journal of Neurology, Neurosurgery and Psychiatry*, 89:352–357, 2018.
- T. M. Polvikoski, E. C. Van Straaten, F. Barkhof, R. Sulkava, H. J. Aronen, L. Niinistö, M. Oinas, P. Scheltens, T. Erkinjuntti, and R. N. Kalaria. Frontal lobe white matter hyperintensities and neurofibrillary pathology in the oldest old. *Neurology*, 75:2071–2078, 2010.
- O. Preische, S. A. Schultz, A. Apel, J. Kuhle, S. A. Kaeser, C. Barro, S. Gräber, E. Kuder-Buletta, C. LaFougere, C. Laske, J. Vöglein, J. Levin, C. L. Masters, R. Martins, P. R. Schofield, M. N. Rossor, N. R. Graff-Radford, S. Salloway, B. Ghetti, J. M. Ringman, J. M. Noble, J. Chhatwal, A. M. Goate, T. L. S. Benzinger, J. C. Morris, R. J. Bateman, G. Wang, A. M. Fagan, E. M. McDade, B. A. Gordon, M. Jucker, R. Allegri, F. Amtashar, R. Bateman, T. Benzinger, S. Berman, C. Bodge, S. Brandon, W. Brooks, J. Buck, V. Buckles, S. Chea, J. Chhatwal, P. Chrem, H. Chui, J. Cinco, J. Clifford, C. Cruchaga, M. D'Mello, T. Donahue, J. Douglas, N. Edigo, N. Erekin-Taner, A. Fagan, M. Farlow, A. Farrar, H. Feldman, G. Flynn, N. Fox, E. Franklin, H. Fujii, C. Gant, S. Gardener, B. Ghetti, A. Goate, J. Goldman, B. Gordon, N. Graff-Radford, J. Gray, J. Gurney, J. Hassenstab, M. Hirohara, D. Holtzman, R. Hornbeck, S. H. DiBari, T. Ikeuchi, S. Ikonovic, G. Jerome, M. Jucker, C. Karch, K. Kasuga, T. Kawarabayashi, W. Klunk, R. Koeppe, E. Kuder-Buletta, C. Laske, J.-H. Lee, J. Levin, D. Marcus, R. Martins, N. S. Mason, C. Masters, D. Maue-Dreyfus, E. McDade, L. Montoya, H. Mori, J. Morris, A. Nagamatsu, K. Neimeyer, J. Noble, et al. Serum neurofilament dynamics predicts neurodegeneration and clinical progression in presymptomatic alzheimer's disease. *Nature Medicine*, 25(2): 277–283, 2019.
- M. Prince, E. Albanese, M. Guerchet, and M. Prina. World alzheimer report 2014 dementia and risk reduction an analysis of protective and modifiable factors. *Alzheimer's Disease International*, 2014a.

- M. Prince, M. Knapp, M. Guerchet, P. McCrone, M. Prina, A. Comas-Herrera, R. Wittenberg, B. Adelaja, B. Hu, D. King, A. Rehill, and D. Salimkumar. Dementia uk: Update. alzheimer's society. Report, 2014b.
- M. Prince, A. Wimo, M. Guerchet, G. Ali, Y. Wu, and M. Prina. World alzheimer report 2015 the global impact of dementia. *Alzheimer's Disease International*, 2015.
- N. D. Prins and P. Scheltens. White matter hyperintensities, cognitive impairment and dementia: An update. *Nature Reviews Neurology*, 11:157–165, 2015.
- N. D. Prins, E. J. van Dijk, T. den Heijer, S. E. Vermeer, J. Jolles, P. J. Koudstaal, A. Hofman, and M. M. Breteler. Cerebral small-vessel disease and decline in information processing speed, executive function and memory. *Brain*, 128(Pt 9): 2034–41, 2005.
- F. A. Provenzano, J. Muraskin, G. Tosto, A. Narkhede, B. T. Wasserman, E. Y. Griffith, V. A. Guzman, I. B. Meier, M. E. Zimmerman, and A. M. Brickman. White matter hyperintensities and cerebral amyloidosis: Necessary and sufficient for clinical expression of alzheimer disease? *JAMA Neurology*, 70:455–461, 2013.
- N. Qizilbash, J. Gregson, M. E. Johnson, N. Pearce, I. Douglas, K. Wing, S. J. W. Evans, and S. J. Pocock. Bmi and risk of dementia in two million people over two decades: a retrospective cohort study. *Lancet Diabetes Endocrinol*, 3(6): 431–436, 2015.
- J. S. Rabin, A. P. Schultz, T. Hedden, A. Viswanathan, G. A. Marshall, E. Kilpatrick, H. Klein, R. F. Buckley, H. S. Yang, M. Properzi, V. Rao, D. R. Kirn, K. V. Papp, D. M. Rentz, K. A. Johnson, R. A. Sperling, and J. P. Chhatwal. Interactive associations of vascular risk and beta-amyloid burden with cognitive decline in clinically normal elderly individuals: Findings from the harvard aging brain study. *JAMA Neurol*, 75(9):1124–1131, 2018.

- J. S. Rabin, H. S. Yang, A. P. Schultz, B. J. Hanseeuw, T. Hedden, A. Viswanathan, J. R. Gatchel, G. A. Marshall, E. Kilpatrick, H. Klein, V. Rao, R. F. Buckley, W. W. Yau, D. R. Kirn, D. M. Rentz, K. A. Johnson, R. A. Sperling, and J. P. Chhatwal. Vascular risk and beta-amyloid are synergistically associated with cortical tau. *Ann Neurol*, 85(2):272–279, 2019.
- J. Ramirez, A. A. McNeely, C. Berezuk, F. Gao, and S. E. Black. Dynamic progression of white matter hyperintensities in alzheimer’s disease and normal aging: Results from the sunnybrook dementia study. *Front Aging Neurosci*, 8:62, 2016.
- N. Raz, Y. Yang, C. L. Dahle, and S. Land. Volume of white matter hyperintensities in healthy adults: contribution of age, vascular risk factors, and inflammation-related genetic variants. *Biochim Biophys Acta*, 1822(3):361–9, 2012.
- Y. D. Reijmer, S. J. van Veluw, and S. M. Greenberg. Ischemic brain injury in cerebral amyloid angiopathy. *Journal of cerebral blood flow and metabolism : official journal of the International Society of Cerebral Blood Flow and Metabolism*, 36(1):40–54, 2016.
- D. Renard, G. Castelnovo, A. Wacogne, A. Le Floch, E. Thouvenot, J. Mas, A. Gabelle, P. Labauge, and S. Lehmann. Interest of csf biomarker analysis in possible cerebral amyloid angiopathy cases defined by the modified boston criteria. *Journal of Neurology*, 259(11):2429–2433, 2012.
- T. Revesz, C. P. Hawkins, E. P. du Boulay, R. O. Barnard, and W. I. McDonald. Pathological findings correlated with magnetic resonance imaging in subcortical arteriosclerotic encephalopathy (binswanger’s disease). *J Neurol Neurosurg Psychiatry*, 52(12):1337–44, 1989.
- T. Revesz, J. L. Holton, T. Lashley, G. Plant, A. Rostagno, J. Ghiso, and B. Frangione. Sporadic and familial cerebral amyloid angiopathies. *Brain Pathol*, 12(3):343–57, 2002.
- T. Revesz, J. L. Holton, T. Lashley, G. Plant, B. Frangione, A. Rostagno, and

- J. Ghiso. Genetics and molecular pathogenesis of sporadic and hereditary cerebral amyloid angiopathies. *Acta Neuropathologica*, 118(1):115–130, 2009.
- S. Richardson, B. Siow, E. Panagiotaki, T. Schneider, M. F. Lythgoe, and D. C. Alexander. Viable and fixed white matter: diffusion magnetic resonance comparisons and contrasts at physiological temperature. *Magn Reson Med*, 72(4): 1151–61, 2014.
- B. H. Ridha, J. Barnes, J. W. Bartlett, A. Godbolt, T. Pepple, M. N. Rossor, and N. C. Fox. Tracking atrophy progression in familial alzheimer’s disease: a serial mri study. *Lancet Neurol*, 5(10):828–34, 2006.
- J. M. Ringman, J. O’Neill, D. Geschwind, L. Medina, L. G. Apostolova, Y. Rodriguez, B. Schaffer, A. Varpetian, B. Tseng, F. Ortiz, J. Fitten, J. L. Cummings, and G. Bartzokis. Diffusion tensor imaging in preclinical and presymptomatic carriers of familial alzheimer’s disease mutations. *Brain*, 130(Pt 7):1767–76, 2007.
- J. D. Rohrer, I. O. Woollacott, K. M. Dick, E. Brotherhood, E. Gordon, A. Fellows, J. Toombs, R. Druyeh, M. J. Cardoso, S. Ourselin, J. M. Nicholas, N. Norgren, S. Mead, U. Andreasson, K. Blennow, J. M. Schott, N. C. Fox, J. D. Warren, and H. Zetterberg. Serum neurofilament light chain protein is a measure of disease intensity in frontotemporal dementia. *Neurology*, 87(13):1329–36, 2016.
- G. Roks, F. Van Harskamp, I. De Koning, M. Cruts, C. De Jonghe, S. Kumar-Singh, A. Tibben, H. Tanghe, M. F. Niermeijer, A. Hofman, J. C. Van Swieten, C. Van Broeckhoven, and C. M. Van Duijn. Presentation of amyloidosis in carriers of the codon 692 mutation in the amyloid precursor protein gene (app692). *Brain*, 123 (Pt 10):2130–40, 2000.
- A. Roseborough, J. Ramirez, S. E. Black, and J. D. Edwards. Associations between amyloid β and white matter hyperintensities: A systematic review. *Alzheimer’s and Dementia*, 13:1154–1167, 2017.

- A. D. Roseborough, K. D. Langdon, R. Hammond, L. E. Cipriano, S. H. Pasternak, S. N. Whitehead, and A. R. Khan. Post-mortem 7 tesla mri detection of white matter hyperintensities: A multidisciplinary voxel-wise comparison of imaging and histological correlates. *Neuroimage Clin*, 27:102340, 2020.
- N. S. Ryan and M. N. Rossor. Correlating familial alzheimer's disease gene mutations with clinical phenotype. *Biomark Med*, 4(1):99–112, 2010.
- N. S. Ryan, S. Keihaninejad, T. J. Shakespeare, M. Lehmann, S. J. Crutch, I. B. Malone, J. S. Thornton, L. Mancini, H. Hyare, T. Yousry, G. R. Ridgway, H. Zhang, M. Modat, D. C. Alexander, M. N. Rossor, S. Ourselin, and N. C. Fox. Magnetic resonance imaging evidence for presymptomatic change in thalamus and caudate in familial alzheimer's disease. *Brain*, 136(Pt 5):1399–414, 2013.
- N. S. Ryan, G. J. Biessels, L. Kim, J. M. Nicholas, P. A. Barber, P. Walsh, P. Gami, H. R. Morris, A. J. Bastos-Leite, J. M. Schott, J. Beck, S. Mead, L. Chavez-Gutierrez, B. de Strooper, M. N. Rossor, T. Revesz, T. Lashley, and N. C. Fox. Genetic determinants of white matter hyperintensities and amyloid angiopathy in familial alzheimer's disease. *Neurobiol Aging*, 36(12):3140–3151, 2015.
- N. S. Ryan, J. M. Nicholas, P. S. J. Weston, Y. Liang, T. Lashley, R. Guerreiro, G. Adamson, J. Kenny, J. Beck, L. Chavez-Gutierrez, B. de Strooper, T. Revesz, J. Holton, S. Mead, M. N. Rossor, and N. C. Fox. Clinical phenotype and genetic associations in autosomal dominant familial alzheimer's disease: a case series. *Lancet Neurol*, 15(13):1326–1335, 2016.
- D. C. Ryman, N. Acosta-Baena, P. S. Aisen, T. Bird, A. Danek, N. C. Fox, A. Goate, P. Frommelt, B. Ghetti, J. B. Langbaum, F. Lopera, R. Martins, C. L. Masters, R. P. Mayeux, E. McDade, S. Moreno, E. M. Reiman, J. M. Ringman, S. Salloway, P. R. Schofield, R. Sperling, P. N. Tariot, C. Xiong, J. C. Morris, and R. J. Bateman. Symptom onset in autosomal dominant alzheimer disease: a systematic review and meta-analysis. *Neurology*, 83(3):253–60, 2014.

- P. Sachdev, W. Wen, X. Chen, and H. Brodaty. Progression of white matter hyperintensities in elderly individuals over 3 years. *Neurology*, 68(3):214–22, 2007.
- S. Salloway, R. Sperling, S. Gilman, N. C. Fox, K. Blennow, M. Raskind, M. Sabagh, L. S. Honig, R. Doody, C. H. van Dyck, R. Mulnard, J. Barakos, K. M. Gregg, E. Liu, I. Lieberburg, D. Schenk, R. Black, and M. Grundman. A phase 2 multiple ascending dose trial of bapineuzumab in mild to moderate alzheimer disease. *Neurology*, 73(24):2061–70, 2009.
- S. Salloway, R. Sperling, N. C. Fox, K. Blennow, W. Klunk, M. Raskind, M. Sabagh, L. S. Honig, A. P. Porsteinsson, S. Ferris, M. Reichert, N. Ketter, B. Nejadnik, V. Guenzler, M. Miloslavsky, D. Wang, Y. Lu, J. Lull, I. C. Tudor, E. Liu, M. Grundman, E. Yuen, R. Black, and H. R. Brashear. Two phase 3 trials of bapineuzumab in mild-to-moderate alzheimer’s disease. *N Engl J Med*, 370(4):322–33, 2014.
- R. Sánchez-Valle, G. C. Monté, R. Sala-Llonch, B. Bosch, J. Fortea, A. Lladó, A. Antonell, M. Balasa, N. Bargalló, and J. L. Molinuevo. White matter abnormalities track disease progression in psen1 autosomal dominant alzheimer’s disease. *Journal of Alzheimer’s Disease*, 51:827–835, 2016.
- C. Y. Santos, P. J. Snyder, W. C. Wu, M. Zhang, A. Echeverria, and J. Alber. Pathophysiologic relationship between alzheimer’s disease, cerebrovascular disease, and cardiovascular risk: A review and synthesis. *Alzheimers Dement (Amst)*, 7:69–87, 2017.
- N. Sarbu, R. Y. Shih, R. V. Jones, I. Horkayne-Szakaly, L. Oleaga, and J. G. Smirniotopoulos. White matter diseases with radiologic-pathologic correlation. *Radiographics*, 36(5):1426–47, 2016.
- R. I. Scahill, J. M. Schott, J. M. Stevens, M. N. Rossor, and N. C. Fox. Mapping the evolution of regional atrophy in alzheimer’s disease: unbiased analysis of fluid-registered serial mri. *Proc Natl Acad Sci U S A*, 99(7):4703–7, 2002.

- M. Scarpelli, U. Salvolini, L. Diamanti, R. Montironi, L. Chiaromoni, and M. Maricotti. Mri and pathological examination of post-mortem brains: the problem of white matter high signal areas. *Neuroradiology*, 36(5):393–8, 1994.
- P. Scheltens, F. Barkhof, J. Valk, P. R. Algra, R. G. van der Hoop, J. Nauta, and E. C. Wolters. White matter lesions on magnetic resonance imaging in clinically diagnosed alzheimer’s disease. evidence for heterogeneity. *Brain*, 115 (Pt 3): 735–48, 1992.
- P. Scheltens, F. Barkhof, D. Leys, J. P. Pruvo, J. J. Nauta, P. Vermersch, M. Steinling, and J. Valk. A semiquantative rating scale for the assessment of signal hyperintensities on magnetic resonance imaging. *J Neurol Sci*, 114(1):7–12, 1993.
- P. Scheltens, F. Barkhof, D. Leys, E. C. Wolters, R. Ravid, and W. Kamphorst. Histopathologic correlates of white matter changes on mri in alzheimer’s disease and normal aging. *Neurology*, 45(5):883–8, 1995.
- P. Scheltens, K. Blennow, M. M. Breteler, B. de Strooper, G. B. Frisoni, S. Salloway, and W. M. Van der Flier. Alzheimer’s disease. *Lancet*, 388(10043):505–17, 2016.
- S. Schilling, A. L. DeStefano, P. S. Sachdev, S. H. Choi, K. A. Mather, C. D. DeCarli, W. Wen, P. Høgh, N. Raz, R. Au, A. Beiser, P. A. Wolf, J. R. Romero, Y.-C. Zhu, K. L. Lunetta, L. Farrer, C. Dufouil, L. H. Kuller, B. Mazoyer, S. Seshadri, C. Tzourio, and S. Debette. Apoe genotype and mri markers of cerebrovascular disease: systematic review and meta-analysis. *Neurology*, 81(3):292–300, 2013.
- R. Schmidt, S. Ropele, C. Enzinger, K. Petrovic, S. Smith, H. Schmidt, P. M. Matthews, and F. Fazekas. White matter lesion progression, brain atrophy, and cognitive decline: the austrian stroke prevention study. *Ann Neurol*, 58(4):610–6, 2005.
- J. A. Schneider, Z. Arvanitakis, W. Bang, and D. A. Bennett. Mixed brain pathologies account for most dementia cases in community-dwelling older persons. *Neurology*, 69(24):2197–204, 2007.

- J. A. Schneider, Z. Arvanitakis, S. E. Leurgans, and D. A. Bennett. The neuropathology of probable alzheimer disease and mild cognitive impairment. *Ann Neurol*, 66(2):200–8, 2009.
- J. A. Scott, M. N. Braskie, D. Tosun, P. Maillard, P. M. Thompson, M. Weiner, C. DeCarli, and O. T. Carmichael. Cerebral amyloid is associated with greater white-matter hyperintensity accrual in cognitively normal older adults. *Neurobiology of Aging*, 48:48–52, 2016.
- D. J. Selkoe. Alzheimer’s disease: genotypes, phenotypes, and treatments. *Science*, 275(5300):630–1, 1997.
- D. J. Selkoe and J. Hardy. The amyloid hypothesis of alzheimer’s disease at 25 years. *EMBO molecular medicine*, 8(6):595–608, 2016.
- P. Shahim, Y. Tegner, N. Marklund, K. Blennow, and H. Zetterberg. Neurofilament light and tau as blood biomarkers for sports-related concussion. *Neurology*, 90(20):e1780–e1788, 2018.
- S. Shams, T. Granberg, J. Martola, X. Li, M. Shams, S. M. Fereshtehnejad, L. Cavallin, P. Aspelin, M. Kristoffersen-Wiberg, and L. O. Wahlund. Cerebrospinal fluid profiles with increasing number of cerebral microbleeds in a continuum of cognitive impairment. *Journal of Cerebral Blood Flow and Metabolism*, 36:621–628, 2016.
- G. M. Shankar, S. Li, T. H. Mehta, A. Garcia-Munoz, N. E. Shepardson, I. Smith, F. M. Brett, M. A. Farrell, M. J. Rowan, C. A. Lemere, C. M. Regan, D. M. Walsh, B. L. Sabatini, and D. J. Selkoe. Amyloid-beta protein dimers isolated directly from alzheimer’s brains impair synaptic plasticity and memory. *Nat Med*, 14(8):837–42, 2008.
- A. S. Shatil, M. N. Uddin, K. M. Matsuda, and C. R. Figley. Quantitative ex vivo mri changes due to progressive formalin fixation in whole human brain specimens: Longitudinal characterization of diffusion, relaxometry, and myelin water fraction measurements at 3t. *Front Med (Lausanne)*, 5:31, 2018.

- Y. F. Shea, L. W. Chu, A. O. Chan, J. Ha, Y. Li, and Y. Q. Song. A systematic review of familial alzheimer's disease: Differences in presentation of clinical features among three mutated genes and potential ethnic differences. *J Formos Med Assoc*, 115(2):67–75, 2016.
- C. Shepherd, H. McCann, and G. M. Halliday. Variations in the neuropathology of familial alzheimer's disease. *Acta Neuropathologica*, 118(1):37–52, 2009.
- R. Sherrington, E. I. Rogaev, Y. Liang, E. A. Rogaeva, G. Levesque, M. Ikeda, H. Chi, C. Lin, G. Li, K. Holman, T. Tsuda, L. Mar, J. F. Foncin, A. C. Bruni, M. P. Montesi, S. Sorbi, I. Rainero, L. Pinessi, L. Nee, I. Chumakov, D. Pollen, A. Brookes, P. Sanseau, R. J. Polinsky, W. Wasco, H. A. Da Silva, J. L. Haines, M. A. Pericak-Vance, R. E. Tanzi, A. D. Roses, P. E. Fraser, J. M. Rommens, and P. H. St George-Hyslop. Cloning of a gene bearing missense mutations in early-onset familial alzheimer's disease. *Nature*, 375(6534):754–60, 1995.
- Y. S. Shim, D. W. Yang, C. M. Roe, M. A. Coats, T. L. Benzinger, C. Xiong, J. E. Galvin, N. J. Cairns, and J. C. Morris. Pathological correlates of white matter hyperintensities on magnetic resonance imaging. *Dement Geriatr Cogn Disord*, 39(1-2):92–104, 2015.
- L. C. Silbert, H. H. Dodge, L. G. Perkins, L. Sherbakov, D. Lahna, D. Erten-Lyons, R. Woltjer, L. Shinto, and J. A. Kaye. Trajectory of white matter hyperintensity burden preceding mild cognitive impairment. *Neurology*, 79(8):741–7, 2012.
- R. S. Silva, G. Santos, A. T. Alho, R. C. Neves, L. Luzia, L. T. Grinberg, H. Heinsen, and E. Amaro. White matter hyperintensities analysis by diffusion tensor images obtained from postmortem in cranium whole brain tissue. *Journal of forensic radiology and imaging*, 6:21–27, 2016.
- J. E. Simpson, M. S. Fernando, L. Clark, P. G. Ince, F. Matthews, G. Forster, J. T. O'Brien, R. Barber, R. N. Kalaria, C. Brayne, P. J. Shaw, C. E. Lewis, and S. B. Wharton. White matter lesions in an unselected cohort of the elderly: astrocytic,

- microglial and oligodendrocyte precursor cell responses. *Neuropathol Appl Neurobiol*, 33(4):410–9, 2007a.
- J. E. Simpson, P. G. Ince, C. E. Higham, C. H. Gelsthorpe, M. S. Fernando, F. Matthews, G. Forster, J. T. O'Brien, R. Barber, R. N. Kalaria, C. Brayne, P. J. Shaw, K. Stoeber, G. H. Williams, C. E. Lewis, and S. B. Wharton. Microglial activation in white matter lesions and nonlesional white matter of ageing brains. *Neuropathol Appl Neurobiol*, 33(6):670–83, 2007b.
- M. Sjogren, M. Blomberg, M. Jonsson, L. O. Wahlund, A. Edman, K. Lind, L. Rosengren, K. Blennow, and A. Wallin. Neurofilament protein in cerebrospinal fluid: a marker of white matter changes. *J Neurosci Res*, 66(3):510–6, 2001.
- T. Skillback, B. Farahmand, J. W. Bartlett, C. Rosen, N. Mattsson, K. Nagga, L. Kilander, D. Religa, A. Wimo, B. Winblad, L. Rosengren, J. M. Schott, K. Blennow, M. Eriksson, and H. Zetterberg. Csf neurofilament light differs in neurodegenerative diseases and predicts severity and survival. *Neurology*, 83(21):1945–53, 2014.
- T. Skillback, B. Y. Farahmand, C. Rosén, N. Mattsson, K. Naggga, L. Kilander, D. Religa, A. Wimo, B. Winblad, J. M. Schott, K. Blennow, M. Eriksson, and H. Zetterberg. Cerebrospinal fluid tau and amyloid- β_{1-42} in patients with dementia. *Brain*, 138:2716–2731, 2015.
- I. Skoog, B. Lernfelt, S. Landahl, B. Palmertz, L. A. Andreasson, L. Nilsson, G. Persson, A. Oden, and A. Svanborg. 15-year longitudinal study of blood pressure and dementia. *Lancet*, 347(9009):1141–5, 1996.
- A. J. Slooter, M. Cruts, S. Kalmijn, A. Hofman, M. M. Breteler, C. Van Broeckhoven, and C. M. van Duijn. Risk estimates of dementia by apolipoprotein e genotypes from a population-based incidence study: the rotterdam study. *Arch Neurol*, 55(7):964–8, 1998.
- C. D. Smith, D. Snowden, and W. R. Markesbery. Periventricular white matter hy-

- perintensities on mri: correlation with neuropathologic findings. *J Neuroimaging*, 10(1):13–6, 2000.
- C. D. Smith, E. S. Johnson, L. J. Van Eldik, G. A. Jicha, F. A. Schmitt, P. T. Nelson, R. J. Kryscio, R. R. Murphy, and C. V. Wellnitz. Peripheral (deep) but not periventricular mri white matter hyperintensities are increased in clinical vascular dementia compared to alzheimer’s disease. *Brain Behav*, 6(3):e00438, 2016.
- E. E. Smith. Cerebral amyloid angiopathy as a cause of neurodegeneration. *J Neurochem*, 144(5):651–658, 2018.
- E. E. Smith and S. M. Greenberg. Beta-amyloid, blood vessels, and brain function. *Stroke; a journal of cerebral circulation*, 40:2601–6, 2009.
- D. A. Snowdon, L. H. Greiner, J. A. Mortimer, K. P. Riley, P. A. Greiner, and W. R. Markesbery. Brain infarction and the clinical expression of alzheimer disease. the nun study. *Jama*, 277(10):813–7, 1997.
- R. A. Sperling, J. Jack, C. R., and P. S. Aisen. Testing the right target and right drug at the right stage. *Sci Transl Med*, 3(111):111cm33, 2011.
- M. G. Spillantini and M. Goedert. Tau protein pathology in neurodegenerative diseases. *Trends Neurosci*, 21(10):428–33, 1998.
- M. G. Spillantini and M. Goedert. Tau pathology and neurodegeneration. *The Lancet Neurology*, 12(6):609–622, 2013.
- D. Strozzyk, K. Blennow, L. R. White, and L. J. Launer. Csf abeta 42 levels correlate with amyloid-neuropathology in a population-based autopsy study. *Neurology*, 60(4):652–6, 2003.
- C. H. Sudre, M. J. Cardoso, W. H. Bouvy, G. J. Biessels, J. Barnes, and S. Ourselin. Bayesian model selection for pathological neuroimaging data applied to white matter lesion segmentation. *IEEE Trans Med Imaging*, 34(10):2079–102, 2015.

- W. Swardfager, D. Yu, J. Ramirez, H. Cogo-Moreira, G. Szilagyi, M. F. Holmes, C. J. M. Scott, G. Scola, P. C. Chan, J. Chen, P. Chan, D. J. Sahlas, N. Herrmann, K. L. Lanctôt, A. C. Andreazza, J. A. Pettersen, and S. E. Black. Peripheral inflammatory markers indicate microstructural damage within periventricular white matter hyperintensities in alzheimer's disease: A preliminary report. *Alzheimer's and Dementia: Diagnosis, Assessment and Disease Monitoring*, 7:56–60, 2017.
- R. H. Swerdlow. Mitochondria and mitochondrial cascades in alzheimer's disease. *J Alzheimer's Dis*, 62(3):1403–1416, 2018.
- M. Szaruga, S. Veugelen, M. Benurwar, S. Lismont, D. Sepulveda-Falla, A. Lleo, N. S. Ryan, T. Lashley, N. C. Fox, S. Murayama, H. Gijzen, B. De Strooper, and L. Chávez-Gutiérrez. Qualitative changes in human γ -secretase underlie familial alzheimer's disease. *Journal of Experimental Medicine*, 212(12):2003–2013, 2015.
- M. Tang, D. C. Ryman, E. McDade, M. S. Jasielec, V. D. Buckles, N. J. Cairns, A. M. Fagan, A. Goate, D. S. Marcus, C. Xiong, R. F. Allegri, J. P. Chhatwal, A. Danek, M. R. Farlow, N. C. Fox, B. Ghetti, N. R. Graff-Radford, C. Laske, R. N. Martins, C. L. Masters, R. P. Mayeux, J. M. Ringman, M. N. Rossor, S. P. Salloway, P. R. Schofield, J. C. Morris, and R. J. Bateman. Neurological manifestations of autosomal dominant familial alzheimer's disease: a comparison of the published literature with the dominantly inherited alzheimer network observational study (dian-obs). *Lancet Neurol*, 15(13):1317–1325, 2016.
- T. Tapiola, M. Overmyer, M. Lehtovirta, S. Helisalmi, J. Ramberg, I. Alafuzoff, S. Riekkinen, P., and H. Soininen. The level of cerebrospinal fluid tau correlates with neurofibrillary tangles in alzheimer's disease. *Neuroreport*, 8(18):3961–3, 1997.
- J. M. Tarasoff-Conway, R. O. Carare, R. S. Osorio, L. Glodzik, T. Butler, E. Fieremans, L. Axel, H. Rusinek, C. Nicholson, B. V. Zlokovic, B. Frangione, K. Blennow, J. Ménard, H. Zetterberg, T. Wisniewski, and M. J. de Leon. Clear-

- ance systems in the brain-implications for alzheimer disease. *Nature reviews. Neurology*, 11(8):457–470, 2015.
- C. E. Teunissen and M. Khalil. Neurofilaments as biomarkers in multiple sclerosis. *Mult Scler*, 18(5):552–6, 2012.
- D. R. Thal, E. Ghebremedhin, U. Rub, H. Yamaguchi, K. Del Tredici, and H. Braak. Two types of sporadic cerebral amyloid angiopathy. *J Neuropathol Exp Neurol*, 61(3):282–93, 2002a.
- D. R. Thal, U. Rüb, M. Orantes, and H. Braak. Phases of a beta-deposition in the human brain and its relevance for the development of ad. *Neurology*, 58(12):1791–800, 2002b.
- D. R. Thal, L. T. Grinberg, and J. Attems. Vascular dementia: different forms of vessel disorders contribute to the development of dementia in the elderly brain. *Exp Gerontol*, 47(11):816–24, 2012.
- S. Thanprasertsuk, S. Martinez-Ramirez, O. M. Pontes-Neto, J. Ni, A. Ayres, A. Reed, K. Swords, M. E. Gurol, S. M. Greenberg, and A. Viswanathan. Posterior white matter disease distribution as a predictor of amyloid angiopathy. *Neurology*, 83(9):794–800, 2014.
- K. L. Todd, T. Brighton, E. S. Norton, S. Schick, W. Elkins, O. Pletnikova, R. H. Fortinsky, J. C. Troncoso, P. J. Molfese, S. M. Resnick, J. C. Conover, and I. Alzheimer’s Disease Neuroimaging. Ventricular and periventricular anomalies in the aging and cognitively impaired brain. *Frontiers in aging neuroscience*, 9:445–445, 2018.
- J. B. Toledo, S. X. Xie, J. Q. Trojanowski, and L. M. Shaw. Longitudinal change in csf tau and abeta biomarkers for up to 48 months in adni. *Acta Neuropathol*, 126(5):659–70, 2013.
- E. Tonnes and E. Trushina. Oxidative stress, synaptic dysfunction, and alzheimer’s disease. *Journal of Alzheimer’s disease : JAD*, 57(4):1105–1121, 2017.

- G. Tosto, M. E. Zimmerman, J. L. Hamilton, O. T. Carmichael, and A. M. Brickman. The effect of white matter hyperintensities on neurodegeneration in mild cognitive impairment. *Alzheimer's and Dementia*, 11:1510–1519, 2015.
- M. Tullberg, E. Fletcher, C. DeCarli, D. Mungas, B. R. Reed, D. J. Harvey, M. W. Weiner, H. C. Chui, and W. J. Jagust. White matter lesions impair frontal lobe function regardless of their location. *Neurology*, 63(2):246–53, 2004.
- M. Vagberg, N. Norgren, A. Dring, T. Lindqvist, R. Birgander, H. Zetterberg, and A. Svenningsson. Levels and age dependency of neurofilament light and glial fibrillary acidic protein in healthy individuals and their relation to the brain parenchymal fraction. *PLoS One*, 10(8):e0135886, 2015.
- W. M. van der Flier, I. Skoog, J. A. Schneider, L. Pantoni, V. Mok, C. L. H. Chen, and P. Scheltens. Vascular cognitive impairment. *Nat Rev Dis Primers*, 4:18003, 2018.
- M. S. van der Knaap, I. Boor, and R. Estévez. Megalencephalic leukoencephalopathy with subcortical cysts: chronic white matter oedema due to a defect in brain ion and water homeostasis. *Lancet Neurol*, 11(11):973–85, 2012.
- E. J. van Dijk, N. D. Prins, H. A. Vrooman, A. Hofman, P. J. Koudstaal, and M. M. Breteler. Progression of cerebral small vessel disease in relation to risk factors and cognitive consequences: Rotterdam scan study. *Stroke*, 39(10):2712–9, 2008.
- E. M. van Leijsen, I. W. van Uden, M. Ghafoorian, M. I. Bergkamp, V. Lohner, E. C. Kooijmans, H. M. van der Holst, A. M. Tuladhar, D. G. Norris, E. J. van Dijk, L. C. Rutten-Jacobs, B. Platel, C. J. Klijn, and F.-E. de Leeuw. Nonlinear temporal dynamics of cerebral small vessel disease. *The RUN DMC study*, 89(15):1569–1577, 2017a.
- E. M. van Leijsen, M. I. Bergkamp, I. W. van Uden, S. Cooijmans, M. Ghafoorian, H. M. van der Holst, D. G. Norris, R. P. Kessels, B. Platel, A. M. Tuladhar, and F. E. de Leeuw. Cognitive consequences of regression of cerebral small vessel disease. *Eur Stroke J*, 4(1):85–89, 2019.

- E. M. C. van Leijsen, F. E. de Leeuw, and A. M. Tuladhar. Disease progression and regression in sporadic small vessel disease-insights from neuroimaging. *Clin Sci (Lond)*, 131(12):1191–1206, 2017b.
- E. M. C. van Leijsen, M. I. Bergkamp, I. W. M. van Uden, M. Ghafoorian, H. M. van der Holst, D. G. Norris, B. Platel, A. M. Tuladhar, and F. E. de Leeuw. Progression of white matter hyperintensities preceded by heterogeneous decline of microstructural integrity. *Stroke*, 49(6):1386–1393, 2018.
- S. van Rooden, A. M. van Opstal, G. Labadie, G. M. Terwindt, M. J. Wermer, A. G. Webb, H. A. Middelkoop, S. M. Greenberg, J. van der Grond, and M. A. van Buchem. Early magnetic resonance imaging and cognitive markers of hereditary cerebral amyloid angiopathy. *Stroke*, 47(12):3041–3044, 2016.
- E. C. van Straaten, D. Harvey, P. Scheltens, F. Barkhof, R. C. Petersen, L. J. Thal, J. Jack, C. R., and C. DeCarli. Periventricular white matter hyperintensities increase the likelihood of progression from amnesic mild cognitive impairment to dementia. *J Neurol*, 255(9):1302–8, 2008.
- J. C. van Swieten, J. H. van den Hout, B. A. van Ketel, A. Hijdra, J. H. Wokke, and J. van Gijn. Periventricular lesions in the white matter on magnetic resonance imaging in the elderly. a morphometric correlation with arteriolosclerosis and dilated perivascular spaces. *Brain*, 114 (Pt 2):761–74, 1991.
- D. van Westen, D. Lindqvist, K. Blennow, L. Minthon, K. Nägga, E. Stomrud, H. Zetterberg, and O. Hansson. Cerebral white matter lesions – associations with $\alpha\beta$ isoforms and amyloid pet. *Scientific Reports*, 6:20709, 2016.
- R. Vandenberghe, J. O. Rinne, M. Boada, S. Katayama, P. Scheltens, B. Vellas, M. Tuchman, A. Gass, J. B. Fiebach, D. Hill, K. Lobello, D. Li, T. McRae, P. Lucas, I. Evans, K. Booth, G. Luscan, B. T. Wyman, L. Hua, L. Yang, H. R. Brashear, and R. S. Black. Bapineuzumab for mild to moderate alzheimer’s disease in two global, randomized, phase 3 trials. *Alzheimers Res Ther*, 8(1):18, 2016.

- P. Vemuri and D. S. Knopman. The role of cerebrovascular disease when there is concomitant alzheimer disease. *Biochimica et Biophysica Acta - Molecular Basis of Disease*, 1862:952–956, 2016.
- P. Vemuri, T. G. Lesnick, S. A. Przybelski, D. S. Knopman, G. M. Preboske, K. Kantarci, M. R. Raman, M. M. Machulda, M. M. Mielke, V. J. Lowe, M. L. Senjem, J. L. Gunter, W. A. Rocca, R. O. Roberts, R. C. Petersen, and C. R. Jack. Vascular and amyloid pathologies are independent predictors of cognitive decline in normal elderly. *Brain*, 138:761–771, 2015.
- P. Vemuri, T. G. Lesnick, S. A. Przybelski, D. S. Knopman, V. J. Lowe, J. Graff-Radford, R. O. Roberts, M. M. Mielke, M. M. Machulda, R. C. Petersen, and C. R. Jack. Age, vascular health, and alzheimer disease biomarkers in an elderly sample. *Annals of Neurology*, 82:706–718, 2017.
- V. Venkatraghavan, E. E. Bron, W. J. Niessen, and S. Klein. Disease progression timeline estimation for alzheimer’s disease using discriminative event based modeling. *NeuroImage*, 186:518–532, 2019.
- M. M. Verbeek, B. P. H. Kremer, M. O. Rikkert, P. H. M. F. Van Domburg, M. E. Skehan, and S. M. Greenberg. Cerebrospinal fluid amyloid β 40 is decreased in cerebral amyloid angiopathy. *Annals of Neurology*, 66(2):245–249, 2009.
- V. L. Villemagne, R. S. Mulligan, S. Pejoska, K. Ong, G. Jones, G. O’Keefe, J. G. Chan, K. Young, H. Tochon-Danguy, C. L. Masters, and C. C. Rowe. Comparison of 11c-pib and 18f-florbetaben for $a\beta$ imaging in ageing and alzheimer’s disease. *Eur J Nucl Med Mol Imaging*, 39(6):983–9, 2012.
- H. V. Vinters. Cerebral amyloid angiopathy. a critical review. *Stroke*, 18(2):311–24, 1987.
- A. K. Wallin, K. Blennow, H. Zetterberg, E. Londos, L. Minthon, and O. Hansson. Csf biomarkers predict a more malignant outcome in alzheimer disease. *Neurology*, 74(19):1531–7, 2010.

- P. Walsh, C. H. Sudre, C. M. Fiford, N. S. Ryan, T. Lashley, C. Frost, and J. Barnes. Csf amyloid is a consistent predictor of white matter hyperintensities across the disease course from ageing to alzheimer's disease. *Neurobiology of Aging*, 2020.
- P. Walsh, C. H. Sudre, C. M. Fiford, N. S. Ryan, T. Lashley, C. Frost, and J. Barnes. The age-dependent associations of white matter hyperintensities and neurofilament light in early- and late-stage alzheimer's disease. *Neurobiol Aging*, 97: 10–17, 2021.
- J. M. Wardlaw, E. E. Smith, G. J. Biessels, C. Cordonnier, F. Fazekas, R. Frayne, R. I. Lindley, J. T. O'Brien, F. Barkhof, O. R. Benavente, S. E. Black, C. Brayne, M. Breteler, H. Chabriat, C. Decarli, F. E. de Leeuw, F. Doubal, M. Duering, N. C. Fox, S. Greenberg, V. Hachinski, I. Kilimann, V. Mok, R. Oostenbrugge, L. Pantoni, O. Speck, B. C. Stephan, S. Teipel, A. Viswanathan, D. Werring, C. Chen, C. Smith, M. van Buchem, B. Norrving, P. B. Gorelick, M. Dichgans, and S. T. f. R. V. c. o. nEuroimaging. Neuroimaging standards for research into small vessel disease and its contribution to ageing and neurodegeneration. *Lancet Neurol*, 12(8):822–38, 2013.
- J. M. Wardlaw, M. C. Valdés Hernández, and S. Muñoz-Maniega. What are white matter hyperintensities made of? relevance to vascular cognitive impairment. *Journal of the American Heart Association*, 4:001140, 2015.
- J. M. Wardlaw, S. J. Makin, M. C. Valdés Hernández, P. A. Armitage, A. K. Heye, F. M. Chappell, S. Muñoz-Maniega, E. Sakka, K. Shuler, M. S. Dennis, and M. J. Thruppelton. Blood-brain barrier failure as a core mechanism in cerebral small vessel disease and dementia: evidence from a cohort study. *Alzheimers Dement*, 13(6):634–43, 2017.
- N. A. Weaver, T. Doeven, F. Barkhof, J. M. Biesbroek, O. N. Groeneveld, H. J. Kuijf, N. D. Prins, P. Scheltens, C. E. Teunissen, W. M. van der Flier, and G. J. Biessels. Cerebral amyloid burden is associated with white matter hyperintensity

- location in specific posterior white matter regions. *Neurobiol Aging*, 84:225–234, 2019.
- R. O. Weller, M. Subash, S. D. Preston, I. Mazanti, and R. O. Carare. Perivascular drainage of amyloid- β peptides from the brain and its failure in cerebral amyloid angiopathy and alzheimer's disease. *Brain Pathology*, 18:253–266, 2008.
- R. O. Weller, C. A. Hawkes, R. N. Kalaria, D. J. Werring, and R. O. Carare. White matter changes in dementia: role of impaired drainage of interstitial fluid. *Brain Pathol*, 25(1):63–78, 2015.
- P. S. Weston, T. Poole, N. S. Ryan, A. Nair, Y. Liang, K. Macpherson, R. Drueyeh, I. B. Malone, R. L. Ahsan, H. Pemberton, J. Klimova, S. Mead, K. Blennow, M. N. Rossor, J. M. Schott, H. Zetterberg, and N. C. Fox. Serum neurofilament light in familial alzheimer disease. *A marker of early neurodegeneration*, 89(21): 2167–2175, 2017.
- P. S. J. Weston, T. Poole, A. O'Connor, A. Heslegrave, N. S. Ryan, Y. Liang, R. Drueyeh, S. Mead, K. Blennow, J. M. Schott, C. Frost, H. Zetterberg, and N. C. Fox. Longitudinal measurement of serum neurofilament light in presymptomatic familial alzheimer's disease. *Alzheimer's Research Therapy*, 11(1):19, 2019.
- M. Wilke, B. de Haan, H. Juenger, and H. O. Karnath. Manual, semi-automated, and automated delineation of chronic brain lesions: a comparison of methods. *Neuroimage*, 56(4):2038–46, 2011.
- L. E. M. Wisse, D. H. Adler, R. Ittyerah, J. B. Pluta, J. L. Robinson, T. Schuck, J. Q. Trojanowski, M. Grossman, J. A. Detre, M. A. Elliott, J. B. Toledo, W. Liu, S. Pickup, S. R. Das, D. A. Wolk, and P. A. Yushkevich. Comparison of in vivo and ex vivo mri of the human hippocampal formation in the same subjects. *Cerebral Cortex*, 27(11):5185–5196, 2016.
- M. S. Wolfe. The role of tau in neurodegenerative diseases and its potential as a therapeutic target. *Scientifica*, 2012:796024, 2012.

- I. O. C. Woollacott, M. Bocchetta, C. H. Sudre, B. H. Ridha, C. Strand, R. Courtney, S. Ourselin, M. J. Cardoso, J. D. Warren, M. N. Rossor, T. Revesz, N. C. Fox, J. L. Holton, T. Lashley, and J. D. Rohrer. Pathological correlates of white matter hyperintensities in a case of progranulin mutation associated frontotemporal dementia. *Neurocase*, 24(3):166–174, 2018.
- T. Wyss-Coray and J. Rogers. Inflammation in alzheimer disease-a brief review of the basic science and clinical literature. *Cold Spring Harb Perspect Med*, 2(1):a006346, 2012.
- C. Xia, S. J. Makaretz, C. Caso, S. McGinnis, S. N. Gomperts, J. Sepulcre, T. Gomez-Isla, B. T. Hyman, A. Schultz, N. Vasdev, K. A. Johnson, and B. C. Dickerson. Association of in vivo [18f]av-1451 tau pet imaging results with cortical atrophy and symptoms in typical and atypical alzheimer disease. *JAMA Neurol*, 74(4):427–436, 2017.
- E. Yang, M. Farnum, V. Lobanov, T. Schultz, N. Raghavan, M. N. Samtani, G. Novak, V. Narayan, A. DiBernardo, , and I. the Alzheimer’s Disease Neuroimaging. Quantifying the pathophysiological timeline of alzheimer’s disease. *Journal of Alzheimer’s Disease*, 26:745–753, 2011.
- A. Ylikoski, T. Erkinjuntti, R. Raininko, S. Sarna, R. Sulkava, and R. Tilvis. White matter hyperintensities on mri in the neurologically nondiseased elderly. analysis of cohorts of consecutive subjects aged 55 to 85 years living at home. *Stroke*, 26(7):1171–7, 1995.
- M. Yoshita, E. Fletcher, D. Harvey, M. Ortega, O. Martinez, D. M. Mungas, B. R. Reed, and C. S. DeCarli. Extent and distribution of white matter hyperintensities in normal aging, mci, and ad. *Neurology*, 67(12):2192–8, 2006.
- V. G. Young, G. M. Halliday, and J. J. Kril. Neuropathologic correlates of white matter hyperintensities. *Neurology*, 71(11):804–11, 2008.
- H. Zetterberg and K. Blennow. From cerebrospinal fluid to blood: The third wave

- of fluid biomarkers for alzheimer's disease. *J Alzheimers Dis*, 64(s1):S271–s279, 2018.
- H. Zetterberg, T. Skillback, N. Mattsson, J. Q. Trojanowski, E. Portelius, L. M. Shaw, M. W. Weiner, and K. Blennow. Association of cerebrospinal fluid neurofilament light concentration with alzheimer disease progression. *JAMA Neurol*, 73(1):60–7, 2016.
- B. Zhou, S. Teramukai, K. Yoshimura, and M. Fukushima. Validity of cerebrospinal fluid biomarkers as endpoints in early-phase clinical trials for alzheimer's disease. *J Alzheimers Dis*, 18(1):89–102, 2009.
- Y. Zhou, F. Yu, and T. Q. Duong. White matter lesion load is associated with resting state functional mri activity and amyloid pet but not fdg in mild cognitive impairment and early alzheimer's disease patients. *Journal of Magnetic Resonance Imaging*, 41:102–109, 2015.
- B. V. Zlokovic. Neurovascular pathways to neurodegeneration in alzheimer's disease and other disorders. *Nature Reviews Neuroscience*, 12(12):723–738, 2011.